Durham E-Theses

Resonant Soft X-ray Scattering from Complex Magnetic Structures

DEAN, PHILIP,RICHARD

Resonant Soft X-ray Scattering from Complex Magnetic Structures

Philip R. Dean

A Thesis Presented for the Degree of

Doctor of Philosophy

Supervised by Proffessor Peter Hatton

X-ray Scattering and Magnetism

Department of Physics

University of Durham

England

November 2016

"Philosophy" means "love of wisdom". It comes from the ancient Greek words "philo", meaning "love", and "sophia", meaning wisdom.

Abstract

This thesis lays out a number of investigations into different magnetic systems governed by short- and long-range magnetic interactions. We take advantage of the sensitivity of soft x-rays to magnetism and the polarisation dependence of magnetic x-ray scattering to investigate these systems.

Full polarisation analysis is a highly sensitive technique which can be utilised to refine small deviations in magnetic structures. We present work on improving the efficiency of these measurements, finding efficiencies of up to 75% in the measurement method by rotating the incident light angle with the polarisation analyser fixed at the peak of intensity.

Full polarisation analysis has been applied to the study of magnetism in the heavy fermion system $CeRu_2Al_{10}$. Although this system has a relatively simple magnetic structure it is highly unstable to doping and has an anomalously high transition temperature. Magnetic scattering was observed at the cerium M-edges and the polarisation dependence of the scattering is only consistent with a non-collinear magnetic structure. Least squares fitting of the non-collinear structure revealed a small spin canting of the magnetic structure towards the a-axis. This canting requires a symmetry lowering of the space group from $Cmcm$ to the subgroup $Pmnm$ to allow for the Dzyaloshinskii-Moriya interaction.

Full polarisation analysis as well as neutron powder and single crystal measurements have been undertaken on the multiferroic skyrmion system Cu_2OSeO_3. Measurements were taken in the helical, conical, skyrmion, and ferrimagnetic regions. The $(1, 0, 0)$ reflection at the Cu L-edge was found to be due to the anisotropy of the tensor of x-ray susceptibility (ATS). The satellite reflections around the ATS peak were observed not to display the polarisation dependence expected for a helix. The polarisation dependence observed is not consistent with a non-collinear structure and can be fitted with a long spin density wave with the moment pointing along the scattering vector. This structure would be expected to produce stepped features in the magnetisation measurements which are not observed. This long spin density wave structure is also not consistent with previous Lorentz transmission electron microscopy measurements. Neutron scattering measurements confirm the three up one down magnetic structure in the ferrimagnetic phase. However, the magnetic

intensity at the $(1, 0, 0)$ position in the helical phase indicates a change in the magnetic structure Rietveld refinement fitting with a reduced ferrimagnetic structure where one of the $4a$ site copper moments is coupled antiferromagnetically to the $12b$ and remaining $4a$ site moments.

Finally, the magnetic properties of thin films have been investigated using absorption techniques and x-ray magnetic circular dichroism. Manganese oxide monolayers and bilayers have been grown in different charge environments provided by heterostructuring with $SrTiO_3$ and $LaAlO_3$, with the aim of controlling the magnetic properties of the manganese *via* charge transfer. It was found that the magnetic properties of the manganese is strongly linked to the capping layer used. This is due to different effects introduced by the growth of the different capping layers; $LaAlO_3$ introducing strong ion intermixing, and $SrTiO_3$ introducing oxygen vacancies. Both capping layers displayed superparamagnetic temperature and field dependent properties with small clusters (around 4) of strongly interacting manganese ions. The strongly interacting manganese ions are separated by either the ion intermixing or oxygen vacancies. Both capping layers displayed superparamagnetic temperature and field dependent properties. Superparamagnetism is usually only observed in nanoparticles. The elimination of the magnetic interactions required for nanoparticle-like properties to be possible are due to a combination of ion intermixing and oxygen vacancies.

Declaration

The work in this thesis is based on research carried out at the Department of Physics, Durham, England. No part of this thesis has been submitted elsewhere for any other degree or qualification and it is all my own work unless referenced to the contrary in the text.

Acknowledgements

I would like to take this opportunity to thank the many people who have worked behind the scenes, as it were, in the production of this thesis.

I would like to begin by thanking M. Imran who wrote the basis for this thesis template, albeit now largely adapted.

I acknowledge all the staff at the beamlines who worked weekends and evenings to ensure that our experiments ran effectively. From the beamlines at the Diamond light source: I16; Dan Porter, and Steve Collins, I06; Sarnjeet Dhesi, I10; Alexey Dobrynin, Raymond Fan, Paul Steadman, and Mark Sussmuth. From XMaS at the ESRF; Simon Brown, Oier Bikondoa, Didier Wermeille, Laurence Bouchenoire, and Paul Thompson, and from P09 at the PETRA III synchrotron; Jorg Strempfer. I would like to thank Pascal Manuel and Dmitry Khalyavin from the Wish beamline at ISIS who were not only there day and night during our experiment but have also been invaluable in the analysis process afterwards.

My thanks to Branton Campbell who helped with the use of his program ISODIS-TORT and to Qing (Helen) He who supervised my XMCD measurements. The members of staff in the Durham Physics department, in particular John Dobson without whom the rotating anode x-ray generator would have been cast out as scrap many years ago. Also Stephen Lishman and the mechanical workshop team who always found the time to get jobs done in time.

I would also like to thank Ales Štefančič for his help with a very temperamental MPMS. And Thomas Frawley for being a year ahead of me in his studies and being both able and willing to guide me through my PhD.

Finally I would like to thank Francis Ridgeon and Tim Dean, who have proofread this thesis and corrected many of it's spelling and grammars.

To my family,

for their support throughout my life and for allowing me to follow my curiosity.

I'll get a real job at some point.

Probably.

Contents

All the text in red throughout this thesis is hyperlinked to the page/figure/chapter/reference within this document. Where possible references are also linked, in blue, to the external website where they are available.

II   Magnetic Structure Determination in Single Crystals

III   The Magnetic Properties of Manganese Oxide Mono- and Bi-layers in Different Charge Environments   175

7   Sample Growth and the Properties of Thin-Film Perovskite Structures   177

Part I

Background

Chapter 1

Introduction

Modern technology is based on the electronic properties of crystalline systems. *p-n* junctions between semiconductors form the transistors which make up the processing power of computer chips, and magnetism giving the ability to store data by the magnetisation direction of metals. X-rays scatter from the electron cloud and are therefore sensitive to electronic properties of materials, as the electric and magnetic forces are coupled x-rays are also sensitive to magnetism, although weakly. The first example of this was shown in nickel oxide by DeBergevin and Brunel in 1972 [1] with a count rate of just 125 counts per hour. This thesis focusses on using resonant x-rays to study magnetism. Resonant x-rays are tuned to specific energies to excite electronic transitions of specific elements. Resonant scattering gives a large increase in the scattered intensity and also increases the sensitivity to magnetism. A resonant enhancement was first predicted by Blume in 1985 [2] with the first example of resonant magnetic scattering from a ferromagnet observed in 1985 in nickel by Namikawa *et al.* [3]. The first example of resonant magnetic scattering from an antiferromagnet was seen in 1988 in holmium by Gibbs *et al.* [4] (holmium has a long-period antiferromagnetic helical structure). This included observation of a polarisation dependence to the scattering. The theory for resonant magnetic x-ray scattering including its polarisation dependence was then formulated a year later in 1989 by Hannon, Trammel, Blume, and Gibbs [5].

The focus of this thesis is the study of magnetic systems, it is however, not limited to the study of materials with magnetic properties that can necessarily be applied to make useful devices. It is instead concerned with the study of magnetic

systems from a more fundamental viewpoint where systems with interesting and novel properties are investigated. Magnetism is a rich subject where the magnetic moments in materials can form exotic shapes, for example, magnetic helices (where the head of the magnetic moment follows a helix as you travel through a material) can form or the recent hot topic of skyrmions where the moments form into a whirlpool-like vortex. It is systems such as these that will be investigated here.

This thesis primarily uses soft x-rays which are in the approximate range 100-5000 eV. X-rays in this energy range are strongly absorbed by air and experiments must be carried out in vacuum. The advantage of soft x-rays is that they excite electrons from the core levels to the orbitals near the Fermi level which are directly involved in the magnetism. This is in contrast to the use of hard x-rays which excite electrons to higher orbitals which are only sensitive to the magnetism by exchange. However, as the diffraction pattern is dependent upon Bragg's law, $n\lambda = 2d\sin\theta$, where λ is the wavelength, d is the lattice spacing, and θ is half the scattering angle, at lower energies (longer wavelengths) the scattering angle increases. This often pushes the Bragg peaks above $90°$ in θ which would require the detector to be placed above $180°$ which is not possible.

1.1   Plan of Thesis

The remainder of this chapter will introduce x-rays and their basic interactions with free electrons and then materials and then ordered crystal systems. Some of the basic crystal properties which can be observed with x-rays will then be introduced. Chapter 2 describes the theoretical basis for both resonant and non-resonant magnetic scattering and derives how the x-ray polarisation is affected when scattering from a magnetic Bragg peak. Chapter 3 describes the experimental techniques used with descriptions of the production of x-rays and neutrons as well as descriptions of the different synchrotron beamlines used.

The remainder of the thesis is split into two parts. Part one focusses on the study of magnetism in bulk single crystals using the polarisation dependence of magnetic scattering to determine magnetic structures. Chapter 4 introduces the formalism for polarisation analysis and investigates improvements to the measurement metrol-

ogy. Chapter 5 investigates the heavy fermion Kondo semiconducting compound $CeRu_2Al_{10}$ with an unusually high magnetic transition temperature. Chapter 6 investigates the multiferroic system Cu_2OSeO_3 which displays a magnetic skyrmion phase.

The second part uses x-ray magnetic circular dichroism and x-ray absorption measurements to determine the magnetic properties of thin film samples of MnO_2 mono- and bi-layers in different charge environments. This section is split into three chapters. The first chapter in this part, chapter 7 is an introductory chapter covering the properties of thin films as well as sample growth. Chapter 8 comprises the experimental results and analysis of the monolayer samples. Chapter 9 comprises the experimental results and analysis of the bilayer samples. The final chapter of this thesis, chapter 10, is a summary of the overall conclusions and suggestions for future work.

1.2   X-rays

X-rays were first discovered by Wilhelm Röentgen in 1895 [6][1] while studying cathode ray tubes. He studied them so thoroughly that no new information was discovered about them for over a decade. X-rays were already being used in medicine as little as a month after their discovery, but it was not until the later discovery of interference effects in scattering from crystal systems by Max von Laué in 1912 [7,8] that their uses in the study of condensed matter systems began to be realised. This was furthered by the development of Bragg's law named after William Lawrence Bragg in 1915 [9]. Bragg was later awarded the Nobel Prize in physics along with his father William Henry Bragg for their important work on crystal structures[2]. Synchrotron radiation is created when charged particles are accelerated[3], the energy of the emitted radiation being dependent upon the acceleration particle speed and mass [10]. Originally synchrotron radiation was an inhibiting factor in particle

---

[1]This reference is a reprint of the original work.

[2]At the age of 25 William Lawrence Bragg remains the youngest ever recipient of the Physics prize.

[3]Here acceleration is taken to be a change in velocity so a particle with a constant velocity travelling on a curved path is accelerating.

collider efficiency[4], however, it was realised that this radiation could be utilised for condensed matter physics applications. A new generation of synchrotrons was built where a constant beam of electrons/positrons was maintained in the ring for the sole purpose of producing radiation in the x-ray regime. Modern synchrotrons have insertion devices which utilise permanent magnets to make the electrons follow tight sinusoidal paths. The magnet spacing and separation can be altered to change the emitted photon energy and polarisation [11].

With the advent of high intensity tuneable x-ray sources, in the form of synchrotron particle accelerators [12], a wide range of different techniques are now available to study anything from the structures of proteins [13] to determining complex magnetic structures [14,15] or building 3D models of objects using x-ray tomography [16]. The tunability of synchrotron sources allows the generation of x-rays with specific energies, these can be tuned to correspond to electronic transitions specific to certain elements (resonant scattering). In this resonant scattering the x-rays can become sensitive to magnetism and other properties of the specific atoms being excited.

1.3   Photons and Free Electrons

Within quantum electrodynamics [17] the photon is the gauge boson of the electromagnetic force and mediates any interaction between charged particles. As such, interactions between photons and electrons can occur. Referring to Feynman diagrams, at each vertex one photon can interact with two electrons, for a real process at least two vertices are required. The minimal process for a photon and a free electron is described by the Feynman diagram [18] shown in figure 1.1. As two vertices must be present the processes of a single photon being absorbed by an electron, or of a single photon being emitted by an electron, are not possible.

This is due to the conservation of energy and momentum where the equation, $E^2 = p^2 c^2 + m^2 c^4$, must hold. As a free electron only has kinetic energy it cannot absorb both the momentum and the energy of the photon while conserving both values. This then explains why two vertices are needed (so that two photons are

---

[4]The energy being radiated by the particles as photons instead of increasing their kinetic energy.
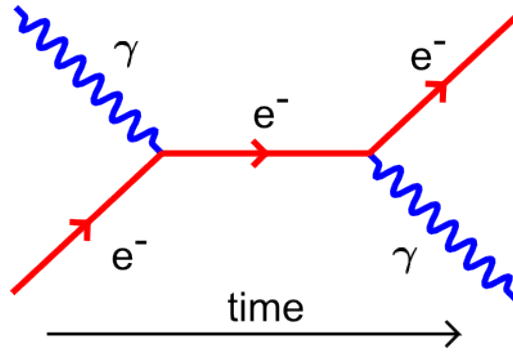
Figure 1.1: Feynman diagram for interaction of a photon and an electron.

involved), we can see that when a photon and an electron are incident we must have a photon and an electron after the interaction, but with different momenta. This would appear to cause problems later on in this thesis where we will discuss free electrons emitting photons whilst accelerated under a magnetic field in a synchrotron. However, this is easily solved by moving to the centre of mass frame of the electron where now the electron sees a moving magnetic field which is equivalent to a changing electric field and hence a photon.

1.4 Photons in a Dielectric Medium - Absorption

The classical interactions of light with materials are governed simply by the three processes of reflection, refraction, and diffraction. Absorption adds anomalous effects from the quantised nature of the electron energy levels and only changes the lights intensity[5]. Absorption can only occur in atomic systems where the photon causes a promotion of electrons between lower and higher energy levels. This again stems from the conservation of energy-momentum where now with the electron bound to an atom the energy level of the electron orbit can change.

To describe absorption effects the starting point of Maxwell's equations in a

---

[5]Non-linear optical effects such as birefringence can effect the lights properties, such as its polarisation, through processes such as absorption.

dielectric material is taken [19]:

$$\boldsymbol{\nabla}.\mathbf{E} = -\frac{1}{\epsilon}\boldsymbol{\nabla}.\mathbf{P}\,, \tag{1.1a}$$

$$\boldsymbol{\nabla}.\mathbf{B} = 0\,, \tag{1.1b}$$

$$\boldsymbol{\nabla}\times\mathbf{E} = -\frac{\delta\mathbf{B}}{\delta t}\,, \tag{1.1c}$$

$$\boldsymbol{\nabla}\times\mathbf{B} = \mu\frac{\delta\mathbf{P}}{\delta t} + \mu\epsilon\frac{\delta\mathbf{E}}{\delta t}\,. \tag{1.1d}$$

Where $\mathbf{E}$ and $\mathbf{B}$ are the electric and magnetic fields, $\mathbf{P}$ is the polarisation of the dielectric, μ and ϵ are the permeability and permittivity of the dielectric. Taking the curl of 1.1c and using the vector identity $\boldsymbol{\nabla}\times(\boldsymbol{\nabla}\times\mathbf{E}) = \boldsymbol{\nabla}(\boldsymbol{\nabla}.\mathbf{E}) - \nabla^2\mathbf{E}$ and substituting into 1.1d gives the following:

$$\boldsymbol{\nabla}(\boldsymbol{\nabla}.\mathbf{E}) - \nabla^2\mathbf{E} = -\frac{1}{\epsilon c^2}\frac{\delta^2\mathbf{P}}{\delta t^2} - \frac{1}{c^2}\frac{\delta^2\mathbf{E}}{\delta t^2}\,. \tag{1.2}$$

Substituting this into 1.1a results in:

$$\nabla^2\mathbf{E} - \frac{1}{c^2}\frac{\delta^2\mathbf{E}}{\delta t^2} = -\frac{1}{\epsilon}\boldsymbol{\nabla}(\boldsymbol{\nabla}.\mathbf{P}) + \frac{1}{\epsilon c^2}\frac{\delta^2\mathbf{P}}{\delta t^2}\,. \tag{1.3}$$

To make progress we assume that our dielectric is isotropic so that $\boldsymbol{\nabla}.\mathbf{P} = 0$ and taking the electric field described for a plane wave of amplitude E_0, travelling along z with angular frequency, ω and wavevector, k, as $E_x = E_0 e^{i(\omega t - kz)}$, we can obtain the result:

$$-k^2 E_x + \frac{\omega^2}{c^2}E_x = \frac{1}{\epsilon c^2}\frac{\delta^2\mathbf{P}}{\delta t^2}\,. \tag{1.4}$$

As the polarisation is dependent upon the stimulus of the electric field it can be assumed to have the same time dependence as the electric field from $E_x = E_0 e^{i(\omega t - kz)}$, then equation 1.4 becomes:

$$-k^2 E_x + \frac{\omega^2}{c^2}E_x = -\frac{\omega^2}{\epsilon c^2}P_x\,. \tag{1.5}$$

For an electron cloud of charge q, bound classically, and acted on by a varying electric field, the following relation is derived (Appendix A):

$$P = \frac{q^2/m}{-i\gamma\omega t + \omega^2 - \omega_0^2}E\,. \tag{1.6}$$

Where the γ term is a damping term carried through from the equations of a harmonic oscillator, ω_0 is the resonant frequency of the electron. Substituting this into

1.5 gives the following equation:

$$-k^2 E_x + \frac{\omega^2}{c^2} E_x = -\frac{\omega^2}{\epsilon c^2} \frac{q^2/m}{-i\gamma\omega t + \omega^2 - \omega_0^2} E_x \, . \tag{1.7}$$

Then the E_x terms cancel and rearranging gives the result:

$$1 + \frac{1}{\epsilon} \frac{q^2/m}{-i\gamma wt + w^2 - w_0^2} = \frac{k^2 c^2}{\omega^2} = n^2 \, . \tag{1.8}$$

Where n is the refractive index, which in a material, as we have seen, becomes complex. This imaginary term now acts as a decaying exponential for the magnitude of a travelling wave through a material.

Expanding the definition of the refractive index to $n = 1 - \delta + i\beta$ where δ and β are known as the optical constants. The real part of the optical constant is then linked to the imaginary part as the material is undergoing a linear physical response to a stimulus. If one of the properties is known over a large range in frequency space the other parameter can be determined *via* a Kramers-Kronig relation [20]:

$$\beta(\omega) = \frac{2}{\pi} P \int_0^\infty \frac{\omega' \sigma(\omega')}{\omega'^2 - \omega^2} d\omega' \, . \tag{1.9}$$

Where P is the Cauchy principle value, which allows the evaluation of certain, usually undefined, improper integrals. σ denotes the real part of the refractive index defined as $\sigma = 1 - \delta$.

1.4.1 Refractive Index for X-rays

Using a simple model for a copper atom, consisting of simple harmonic oscillators with resonant frequencies corresponding to the different electronic transitions can provide a useful insight into the optical properties of solids. Using a simplified version of equation 1.8 where q, m, $\epsilon_0 = 1$ we can plot the delta and beta optical constants, this is done in figure 1.2. To provide an appreciable width to the resonant features gamma is set to 4.

The visible light spectrum is in the range $\sim$2-3.5 eV, from the figure this region lies below any of the absorption edges and has negative δ values, giving refractive indices larger than 1. It is often quoted that the refractive index for x-rays is less than one, however, we can see that this is not always the case and that this is a generalisation, referring to high energy x-rays which will be on the positive tail
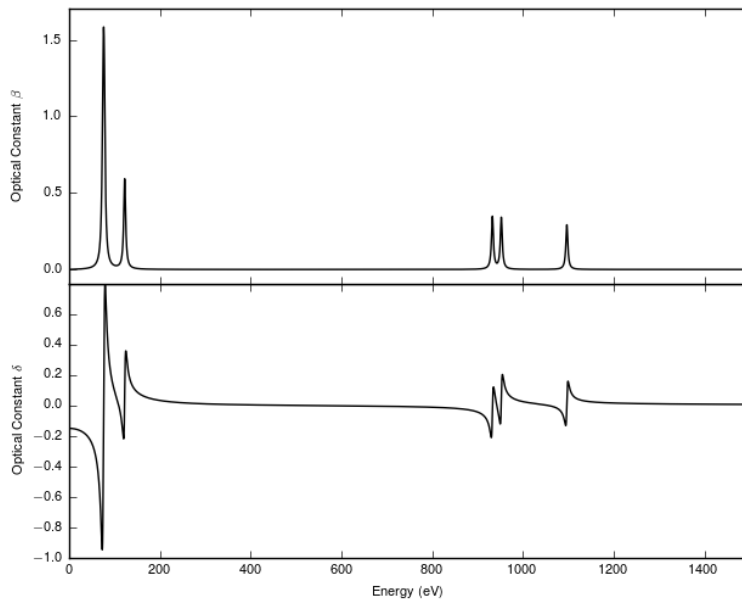
Figure 1.2: Model of a copper atom as a number of simple harmonic oscillators with β (top) and δ (bottom) optical constants.

above the highest energy absorption edge. For the case of a refractive index less than one, refraction will occur away from the interface when going from a less dense to a more dense medium. The relation $v = c/n$ gives the speed of light in the media to be greater than the speed of light in a vacuum. This velocity derives from the dispersion relation ω/k which gives the phase velocity of light, the group velocity is the speed of information transfer and it is this that cannot be exceeded.

1.5 Long Range Order, Crystals, Diffraction, and Symmetry

In this section we will look at different long range orderings that crystals can display and then how these can affect diffraction. Finally we will introduce irreducible representations which are a useful basis for analysis.

1.5.1 Charge Ordering

Charge ordering is characterised by a phase transition involving charge segregation from a mixed valence state to an ordered arrangement of localised ions, it was first observed by E. J. W. Verwey in 1939 [21]. A system with a mixed valence of $Mn^{3.5+}$,

can undergo a lower temperature charge ordering transition to Mn^{3+} and Mn^{4+}. These localised Mn^{3+} and Mn^{4+} can form into a number of different long range ordered arrangements such as stripes or checkerboard patterns. Charge segregation is not always complete and in such cases must be thought of as a charge density wave, the peaks and troughs of the charge density wave are then not constrained to coincide with the atomic positions (although they often do) and in this case are generally called incommensurate charge density waves.

In an ionic picture of a lattice the mixed valence state could be thought of as localised ions and as such there is only ever Mn^{3+} and Mn^{4+}, however, their positions are constantly changing as they exchange electrons and could be thought of as being in a similar state to a paramagnet. An alternate picture could be of a band structure where the electronic charges on the manganese are evenly spread out across all the sites and there is truly an $Mn^{3.5+}$ valence. The band structure picture is more useful when thinking about incommensurate structures and charge density waves, as it is difficult to picture a repeating structure of a different periodicity to the lattice with fixed charges.

1.5.2   Orbital Ordering and Jahn-Teller Distortions

Orbital ordering is a preferential occupation of one (usually degenerate) orbital over another or where the orbital orientation/occupation is ordered in some long-range pattern. Orbital ordering was first predicted by J. B. Goodenough in 1955 [22] when investigating the ground state of cubic perovskite manganites. Jahn-Teller distortions are a special case of orbital ordering which induce a structural distortion and it was actually Jahn-Teller distortions which were predicted by Goodenough. Jahn-Teller distortions are prevalent in transition metals in octahedral crystal fields. In the octahedral arrangement the degeneracy of the $5d$-orbitals (whose spatial distribution is depicted in figure 1.3) is lifted and two higher energy (e_g) and three lower energy (t_{2g}) states form. This is due to symmetry, as the e_g orbitals have electron density oriented directly towards the surrounding negatively charged ligands and so require more energy to fill. The electrons preferentially fill the lower energy t_{2g} orbitals and this causes the distortion.

Jahn and Teller [24] found that systems with unequally occupied degenerate
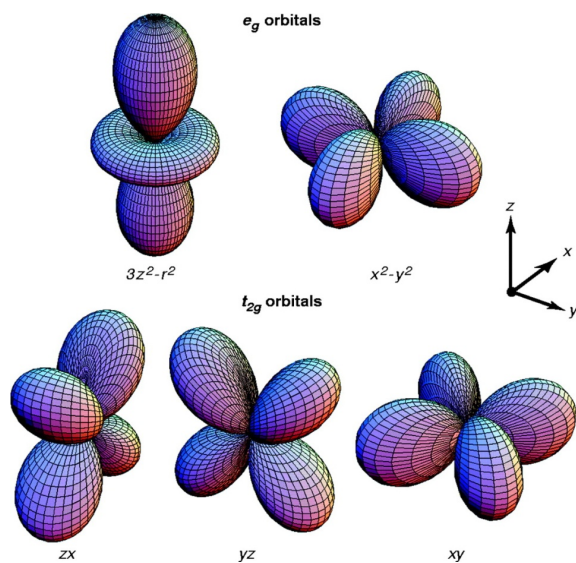
Figure 1.3: The 5 degenerate d-orbitals for a free atom [23]
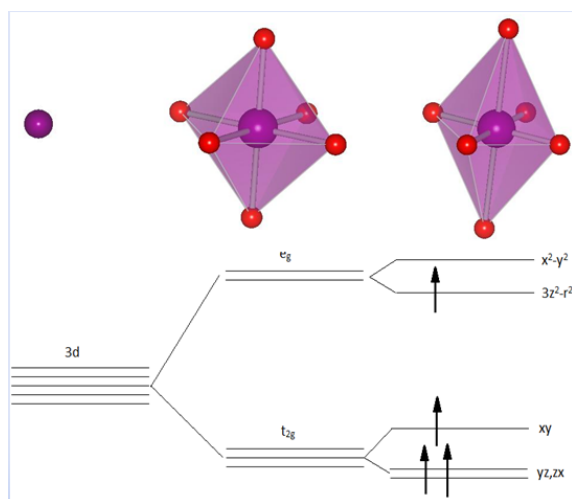
Figure 1.4: Schematic of the energy levels for a free atom, an atom in an octahedral crystal field, and an atom in a Jahn-Teller distorted Mn^{3+} octahedra.

states cannot be stable and a structural distortion will occur which will lift the degeneracy. We will take the case of an Mn^{3+} ion which has four outer electrons, filling the states *via* Hund's rules each of the three t_{2g} states will contain one electron. The position of the final electron then depends upon the specific crystal field environment. In manganese the crystal field splitting is small enough so the final electron occupies the e_g level, instead of pairing with one of the electrons in the t_{2g}. There is then an unequally occupied degenerate state in the e_g level so from Jahn and Teller [24] a structural distortion is expected. In this case the structural distortion manifests as a lengthening of the manganese oxygen bonds for the apical (top and bottom) oxygens and a reduction in the planar bond distances. The result of this distortion is a lifting of the degeneracy of the e_g levels with the $3z^2 - r^2$ orbital becoming lower in energy and the $x^2 - y^2$ orbital increasing in energy, resulting in a net lowering of the energy of the system, this is shown in figure 1.4. For other manganese valencies, for example Mn^{4+}, which has three outer electrons, all in the t_{2g} levels, there will not be a Jahn-Teller distortion. This is because the splitting caused by a Jahn-Teller distortion keeps the same average energy of the d-orbitals. So for the Mn^{4+} case where the t_{2g} orbitals are equally occupied the decrease in energy of the zx and yz orbitals will be counteracted by the increase in energy of the xy orbital and there will be no net energy gain. Co-operative Jahn-Teller distortions are where the Jahn-Teller distortions form an ordered pattern within a lattice.

1.6 Magnetism

Magnetic fields are generated by moving charges. On a macroscopic level this is realised as the magnetic fields set up around wires carrying current. Just as a magnetic field can be generated by electrons travelling in a current loop, on an atomic level magnetism derives from the spin and orbital properties of the electrons, and creates a field of the same shape. The magnetic moment of the atom is described by a dipolar vector quantity. The electrons in an atom fill up the energy levels according to Hund's rules, coupling electrons with opposite spins and electrons with opposite orbital motions such that a complete sub-shell will have no magnetic moment, this can be seen as the total angular momentum of a complete sub-shell is

zero. Magnetism therefore only occurs due to the unpaired outer electrons. Any atom with a non-zero total angular momentum quantum number j would therefore be expected to posses a magnetic moment.

However, all atoms regardless of whether they have a magnetic moment or not still interact with external magnetic fields. On a macroscopic level this is a result of Lenz's law and the electrons in conducting materials in a varying magnetic field will set up eddy currents which produce magnetic fields opposing the external field. At the atomic level an analogous effect occurs for all atoms and is called diamagnetism. Now the external field does not need to be changing as the electrons around the atoms are in motion. This effect causes a depression in the surface of water close to a strong permanent magnet or can be used to levitate what would normally be considered non-magnetic objects, such as frogs [25].

Arrays of magnetic atoms

In a crystalline solid there are magnetic moments on a lattice. At high temperatures the direction of the moments fluctuate and no net moment is observable, these materials are called paramagnetic and are attracted towards high field densities. At lower temperatures interactions between neighbouring moments can override the effects of temperature and cause them to align. There are many different magnetic interactions which can cause different couplings between spins. The simplest case is described by direct interactions between neighbouring magnetic ions by the Heisenberg model. In the Heisenberg model a spin-spin interaction is introduced into the Coulomb interaction when quantum mechanics is considered, this is known as the exchange interaction. The lowest energy state is then achieved if the neighbouring spins are aligned in a ferromagnetic structure.

Ferromagnetism is where all the magnetic moments are (locally) all aligned in the same direction. In real systems there can be domains where all the moments point in the same direction but there can be many domains all oriented randomly such that there is no appreciable external field created by the system. These domains can be aligned by external fields such that the domains all have moments pointing in the same directions and a magnetic field can persist when the external field is removed. These are permanent magnets that we come across in our everyday lives.

Other interactions can cause antiferromagnetic arrangements of spins where neighbouring spins point in opposite directions and it is these that change the symmetry of the crystal structure and are therefore interesting for study with x-rays[6]. Only very large external fields can break this coupling and cause the moments to align, however, once the field is removed the moments will go back to coupling pointing in different directions. These interactions can cause coupling through an oxygen ligand in the case of transition metal oxides in a process called superexchange. The RKKY interaction allows the coupling between f-electron spins which would usually be weakly interacting as they are localised close to the nucleus and are screened by the outer electrons. The Dzyaloshinskii-Moriya interaction causes a canted coupling from the spin orbit interaction which induces long range magnetic structures such as helices and cycloids.

1.6.1   RKKY Interaction

The RKKY interaction, named after Ruderman, Kittel, Kasuya and Yoshida describes the mechanism for indirect exchange which couples the localised f-electrons of neighbouring atoms resulting in long-range (ferro and antiferro) magnetic ordering. The basis of the theory was originally developed by Ruderman and Kittel [26] to describe coupling of nuclear spins where an indirect exchange interaction takes place *via* the hyperfine interaction. It was later realised to also be applicable to localised d- and f-electron states by Kasuya [27] and the Hamiltonian further refined by Yoshida [28]. The small energy difference between the conduction and f-electrons allows for an antiferromagnetic exchange between the two, resulting in a spin-polarised conduction band. The locally spin-polarised conduction band takes the form of a magnetic impurity and long-range Friedel oscillations [29] occur. This lowers the energy for a moment on a different site to be aligned ferro- or antiferromagnetically depending upon the distance. Friedel oscillations are a general phenomenon of screening of a fixed charge by mobile electrons. The oscillations are a

---

[6]Antiferromagnetic structures do not always break symmetries within the space group. In the example of $LaMnO_3$, the moments are oriented parallel to a mirror plane and then the moments will only cause changes in intensity at already allowed Bragg peak positions and no superlattice reflections will be observed.

direct result of the wave particle duality of electrons and the Friedel oscillations are a result of the interference of the electrons. As such the period of the oscillations depend upon the energy of the electrons, and hence their wavelength[7]. An analogous effect occurs for a magnetic moment in the conduction band of a material where the amplitude of the Friedel oscillations represent the conduction band polarisation (ρ_c). Friedel oscillations take the functional form shown below and plotted in figure 1.6:

$$\rho_c = \frac{\sin(2k_f\mathbf{r}) - 2k_f\mathbf{r}\cos(2k_f\mathbf{r})}{(2k_f\mathbf{r})^4} \, , \tag{1.10}$$

where k_f is the Fermi wavevector.
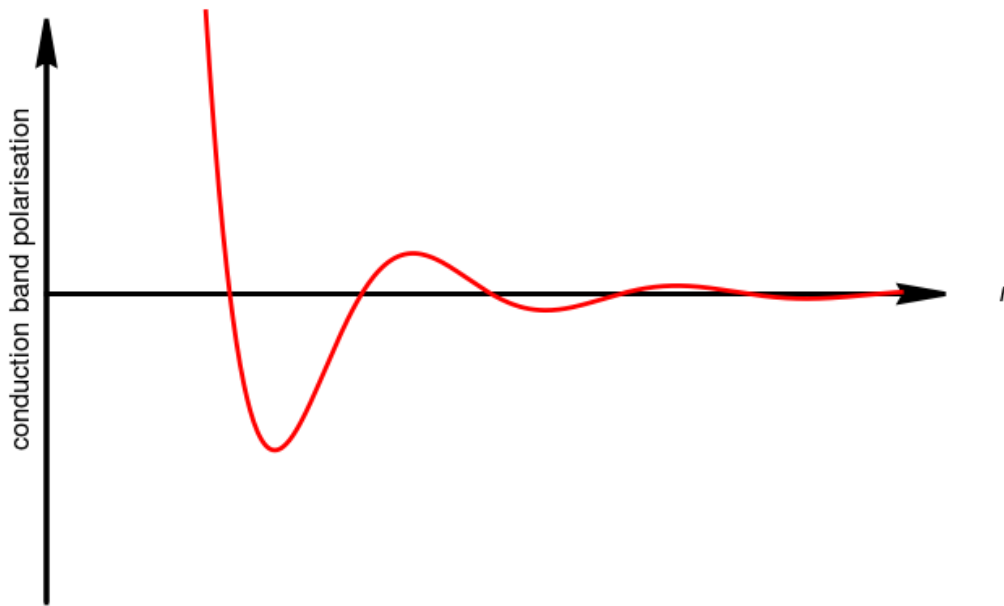
Figure 1.5: Visualisation of Friedel oscillations of the conduction band polarisation as a function of r away from a magnetic impurity at $r = 0$.

---

[7]In charge screening this effect is only seen at low temperatures due to the Boltzmann distribution of electron energies.

1.6.2 Superexchange

In perovskites the magnetic species are separated by intervening oxygen ions and the exchange interaction is therefore blocked, as such a process called superexchange is required to explain the antiferromagnetic properties of many transition metal oxide systems [30].

Superexchange involves the exchange of an electron with a neighbouring oxygen ligand. The exchange favours a ferromagnetic exchange between the transition metal and the ligand. The lowest energy state of the system is then achieved if the nearest neighbour transition metal ion exchanges an electron of the opposite spin with the ligand, resulting in an antiferromagnetic coupling. If the bond angle deviates from 180° the coupling between the transition metal ions becomes more complicated and can become ferromagnetic. Ferromagnetism can also occur through a different mechanism if there is a charge segregation in the system *via* a process called double exchange [31]. Double exchange occurs between transition metal ions of different valences still exchanging *via* the intermediary oxygen ligand. However, now a transfer of charge is involved and an electron hops from, for example, a Mn^{3+} *via* the intermediary oxygen to an Mn^{4+} while maintaining its spin, in this case a ferromagnetic coupling is favoured.
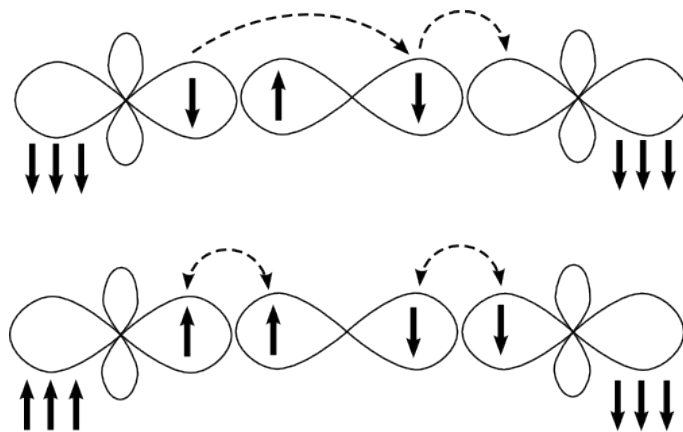
Figure 1.6: (top) Double exchange, the central ligand gives up an electron first and then the ion on the left fills in the gap with an electron of the same spin. (bottom) Superexchange, where there is a ferromagnetic coupling between each outer ion and the central ligand.

1.6.3   The Dzyaloshinskii-Moriya Interaction

The Dzyaloshinskii-Moriya (DM) [32, 33] interaction is an antisymmetric contribution to the superexchange interaction. When the bond angle deviates from $180°$ in a system where two magnetic species are separated, for example by an oxygen ion, a spin canting can be induced between the moments. This can cause weak ferromagnetism in antiferromagnetic systems or long-range spin helices in ferromagnetic systems. The Dzyaloshinskii-Moriya interaction is present in systems where the magnetic ions are separated by a bond not on an inversion centre. The canting in this case is much stronger than for the dipole-dipole case and can produce much shorter structures between 5-100 nm. The strength of the Dzyaloshinskii-Moriya interaction is proportional to the spin-orbit coupling and it is relativistic spin-orbit coupling that causes the interaction in the place of the oxygen ion in superexchange. The Dzyaloshinskii-Moriya interaction can be described by the following equation:

$$H_{DM} = \mathbf{D} \cdot (\mathbf{s}_i \times \mathbf{s}_j).$$ (1.11)

Where $\mathbf{s}_i$ and $\mathbf{s}_j$ are the moments spins, $\mathbf{D}$ is the DM vector which points perpendicular to the plane of the canting. The directions $\mathbf{D}$ can point is dependent upon the symmetry of the magnetic atoms. For example if there is an inversion centre bisecting the two atoms then $\mathbf{D} = 0$ and there can be no spin canting.

1.6.4   The Crystal Lattice and Diffraction

A crystal system can be described by its smallest repeating element, known as the unit cell. There are seven crystal families which depend upon the shape of the unit cell[8]. The arrangement of atoms within the unit cell are linked by certain symmetry operations, rotations, reflections, translations, and the more complex transforms of glide planes and screw axes. X-ray scattering is highly sensitive to these symmetries, long range ordered phenomena involving the electrons can break these symmetries and therefore be detected in the x-ray diffraction pattern. Such phenomena include but are not exclusive to; charge, orbital, and magnetic orderings.

---

[8]Cubic, tetragonal, orthorhombic, hexagonal, trigonal, triclinic, and monoclinic.
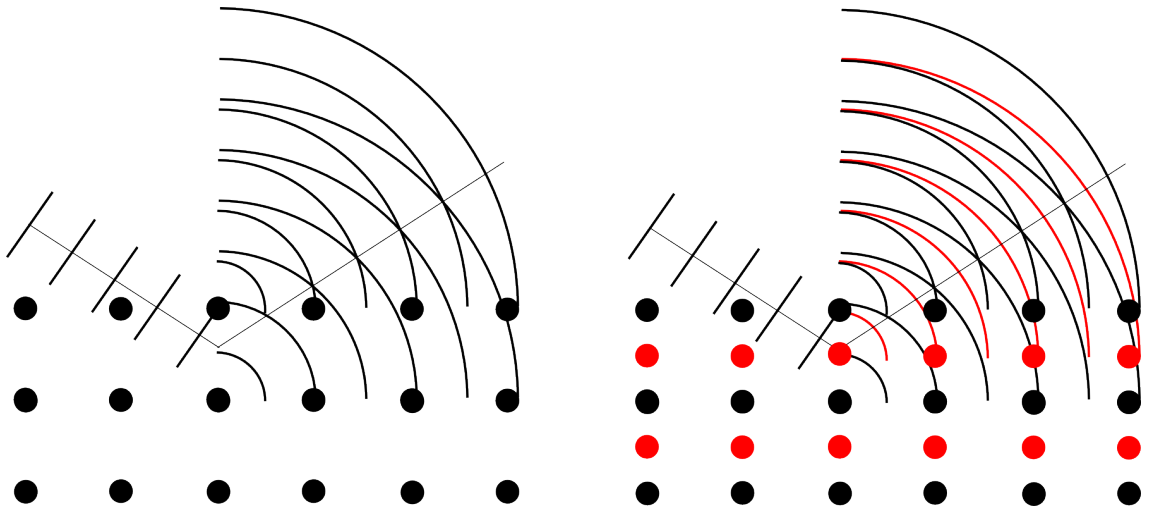
Figure 1.7: The lines are lines of constant phase. (left) For the outgoing light where the two lines cross from the radiated light from the two atoms constructive interference will occur. (right) For the outgoing light the red atoms at the half way point produce light out of phase and destructive interference will occur.

When an x-ray is incident upon an atom the electron cloud oscillates, the oscillating electrons then radiate light in (almost[9]) all directions. When we have an array of atoms the radiated light will constructively and destructively interfere. An example of this is shown in figure 1.7 where a plane wave is incident from the left and exciting two atoms in a crystal. This is the basis for diffraction and Bragg's law and the outgoing intensity is known as a Bragg peak. For this to occur the wavelength and angle of the incidence of the light must be matched to the lattice spacing of the crystal. If however, there was an atom placed half way between the two being excited this would radiate light half a wavelength out of phase and destructive interference would occur, this is shown in the right hand side of figure 1.7. A reduced scattering might still occur in this case if the red atoms were of a different element and therefore the radiated light had a different intensity.

Now considering a magnetic crystal where destructive interference is occurring any change in the atoms that can cause them to scatter light differently will cause a Bragg peak to occur. A simple model example of this is shown for magnetism with a rudimentary unit cell in figure 1.8. In this example the smallest repeating unit

---

[9]there is some angular dependence which depends upon the polarisation as we shall see later.
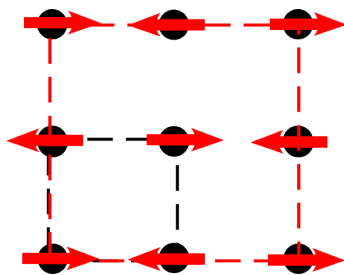
Figure 1.8: Example of how magnetism can change the unit cell size. Structural unit cell denoted by black dashed line, magnetic unit cell denoted by red dashed line.

has doubled in each direction and the red dashed lines represent the magnetic unit cell. In another phraseology the magnetism has broken the symmetry of the unit cell. X-rays produce a Fourier transform of the crystal. As such the doubling of the structural unit cell to the magnetic unit cell in figure 1.8 will result in magnetic Bragg peaks at half the distance in the scattered pattern.

1.6.5   Irreducible Representations

We shall now look a bit more at crystal symmetry and the irreducible representations of symmetry groups. Point groups are composed of a number of symmetry elements that can describe the symmetries around atoms. The group of symmetry elements can be constructed into a representation matrix. This representation matrix is built up of a number of irreducible components known as irreducible representations. Taking the point group C_{3v} (an example of a molecule with this symmetry is shown in figure 1.9) each symmetry element can be described by a 3×3 matrix which describes the symmetry operation. The C_{3v} point group has three vertical mirror planes (σ) oriented at 60° to each other and a 3-fold rotation along the vertical axis (C_3), as well as the identity operation (E) which leaves the system unchanged. The
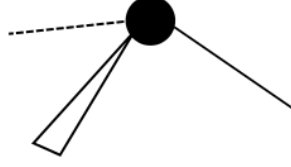
Figure 1.9: Illustration of a molecule belonging to the C_{3v} point group. With three mirror planes formed by each of the three bonds with the vertical axis and a threefold rotation axis along the vertical direction.

	E	C_3	C_3^2	σ_1	σ_2	σ_3
Γ_1	(1)	(1)	(1)	(1)	(1)	(1)
Γ_2	$\begin{pmatrix} 1 & 0 \\ 0 & 1 \end{pmatrix}$	$\begin{pmatrix} \frac{1}{2} & -\frac{\sqrt{3}}{2} \\ -\frac{\sqrt{3}}{2} & -\frac{1}{2} \end{pmatrix}$	$\begin{pmatrix} -\frac{1}{2} & \frac{\sqrt{3}}{2} \\ -\frac{\sqrt{3}}{2} & -\frac{1}{2} \end{pmatrix}$	$\begin{pmatrix} -1 & 0 \\ 0 & 1 \end{pmatrix}$	$\begin{pmatrix} \frac{1}{2} & -\frac{\sqrt{3}}{2} \\ -\frac{\sqrt{3}}{2} & -\frac{1}{2} \end{pmatrix}$	$\begin{pmatrix} \frac{1}{2} & \frac{\sqrt{3}}{2} \\ \frac{\sqrt{3}}{2} & -\frac{1}{2} \end{pmatrix}$

Table 1.1: One (Γ_1) and two (Γ_2) dimensional irreducible representations for the symmetry operations of the C_{3v} space group.

matrices describing these transformations are as follows,

$$E = \begin{pmatrix} 1 & 0 & 0 \\ 0 & 1 & 0 \\ 0 & 0 & 1 \end{pmatrix}, C_3 = \begin{pmatrix} -\frac{1}{2} & -\frac{\sqrt{3}}{2} & 0 \\ \frac{\sqrt{3}}{2} & -\frac{1}{2} & 0 \\ 0 & 0 & 1 \end{pmatrix}, C_3^2 = \begin{pmatrix} -\frac{1}{2} & \frac{\sqrt{3}}{2} & 0 \\ -\frac{\sqrt{3}}{2} & -\frac{1}{2} & 0 \\ 0 & 0 & 1 \end{pmatrix},$$

$$\sigma_1 = \begin{pmatrix} -1 & 0 & 0 \\ 0 & 1 & 0 \\ 0 & 0 & 1 \end{pmatrix}, \sigma_2 = \begin{pmatrix} \frac{1}{2} & \frac{\sqrt{3}}{2} & 0 \\ \frac{\sqrt{3}}{2} & -\frac{1}{2} & 0 \\ 0 & 0 & 1 \end{pmatrix}, \sigma_3 = \begin{pmatrix} \frac{1}{2} & -\frac{\sqrt{3}}{2} & 0 \\ -\frac{\sqrt{3}}{2} & -\frac{1}{2} & 0 \\ 0 & 0 & 1 \end{pmatrix}.$$

The C_3 and C_3^2 matrices describe rotations of 120° and 240° respectively. A reducible representation is one that is can be transformed into a block-diagonal matrix consisting of square matrices along the diagonal and zero's everywhere else. The irreducible representations are then these matrices along the diagonal. The symmetry operations above are already in block diagonal form and each can be decomposed into two irreducible representations (denoted Γ), these are shown in table 1.1. Irreducible

representations then are the basic building blocks of the symmetry operations. This can be useful as the irreducible representations of a magnetic space group define the possible magnetic structures which are possible within that space group and form a useful basis for magnetic structure determination.

Chapter 2

Scattering Theory

Having given a broad introduction into both x-rays and the properties of materials detectable by them. We now move on to the theoretical framework of resonant x-ray scattering and the mathematical basis for the sensitivity of both resonant and non-resonant x-ray scattering to magnetism.

In this chapter we introduce the Hamiltonian for an electron being excited by a photon and extend this to a crystal system. We then develop the Hamiltonian to show the sensitivity of x-rays to magnetism for both resonant and non-resonant x-rays as well as their polarisation dependences for these cases. Finally we introduce neutron scattering and show the basic theory for the sensitivity of neutrons to magnetic structures.

The information in the following sections largely derives from the section Resonant X-ray Scattering: A Theoretical Introduction, in the book, Magnetism: A Synchrotron Radiation Approach by Altarelli [34]. The Hamiltonian for the electron in the following section is derived in two books, Quantum Electrodynamics, Landau and Lifshitz Course of Theoretical Physics, Vol. 4, Chapter 4, Particles in an external field, Sections 33 and 34 [35], and Quantum Electrodynamics, Monographs and Texts in Physics and Astronomy, Vol. 11, Chapter 2, Relativistic quantum mechanics of the electron, Section 12 and 15 [36].

2.1   The Interaction Hamiltonian

The below equation describes the Hamiltonian for an electron with kinetic and potential energy, the third term is a relativistic correction to the kinetic energy, and the final term contains information about the electron spin:

$$H = \frac{\mathbf{p}^2}{2m} + V - \frac{\mathbf{p}^4}{8m^3c^2} - \frac{e\hbar}{4m^2c^2}\boldsymbol{\sigma}[\mathbf{E}, \mathbf{p}]. \tag{2.1}$$

Where $\mathbf{p}$ is the electron momentum, V is the external potential, $\boldsymbol{\sigma}$ is the vector of Pauli spin matrices with: $\sigma_x = \left(\begin{smallmatrix} 0 & 1 \\ 1 & 0 \end{smallmatrix}\right)$, $\sigma_y = \left(\begin{smallmatrix} 0 & -i \\ i & 0 \end{smallmatrix}\right)$, $\sigma_z = \left(\begin{smallmatrix} 1 & 0 \\ 0 & -1 \end{smallmatrix}\right)$, and $\mathbf{E}$ is the external field. Applying an external field transforms the momentum as follows, $\mathbf{p} \to \mathbf{p} - \frac{e}{c}\mathbf{A}$[1], where $\mathbf{A}$ is the vector potential, expanding the commutator $([\mathbf{E}, \mathbf{p}])$ results in:

$$H = \frac{(\mathbf{p} - \frac{e}{c}\mathbf{A})^2}{2m} - \frac{\mathbf{p}^4}{8m^3c^2} + V - \frac{e\hbar}{mc}\mathbf{s_i}.\mathbf{B} - \frac{e\hbar}{2m^2c^2}\mathbf{s_i}\left(\mathbf{E}.\left(\mathbf{p} - \frac{e}{c}\mathbf{A}\right)\right) + \frac{e\hbar^2}{8m^2c^2}\nabla.\mathbf{E}. \tag{2.2}$$

Where $\mathbf{s_i} = \boldsymbol{\sigma}/2$, the $\mathbf{p}^4$ term is not modified by the field as the Hamiltonian is derived within a $1/c^2$ approximation. The interaction Hamiltonian for an electron in an external field is obtained by first removing the relativistic terms (those independent of the field). The final term, known as the Darwin correction is independent of external field as for an electromagnetic wave $\mathbf{k}.\mathbf{E} = 0$, leaving:

$$H = \frac{(\mathbf{p} - \frac{e}{c}\mathbf{A})^2}{2m} + V - \frac{e\hbar}{mc}\mathbf{s_i}.\mathbf{B} - \frac{e\hbar}{2m^2c^2}\mathbf{s_i}\left(\mathbf{E}.\left(\mathbf{p} - \frac{e}{c}\mathbf{A}\right)\right). \tag{2.3}$$

Then splitting the Hamiltonian into parts independent and dependent of $\mathbf{A}$ using the relation $ie\hbar(\nabla V + \frac{1}{c}\frac{\delta \mathbf{A}}{\delta t}) = -ie\hbar\mathbf{E}$, we get the Hamiltonians for the electron H_{el} and interaction H_{int}:

$$H_{el} = \frac{\mathbf{p}^2}{2m} + V + \frac{e\hbar}{2m^2c^2}\mathbf{s_i}(\nabla V \times \mathbf{p}), \tag{2.4}$$

$$H_{int} = \frac{e^2}{2mc^2}\mathbf{A}^2 - \frac{e}{mc}\mathbf{A}.\mathbf{p} - \frac{e\hbar}{mc}\mathbf{s_i}.(\nabla \times \mathbf{A}) + \frac{e\hbar}{2m^2c^3}\mathbf{s_i}\left(\frac{\delta \mathbf{A}}{\delta t} \times \left(\mathbf{p} - \frac{e}{c}\mathbf{A}\right)\right),$$

$$= H_1' + H_2' + H_3' + H_4'. \tag{2.5}$$

Here $\mathbf{A}$, the vector potential can be described in terms of the creation and annihilation operators as follows:

$$\mathbf{A}(\mathbf{r}, t) = \sum_{\mathbf{k},\lambda} \left(\frac{hc^2}{\Omega\omega_\mathbf{k}}\right)^{1/2} \left[\boldsymbol{\varepsilon}_\lambda(\mathbf{k})a(\mathbf{k}, \lambda)e^{i(\mathbf{k}.\mathbf{r}-\omega_\mathbf{k}t)} + \boldsymbol{\varepsilon}_\lambda^*(\mathbf{k})a^\dagger(\mathbf{k}, \lambda)e^{-i(\mathbf{k}.\mathbf{r}-\omega_\mathbf{k}t)}\right]. \tag{2.6}$$

---

[1]This transform is derived in appendix B

Where the ε_λ terms are the photon polarisations, the a terms are the creation and annihilation operators, and Ω is the volume of the quantisation box. As $\mathbf{A}$ is first order in the creation and annihilation operators for a scattering process we require it to operate twice.

The four terms in the interaction Hamiltonian correspond to different scattering mechanisms, the first and last terms correspond to normal scattering as they are second order in $\mathbf{A}$, the first being normal Thomson scattering and the second term being scattering from magnetic moments. The two middle terms are only first order in $\mathbf{A}$ so must operate twice for a photon to be absorbed and then re-emitted. This requires second order perturbation theory which introduces an energy dependence to the process. So using Fermi's golden rule of time dependent perturbation theory we get the transition rate which is proportional to:

$$w = \frac{2\pi}{\hbar} \left| \langle f|H_1' + H_4'|i\rangle + \sum_n \frac{\langle i|H_2' + H_3'|n\rangle \langle n|H_2' + H_3'|f\rangle}{E_0 - E_n + \hbar w_{\mathbf{k}}} \right|^2 \delta(\hbar(w_{\mathbf{k}} - w_{\mathbf{k}}')). \quad (2.7)$$

Then when the incident energy approaches an absorption edge these terms become large and a resonant enhancement of the scattering will occur.

2.2 The Laué Condition

We now expand the Thomson part of the interaction Hamiltonian and derive the scattering from a periodic array of atoms. This will give us the conditions which must be met for a peak in the scattered intensity to occur from a crystal system.

2.2.1 Thomson Scattering

Expanding the Thomson scattering term in the interaction Hamiltonian $\frac{2\pi}{\hbar} |\langle f|H_1'|i\rangle|$, where f and i become $\langle 0; (\varepsilon_\lambda', \mathbf{k}')|$ and $|0; (\varepsilon_\lambda, \mathbf{k})\rangle$ where 0 denotes the ground state of the atom and $\mathbf{k}$ and $\mathbf{k}'$ are the incident and scattered photons which have polarisations ε_λ' and ε_λ. This can be expanded out as follows:

$$\langle f|H_1'|i\rangle = \frac{hc^2}{\Omega w_k} \frac{e^2}{mc^2} \sum_i \left\langle 0; (\varepsilon_\lambda', \mathbf{k}') \left| \varepsilon_\lambda'^* . \varepsilon_\lambda a^\dagger(\mathbf{k}', \lambda') a(\mathbf{k}, \lambda) e^{i(\mathbf{k}-\mathbf{k}').\mathbf{r}_i} \right| 0; (\varepsilon_\lambda, \mathbf{k}) \right\rangle.$$

$$= \frac{hc^2}{\Omega w_k} \frac{e^2}{mc^2} (\varepsilon_\lambda'^* . \varepsilon_\lambda) \sum_i \left\langle 0 \left| e^{i(\mathbf{k}-\mathbf{k}').\mathbf{r}_i} \right| 0 \right\rangle. \quad (2.8)$$

We then define $F(\mathbf{q})$ as the form factor and taking $\mathbf{q} = \mathbf{k} - \mathbf{k}'$ which is described as:

$$F(\mathbf{q}) = \sum_i \langle 0 \left| e^{i\mathbf{q}\cdot\mathbf{r}} \right| 0 \rangle. \tag{2.9}$$

This only treats single electrons, it will now be extended to the case of an atom. The scattering object becomes a system of N particles with a ground state $|0\rangle$. Electrons are fermions so the ground state can be described by the antisymmetric wavefunction $\psi(\mathbf{r}_1, \mathbf{r}_2, \mathbf{r}_3, \cdots, \mathbf{r}_n)$. The electron density is then described as:

$$\rho(\mathbf{r}) = N \int d\mathbf{r}_1 d\mathbf{r}_2 \cdots d\mathbf{r}_n \left| \psi(\mathbf{r}_1, \mathbf{r}_2, \mathbf{r}_3, \cdots, \mathbf{r}_n) \right|^2. \tag{2.10}$$

From which we see that the form factor is transformed as follows:

$$\begin{aligned}
F(\mathbf{q}) &= \langle \psi(\mathbf{r}_1, \cdots, \mathbf{r}_n) \left| e^{i\mathbf{q}\cdot\mathbf{r_1}}, \cdots, e^{i\mathbf{q}\cdot\mathbf{r_n}} \right| \psi(\mathbf{r}_1, \cdots, \mathbf{r}_n) \rangle, \\
&= N \int d\mathbf{r} e^{i\mathbf{q}\cdot\mathbf{r}} \int d\mathbf{r}_1 \cdots d\mathbf{r}_n \psi(\mathbf{r}_1, \cdots, \mathbf{r}_n)^2, \\
&= \int d\mathbf{r} e^{i\mathbf{q}\cdot\mathbf{r}} \rho(\mathbf{r}).
\end{aligned} \tag{2.11}$$

It is now apparent that the form factor is the Fourier transform of the electron density. When the N-electron system is an atom $F(\mathbf{q})$ is called the *atomic form factor*.

2.2.2   Scattering from a Periodic Array of Atoms

If we consider the case of a crystalline solid, where the electron density is well described as:

$$\rho(\mathbf{r}) = \sum_{l,m,n} \sum_{i=1}^{I} \rho_i(\mathbf{r} - \mathbf{R}_{l,m,n} - \mathbf{r}_i). \tag{2.12}$$

Which represents a crystal in which I atoms are located at positions $\mathbf{r}_i$, with $i = 1, 2, 3 \cdots, I$ in each unit cell. The unit cell positions are described in terms of the unit vectors $\mathbf{a}_1, \mathbf{a}_2, \mathbf{a}_3$ as follows $R_{l,m,n} = l\mathbf{a}_1 + m\mathbf{a}_2 + n\mathbf{a}_3$ where l, m, n are integers. The form factor then becomes:

$$\begin{aligned}
F(\mathbf{q}) &= \sum_{l,m,n} e^{i\mathbf{q}\cdot\mathbf{R}_{l,m,n}} \sum_{i=1}^{I} e^{i\mathbf{q}\cdot\mathbf{r}_i} \int e^{i\mathbf{q}\cdot(\mathbf{r}-\mathbf{R}_{l,m,n}-\mathbf{r}_i)} \rho_i(\mathbf{r} - \mathbf{R}_{l,m,n} - \mathbf{r}_i), \\
&= \sum_{l,m,n} e^{i\mathbf{q}\cdot\mathbf{R}_{l,m,n}} \sum_{i=1}^{I} e^{i\mathbf{q}\cdot\mathbf{r}_i} f_i(\mathbf{q}).
\end{aligned} \tag{2.13}$$

Where $f_i(\mathbf{q})$ is the atomic form factor for the i-th atom. As the sum over l, m, n runs to infinity, unless $\mathbf{q}.\mathbf{R}_{l,m,n} = 2\pi n$ there will be some unit cell whose phase destructively interferes with the first unit cell. The values of $\mathbf{q}$ that satisfy this condition are known as $\mathbf{G}_{hkl}$ which is described with reciprocal lattice vectors $\mathbf{a}_1^*, \mathbf{a}_2^*, \mathbf{a}_3^*$ as follows $\mathbf{G}_{hkl} = h\mathbf{a}_1^* + k\mathbf{a}_2^* + l\mathbf{a}_3^*$ where the reciprocal lattice vectors in terms of the real space vectors are as:

$$\mathbf{a}_1^* = 2\pi \frac{\mathbf{a}_2 \times \mathbf{a}_3}{\mathbf{a}_1.\mathbf{a}_2 \times \mathbf{a}_3}; \qquad \mathbf{a}_2^* = 2\pi \frac{\mathbf{a}_3 \times \mathbf{a}_1}{\mathbf{a}_2.\mathbf{a}_3 \times \mathbf{a}_1}; \qquad \mathbf{a}_3^* = 2\pi \frac{\mathbf{a}_1 \times \mathbf{a}_2}{\mathbf{a}_3.\mathbf{a}_1 \times \mathbf{a}_2}. \qquad (2.14)$$

So again taking $\mathbf{q}.\mathbf{R}_{l,m,n} = 2\pi n$ we must then have $\mathbf{G}.\mathbf{R}_{l,m,n} = 2\pi n$. We arrive at the Laué conditions for scattering:

$$\mathbf{a}_1.(\mathbf{k} - \mathbf{k}') = 2\pi h; \qquad \mathbf{a}_2.(\mathbf{k} - \mathbf{k}') = 2\pi k; \qquad \mathbf{a}_3.(\mathbf{k} - \mathbf{k}') = 2\pi l. \qquad (2.15)$$

This shows that when scattering from a crystal there will be intensity at specific points which relates to the Fourier transform of the electron density.

2.3 Non-Resonant Magnetic Scattering

We now investigate the interaction Hamiltonian to determine energy independent terms which are reliant on the electron spin as these will give us non-resonant scattering which depends upon the magnetic properties of the system.

Taking just the spin dependent terms of the interaction Hamiltonian and first investigating the most simple spin dependent case (H_4'). H_4' has two terms, the first of which is a factor $(\hbar\omega/mc^2)^2$ weaker than the second as it requires a second order perturbation (although maintains an energy independent term). Expanding the H_4' term using $\mathbf{A}$ from equation 2.6, and its time derivative:

$$\delta\mathbf{A}/\delta t = \sum_{\mathbf{k},\lambda} \left(\frac{hc^2}{\Omega\omega_{\mathbf{k}}}\right)^{1/2} \left[-i\omega_{\mathbf{k}}\boldsymbol{\varepsilon}_\lambda(\mathbf{k})a(\mathbf{k}, \lambda)e^{i(\mathbf{k}.\mathbf{r}-\omega_{\mathbf{k}}t)} + i\omega_{\mathbf{k}}\boldsymbol{\varepsilon}_\lambda^*(\mathbf{k})a^\dagger(\mathbf{k}, \lambda)e^{-i(\mathbf{k}.\mathbf{r}-\omega_{\mathbf{k}}t)}\right].$$
$$(2.16)$$

Then H_4' becomes:

$$\langle f | H_4' | i \rangle = -i \left(\frac{e^2}{mc^2}\right) \left(\frac{\hbar\omega_{\mathbf{k}}}{mc^2}\right) \left(\frac{hc^2}{\Omega\omega_{\mathbf{k}}}\right) \sum_i \left\langle 0 \left| e^{i()\mathbf{k}-\mathbf{k}').\mathbf{r}_i}\mathbf{s}_i.(\boldsymbol{\varepsilon}_{\lambda'}^*(\mathbf{k}') \times \boldsymbol{\varepsilon}_\lambda(\mathbf{k})) \right| 0 \right\rangle.$$
$$(2.17)$$

This is weak compared to Thomson scattering as it is reduced by the factor $\hbar\omega_{\mathbf{k}}/mc^2$. On further investigation an energy independent component is realised from the resonant terms (H_2' and H_3'). The intermediate state can either have two or zero photons. In the case of two photons a $+2\hbar\omega_k$ term is added to E_n, the denominators for these two cases then become $E_0 - E_n - \hbar\omega_k$ (for the intermediate state with two photons) and $E_0 - E_n + \hbar\omega_k$ (for zero photons). We can see that when $\hbar\omega_k = E_n - E_0$ an unphysical situation occurs for the zero photon case. This is alleviated by noting that the intermediate states are of a finite size and have a lifetime $i\Gamma_n/2$. The energy dependences can then be rearranged as follows to give a term independent of energy:

$$\frac{1}{E_0 - E_n + \hbar\omega_k + i\Gamma_n/2} = \frac{1}{\hbar\omega_k} + \frac{E_n - E_0 - i\Gamma_n/2}{\hbar\omega_k} \frac{1}{E_0 - E_n + \hbar\omega_k + i\Gamma_n/2} ,$$

$$\frac{1}{E_0 - E_n - \hbar\omega_k} = -\frac{1}{\hbar\omega_k} + \frac{E_n - E_0}{\hbar\omega_k} \frac{1}{E_0 - E_n - \hbar\omega_k} . \tag{2.18}$$

Then for the zero photon case we get:

$$\langle f|H_2' + H_3'|n\rangle \langle n|H_2' + H_3'|i\rangle = \frac{hc^2}{\Omega\omega_k}\left(\frac{e}{mc}\right)^2 \langle 0|[\boldsymbol{\varepsilon}'^*_{\lambda'}.\mathbf{p}_i - i\hbar(\mathbf{k}' \times \boldsymbol{\varepsilon}'^*_{\lambda'}).\mathbf{s}_i]e^{-i\mathbf{k}'.\mathbf{r}_i}|n\rangle$$

$$\langle n|[\boldsymbol{\varepsilon}_\lambda.\mathbf{p}_i + i\hbar(\mathbf{k} \times \boldsymbol{\varepsilon}_\lambda).\mathbf{s}_i]e^{i\mathbf{k}.\mathbf{r}_i}|0\rangle . \tag{2.19}$$

The two photon case is very similar but the terms between $\langle 0|$ and $|n\rangle$ and between $\langle 0|$ and $|n\rangle$ are switched, which changes the sign of the energy independent part $\left(\frac{1}{\hbar\omega_k}\right)$. The sign change of the denominator means that when the sum is computed the result will be a commutator:

$$\sum_n \frac{\langle f|H_2' + H_3'|n\rangle \langle n|H_2' + H_3'|i\rangle}{E_0 - E_n + \hbar\omega_k} \simeq \left(\frac{hc^2}{\Omega\omega_k}\right)\left(\frac{e}{mc}\right)^2 \langle 0|[C', C]|0\rangle . \tag{2.20}$$

Where:

$$C = [\boldsymbol{\varepsilon}_\lambda.\mathbf{p}_i + i\hbar(\mathbf{k} \times \boldsymbol{\varepsilon}_\lambda).\mathbf{s}_i]e^{i\mathbf{k}.\mathbf{r}_i} ,$$

$$C' = [\boldsymbol{\varepsilon}'^*_{\lambda'}.\mathbf{p}_i - i\hbar(\mathbf{k}' \times \boldsymbol{\varepsilon}'^*_{\lambda'}).\mathbf{s}_i]e^{-i\mathbf{k}'.\mathbf{r}_i} . \tag{2.21}$$

After assessing all the commutators the following equation should hopefully be

reached:

$$\sum_n \frac{\langle f|H_2' + H_3'|n\rangle \langle n|H_2' + H_3'|i\rangle}{\hbar\omega_k} = -i\left(\frac{e^2}{mc^2}\right)\left(\frac{\hbar\omega_{\mathbf{k}}}{mc^2}\right)\left(\frac{hc^2}{\Omega\omega_{\mathbf{k}}}\right)\Bigg[$$

$$\langle 0|\sum_i e^{i\mathbf{q}\cdot\mathbf{r}_i}\frac{i\mathbf{q}\times\mathbf{p}_i}{\hbar k^2}|0\rangle(\boldsymbol{\varepsilon}_{\lambda'}'^* \times \boldsymbol{\varepsilon}_\lambda)+$$

$$\langle 0|\sum_i e^{i\mathbf{q}\cdot\mathbf{r}_i}\mathbf{s}_i|0\rangle\left((\mathbf{k}'\times\boldsymbol{\varepsilon}_{\lambda'}'^*).(\boldsymbol{\varepsilon}_\lambda.\mathbf{k}') - (\mathbf{k}\times\boldsymbol{\varepsilon}_\lambda).(\boldsymbol{\varepsilon}_{\lambda'}'^*.\mathbf{k}) - (\mathbf{k}'\times\boldsymbol{\varepsilon}_{\lambda'}'^*)\times(\mathbf{k}\times\boldsymbol{\varepsilon}_\lambda))\Bigg].$$

$$(2.22)$$

Combining this with the H_4' term this gives:

$$\sum_n \frac{\langle f|H_2' + H_3'|n\rangle \langle n|H_2' + H_3'|i\rangle}{\hbar\omega_k} + \langle f|H_4'|i\rangle =$$

$$-i\left(\frac{e^2}{mc^2}\right)\left(\frac{\hbar\omega_{\mathbf{k}}}{mc^2}\right)\left(\frac{hc^2}{\Omega\omega_{\mathbf{k}}}\right)\Bigg[\langle 0|\sum_i e^{i\mathbf{q}\cdot\mathbf{r}_i}\frac{i\mathbf{q}\times\mathbf{p}_i}{\hbar k^2}|0\rangle.\mathbf{A} + \langle 0|\sum_i e^{i\mathbf{q}\cdot\mathbf{r}_i}\mathbf{s}_i|0\rangle.\mathbf{B}\Bigg].$$

$$(2.23)$$

The terms inside the bra-ket's can be shown to be the Fourier transforms of the orbital magnetisation and spin densities respectively with $\mathbf{A}$ and $\mathbf{B}$ as:

$$\mathbf{A} = (\boldsymbol{\varepsilon}_{\lambda'}'^* \times \boldsymbol{\varepsilon}_\lambda),$$

$$\mathbf{B} = (\boldsymbol{\varepsilon}_{\lambda'}'^* \times \boldsymbol{\varepsilon}_\lambda) + (\mathbf{k}'\times\boldsymbol{\varepsilon}_{\lambda'}'^*).(\boldsymbol{\varepsilon}_\lambda.\mathbf{k}') - (\mathbf{k}\times\boldsymbol{\varepsilon}_\lambda).(\boldsymbol{\varepsilon}_{\lambda'}'^*.\mathbf{k}) - (\mathbf{k}'\times\boldsymbol{\varepsilon}_{\lambda'}'^*)\times(\mathbf{k}\times\boldsymbol{\varepsilon}_\lambda).$$

$$(2.24)$$

From this we can see that we are separately sensitive to the orbital and spin magnetic moments with non resonant magnetic scattering and that they obey different polarisation dependences.

2.4 Resonant Scattering

Tuning the incident x-ray energy to an absorption edge of a specific element can give a large increase in the flux of weak reflections while giving information specific to the element being excited. Non-resonant magnetic scattering is usually very weak and resonant scattering can give an invaluable boost to the scattering intensity, although at the cost of some information about the spin and orbital properties of the magnetism.

2.4.1 The Electric Dipole Approximation

Going back to the resonant parts of the Hamiltonian H_2, and H_3 for the case where $\hbar\omega \simeq E_n - E_0$ we begin by noting that this can be well described by an overlap integral of the initial and final states. It can then be noted that the excitation of a core electron is the dominant process for an atom. Taking a hydrogen-like atom $k.r \simeq \sqrt{E/2mc^2} << 1$, for the most extreme case of uranium where $k.r = 0.34$ for all other cases it is less and this is a good approximation. A Taylor expansion for an exponential[2] can then be used to simplify equation 2.19 which we repeat here:

$$\langle f|H_2' + H_3'|n\rangle \langle n|H_2' + H_3'|i\rangle =$$
$$\frac{hc^2}{\Omega\omega_k}\left(\frac{e}{mc}\right)^2 \sum_i \langle 0|\left[\boldsymbol{\varepsilon}_{\lambda'}'^*.\mathbf{p}_i - i\hbar(\mathbf{k}' \times \boldsymbol{\varepsilon}_{\lambda'}'^*).\mathbf{s}_i\right][1 - i\mathbf{k}.\mathbf{r}_i + \cdots]|n\rangle$$
$$\langle n|\left[\boldsymbol{\varepsilon}_{\lambda}.\mathbf{p}_i + i\hbar(\mathbf{k} \times \boldsymbol{\varepsilon}_{\lambda}).\mathbf{s}_i\right][1 + i\mathbf{k}.\mathbf{r}_i + \cdots]|0\rangle \ . \tag{2.25}$$

Then just taking the first term of the Taylor expansion, this is the electric dipole approximation as all of these states are available to electric dipole transitions. Neglecting the spin-orbit interaction and taking a non-relativistic approach we can use $\mathbf{p}_i = \frac{-im}{\hbar}[\mathbf{r}_i, H_{el}]$ where $H_{el} = \sum_i(\mathbf{p}_i^2/2m + V(\mathbf{r}_i))$ then:

$$\langle n|\boldsymbol{\varepsilon}_{\lambda}.\mathbf{p}_i|0\rangle = -\frac{im}{\hbar}\langle n|\sum_i \boldsymbol{\varepsilon}_{\lambda}.[\mathbf{r}_i, H_{el}]|0\rangle$$
$$= \frac{im}{\hbar}[E_n - E_0]\langle n|\sum_i \boldsymbol{\varepsilon}_{\lambda}.\mathbf{r}_i|0\rangle \ . \tag{2.26}$$

Taking the remainder of the energy dependence not already accounted for in the non-resonant scattering section and neglecting the $i\Gamma_n/2$ term from the numerator as it is small gives the sum:

$$\sum_n \frac{\langle f|H_2' + H_3'|n\rangle \langle n|H_2' + H_3'|i\rangle}{\hbar\omega_k} = \left(\frac{m}{\hbar}\right)^2 \sum_n \frac{(E_n - E_0)^3}{\hbar\omega_k}\frac{\langle 0|\boldsymbol{\varepsilon}_{\lambda'}'^*.\mathbf{R}|n\rangle \langle n|\boldsymbol{\varepsilon}_{\lambda}.\mathbf{R}|0\rangle}{E_n - E_0 + \hbar\omega_k + i\Gamma_n/2} \ . \tag{2.27}$$

---

[2]$e^{i\mathbf{k}.\mathbf{r}} \simeq 1 + i\mathbf{k}.\mathbf{r} + \frac{(i\mathbf{k}.\mathbf{r})^2}{2} \cdots$

Where $\mathbf{R} = \sum_i \mathbf{r}_i$, which can be expressed in spherical components as follows:

$$R_0 = iR_z \,, \tag{2.28}$$

$$R_{-1} = \frac{i}{\sqrt{2}}(R_x - iR_y) \,, \tag{2.29}$$

$$R_1 = -\frac{i}{\sqrt{2}}(R_x + iR_y) \,. \tag{2.30}$$

With the obvious link with notation to spherical harmonics which, for $l = 1$, are:

$$Y_0 = i\sqrt{\frac{3}{4\pi}}\frac{z}{r} \,, \tag{2.31}$$

$$Y_{-1} = i\sqrt{\frac{3}{8\pi}}\frac{(x - iy)}{r} \,, \tag{2.32}$$

$$Y_1 = -i\sqrt{\frac{3}{8\pi}}\frac{(x + iy)}{r} \,. \tag{2.33}$$

The dot product now becomes:

$$\boldsymbol{\varepsilon}_\lambda.\mathbf{R} = \sum_{m-1}^{1}(-1)^{m-1}\varepsilon_m R_{-m} \,. \tag{2.34}$$

It then follows that:

$$\langle 0|\,\boldsymbol{\varepsilon}'^*_{\lambda'}.\mathbf{R}\,|n\rangle\,\langle n|\,\boldsymbol{\varepsilon}_\lambda.\mathbf{R}\,|0\rangle = \sum_{m,m'}(-1)^{m+m'}\varepsilon'^*_{\lambda'm}\varepsilon_{\lambda m'}\,\langle 0|\,R_{-m}\,|n\rangle\,\langle n|\,R_{-m'}\,|0\rangle \,. \tag{2.35}$$

Now for a spherical atom the eigenstates $|0\rangle$ and $|n\rangle$ are eigenstates of the angular momentum which must be conserved therefore $m = -m'$ and we can see that:

$$\langle 0|\,\boldsymbol{\varepsilon}'^*_{\lambda'}.\mathbf{R}\,|n\rangle\,\langle n|\,\boldsymbol{\varepsilon}_\lambda.\mathbf{R}\,|0\rangle = -\,\varepsilon'^*_{\lambda'0}\varepsilon_{\lambda 0}\,|\langle n|\,R_0\,|0\rangle|^2 + \varepsilon'^*_{\lambda'1}\varepsilon_{\lambda-1}\,|\langle n|\,R_1\,|0\rangle|^2$$
$$+\,\varepsilon'^*_{\lambda'-1}\varepsilon_{\lambda 1}\,|\langle n|\,R_{-1}\,|0\rangle|^2 \,. \tag{2.36}$$

Converting back to cartesian coordinates for the polarisation vectors we can attain the following:

$$\langle 0|\,\boldsymbol{\varepsilon}'^*_{\lambda'}.\mathbf{R}\,|n\rangle\,\langle n|\,\boldsymbol{\varepsilon}_\lambda.\mathbf{R}\,|0\rangle = \varepsilon'^*_{\lambda'z}\varepsilon_{\lambda z}\,|\langle n|\,R_0\,|0\rangle|^2$$
$$+\frac{1}{2}(\varepsilon'^*_{\lambda'x}\varepsilon_{\lambda x} + \varepsilon'^*_{\lambda'y}\varepsilon_{\lambda y})\left(|\langle n|\,R_1\,|0\rangle|^2 + |\langle n|\,R_{-1}\,|0\rangle|^2\right)$$
$$+\frac{i}{2}(\varepsilon'^*_{\lambda'x}\varepsilon_{\lambda y} - \varepsilon'^*_{\lambda'y}\varepsilon_{\lambda x})\left(|\langle n|\,R_1\,|0\rangle|^2 - |\langle n|\,R_{-1}\,|0\rangle|^2\right) \,. \tag{2.37}$$

Now defining:

$$F_{1,m} = m_e \sum_n \frac{(E_n - E_0)^3}{\hbar^3\omega_k}\frac{|\langle n|\,R_m\,|0\rangle|^2}{E_n - E_0 + \hbar\omega_k + i\Gamma_n/2} \,. \tag{2.38}$$

The scattering amplitude then becomes:

$$f^{E1} \propto (\boldsymbol{\varepsilon}'^{*}_{\lambda'} . \boldsymbol{\varepsilon}_{\lambda})[F_{1,1} + F_{1,-1}] - i(\boldsymbol{\varepsilon}'^{*}_{\lambda'} \times \boldsymbol{\varepsilon}_{\lambda}) . \hat{\mathbf{z}}_i)[F_{1,1} - F_{1,-1}]$$
$$+ (\boldsymbol{\varepsilon}'^{*}_{\lambda'} . \hat{\mathbf{z}}_i)(\boldsymbol{\varepsilon}_{\lambda} . \hat{\mathbf{z}}_i)[[2F_{1,0} - F_{1,1} + F_{1,-1}] . \tag{2.39}$$

Where $\hat{\mathbf{z}}_i$ is a unit vector in the direction of the magnetic moment of atom at position i. We can now see that there is a polarisation dependence introduced into the scattering. The first term denotes resonantly enhanced charge scattering and has the same polarisation dependence as non-resonant charge scattering.

The $\hat{\mathbf{z}}$ dependent second two terms are magnetic scattering where the polarisation is dependent upon the magnetic moment orientation. The second term of $\hat{\mathbf{z}}$ is second order in $\hat{\mathbf{z}}$ and produces reflections at twice the propagation vector (although the second order terms can contribute to first order reflections if there is a ferromagnetic component to the moment).

This shows us that along with the resonant enhancement of the intensity we are also sensitive to magnetism and that there is a polarisation dependence different from both non-resonant magnetic scattering and Thomson scattering.

2.5   Polarisation Dependence

From the resonant scattering amplitude (equation 2.39) we can see that a polarisation dependence is introduced by the pre-factors to the $F_{l,m}$ terms. Where $\boldsymbol{\varepsilon}$ is the polarisation with the prime denoting the scattered beam, $\hat{\mathbf{z}}$ is a unit vector in the direction of the magnetic moment[3] and F are the amplitudes and dependent upon the overlap integrals of the initial and final states. Expanding the terms from this equation and working in the experimental basis shown in figure 2.1, ψ is the angle of linear polarisation with special notation for polarisations parallel and perpendicular to the scattering plane denoted π and σ. They depend upon the scattering angle,

---

[3]Within the (U_1, U_2, U_3) basis
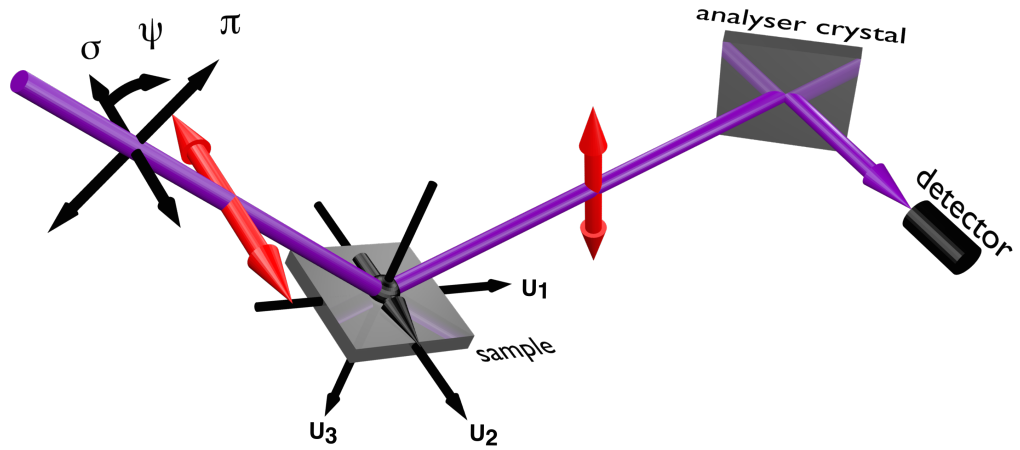
Figure 2.1: Experimental geometry with scattering vector along -U_3. With polarisation given as angle ψ. The scattered polarisation ψ' can be analysed with an analyser crystal shown before the detector.

θ, as follows:

$$\hat{\boldsymbol{\varepsilon}}_\sigma = (0, 1, 0),$$ (2.40)

$$\hat{\boldsymbol{\varepsilon}}'_\sigma = (0, 1, 0),$$ (2.41)

$$\hat{\boldsymbol{\varepsilon}}_\pi = (\sin\theta, 0, -\cos\theta),$$ (2.42)

$$\hat{\boldsymbol{\varepsilon}}'_\pi = (-\sin\theta, 0, -\cos\theta).$$ (2.43)

More generally, for the incident polarisation we have that:

$$\hat{\boldsymbol{\varepsilon}} = (\sin\psi\sin\theta, \cos\psi, -\sin\psi\cos\theta).$$ (2.44)

With just a change of sign on the U_1 component for scattered polarisation we get the scattered polarisation as:

$$\hat{\boldsymbol{\varepsilon}}' = (-\sin\psi\sin\theta, \cos\psi, -\sin\psi\cos\theta).$$ (2.45)

From this we can see that for the first term in the resonant scattering amplitude, or for Thomson scattering, which both have an $\hat{\boldsymbol{\varepsilon}}' \cdot \hat{\boldsymbol{\varepsilon}}$ pre-factor, the polarisation is unchanged for σ or π incident light with scattering. As both $\hat{\boldsymbol{\varepsilon}}'_\sigma \cdot \hat{\boldsymbol{\varepsilon}}_\pi$ and $\hat{\boldsymbol{\varepsilon}}'_\pi \cdot \hat{\boldsymbol{\varepsilon}}_\sigma$ are zero. For the second term, where the magnetism is involved, a more complex scattering results. The $\hat{\boldsymbol{\varepsilon}}' \times \hat{\boldsymbol{\varepsilon}}$ results in a rotation of the incident polarisation as now $\hat{\boldsymbol{\varepsilon}}'_\sigma \cdot \hat{\boldsymbol{\varepsilon}}_\sigma$ is zero, but $\hat{\boldsymbol{\varepsilon}}'_\pi \cdot \hat{\boldsymbol{\varepsilon}}_\sigma$ is non-zero.

This will be covered further in the introduction to Chapter 4 Full Polarisation Analysis Metrology where the formalism for dealing with polarisation dependences will be introduced.

The polarisation analyser depicted after scattering from the sample in figure 2.1 uses the fact that $\hat{\varepsilon}_\pi.\hat{\varepsilon}'_\pi = \cos^2\theta - \sin^2\theta$ which for a scattering angle of $90°$ reduces to zero. This is for definitions of σ and π in the scattering geometry of the analyser[4] and the polarisation can therefore be measured by rotating the analyser detector setup around the axis of the scattered beam.

2.6   Neutron Scattering

Neutrons travelling at around 4000 ms^{-1} will have a de Broglie wavelength of around 1 Å. Neutrons can be produced by nuclear fission or spallation and used in scattering experiments. As neutrons have no net charge they scatter from the nucleus and not from the electron cloud, however, the neutron has a magnetic moment so is affected by the moment of the scattering atom. Neutrons have a moment of 1.913 μ_N; μ_N is the nuclear magneton and is roughly 2000 times weaker than the Bohr magneton making it an excellent probe for magnetic systems as it will not affect the magnetism in the system.

Neutron scattering takes a very similar form to Thomson scattering, however, as the nucleus is much smaller than the electron cloud the potential is much smaller resulting in only a small form factor drop off.

2.6.1   Magnetic Scattering of Neutrons

The information in this section loosely follows Chapter 1 of the book 'Modern Techniques for Characterizing Magnetic Material' by Igor A. Zaliznyak and Seung-Hun Lee, available from the BNL website [37].

The interaction potential for magnetic neutron scattering is as follows:

$$V_{mag}(\mathbf{r}) = -\boldsymbol{\mu}_n.B(\mathbf{r})\,. \tag{2.46}$$

---

[4]in the figure the scattered polarisation from the sample is π polarised, however, to the analyser this is polarised perpendicular to the scattering plane and would be denoted σ.

Where μ_n is the neutron magnetic moment and $B(\mathbf{r})$ is the magnetic field inside the sample and is given as:

$$B(\mathbf{r}) = -\frac{\mu_0 \mu_B}{2\pi} \sum_j \left\{ \nabla \times \left[s_j \times \frac{\mathbf{r} + \mathbf{r}_j}{|\mathbf{r} - \mathbf{r}_j|^3} \right] - \frac{1}{\hbar} p_j \times \frac{\mathbf{r} - \mathbf{r}_j}{|\mathbf{r} - \mathbf{r}_j|^3} \right\}. \qquad (2.47)$$

Where the first term is due to the electron spin moment and the second term is due to its orbital moment. The Fourier transforms of these are as follows:

$$V_{spin}(\mathbf{Q}) = 2\mu_0 \mu_B \boldsymbol{\mu}_n \cdot \sum_j e^{i\mathbf{Q}\cdot\mathbf{r}_j} \mathbf{Q} \times (s_j \times \mathbf{Q}), \qquad (2.48)$$

$$V_{orbit}(\mathbf{Q}) = \mu_0 \boldsymbol{\mu}_n \cdot \sum_j e^{i\mathbf{Q}\cdot\mathbf{r}_j} \frac{2i\mu_B}{\hbar|Q|} (\mathbf{p}_j \times \mathbf{Q}). \qquad (2.49)$$

From this we can see that magnetic scattering is only possible if the moment is not parallel to $\mathbf{Q}$, this is equivalent to:

$$\mathbf{M}(\mathbf{Q}) = \mathbf{Q} \times (\mathbf{F}_M(\mathbf{Q}) \times \mathbf{Q}), \qquad (2.50)$$

where $\mathbf{F}_M(Q)$ is the magnetic structure factor.

Chapter 3

Experimental Techniques

3.1 Neutron Spallation

Spallation is a process where nuclei bombarded with particles emit a large number of subsequent particles. For neutron production[1] this is achieved by accelerating H^- ions (one proton two electrons) in a linear accelerator. At the end of this they are travelling at 37% the speed of light and collide with a thin alumina foil to strip the electrons before entering a synchrotron. In the synchrotron the now H^+ ions (protons) form into two bunches which are accelerated to 84% of the speed of light. Once this speed is achieved fast switching magnets strip off the bunches from the ring and direct them to the target stations where the protons collide with a tungsten target coated in tantalum where neutrons are produced *via* spallation [38–40]. A schematic of this is shown in figure 3.1. The neutrons are then passed through a moderator to slow them down to different speeds depending on the requirement for different instruments. The neutrons are produced in a range of energies which therefore have different velocities and arrive to the sample position at different times. As the exact time of the spallation is known, the time at which the neutron hits the detector is directly related to its energy. In this way all the neutrons can be used effectively for scattering. This is in contrast to a reactor source which is continuous so the energy of the neutron being detected is unknown. As a result the neutrons

---

[1]This details the production of neutrons at ISIS and parameters will vary between different facilities
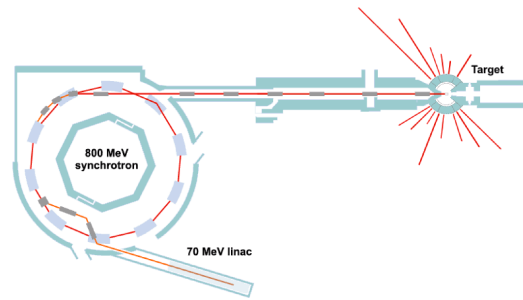
Figure 3.1: Schematic of the ISIS neutron spallation facility from [41].

must be monochromated to a narrow energy range to be useful. Due to this the useful flux of spallation sources in the latest generation facilities are actually higher than those at reactor sources.

3.2 Production of X-rays

X-rays are generally considered to be electromagnetic radiation in the rough range 100-200,000 eV, however, the boundaries are arbitrary and there is no real distinction between x-rays and gamma rays. X-rays are usually produced by either electron transitions with atoms or by accelerating or decelerating charged particles. The first dedicated x-ray sources produced x-rays by accelerating electrons into a dense metal target where characteristic lines are produced by the electronic transitions of the target element on top of a broad spectrum of x-rays (Brehmstrahlung).

3.2.1 Synchrotron Radiation Sources

Synchrotrons are a type of particle accelerator that use radio frequency klystrons to maintain the electron energy. This has the side-effect of forming the electrons into bunches. Synchrotrons consist of straight sections and bending magnets to form the ring, it is the acceleration in the bending magnets that produces the x-rays. The first synchrotron sources were developed for particle physics experiments, and were later adapted and tuned to produce x-rays from the electron acceleration. The second generation of synchrotrons were purpose built for condensed matter experiments. The third generation of synchrotron sources involves undulators and wigglers which are devices that can be inserted in the synchrotron, they have an

array of permanent magnets aligned in opposite directions to accelerate the electrons on an oscillatory path with the aim of increasing photon flux. Typically the energy of the electrons in the ring is around 5 GeV, at this energy using the electron rest mass as $m_0 = 9.109 \times 10^{-31}$ gives the relativistic momentum as 2.67×10^{-18} and v as 0.999999995 c.

3.2.2 Insertion Devices

Undulators and wigglers are fundamentally similar, both deflecting the electrons on a roughly sinusoidal path for an electron travelling along x as, $\ddot{x} = \frac{eB_y}{\gamma m_0 c}$ and $\ddot{y} = 0$ and the magnetic field described by:

$$B_y = -B_0 \sin\left(\frac{2\pi x}{\lambda_u}\right) , \tag{3.1}$$

$$\frac{dB_y}{dx} = \frac{B_0 e}{\gamma m_0 c} \frac{\lambda_u}{2\pi} \cos\left(\frac{2\pi x}{\lambda_u}\right) . \tag{3.2}$$

Where B_0 is the field amplitude, λ_u is the magnet separation (north pole to north pole) or 'wavelength' of the magnets in the undulator. e and m_0 are the electrons charge and rest mass, c is the speed of light , and γ is the Lorentz factor. K is then a useful parameter and denotes whether the radiation produced will interfere and produce high brilliance peaks of constructive interference ($K < 1$) or the radiation will be spread over a large angle and the peaks will broaden to form a smooth continuum ($K > 1$) with a similar shape to that of bending magnet radiation. This is due to the coherence length of the x-rays compared to the magnetic field. K is defined as:

$$K = \frac{B_0 e}{m_0 c} \frac{\lambda_u}{2\pi} . \tag{3.3}$$

Figure 3.2 shows some typical spectra from bending magnets, undulators, and wigglers. Wigglers give a few orders of magnitude increase in brilliance over a bending magnet typically 2N where N is the number of magnet pairs. Undulators are able to produce even more flux but require more tuning to achieve the optimum intensity at a given energy due to the sharp spikes in the spectrum. Where 1st, 3rd, and 5th refer to harmonics which come from interference of the x-rays (odd harmonics are produced in a forward cone and even harmonics are radiated in lobes above and below the electron orbit).
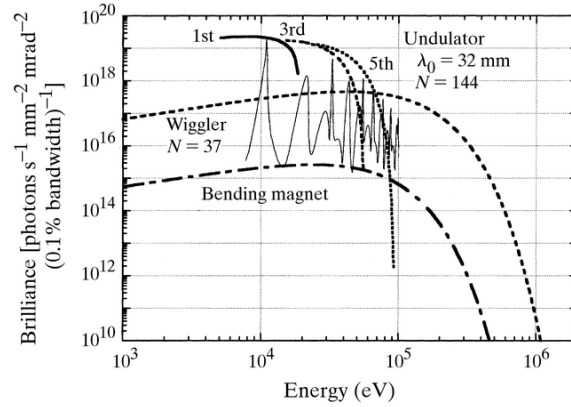
Figure 3.2: The spectral brilliance of the Spring-8 bending magnet, wiggler, and undulator, from [42].

3.3 X-ray Instrumentation

3.3.1 Diffractometer

A diagram of the geometry of a diffractometer is shown in figure 3.3. The motors are built such that θ is always in the scattering plane, χ is on top of the θ motion and is therefore not always in the y, z plane. ϕ is on top of both θ and χ, as only two angles are required to describe a sphere, generally one of these motors is fixed, usually ϕ. The detector angle 2θ is independent of the other motor movements and in this picture 2θ does not always equal $2 \times \theta$, for this reason θ is sometimes given the notation ω.

3.3.2 Diamond RASOR-I10

The RASOR (Reflectivity and Advanced Scattering from Ordered Regimes) endstation is currently situated at the I10:BLADE beamline at the Diamond Light Source Ltd [43]. RASOR is an in vacuum soft x-ray diffractometer with a limited χ motion of only $\pm$ 4 degrees. The χ, θ, 2θ, and sample motion x, y, and z motors[2] are external to the vacuum and motion is allowed through differentially pumped seals. The only in vacuum motors are those on the polarisation analyser stage angles θ_p, $2\theta_p$,

---

[2]The x-motion is along the axis of rotation of θ the directions of y and z depend upon the motor positions, with θ at zero the y-motion is along the beam direction and the z-motion is along the scattering vector.
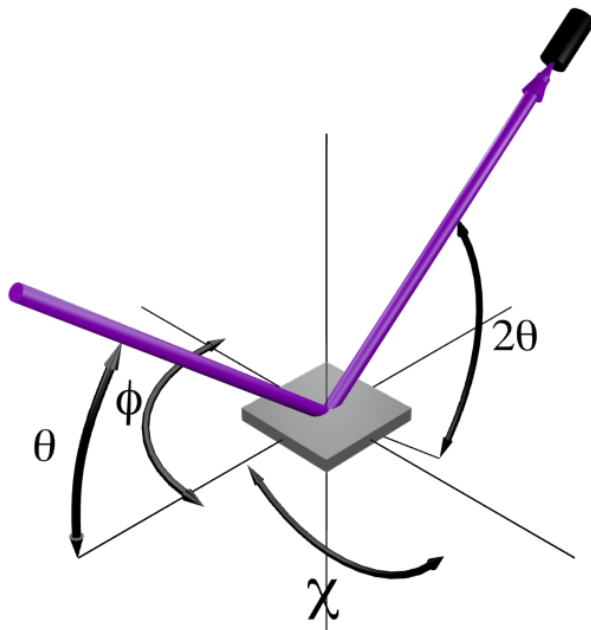
Figure 3.3: Simplified image of a diffractometer showing the sample motions θ, χ, and ϕ as well as the detector angle 2θ.

η and the polarisation analyser crystal translations py and pz as well as the slits. A schematic of the diffractometer is shown in figure 3.4. Due to the high absorption of soft x-rays experiments are carried out in a vacuum with a windowless set up between the sample and the synchrotron. The BLADE beamline consists of grazing incident mirrors and gratings for beam focussing and monochromation. Arbitrary polarisation control is given by manipulating the gap and phase of the four rows of magnets in the APPLE II undulators. Incident beam intensity is monitored from the drain current from the final mirror before the scattering chamber. Post scatter polarisation analysis is given by multilayer crystals. Sample cooling is provided by a liquid helium flow cryostat which can achieve a base temperature of 12 K, an optional ϕ motion is available from an adapted mount with an attocube piezo-motor, this limits the base temperature to roughly 100 K.

3.3.3 Diamond I06

The I06:Nanoscale beam-line at the Diamond Light Source Ltd. is a soft x-ray beam-line with a high field magnet for XMCD measurements. The magnet is composed of liquid helium-cooled superconducting coils and is capable of producing a field of
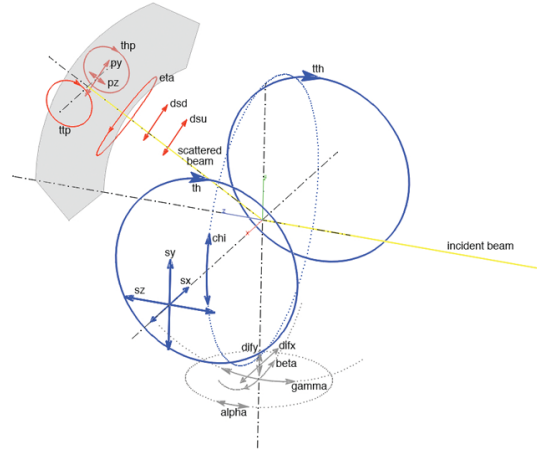
Figure 3.4: Schematic of the RASOR diffractometer [44]. With sample translations denoted sx, sy, sz. Sample rotations denoted chi and th. Diffractometer translations; difx and dify, diffractometer rotations; alpha, beta, and gamma. Detector angle tth, up and down stream detector slits denoted dsd and dsu. Polarisation analyser translations pz and py. Polarisation analyser angles eta and thp and finally polarisation analyser detector angle ttp.

up to 6 tesla in an arbitrary direction. Sample cooling is *via* liquid helium pumped from the outer helium jacket, used to cool the magnet, into a pot close to the sample there is a variable needle valve between the pot and the sample which gives control over the cooling power. This gives good temperature stability at base temperature, however, higher temperatures can only be achieved for a short period of time. Above a certain threshold small amounts of liquid helium can be continuously pumped and the evaporated cold gas is used to cool the sample. This method is effective above roughly 60 K. X-ray absorption measurements are available by fluorescence yield from a detector mounted at 90° to the sample position or total electron yield measurements which are taken *via* the sample rod which is insulated from the rest of the machine. The incident intensity is measured *via* the drain current from a gold grid just before the sample chamber. Due to the high absorption of soft x-rays the whole experiment is carried out in a vacuum with a windowless set up between the sample and the synchrotron. The samples are mounted on a copper mount which is transferred to the chamber *via* a load-lock. Further information about the beamline can be found in reference [45]

3.3.4   ISIS Wish

Wish is a long-wavelength neutron diffractometer with a d-spacing range from 0.7-17 Å [46]. It uses pixellated ^{3}He detectors covering scattering angles from 10 to 170° in the plane and ±12.8 degrees out of the plane. A solid methane moderator is used to thermalise the neutrons produced from the spallation source. It has the option of a high field magnet which can produce fields up to 13.5 T. A lower field 7 T magnet is also available which has less aluminium supports so offers more flux. As the source is polychromatic there is a choice of where to observe your reflections offered by a theta rotation of the sample mount. The highest resolution is offered at high scattering angles which require longer wavelength neutrons where there is more separation in the time of flight. Consideration must be given to the neutron flux as there is less intensity in the long wavelength tail to the neutron spectrum For powder collection the data is usually split up into five different detector banks which are at 27, 58, 90, 121, and 153°.

3.4   X-ray Magnetic Circular Dichroism

Circular dichroism is the differential absorption of right and left circularly polarised light. It is an effect utilised in many areas of physics from studying chiral molecules and the secondary structure of proteins [47] (their formation into α helices and β sheets) to the electronic structure of transition metals *via* $d-d$ excitations [48]. X-ray magnetic circular dichroism (XMCD) is specifically the differential absorption of a magnetic system around an x-ray absorption edge. XMCD is a bulk spectroscopic technique for studying magnetic systems and is most prevalent in investigating ferromagnetic materials, which can be magnetised by an external magnetic field. The advantage over more conventional bulk magnetic measurements is the element selectivity offered by x-rays as well as the sensitivity to the ratio of spin and orbital magnetic moments[3].

---

[3]Interestingly circular dichroism comes from a coupling of electric and magnetic dipole transitions, where x-ray magnetic circular dichroism come purely from electric dipole transitions.

3.4.1 Dipole Selection Rules

To understand the principles behind XMCD it is important to first understand the rules governing the involved electronic transitions. The selection rules for dipole allowed transitions can be derived from within the electric dipole approximation from the total decay rate formula and the expansion of the spherical harmonics with a Clebsch-Gordan series, this gives allowed changes in the quantum numbers of:

$$\Delta\ell = \pm 1\,, \tag{3.4}$$

$$\Delta m = 0, \pm 1\,, \tag{3.5}$$

$$\Delta s = 0\,. \tag{3.6}$$

Where the $\Delta m = 0, \pm 1$ correspond to linear and circularly polarised light respectively. The most important of these being that $\Delta s = 0$, the spin of the excited electron cannot flip.

3.4.2 Principals

X-ray absorption in transition metal systems can provide a multitude of information about the outer shell d-electrons. Due to the dipole selection rule we promote an electron from one of the $2p$, $j = 1/2$ or $j = 3/2$ states, up to the outermost partially filled d-shell. These are known as the L_{II} and L_{III} edges respectively, the L_I edge is the electric dipole forbidden transition from the $2s$ sub-shell (and is around 20 times weaker).

If such a transition is excited by right or left circularly polarised photons they transfer their angular momentum $\pm\hbar$ to the electron. As $\Delta s = 0$ (from section 3.4.1) one can only transfer the photon angular momentum to the orbital part, this is the basis for the orbital sum rule. If the core state is spin-orbit split, it is no longer pure spin state, the angular momentum of the photon is coupled to the electron spin and preferential excitation occurs when the photon and electron spins are parallel. For right (left) circularly polarised x-rays, preferential excitement of more spin-up (spin-down) (62.5%) than spin-down (spin-up) (37.5%) electrons occurs at the L_{III} edge. At the L_{II} edge the moments are antiparallel so right (left) circularly polarised x-rays preferentially excite more spin-down (spin-up) (75%) than spin-up (spin-down) (25%) electrons. It is this spin polarisation of the different L-edges that gives the

sensitivity necessary for determination of the spin moment with the spin sum rules. As such, a strong spin-orbit splitting is required to fully separate the L_{II} and L_{III} edges.

An XMCD signal arises if there is an unequal occupancy of spin-up and spin-down states in the level being excited to. As circular right and circular left polarisations preferentially excite electrons of opposite spins the absorption will be proportional to the number of empty states of that spin direction. This will only give an XMCD signal if the sample has a magnetisation along the beam direction.

There is an informative symmetry-based argument behind XMCD (from [49]) from which we can see why we must only be sensitive to magnetic moments along the beam direction. The electromagnetic force is invariant under reversal of parity, this implies that any measurement must also be invariant under parity transformations. So if we reflect our experiment in a mirror plane the same result would be expected. In figure 3.5 we can see that a moment pointing along the beam propagation direction with right circularly polarised light is indistinguishable from the reflected case with left circularly polarised light and a moment pointing opposite to the beam propagation[4]. This is distinct from the case where the magnetisation points towards the beam for right circularly polarised light, this shows that a differential absorption is possible but of course does not prove its existence. The second example shows that there is no difference between right and left circularly polarised light for a moment pointing perpendicular to the propagation direction as the sample is invariant under the mirror transform, in this case as a current loop reflected in this plane still rotates in the same direction.

3.4.3 XMCD Sum Rules

The sum-rules for XMCD are a direct result of the properties already discussed in this section and allow for quantitive magnetic moment magnitudes for both spin and orbital magnetic moments to be determined. The original work by Thole *et al.* [50] determined the orbital sum rule for determining the orbital magnetic moment.

---

[4]This is equivalent to both switching the direction of the magnetic field and the incident polarisation which in the absence of any hysteresis would give the same result.
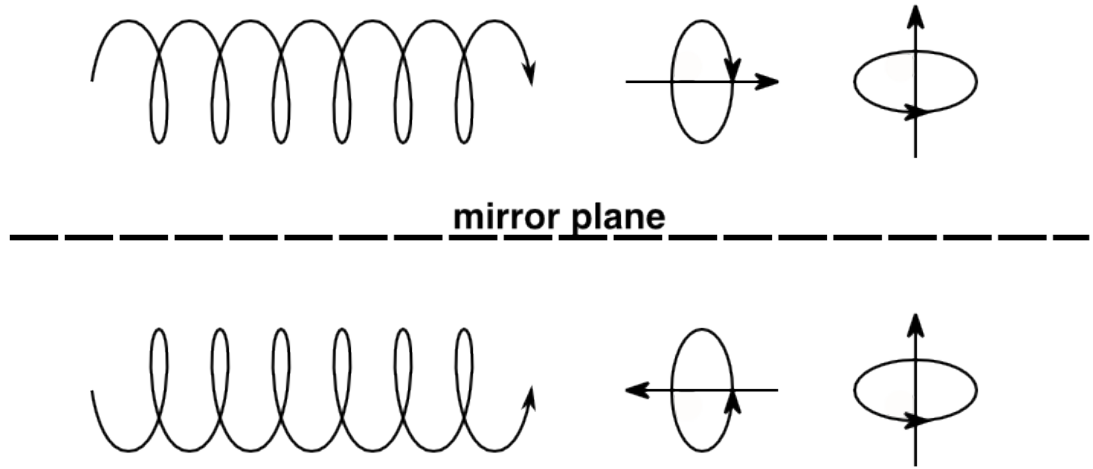
Figure 3.5: (top) Right circularly polarised light and spins described by current loops along and perpendicular to the beam direction. (bottom) Reflection of the top of the diagram in a mirror plane. The right circularly polarised light switches polarisation as does the direction of the moment along the beam direction but the moment out of the plane remains unchanged.

Further work by Carra *et al.* [51] utilised the spin-orbit splitting of the L-edges to extract the spin moment. The sum rules then are:

$$\langle L_z \rangle = \frac{2 \int A + B dE}{\int C dE} \, , \tag{3.7}$$

$$\langle S_z \rangle = \frac{3 \int A - 2B dE}{2 \int C dE} \, . \tag{3.8}$$

Where A and B are the difference spectra (between circular right and circular left) at the L_{III} and L_{II} absorption edges respectively, C is the average of the two polarisations normalised by the number of holes.

3.4.4 The Multiplet Structure of Absorption Edges

The structure of the absorption edges is complex and is dependent upon a number of factors. Mainly the spin and orbital parameters and spin-orbit coupling. These can give many peaks in an absorption spectra with different dependences to the XMCD. Contributing factors to the lineshape are the number of holes, the spin magnetic
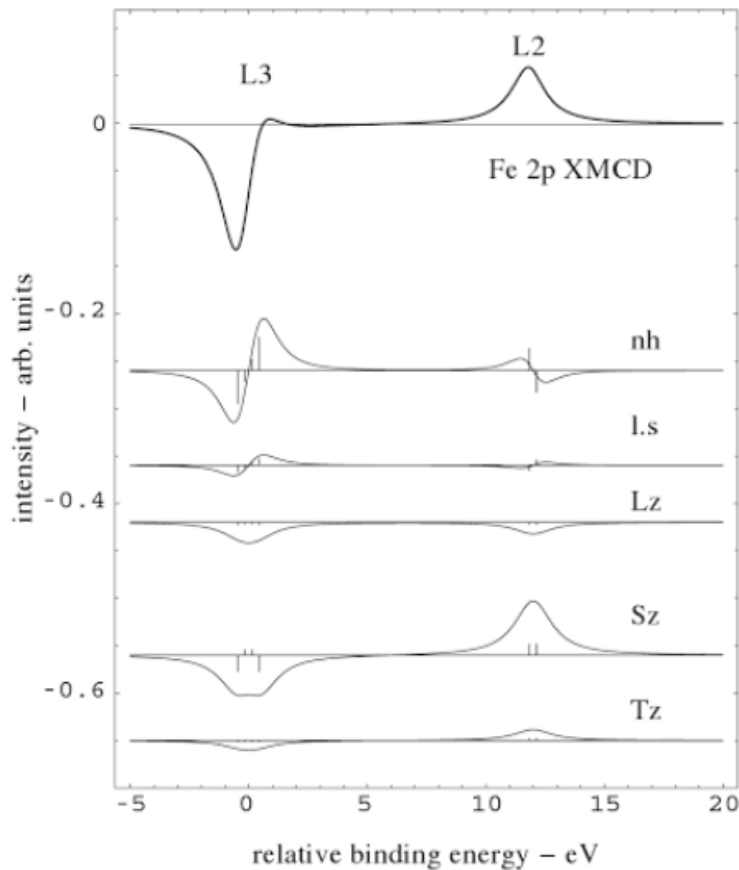
Figure 3.6: Relative contributions to the Fe $2p$ XMCD spectrum from the different ground state moments for Fe metal. The top spectrum is the sum of the different contributions, in order number of holes, spin-orbit coupling, orbital moment, spin moment and dipole contribution. From reference [52].

moment, the orbital magnetic moment, spin-orbit coupling, a magnetic dipole term, and a magnetic quadrupole term. All of these terms give different contributions to the absorption and to the XMCD. An example of the different contributions for the iron $2p$ edge is shown in figure 3.6 reproduced from the chapter Hitchhiker's Guide to Multiplet Calculations from the book, Magnetism: a Synchrotron Radiation Approach [52]. It can be seen that contributions from the number of holes and spin-orbit coupling can produce an asymmetry in the signal with a negative dichroism at higher energies. The quadrupolar term does not contribute in cubic systems and so does not contribute to the spectrum in figure 3.6. This gives some visual explanation for the sum rules.

3.5 Full Polarisation Analysis

Full polarisation analysis is a technique which can be used to determine the magnetic structure of a system by determining the outgoing polarisation for a number of different incoming polarisations.

The incident x-rays are linearly polarised by the insertion device and the polarisation is varied. In the case of soft x-rays this is achieved by altering the magnet geometry of the permanent magnets of the undulator or with hard x-rays by employing diamond phase plates.

The determination of the scattered polarisation is harder than with optical light. The polarisation is determined by the use of Brewster's angle, where only light polarised perpendicular to the scattering plane can be Thomson scattered through an angle of 90° and the intensity of scattered light with polarisation in the scattering plane drops to zero. For hard x-rays high quality single crystals are used with strong Bragg reflections where the d-spacing is matched to give scattering at the correct angle for a given energy. However, different crystals must be selected depending upon the energy range being used and an exact match with scattering at 90° is rarely available. For soft x-rays the wavelengths are longer and high quality single crystals with the correct d-spacing do not exist. As a solution metal multilayers are used where the thickness of the different layers gives a superlattice Bragg peak at the required angle.

Full details of the experimental procedure will be covered in Chapter 4 Full Polarisation Analysis Metrology.

3.6 Data Analysis

The data contained in this thesis was analysed almost exclusively using Python 2.7. Data was extracted from files and peak shapes were fitted with PySpec. PySpec uses the mpfit least squares fitting package. More complex fitting was done outside of PySpec but using the same least squares mpfit package. Graphs were produced using the matplotlib package.

Fitting of neutron data was undertaken using the FullProf suite which uses Rietveld refinement for fitting powder patterns [53].

Part II

Magnetic Structure Determination in Single Crystals Using Polarised X-rays

Chapter 4

Full Polarisation Analysis Metrology

In this chapter the metrology (theoretical and practical aspects) of full polarisation analysis will be detailed, starting with the theoretical framework behind the measurement and detailing the experimental set up. We then investigate some possible improvements to the practical aspects of the measurement in terms of measurement efficiency and data quality.

4.1 Introduction

Full polarisation analysis is a technique for determining the magnetic moment directions in ordered magnetic systems. This is achieved by measuring the scattered polarisation from a magnetic Bragg reflection for a number of different incident polarisations and reverse engineering the magnetic scattering matrix for the sample which contains detailed information about the magnetic ordering of the system, which in the case of resonant scattering is also element specific.

The usual method for taking a full polarisation analysis is slow, with a large proportion of the measurement time consisting of motor movements, and only a small proportion of the time taken up by detector counting.

In Chapter 6 New Magnetic Ground State in the Multiferroic Skyrmion System Cu_2OSeO_3 we investigate a skyrmion phase which only exists over a small range in temperature and field, as such it was important to improve the speed of full

polarisation analysis measurements to ensure we remained in the correct region of the phase diagram. These reflections were also very weak and an increased measurement efficiency would allow for a larger count time and better signal-to-noise ratios[1].

One of the advantages of full polarisation analysis compared to azimuthal scans is that the sample does not need to be moved throughout the data collection process. In an azimuthal scan the crystal is rotated around the scattering vector and then the intensity of the peak must be re-optimised. This is potentially problematic as the beam position on the sample could move. There will be differing sample absorption effects associated with this and if the sample is of a similar size to the beam, not all of the intensity from the main beam could be incident upon the sample. Unlike in full polarisation analysis it is the intensity of the scattered beam which is important so these differences could affect the results. The incident beam could also move between magnetic or crystallographic domains giving a different azimuthal dependence. Further, azimuthal dependences are not as complete, often only measuring two of the scattering channels $\sigma \to \sigma'$ and $\sigma \to \pi'$. It is also not sensitive to variations in the moment along the scattering vector. As the sample does not have to be optimised at each position it might then be imagined that a full polarisation analysis measurement could be much faster as the sample does not need to be moved and realigned throughout the process, however, the measurement of the outgoing polarisation is slow. On the I10 beamline at Diamond the motor movements for a full polarisation analysis take a minimum of around 6 hours (dependent upon the exact scan ranges chosen) compared to around 2 hours of counting time.

Full polarisation analysis is not exclusive to magnetic scattering or the x-ray regime and similar techniques are also used in countless other optical experiments.

4.2 The Polarisation Dependence of Scattering

This section largely follows the review paper by Detlefs *et al.* (2012) on x-ray polarisation analysis [54] and that of Hill and McMorrow X-ray Resonant Exchange

---

[1]It is important to check the polarisation of the incident beam, which would normally take a similar amount of time to measurements of the scattering from the sample, so even if other methods are only suitable for strong reflections a significant time saving can still be achieved.

Scattering: Polarization Dependence and Correlation Functions (1996) [55].

4.2.1 Scattering Matrix Formalism

We now extend the formalism for the polarisation dependence described briefly in Section 2.5 Polarisation Dependence and describe the scattering in terms of a (2 × 2) scattering matrix, which can be used in a similar way to a ray transfer matrix but for propagating polarised light through an optical system. We construct a scattering matrix with the elements of polarisation as follows:

$$
\begin{pmatrix}
\boldsymbol{\sigma} \to \boldsymbol{\sigma}' & \boldsymbol{\pi} \to \boldsymbol{\sigma}' \\
\boldsymbol{\sigma} \to \boldsymbol{\pi}' & \boldsymbol{\pi} \to \boldsymbol{\pi}'
\end{pmatrix} .
\tag{4.1}
$$

Referring back to the first term in the resonant scattering amplitude equation 2.39 of $\hat{\varepsilon}'.\hat{\varepsilon}$ we obtain the scattering matrix:

$$
\hat{\varepsilon}'.\hat{\varepsilon} =
\begin{pmatrix}
1 & 0 \\
0 & \cos 2\theta
\end{pmatrix} .
\tag{4.2}
$$

For the second term in equation 2.39 of $(\hat{\varepsilon}' \times \hat{\varepsilon}).\hat{\mathbf{z}}$ we obtain:

$$
(\hat{\varepsilon}' \times \hat{\varepsilon}).\hat{\mathbf{z}} =
\begin{pmatrix}
0 & z_1 \cos \theta + z_3 \sin \theta \\
-z_1 \cos \theta + z_3 \sin \theta & -z_2 \sin 2\theta
\end{pmatrix} .
\tag{4.3}
$$

To determine a full scattering matrix for a system the structure factor must be taken into account with all the resonant atoms involved, such that:

$$
\mathbf{M} = \sum_n e^{i\mathbf{q}\cdot\mathbf{r}_n}
\begin{pmatrix}
0 & z_1 \cos \theta + z_3 \sin \theta \\
-z_1 \cos \theta + z_3 \sin \theta & -z_2 \sin 2\theta
\end{pmatrix} .
\tag{4.4}
$$

Where $\hat{\mathbf{z}}$ now has a dependence on the atom position in the unit cell and has a periodicity of $\boldsymbol{\tau}$. For an antiferromagnetic system, $\mathbf{z}_n$ will take the form $\cos \boldsymbol{\tau}.\boldsymbol{r}_n$, we can write this in term of exponentials as $\frac{1}{2}(e^{i\boldsymbol{\tau}.\mathbf{r}} + e^{-i\boldsymbol{\tau}.\mathbf{r}})$ inputting this into the sum, and extracting the polarisation dependent terms, as they are independent of $\mathbf{r}$, we get:

$$
\mathbf{M} = \hat{\varepsilon}' \times \hat{\varepsilon} \sum_{n=0}^{\inf} e^{i\mathbf{q}\cdot\mathbf{r}_n} \left(\frac{1}{2} e^{i\boldsymbol{\tau}.\mathbf{r}_n} + \frac{1}{2} e^{-i\boldsymbol{\tau}.\mathbf{r}_n} \right) .
\tag{4.5}
$$

This then simplifies to:

$$
\mathbf{M} = \hat{\varepsilon}' \times \hat{\varepsilon} \sum_{n=0}^{\inf} \frac{1}{2} e^{i(\mathbf{q}\pm\boldsymbol{\tau})\cdot\mathbf{r}_n} .
\tag{4.6}
$$
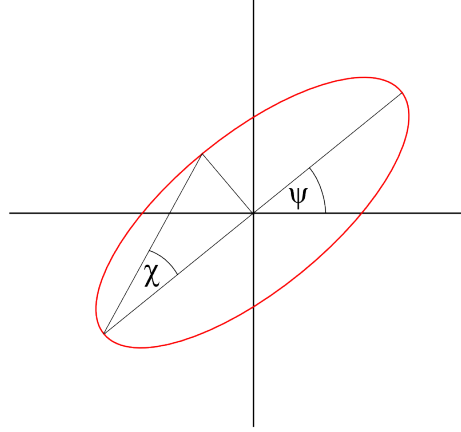
Figure 4.1: Representation of the polarisation ellipse and how the parameters ψ and χ relate to polarisation.

Where we can now see we get peaks at $\pm\boldsymbol{\tau}$. More complex magnetic structures for example a magnetic helix which can be described by $\mathbf{z}_n = (\cos\boldsymbol{\tau}.\boldsymbol{r}_n, \sin\boldsymbol{\tau}.\boldsymbol{r}_n, 0)$ would be dealt with in exactly the same way but would be described as:

$$\mathbf{z}_n = \frac{1}{2}\left(e^{i\boldsymbol{\tau}.\boldsymbol{r}_n} + e^{-i\boldsymbol{\tau}.\mathbf{r}}, e^{i\boldsymbol{\tau}.\boldsymbol{r}_n}e^{i\pi/2} + e^{-i\boldsymbol{\tau}.\boldsymbol{r}_n}e^{-i\pi/2}, 0\right). \tag{4.7}$$

Equivalently this can be written as:

$$\mathbf{z}_n = \frac{1}{2}e^{i\boldsymbol{\tau}.\boldsymbol{r}_n}(1, i, 0) + \frac{1}{2}e^{-i\boldsymbol{\tau}.\boldsymbol{r}_n}(1, -i, 0). \tag{4.8}$$

Where now these vectors are independent of n and can be removed from the structure factor and input into the $(\hat{\boldsymbol{\varepsilon}}' \times \hat{\boldsymbol{\varepsilon}}).\hat{\mathbf{z}}$ matrix.

4.2.2   Application of the Scattering Matrix

To determine how the scattering matrix transforms a ray of polarised light we must also describe the light in terms of a (2×2) matrix. This is done in terms of Poincaré-Stokes parameters, which are defined by the polarisation ellipse, which can be seen in figure 4.1. The Poincaré-Stokes parameters are $\sqrt{P_1^2 + P_2^2 + P_3^2} = 1$ and are described as:

$$P_1 = \cos 2\psi \cos 2\chi \,, \tag{4.9}$$

$$P_2 = \sin 2\psi \cos 2\chi \,, \tag{4.10}$$

$$P_3 = \sin 2\chi \,. \tag{4.11}$$

The matrix describing the light is then constructed using:

$$\boldsymbol{\rho} = \frac{I}{2}(\mathbf{1} + \boldsymbol{\sigma}.\boldsymbol{P})\,. \tag{4.12}$$

Where here $\boldsymbol{\sigma}$ are the Pauli spin matrices. This gives the matrix:

$$\mathbf{rho} \begin{pmatrix} 1 + P_1 & P_2 - iP_3 \\ P_2 + iP_3 & 1 - P_1 \end{pmatrix}\,. \tag{4.13}$$

Which is then transformed by the scattering matrix ($\mathbf{M}$) as:

$$\boldsymbol{\rho}' = \mathbf{M}.\boldsymbol{\rho}.\mathbf{M}^\dagger\,. \tag{4.14}$$

Where $\mathbf{M}^\dagger$ is the conjugate transpose of $\mathbf{M}$. For a number of optical elements in sequence the scattered matrix becomes:

$$\boldsymbol{\rho}' = \mathbf{M}_2.\mathbf{M}_1.\boldsymbol{\rho}.\mathbf{M}_1^\dagger.\mathbf{M}_2^\dagger\,. \tag{4.15}$$

For the case where there are different magnetic domains in a sample, or there is some contamination of the signal, the matrices describing the scattered beam are just summed as:

$$\boldsymbol{\rho}' = \sum_n p_n \boldsymbol{\rho}'_n\,. \tag{4.16}$$

Where p_n are the probabilities of scattering from different domains. The new Poincaré-Stokes parameters are then extracted using the following equations:

$$I = tr(\boldsymbol{\rho})\,, \tag{4.17}$$

$$P_i = \frac{1}{I}tr(\boldsymbol{\sigma}_i.\boldsymbol{\rho}), i = 1, 2, 3\,. \tag{4.18}$$

By measuring the outgoing polarisation for a number of different incoming polarisations the scattering matrix and thus information about the magnetic structure of the system can be determined [56–60].

.

Examples of Full Polarisation Analysis

Here simulations for different full polarisation analysis measurements for different constructs of scattering matrices will be presented. As noted previously for charge scattering the scattering matrix takes the form:

$$\mathbf{M} = \begin{pmatrix} 1 & 0 \\ 0 & \cos 2\theta \end{pmatrix}. \tag{4.19}$$

This matrix will not transform the incoming polarisation, and the outgoing polarisation will therefore be the same (independent of θ), only the intensity will vary. The resulting polarisation dependence in terms of the Poincaré-Stokes parameters is shown in figure 4.2a. For a magnetic sample the possible polarisation dependences are more complex due to the scattering matrix:

$$\mathbf{M} = \begin{pmatrix} 0 & z_1 \cos\theta + z_3 \sin\theta \\ -z_1 \cos\theta + z_3 \sin\theta & -z_2 \sin 2\theta \end{pmatrix}. \tag{4.20}$$

A moment residing purely along U_3 will have a scattering matrix of the form:

$$\mathbf{M} = \begin{pmatrix} 0 & 1 \\ 1 & 0 \end{pmatrix}. \tag{4.21}$$

This has the effect of rotating the incident polarisation by 90 degrees, the corresponding polarisation dependence is shown in figure 4.2b. This can be seen to invert the P_1 dependence. For a moment that resides entirely in the U_1 direction, the scattering matrix takes the form:

$$\mathbf{M} = \begin{pmatrix} 0 & 1 \\ -1 & 0 \end{pmatrix}. \tag{4.22}$$

The corresponding polarisation dependence is shown in figure 4.2c. Now the P_2 dependence has flipped in sign, which corresponds to the outgoing polarisation rotating in the opposite sense to the previous case. More complicated polarisation dependences are possible, for example, a moment residing in the U_2, U_3 plane with a scattering matrix similar to:

$$\mathbf{M} = \begin{pmatrix} 0 & 1 \\ -1 & 1 \end{pmatrix}. \tag{4.23}$$
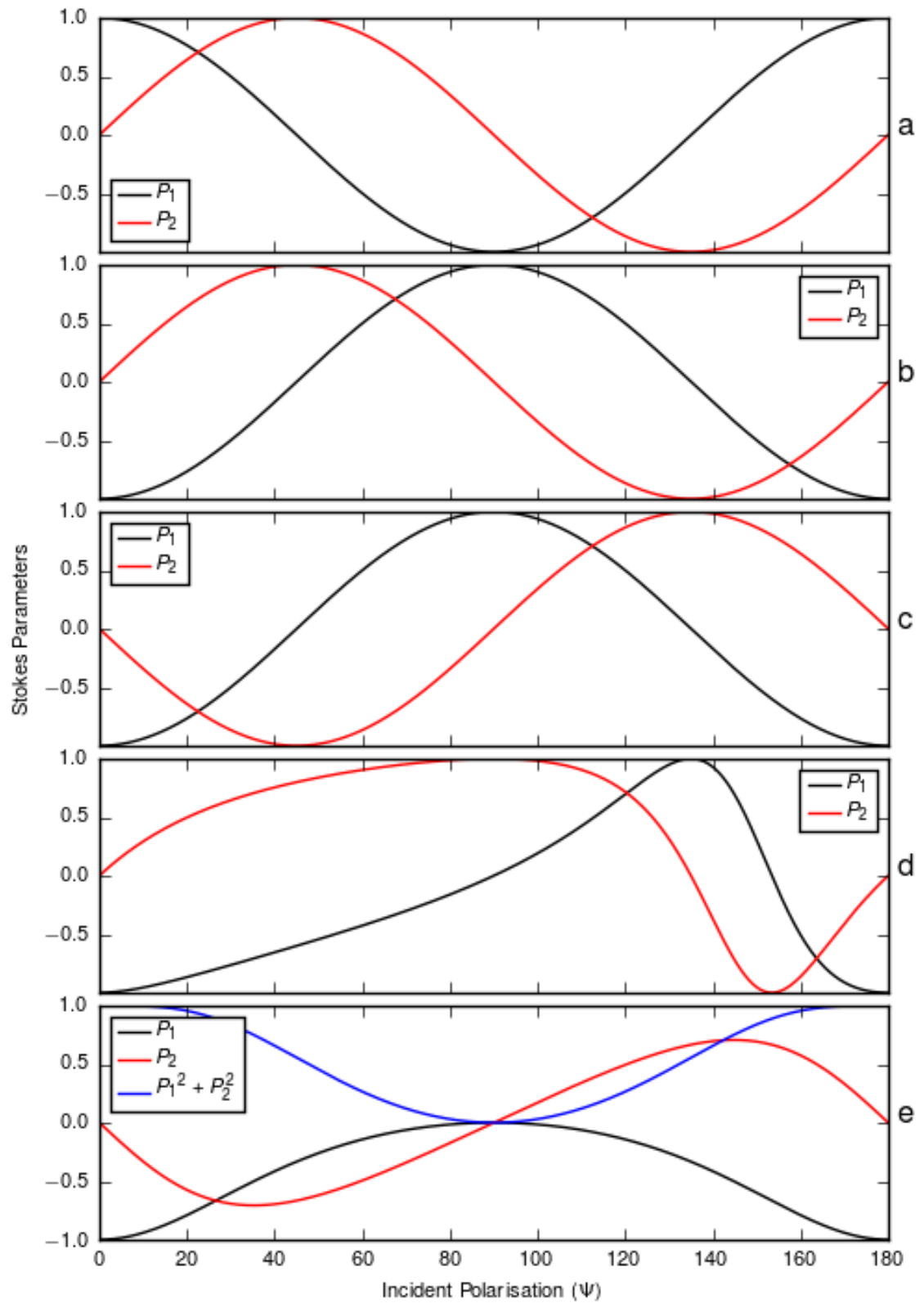
Figure 4.2: (a) Polarisation dependence for charge type scattering. (b-e) Various polarisation dependences of different magnetic scattering matrices. Scattering matrices (a) $\mathbf{M} = \left(\begin{smallmatrix} 1 & 0 \\ 0 & 1 \end{smallmatrix}\right)$, (b) $\mathbf{M} = \left(\begin{smallmatrix} 0 & 1 \\ 1 & 0 \end{smallmatrix}\right)$, (c) $\mathbf{M} = \left(\begin{smallmatrix} 0 & 1 \\ -1 & 0 \end{smallmatrix}\right)$, (d) $\mathbf{M} = \left(\begin{smallmatrix} 0 & 1 \\ 1 & 1 \end{smallmatrix}\right)$, (e) $\left(\begin{smallmatrix} 0 & 1+i \\ 1-i & 0 \end{smallmatrix}\right)$.

This will produce the polarisation dependence shown in figure 4.2d. If there is an imaginary component to the matrix this results in a P_3 component and a deviation from linear light and $\sqrt{P_1^2 + P_2^2} = 1$. This is possible if the moment is more complex with a phase difference (which will result in a non-collinear structure) between the components, for example:

$$\mathbf{M} = \begin{pmatrix} 0 & 1 + i \\ 1 - i & 0 \end{pmatrix}. \tag{4.24}$$

This will produce the polarisation dependence shown in figure 4.2e.

4.3 Current Method of Full Polarisation Analysis

The experimental setup for a polarisation analyser (PA) is shown in figure 4.3. The polarisation as described by the Poincaré-Stokes parameters is determined by finding the intensity at different η rotations. The intensity of the light scattered from the polarisation analyser crystal then takes the form of a sinusoid with η, and can be fitted with the formula:

$$I(\eta) = \frac{I_{max}}{2}(1 + P_1 \cos \eta + P_2 \sin \eta). \tag{4.25}$$

As generally the centre of rotation of the polarisation analyser stage is not perfect this cannot be done by rotating η[2]. To account for this the θ_p angle must be scanned to determine $I(\eta)$ at successive η angles[3]. The integrated intensity (taken as the area of a lineshape fitted to the peak) of these θ_p scans is then plotted against η and used for determining P_1 and P_2. An example of this is shown in the left hand side of figure 4.4 and shows how the η dependence changes with incident angle on the right.

It should be noted that P_3 (the degree of circular polarisation) is not in the fitted equation and cannot be directly determined. Using the relation $P_1^2 + P_2^2 + P_3^2 = 1$

---

[2]The centre of rotation of the polarisation stage is potentially problematic because it moves with the two-theta arm, and also the scattered beam moves depending upon the crystal, so ensuring that the scattered beam coincides with the centre of rotation of the polarisation analyser crystal is non-trivial and will be discussed later in Appendix C.

[3]To collect enough data points for a good fit scans are typically taken at ten η angles (every 20 degrees)
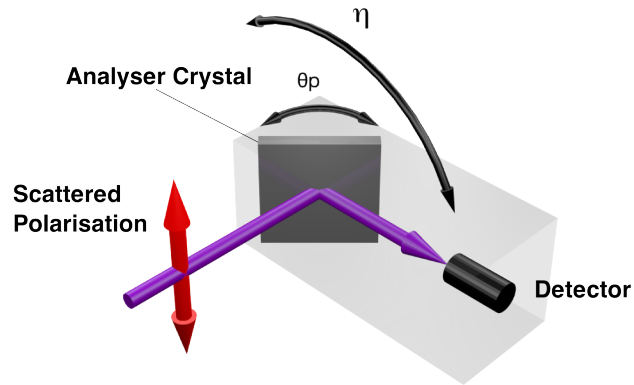
Figure 4.3: Setup of a polarisation analyser crystal on the two theta arm. In the setup shown a maximum in intensity will be observed at the detector. If η is rotated by 90° a minimum in intensity will be observed. In this figure the scattered polarisation is π' and the current eta angle is -90°.

which for linearly polarised light reduces to $P_1^2 + P_2^2 = 1$, the degree of linear polarisation can be determined. It does not however, mean that the remainder is circularly polarised as the scattered beam could become slightly unpolarised. To determine the nature of the density matrix the scattered polarisation must be determined for a number of incident polarisation (ψ) angles (a good point density for this is ten degree increments).
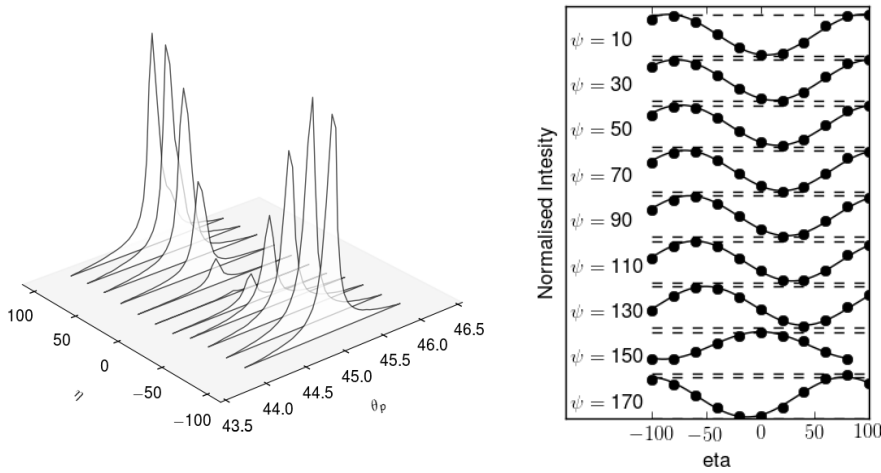
Figure 4.4: (left) Successive θ_p scans at different η angles showing the change in intensity for π' scattered polarisation as the component of the polarisation in the scattering plane changes with the η angle. (right) An example of how the integrated intensity of the θ_p scans can vary with η for different incident light polarisation angles ψ. These lines can be fitted to determine the P_1 and P_2 parameters.

4.4 Improvements to Full Polarisation Analysis

4.4.1 Constant Velocity Scans

The first and possibly most obvious improvement to the methodology is to employ constant velocity (cv) or, fly-scans, on the θ_p scan as the exact θ_p position does not need to be accurately known and only the integrated intensity in this scan is required. A cv scan moves a motor across the scan range at a constant velocity instead of accelerating the motor and decelerating to a stop at each point in the scan before acquiring the detector count. In the cv scan the detector is constantly counting and integrates the counts over a certain motor distance, or time, to build up the scan. Cv scans are likely to decrease the time taken for the measurement of intense peaks much more than for weak peaks as the amount of detector dead time for a scan with a long counting time is proportionally less significant.

4.4.2 Incident Polarisation Scans

As the θ_p scan only needs to be taken due to the alignment of the PA stage there is the possibility that a single θ_p scan could be performed followed by a scan of

the incident light angle on and off the peak in θ_p so that the background can be subtracted. The advantage of this is that it negates the need to scan θ_p at each η for each polarisation, effectively reducing the number of data points which need to be collected by a factor of twenty (it would be a factor of forty but ψ scans need to be taken on and off the peak in θ_p for effective background subtraction). The effectiveness of this is partially dependent upon the relative speeds of the η and incident polarisation (ψ) angles as it requires a large number of ψ motions but relatively few η motions[4]. The data must then be reformatted to be in terms of scans in η instead of scans in ψ before the polarisation can be determined. If only a partial full polarisation analysis is measured how does the information compare to the previous method? As information is obtained about all the incident polarisations in each scan, a complete full polarisation analysis could be plotted after each scan, further scans simply reduce the error bars on that measurement.

4.5 Results and Discussion

All measurements were taken on the RASOR endstation of the I10 beamline at Diamond Light Source Ltd.

4.5.1 Constant Velocity Scans

Comparison of Step and Cv Scans

The cv scans were observed to replicate comparable step scans reasonably well, however, for very fast scans a portion of the beginning of the scan was often missing and a highly distorted scan shape was seen, an example is shown in the top panel of figure 4.5. The difference in the step and cv scan is shown in the bottom panel of figure 4.5, with details of the peak shapes in table 4.1. The step and cv scans look similar other than a shift in the centre positions, however, upon fitting both peaks a significant difference is the areas is observed. As it is only the relative changes

---

[4]As the peak in θ_p is likely to move even with a well aligned analyser to automate the full polarisation analysis θ_p scans would need to be performed at each η to determine the positions for the ψ scans prior to the measurement. This could be completed before the data collection and programmed into the macro as these values will not change when set up on a reflection.
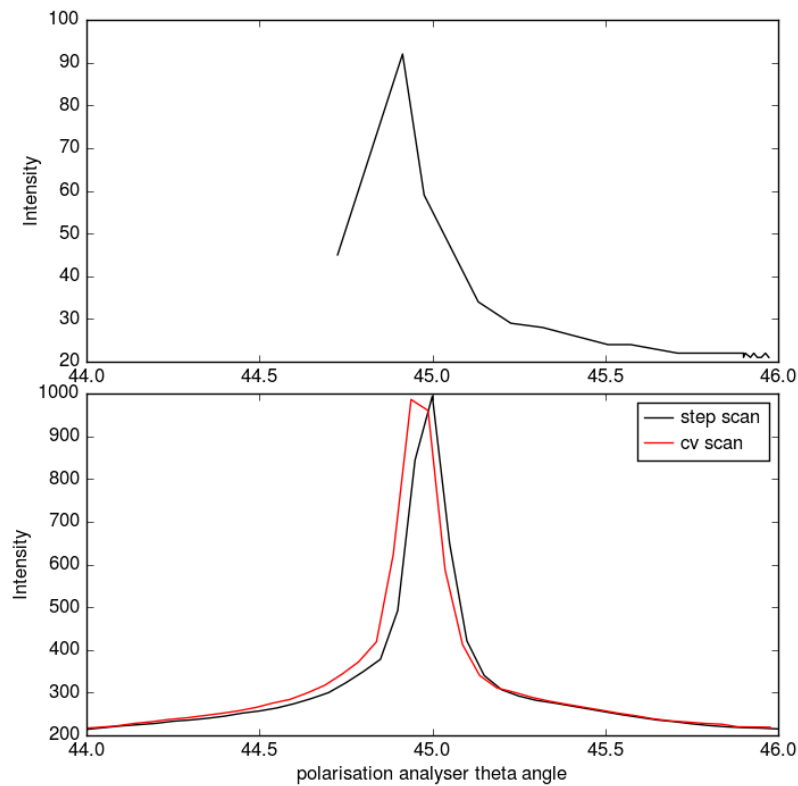
Figure 4.5: (top) Fast cv scan with a very distorted peak shape and missing points at the start of the scan. (bottom) Comparison of step scan and cv scans.

Type	cv scan	step scan
Centre	44.95	44.98
Width	0.145	0.134
Area	185.1	168.6
Time	49	75

Table 4.1: Comparison of parameters for a Lorentzian fit to the data for cv and step scans shown in figure 4.5
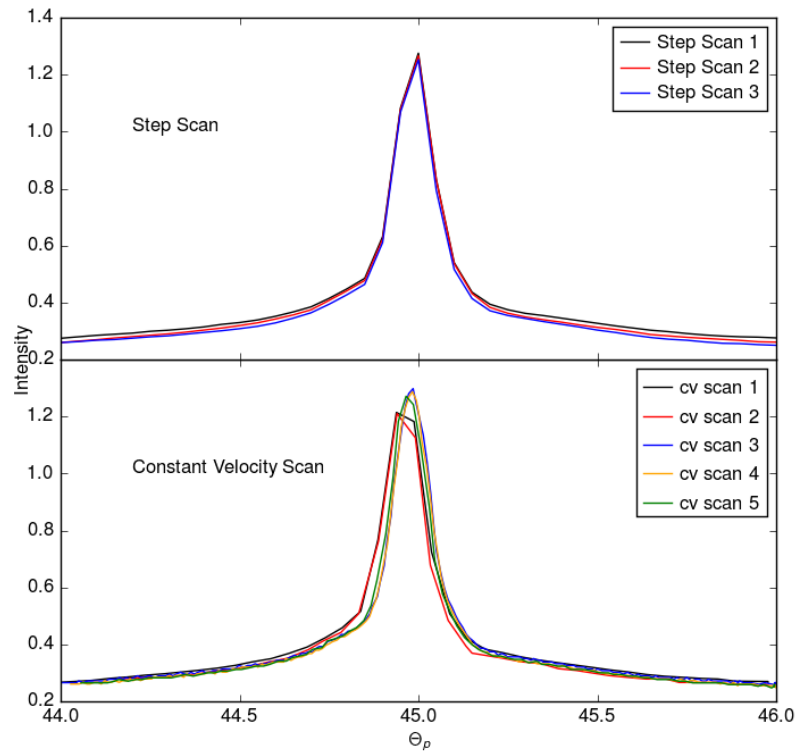
Figure 4.6: (top) Consecutive step scans with identical scan parameters of 0.05 degree step size and 1 second per point count time. (bottom) Comparison of various cv scans with different scan parameters.

between scans that is important for a full polarisation analysis, as long as the peak shape is consistent in successive scans, this change in area is irrelevant. A number of different cv scans are shown in the bottom panel of figure 4.6 compared to a number of identical step scans in the top panel. Only small differences are observed between successive step scans, with a slight variation in the cv scans, however, identical scans were found to be reproducible. The data was fitted with a Lorentzian lineshape, the results of which are shown in table 4.2. While there is more variation in the cv scan areas, the variation in the bottom three scans from the table should be compared to the three step scans. The cv scans appear to have less variation, however, these have more data points which could be a contributing factor and more data would be required for a precise analysis. It is clear that the cv scans show no more variability than the step scans, and have a significantly reduced scan time. The reduction in scan time from 75 to 49 seconds represents a significant saving over a full polarisation analysis which contains 180 scans, so an expected total saving of

Type	step	count time	scan time (s)	area
step scan 1	0.05	1	75	0.2163
step scan 2	0.05	1	75	0.2217
step scan 3	0.05	1	75	0.2152
cv scan 1	0.05	1	49	0.2279
cv scan 2	0.05	0.2	16	0.2149
cv scan 3	0.01	0.2	47	0.2129
cv scan 4	0.01	0.2	48	0.2147
cv scan 5	0.02	0.2	28	0.2156

Table 4.2: Scans are all over the range of θ_p from 44 to 46 degrees. All these scans finish at 46 degrees so included in this scan time is a roughly 2 second motor movement time to get to the starting position.

around 80 minutes. Due to the nature of a cv scan much more information is gained from a scan with a high point density, and even with a poor signal-to-noise ratio there would be a large number of data points to average over, and a good fit can still be produced. Furthermore this is with a 0.05 step size and 1 second counting time which can be reduced when checking the polarisation dependence of Bragg peaks or the main beam.

There is still a reasonable amount of detector dead time due to the η motion which cannot be avoided with this data collection method but may be addressed in the incident polarisation scans.

Comparison of Cv- and Step-Scan Full Polarisation Analysis

Unfortunately we do not have a direct comparison in terms of data quality between a step scan full polarisation analysis and a cv scan full polarisation analysis. This however, should not be a problem as the counting statistics should be the same and should therefore produce the same data quality and only the time of the scans need be compared. The optimum scan conditions for the main beam were found to be a 0.04 degree step size and 0.5 second count time, as the analyser was well aligned and only a 1 degree scan range was needed of θ_p and thus the scan time was reduced to 20 seconds. This reduced the overall full polarisation analysis time from 8 to only 4

hours.

Problems were encountered with the cv scans, however, as the scans were much quicker and the η motor became hot. As detailed in the x-ray instrumentation section the polarisation analyser motors are in-vacuum on RASOR and they are only passively cooled *via* radiation. The reduced time between successive η motions resulted in a large temperature increase. One solution for this is to increase the point density of the η angles which will result in a better fit to the data and result in shorter η motions. This will increase the count time again but provide higher quality data still with an increase in the measurement efficiency.

4.5.2 Incident Polarisation Scans

There is much less fitting of data involved in this method and there is potentially therefore fewer errors. The set up time for this method involves checking the θ_p positions at each η adding an additional hour to the set up process. The effectiveness of this scan depends upon the speed of the undulator motion and how it is set up to deal with polarisation (ψ) scans. As this method does not resemble the previous collection methods used there is no directly comparable scans that can be taken and a comparison of the final full polarisation analysis measurements must be made.

Comparison to Cv-Scan Full Polarisation Analysis

The ψ scans were much quicker than the cv scans and so were taken on the same reflections therefore allowing for a direct comparison between dataset quality. Some of the data points in the cv full polarisation analysis were found to be anomalous and this coincided with the region of the full polarisation analysis where the peak intensity was lowest. Analysis showed that this was due to the width of the θ_p scan changing. The effect of this can be reduced by taking the peak of the Lorentzian fit instead of the area. The top panels in figure 4.7 show θ_p scans from the high intensity region on the left with data from the low intensity region on the right. The resulting η scans are shown in the bottom panels with a comparison between results fitted with the Lorentzian peak height and peak area. The anomalous data point in the dataset fitted with the peak area results in a large variation in the possible fits and a much larger error in the resulting full polarisation analysis when compared to

the peak height.

Full polarisation analysis measurements comparing cv scans and ψ scans are shown in figure 4.8, with fits to peak area in the top panel, peak height in the middle panel, and ψ scans shown in the bottom panel. The data has noticeably larger error bars for the data taken with peak area as expected due to the anomalous data point. The top two data sets taken with cv scans do not look very smooth and the curve appears to be flattened in the region around 100-140 degrees. This is compared to the smoothly varying curve in the bottom panel for the ψ scans. A more informative comparison between the datasets can be obtained by fitting an arbitrary scattering matrix. This allows us to check if the collected data is possible as a polarisation dependence, under the assumption that only one scattering processes is involved. The result of this is shown in figure 4.9. Here it can be seen that the flattening at the top of the cv-scan datasets is unphysical. The ψ scan shows some very good results with a model fitting near-perfectly to the data.

A full polarisation analysis using the ψ scan method is much quicker and therefore allowed for an increased count time from 1 to 2 seconds per data point. Even with this increase the total measurement time was around 1 hour, which including the set up time still ensured that the measurement time was reduced by 75%.

Further improvements may be possible by utilising area detectors. In a paper by Sulyanov *et al.* (2014) [61] the polarisation of the incident beam was measured by the intensity variation in the Airy pattern from the diffraction from a number of sub millimetre thickness glass plates. This allowed the polarisation to be determined from a single collection of the area detector. A full polarisation analysis measurement could then be taken with no movement of the detector or sample, potentially allowing for even more time efficiency savings as only a single data point collection would be required to determine the polarisation and not multiple collections in a scan. The paper claims an accuracy of around 1%. Relatively high energy x-rays were used in this study of 12.6 keV. No lower limit on the beam intensity is given in this case but polarisation analysis of soft x-rays does require analyser crystals of a reflectivity of only few percent and this therefore may be a viable method even for soft x-rays.
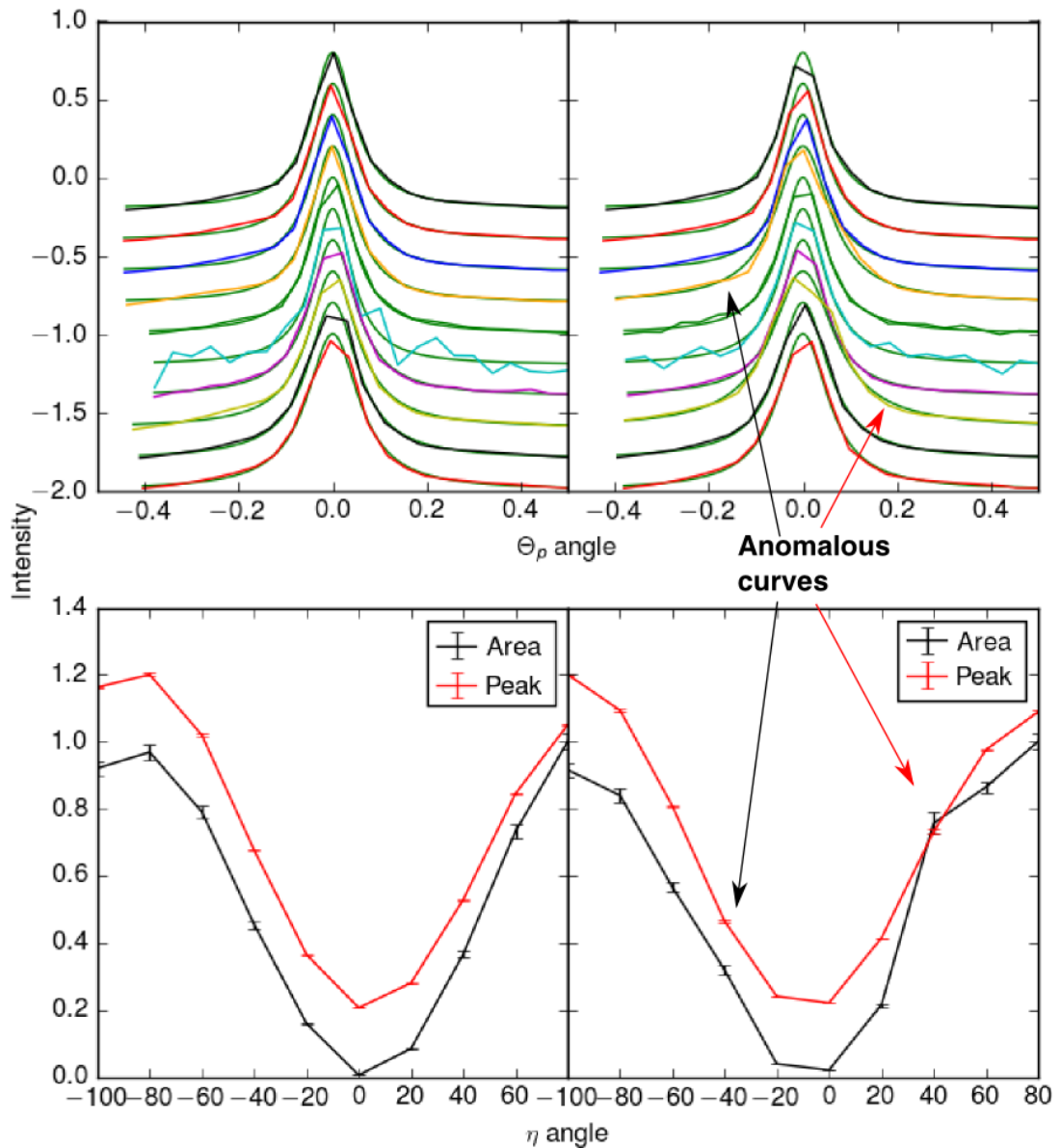
Figure 4.7: (top) cv scans with different η-angles in 10 degree steps from -100 to 80°. The left and right panels show curves for different incident polarisations. The right hand side has a lower scattered beam intensity, peaks with anomalous widths can be observed in this data and are noted by arrows. (bottom) η scans derived from integrating fitted peak shapes of the top graphs. The left and right panels show curves for different incident polarisations. The right hand side has a lower scattered beam intensity, points derived from peaks with anomalous widths can be observed in this data and are noted by arrows. The anomalies can be reduced by taking the fitted peak height instead of area.
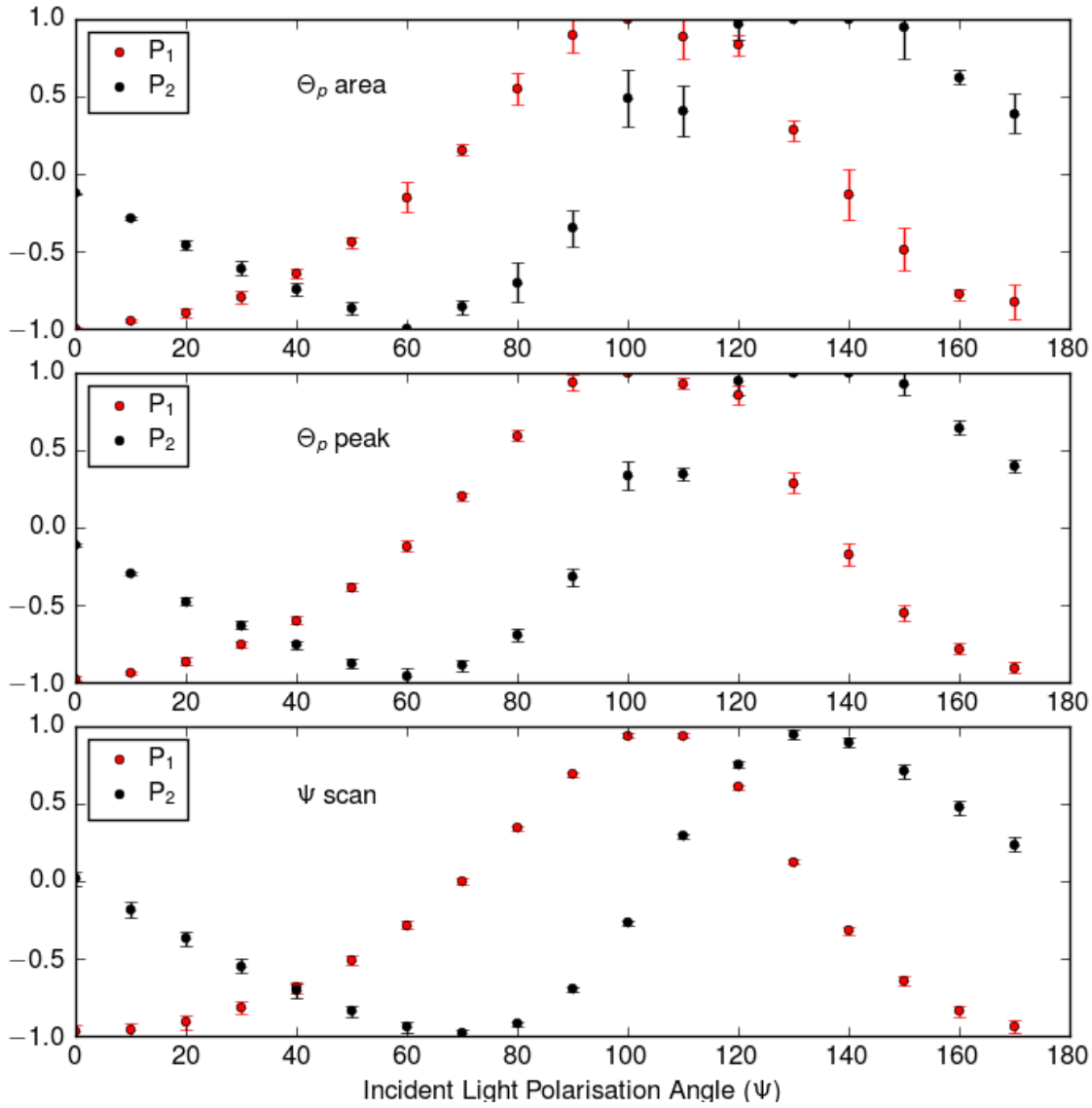
Figure 4.8: (top) Full polarisation analysis taken with cv scans and the θ_p peaks fitted to the peak area. (middle) Full polarisation analysis taken with cv scans and the θ_p peaks fitted to the peak height. (bottom) Full polarisation analysis taken with ψ scans.
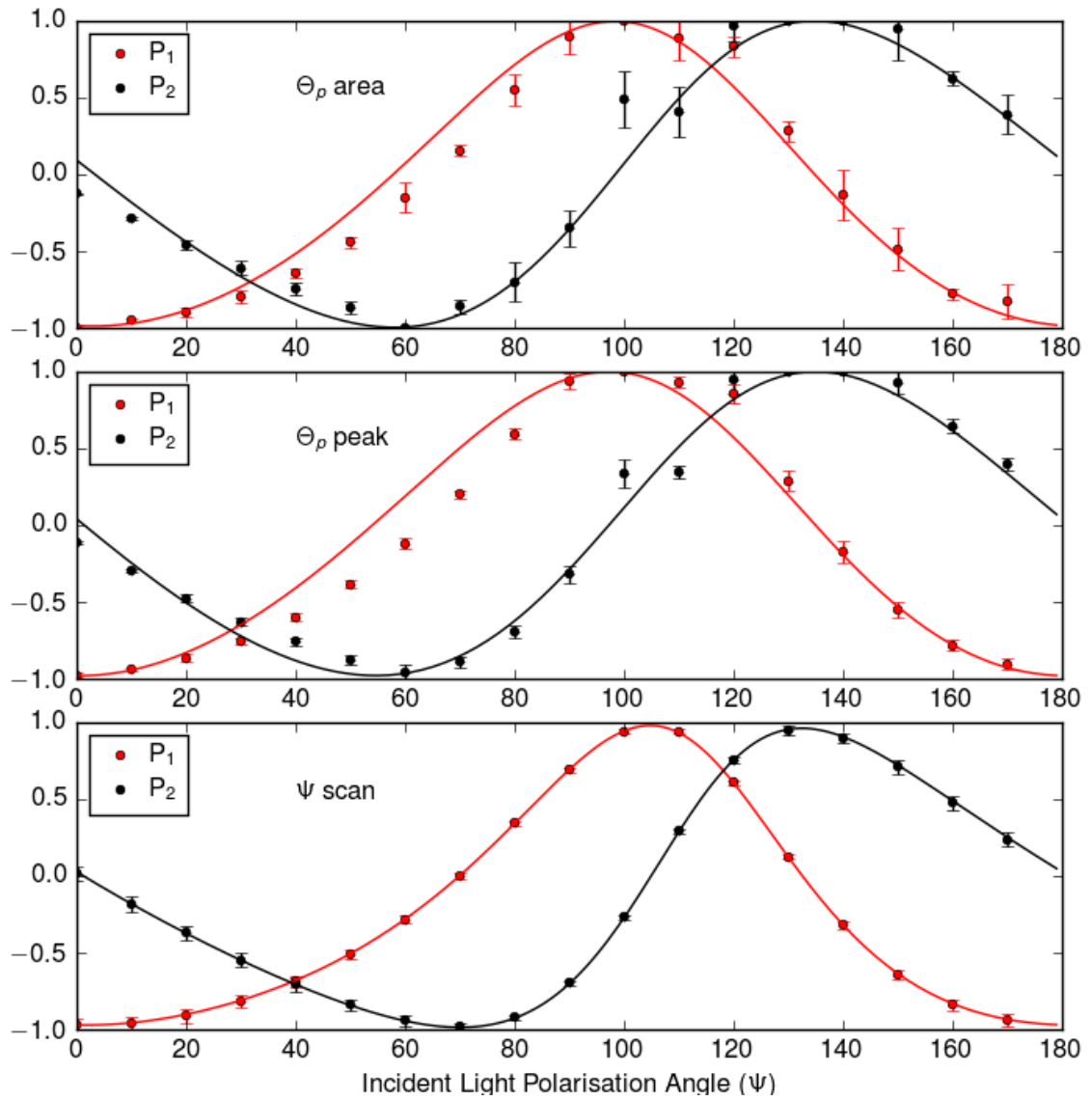
Figure 4.9: (top) Full polarisation analysis taken with cv scans and the θ_p peaks fitted to the peak area. (middle) Full polarisation analysis taken with cv scans and the θ_p peaks fitted to the peak height. (bottom) Full polarisation analysis taken with ψ scans. Solid lines represent a fit with a scattering matrix containing arbitrary elements.

4.6 Conclusions

These results are solely from the I10 beamline and although the time savings are significant may not be directly reproduced with different beamline setups. The financial cost of synchrotron experiments means that any time saving could have a significant impact on the field. Especially with the fierce competition at synchrotrons from protein crystallography beamlines which have a high publication rate. This improvement will allow data on much weaker peaks to be collected as longer count times can be used which could be applied to measuring weak non-resonant scattering. It will also allow full polarisation analysis measurements to be collected on multiple stronger peaks to give a more robust picture of the nature of magnetic systems.

The ψ scans were found to be a highly effective method of taking a full polarisation analysis measurement, producing extremely high quality data in one quarter of the time of the previous method. Cv scans although introducing a significant time saving were unable to produce the same data quality observed in the ψ scans.

Further Work

Further improvements may be possible by utilising area detectors. In a paper by Sulyanov *et al.* (2014) [61] the polarisation of the incident beam was measured by the intensity variation in the Airy pattern from the diffraction from a number of sub millimetre thickness glass plates. This allowed the polarisation to be determined from a single collection of the area detector. The polarisation could then be fully determined by one collection of the area detector potentially allowing for even more time efficiency savings as scans would no longer need to be repeated at different eta angles.

Chapter 5

Spin Canting in the Ground State of CeRu$_2$Al$_{10}$

The work in this chapter has been submitted for publication in The Journal of the Physical Society of Japan.

In this chapter the novel magnetic phase of the heavy fermion Kondo semiconducting compounds CeM_2Al$_{10}$ (M =Os, Ru) are investigated. The compounds CeM_2Al$_{10}$ (M = Os, Ru) display unusually high transition temperatures [62] to an antiferromagnetically ordered state where the moments point away from the magnetic easy axis as determined from measurements of the susceptibility in the paramagnetic state [63–69]. The direction of the ordered moment is also highly unstable to doping with small amounts of doping causing a rotation of the moment direction [70–78]. We use full polarisation analysis of the resonantly enhanced $(0, 1, 0)$ reflection at the cerium M-edges to investigate the magnetic ground state for any peculiarities which might help us understand the unusual properties of this system.

5.1 Introduction

The lanthanide series is a fertile hunting ground for uncovering new and interesting physical properties due to the juxtaposition of the f-electrons being simultaneously highly localised and close to the Fermi level. It is this property that permits the unusual coexistence of magnetism and superconductivity [79]. As a result of the

high localisation of the f-orbitals, the f-electrons are not utilised in bonding and can lead to many unpaired electrons, resulting in strong rare-earth permanent magnets[1]. In these systems long-range effects occur *via* coupling between the highly localised atomic f-orbitals and the crystallographic conduction electrons contained within the band structure. It is this coupling that alters the density of states at the Fermi level, causing the extremely large conduction band effective masses (exceeding 100 m_e), from which the term heavy fermion derives[2] (first observed in CeAl$_3$ by Anderes, Graebner, and Ott [80]).

5.1.1   The Kondo Effect

In metals the electrical resistivity can be thought of as being directly proportional to the scattering rate of electrons from the lattice of positively-charged nuclei. As the temperature decreases the thermal motion of the nuclei reduces, and the scattering rate and hence the resistivity are expected to reduce. A number of metallic systems were found to deviate from this picture displaying a minimum in resistivity upon reducing temperature, and then an increasing resistance as temperature is further reduced. It was not until the early 1960s that this extra scattering was linked to localised magnetic moments and in 1964 Jun Kondo showed the detailed origin of the scattering process [81].

Kondo scattering is a third order spin dependent electron scattering from magnetic impurities. An incident spin-up electron ↑ is scattered from a spin-down magnetic impurity ↓ which flips the spin of the impurity into an intermediate spin up state ↑ before a further scattering process which restores the state of the impurity leaving the electron with in a spin-down state ↓. This process is temperature dependent and has the form:

$$R(T) = R_0 2 J \rho \log \left(\left| \frac{k_B T}{D - \epsilon_F} \right| \right) . \tag{5.1}$$

Where R_0 is the temperature independent resistivity, ϵ_F is the Fermi energy, ρ is the density of states, and D is the energy of the highest state the electron can be

---

[1]The rare earth elements are composed of the lanthanide series as well as the chemically similar elements scandium and yttrium.

[2]First coined in the paper by Steglich [79].

scattered into. This dominates at low temperatures when the exchange coupling $J < 0$ which corresponds to antiferromagnetic coupling between the conduction and f-electrons.

The Kondo effect is an explicit effect for localised non-interacting magnetic impurities and as such should not strictly be considered for systems which display the RKKY interaction. However, Doniach noted the similarities between the two and established the so called Doniach phase diagram [82] for the interplay between the two interactions which has been studied in a number of systems [83–86].

5.1.2 CeM_2Al$_{10}$ (M = Fe, Os, Ru)

The group of systems CeM_2Al$_{10}$ (M = Fe, Os, Ru) are interesting examples of heavy fermion systems because their properties deviate in a number of ways from those expected by extrapolating the results of related compounds. Magnetic phase transitions in lanthanoid compounds depend upon the total angular momentum obeying the de Gennes scale factors [87] given by the following:[3]

$$T_N \approx (g_J - 1)2J(J + 1) \tag{5.2}$$

Where T_N is the Néel temperature, g_J is the Landé g-factor and J is the total angular momentum. In this series gadolinium would be expected to have the largest transition temperature. Comparing the gadolinium to the cerium analogues in table 5.1 the transition temperatures are significantly lower for all the gadolinium analogues as compared to the cerium ones. Interestingly the cerium iron analogue does not show long-range magnetic ordering from bulk measurements [88]. The lattice parameters are also comparable between all the compounds. However, the breakdown of the de Gennes scaling is not unusual [89] and strong $4f$-conduction band coupling can cause this deviation [90] (albeit in superconducting and not magnetic systems). These compounds all crystallise into the $Cmcm$ space group with the cerium 3+ ions surrounded by a complex cage-like arrangement of sixteen aluminiums and four transition metal ions with large separations between the cerium ions (>5 Ångströms), the crystal structure is shown in figure 5.1. In the previously mentioned gadolin-

---

[3]Interestingly the de Gennes scale factors are just as valid for superconducting transition temperatures.

Crystal	$T_N(K)$	Lattice parameters (Å)	Reference
$GdOs_2Al_{10}$	18	9.13, 10.23, 9.17	[91]
$GdRu_2Al_{10}$	16.5	9.09, 10.22, 9.14	[63, 92]
$GdFe_2Al_{10}$	17	-	[93]
$CeOs_2Al_{10}$	27.3	9.16, 10.25, 9.14	[63]
$CeRu_2Al_{10}$	28.7	9.16, 10.27, 9.12	[62]
$CeFe_2Al_{10}$	-	9.01, 10.23, 9.08	[63]

Table 5.1: Table showing the lattice parameters and transition temperatures of the gadolinium compared to the cerium compounds.

ium analogues, the magnetic phase transition can solely be attributed to the RKKY interaction as the mechanism that drives the transition. The high ordering temperature in the cerium compounds means that the RKKY interaction cannot be the cause of the transition, as it strongly depends upon the ion separation, and the underlying origin is still an unresolved question. The strengths of the conduction-f-electron coupling in these compounds, confirmed by soft x-ray resonance photoelectron spectroscopy measurements [94] and consistent with susceptibility measurements [63–66], increases from Ru $\rightarrow$ Os $\rightarrow$ Fe where in terms of the Doniach phase diagram the iron compound traverses from antiferromagnetic ordering to Kondo insulating regimes. Neutron powder and single crystal measurements have shown that the ruthenium and osmium compounds magnetically order to an antiferromagnetic ground state with the propagation vector $(0, 1, 0)$. The moments point along the c-axis with the mY$_3^-$ magnetic irreducible representation and moment sizes of 0.29 μ_B, and 0.42 μ_B for ruthenium and osmium respectively, the magnetic structure is shown in figure 5.2 [67–69]. Interestingly this is not the magnetic easy axis as determined by bulk magnetisation measurements in the paramagnetic state, which is the a-axis for both the cerium and ruthenium compounds [95] [64], the magnetisation data for the osmium compound is reproduced in the left-hand-side of figure 5.3. Strigari *et al.* also uses ionic full multiplet calculations to predict the crystalline electric field ground state wavefunction, from modelling of cerium L-edge absorption spectra, which yields expected moments of (1.44,0.19,0.38) μ_B for the ruthenium analogue and (1.35,0.27,0.30) μ_B for the osmium analogue [96]. These predict small moment
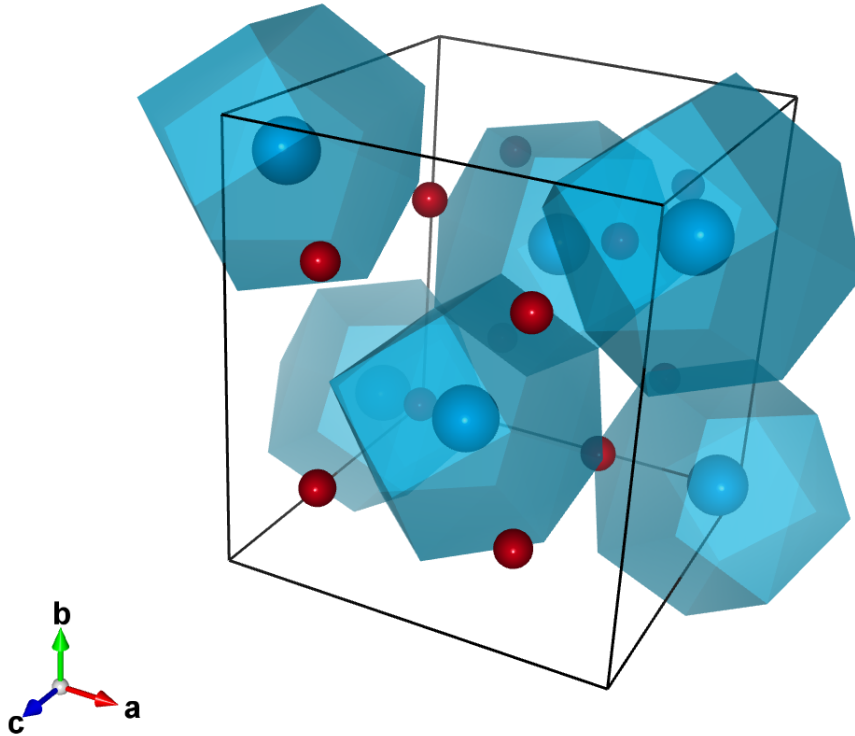
Figure 5.1: Crystal structure of CeM_2Al$_{10}$ (M =Fe, Os, Ru) compounds with transition metal atoms shown in red, cerium in blue and the aluminium at the polyhedral vertices.

size when the moment is oriented along c roughly consistent with measurements by neutron diffraction.

Optical conductivity measurements have found that the c-f coupling is highly anisotropic and resides mainly in the a-c plane [97]. A charge density wave like transition along the b-axis just above the magnetic transition temperature has then been speculated to trigger the transition giving an explanation for the high transition temperature.

The ordered moment along the c-axis is very unstable to electron-doping on the ruthenium site of CeRu$_2$Al$_{10}$, by substitution with rhodium, finds small doping amounts (0.05) cause a sharp reduction in the transition temperature [70–72]. This is coincident with a rotation of the magnetic structure such that the moments point along the bulk paramagnetic easy axis (a-axis) and an increase in the mo-
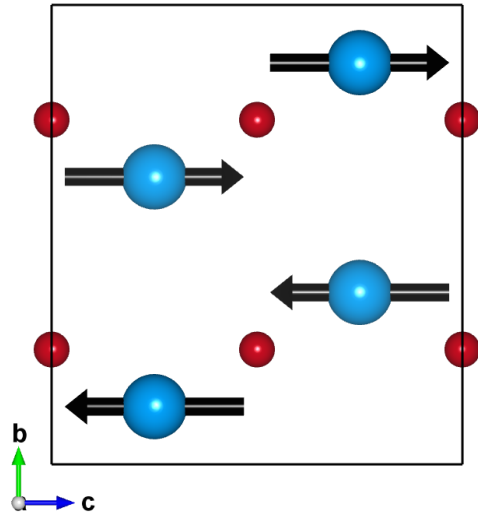
Figure 5.2: Magnetic structure of CeM_2Al_{10} ($M =$Fe, Os, Ru) with the aluminium atoms removed for clarity. Showing the cerium atoms in blue and the transition metal atoms in red

ment size. Conversely, hole-doping with rhenium (with as little as 0.06) induces the magnetic moment direction to switch to along the b-axis with a reduced moment size [73]. The doping was observed to strongly reduce the low-temperature magnetic excitations observed by inelastic neutron scattering, but they still persist and there is a coincident increase in the coupling between the conduction electrons and the $4f$-electrons. The persistence of the spin gap retains the moment orientation with the anisotropic c-f coupling to align pointing away from the a-axis. Similar results have been observed with chemical pressure by doping the cerium site with as little as 0.1 lanthanum [74], or the aluminium site with silicon [75]. Changes in moment direction and size are also observed in the osmium compounds with small doping amounts [74, 76–78].

Due to the small moment size, the number of reflections used to refine the magnetic structures of the undoped compounds was small, and as such any small deviations in the magnetic structure of the parent compound would be within the error of the measurement. Small deviations may be expected due to the unstable nature of the moment, combined with the fact that it does not point along the paramagnetic easy axis. Further, any small moment present on the osmium or ruthenium would likely be too small to be detectable.
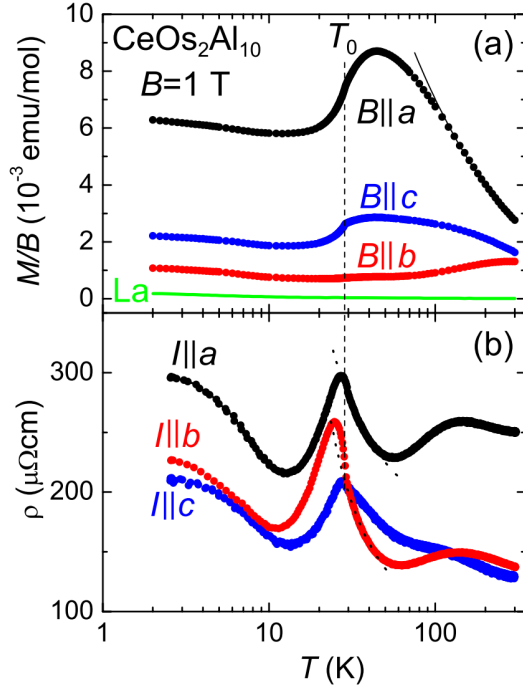
Figure 5.3: (a) Temperature dependence of the magnetic susceptibility M/B for CeOs$_2$Al$_{10}$ in magnetic field B applied along the orthorhombic principal axes. The thin solid curve represents the Curie-Weiss fit. The dashed line indicates the transition temperature T_0. The susceptibility of LaOs$_2$Al$_{10}$ is also shown by the green solid line.(b) Temperature dependence of the electrical resistivity of CeOs$_2$Al$_{10}$ for the three current directions. The dotted lines represent the thermally activating behaviour for $I\|a$ and $I\|c$ (from [64]).

In this chapter we will utilise polarised resonant x-rays to investigate the magnetic structures of CeRu$_2$Al$_{10}$ and CeOs$_2$Al$_{10}$ and determine their exact nature.

5.1.3 Experimental Methods

Single crystals of CeRu$_2$Al$_{10}$ and CeOs$_2$Al$_{10}$ were grown *via* the Al self-flux method by Toshiro Takabatake and Yuji Muro at Hiroshima University in Japan where CeRu$_2$ and CeOs$_2$ were prepared by arc melting of pure elements then mixed with an excess amount of Al in the ratio 1:2:20 and heated in an alumina crucible. Finally the molten Al flux is separated by centrifuging. Crystals were aligned, cut and polished where necessary using an in-house four circle Huber diffractometer. Soft x-ray measurements were taken on the RASOR end station of the I10:BLADE beam-

line at the Diamond Light Source Ltd. Further measurements were taken at the XMaS BM28 beam-line at the ESRF at the ruthenium L-edges. The energy of these edges is between the capabilities of most soft and most hard x-ray diffractometers, being strongly absorbed by air but above the range of the optics usually installed on soft x-ray beam-lines. Vacuum shrouds were custom built to accommodate the angles of the reflections that were required to be accessed, greatly restricting the range of motion.

5.2   Results and Discussion

5.2.1   CeOs$_2$Al$_{10}$ Resonant X-ray Scattering

An $(0,1,0)$ oriented single crystal of CeOs$_2$Al$_{10}$ was measured at the cerium M_{IV} edge, at 14 K. A strong resonance was observed at the disallowed $(0,1,0)$ Bragg peak as shown in the bottom pane of figure 5.4. Temperature dependence measurements show that the peak originates from the magnetic transition, top panel of figure 5.4. A residual peak was observed above the magnetic transition, however, this was sharp and was found to be due to the $(0,2,0)$ Bragg peak with higher harmonics of x-rays with energy $\lambda/2$. These were removed by changing the primary mirror and grating away from the gold coated regions and hence cutting off higher energy x-rays. Interestingly a strong resonance was only observed with π incident light. This is consistent with scattering largely in the $\pi - \pi$ channel and therefore a magnetic moment largely in the U_2 experimental basis direction. This is consistent with a moment along the c-axis. Full polarisation analysis measurements were taken on the peak on resonance at 906.8 eV. Due to a misalignment of the analyser crystal and the crystal azimuth being such that the scattered intensity was weak[4] the data is plagued by errors. The importance of analyser alignment and proper procedure has been discussed in Appendix C. Fitting of the full polarisation analysis is consistent with the proposed c-axis aligned structure. The only fittable parameter is the azimuthal angle that the crystal is mounted at as this is not well known. The noise level is

---

[4]The azimuthal stage in RASOR limits the temperature to above the transition for this sample so the azimuth was unable to be changed.

such that any small deviations from this structure would be well within the margin of error.
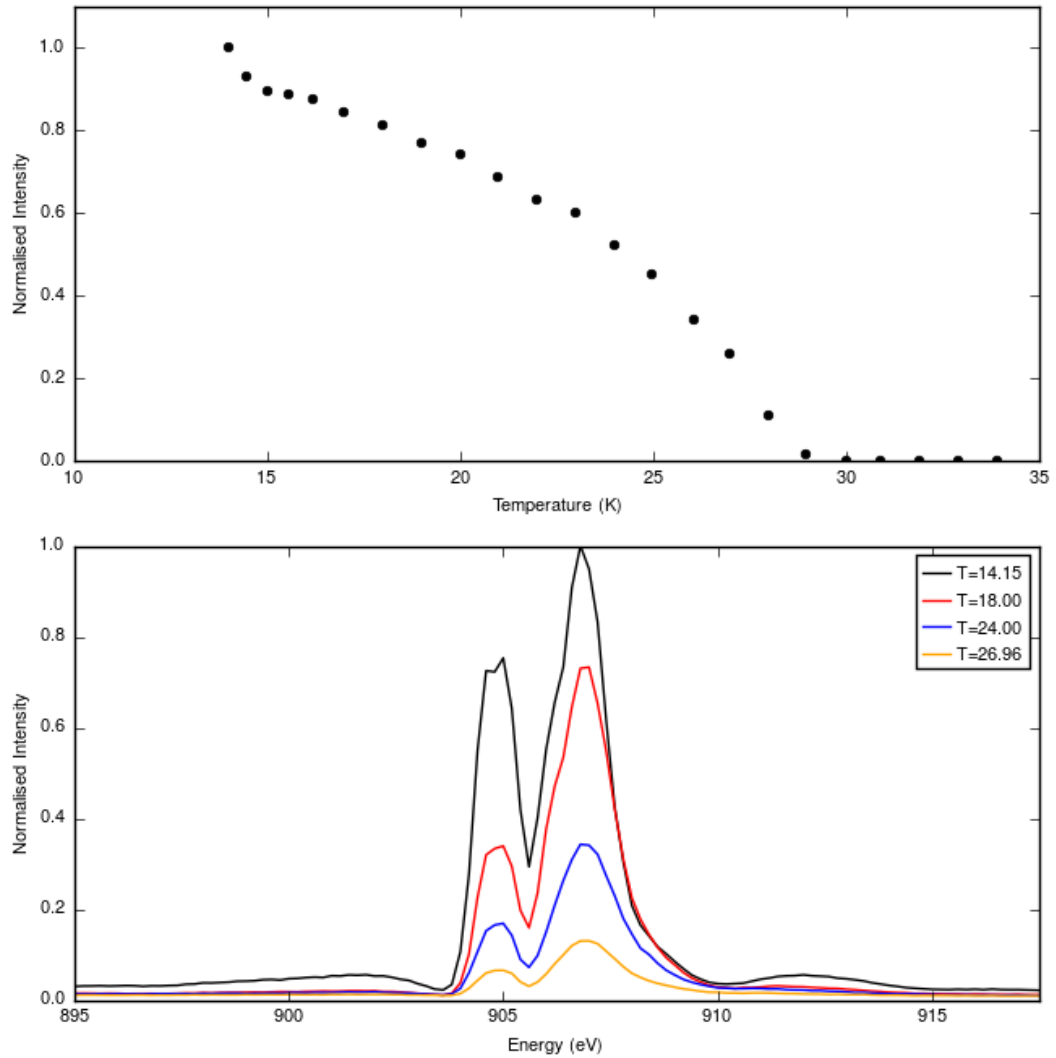
Figure 5.4: (top) Temperature dependence of the $(0, 1, 0)$ superlattice reflection intensity. (bottom) Temperature dependent energy scans of the $(0, 1, 0)$ superlattice reflection at fixed wave-vector.
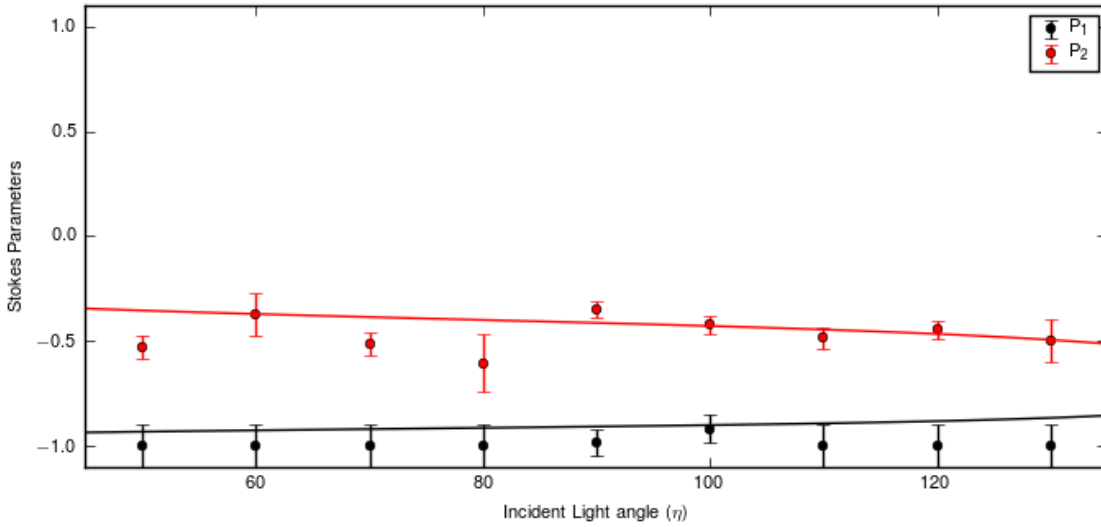
Figure 5.5: Full polarisation analysis of the $(0, 1, 0)$ magnetic reflection data shown as solid circles and fit to mY_3^- magnetic structure as lines.

5.2.2 CeRu$_2$Al$_{10}$ Resonant X-ray Scattering

Measurements at the ruthenium L-edges showed no resonant features at disallowed Bragg peaks. The lack of signal at the highly sensitive L-edges to $5d$ magnetic moments strongly suggests that the ruthenium is not involved in the magnetism even as an exchange site. This is consistent with previous magnetic structure determination that found no moment on the ruthenium, however, a weak hybrid moment has until now been difficult to discount [67–69].

A strong resonance was observed at the cerium M-edges of the $(0, 1, 0)$ disallowed Bragg peak at 14 K, however, the peak was also observed to exist away from resonance. Normalised $(0, k, 0)$ scans $(\theta - 2\theta)$ are shown of the on and off resonance peaks in figure 5.6a. There is a large difference in the peak widths which can to some extent be accounted for by the reduced absorption away from the edge which will mean the x-rays penetrate the sample further resulting in a sharper peak. The normalised temperature dependences of both peaks are shown in figure 5.6b and are observed to have similar temperature dependences although the off-resonant peak is roughly 100 times weaker in peak intensity. The temperature dependence shows a transition for both peaks at 32 K $\pm$ 0.5. This is above what might be expected for a transition at 28.7 K. X-ray measurements, however, are not an ideal tool for

determining transition temperatures. There is a lot of energy in the x-ray beam at a synchrotron which is highly focussed and will provide a heat load to a very localised spot on the sample surface. This can result in transitions being measured at lower temperatures than expected. Synchrotron experiments are also highly time constrained so often temperature dependences are taken as quick checks that the scattered intensity is due to in this case the magnetic transition and not for example higher harmonics of the photon energy diffracting from higher order Bragg peaks. This will result in the sample surface lagging behind the temperature sensor (especially if the sample is not a good conductor) and a measurement of the temperature dependence will produce a higher than expected transition temperature. This discrepancy in the transition temperature measured here and those previously reported is then not anomalous. We therefore link the presence of both peaks to the magnetic transition. Fixed-**q** energy scans of the peak with σ and π incident light are shown in figure 5.6c. As magnetic scattering is described by the cross product of the incident and scattered polarisations, for σ incident light there will be no intensity in the σ' scattered polarisation (as these are both in the direction $(0, 1, 0)$). All polarisations are available (dependent upon the magnetic structure) for scattering when π polarised light is incident. It is therefore expected for magnetic scattering that there will be more scattered intensity with π polarised incident light. The resonance at the cerium edges and the rotation of the polarisation is consistent with the antiferromagnetic structure with the magnetic moments residing on the cerium, described by neutron diffraction measurements.

There are a number of possibilities for the source of the off-resonant peak. Fitting the line-shape of the resonance finds the intensity of the signal at 920 eV to be much smaller than the 1% expected from the peak intensities of the k-scans, suggesting that there is a peak distinguished from the tail of the resonance. The lack of a remnant peak above the transition temperature rules out any contribution from $\lambda/2$ of the allowed $(0, 2, 0)$ Bragg peak or more exotic scattering processes such as the anisotropic tensor of susceptibility [98]. The possibility of a small structural modification occurring at the transition and reducing the symmetry to one of the two subgroups $Cm2m$ or $Pmnm$ has been put forward [99][5]. The existence of the

---

[5]A symmetry lowering has also been observed by electron diffraction in $CeOs_2Al_{10}$ [64]
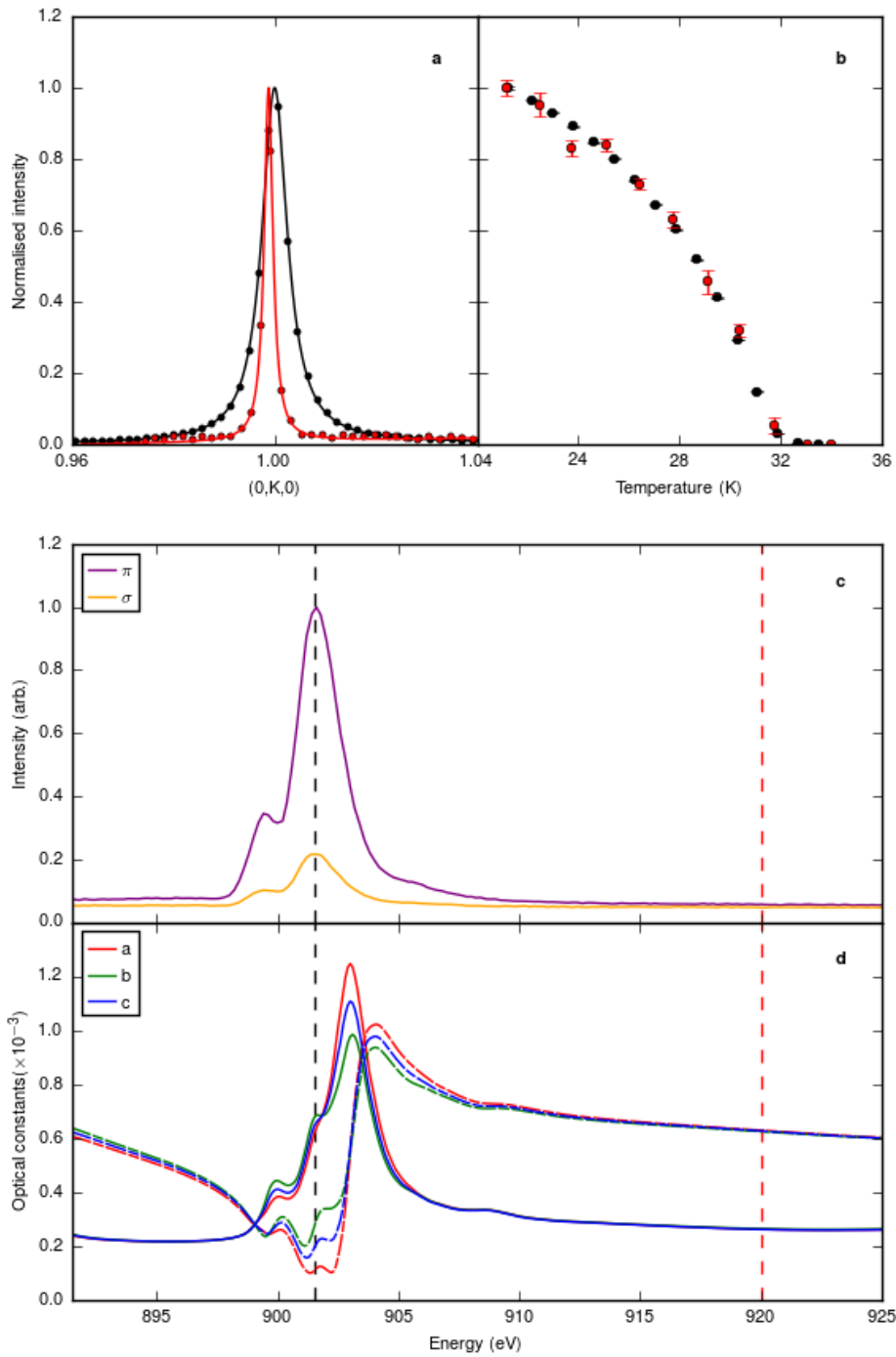
Figure 5.6: (a) θ-2θ scans of the $(0,1,0)$ peak at 901.8 eV (black) fitted with a Lorentzian line-shape of width 0.64° in theta and 920 eV (red) fitted with a Lorentzian line-shape with a width of 0.21° in theta. (b) Normalised temperature dependence of the intensities of the peaks at the two different energies. (c) Energy scan of the $(0,1,0)$ peak at constant wave-vector. (d) Delta (dashed line) and beta (solid line) optical constants derived from absorption spectra along the crystallographic axes a, b, and c from [95].

$(0, 1, 0)$ is consistent with the $Pmnm$ space group as the reflection condition $(0,k,0)$ $= 2n$ is not present in this space group.

As such full polarisation analysis measurements were taken of both the resonant and off-resonance features and are shown in figure 5.7 with the lines corresponding to the mY_3^- structure with the top panel being the resonant data and the bottom panel being the off-resonant data. The azimuth is a fitted parameter and found to be 55.39 which is close to the 55.14 measured before the experiment.

The resonant data deviates from $\sqrt{P_1^2 + P_2^2} = 1$ at $\Psi \approx 155°$ as shown by the blue data points in figure 5.7 this deviation can only be accounted for either by a non-collinear magnetic moment or an effect of x-ray birefringence. A higher order E1-E1 scattering process would be expected to deviate from $P_1 = 0, P_2 = -1$ at an incident light angle of $180°$ due to the $\sigma - \sigma$ component of the matrix as would E2 quadrupolar contributions[6]. The fit of the resonant data with the proposed neutron structure of moments oriented along the c-axis is a collinear structure, and as expected does not deviate from $\sqrt{P_1^2 + P_2^2} = 1$. It is interesting to note that the only noticeable deviation from the proposed structure is in a part of the full polarisation analysis which was not measurable in the case of $CeOs_2Al_{10}$ due to a lack of intensity. The $\sqrt{P_1^2 + P_2^2}$ data points will be omitted from future figures for clarity as they are just composite data and not therefore involved in the fitting. The off-resonant data would not be expected to contribute to the resonant full polarisation analysis in any significant way as the peak intensity is 100 times weaker and any deviation would be within the error of the measurement. The most this could contribute would be a deviation from $\sqrt{P_1^2 + P_2^2} = 1$ by 0.02.

The off-resonant data (bottom panel of figure 5.7) displays a similar shape to the resonant data with deviations from $\sqrt{P_1^2 + P_2^2} = 1$. There is also a deviation from the expected $P_1 = 0, P_2 = -1$ from a normal E1-E1 dipole resonance at an incident light angle of $180°$ (σ incident light). There are a number of factors that we must consider here. If we are too close in energy to the resonance we could still be measuring a small component of the resonant peak. We could also be observing a resonant signal from diffuse magnetic moments in the spin-polarised conduction

---

[6]These processes would still require a non-collinear moment to produce the deviation from $\sqrt{P_1^2 + P_2^2} = 1$

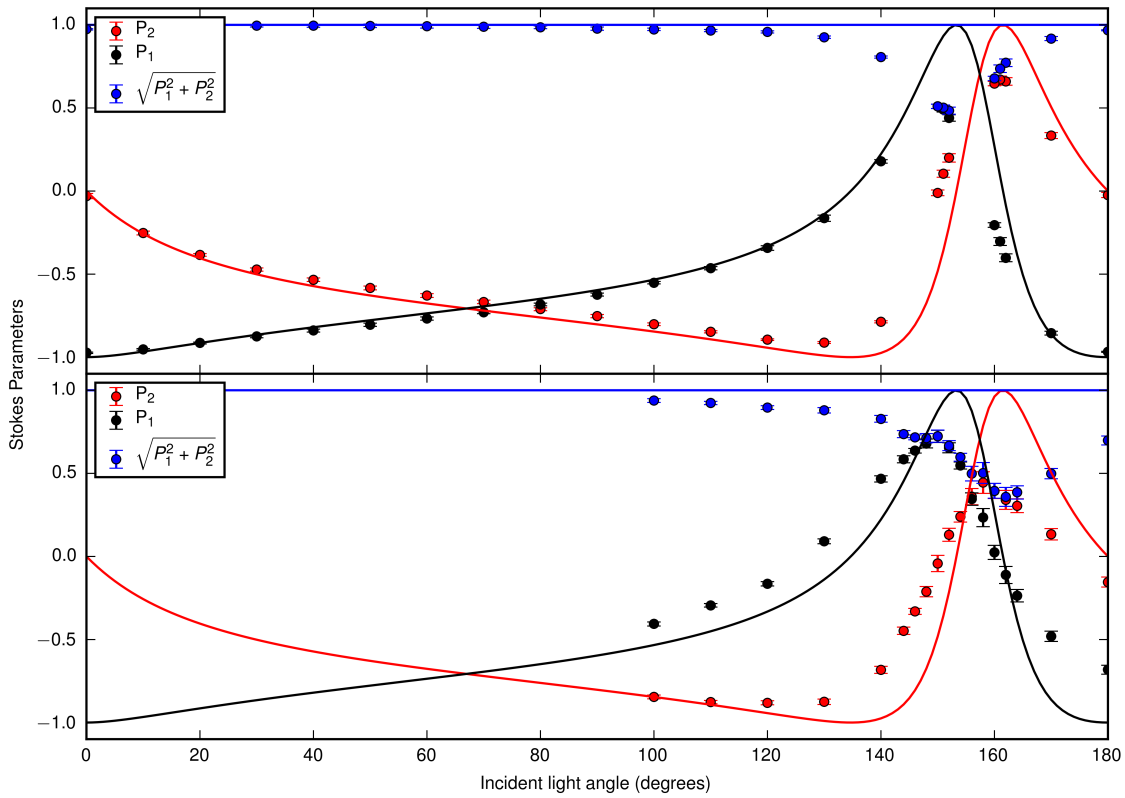Figure 5.7: (top) Full polarisation analysis of the $(0, 1, 0)$ taken on resonance at 901.8 eV at 14 K. (bottom) Full polarisation analysis of the $(0, 1, 0)$ taken off resonance at 920 eV at 14 K. Lines denote the mY_3^- structure at an azimuthal angle of 55.39 away from $(0,0,1)$ in the scattering plane. The blue line $\sqrt{P_1^2 + P_2^2}$ will only deviate from 1 if the light is no longer linear.

band, which will be present above the edge. In these two cases the deviation at the incident light angle of 180° could be accounted for by a weak structural Bragg peak due to a symmetry change with the transition (this could possibly be caused by magnetostriction). The final option is that the signal is truly from non-resonant magnetic scattering. Higher order scattering processes can be ruled out as they would be expected to contribute to the resonant peak as well. It is of course also possible that our signal is coming from a combination of all of these effects. We will start by considering the effects of X-ray birefringence on the resonant fit.

X-ray Birefringence

X-ray birefringence effects are inherent in any non-cubic crystal system where there is a difference in absorption when polarised x-rays have their polarisation vector along different crystallographic directions. It was first noted as an important effect in resonant x-ray scattering in CuO [100] to explain a signal which had been attributed to orbital currents. As the x-ray propagates though the sample it is subject to linear optical processes which transform the polarisation before it is scattered. Dichroism will cause a rotation of the polarisation of x-rays as they travel through the sample while birefringence will cause a conversion from linear to circularly polarised light. Although the difference in lattice parameters is relatively small in $CeRu_2Al_{10}$ the system is anisotropic in many bulk measurements and this is evident in the x-ray absorption spectra. To determine the effects of the propagation through the sample we have used absorption measurements along the three crystallographic axes (taken with permission from [95] Strigari). These were then fitted to textbook values for the absorption calculated from Chantler tables [101] and fitted with an energy shift to our dataset to match measured fluorescence measurements. This allows determination of the beta optical constant and a Kramers Kronig transform determines the delta optical constant. The results of this are shown in the bottom panel of figure 5.6. We must then look again to Jones calculus as to how to incorporate this into our system. For a general system we have the following matrix for propagating through a sample:

$$M = \begin{pmatrix} e^{i\mathbf{k^n \cdot r}} & 0 \\ 0 & 0 \end{pmatrix}. \tag{5.3}$$

Where $\mathbf{k^n}$ has been modified by the refractive index of the sample and becomes imaginary, this matrix corresponds to an arbitrary system where the optical axis and the polarisation of the incident light are parallel and along the experimental x-axis. To account for our crystal system we must take the projections of our three crystallographic axes onto the plane perpendicular to our incident k-vector where we now have three optical axes corresponding to the three crystallographic directions [102]. To determine the propagation matrix we must determine the orientation of these within the ray basis. So for the simple case where we are looking at an $(0,0,L)$ peak at an arbitrary azimuth (ζ) from $(1,0,0)$ we have the situation using the following rotation matrix:

$$R(\zeta) = \begin{pmatrix} \cos(\zeta) & -\sin(\zeta) & 0 \\ \sin(\zeta) & \cos(\zeta) & 0 \\ 0 & 0 & 1 \end{pmatrix}. \tag{5.4}$$

That is in the ray basis we have $(a\cos(\zeta) + b\sin(\zeta), b\cos(\zeta) + a\sin(\zeta), c)$ then for a reflection at a theta angle the projection onto the incident light propagation is given by:

$$R(\theta) = \begin{pmatrix} \cos(\theta) & 0 & \sin(\theta) \\ 0 & 1 & 0 \\ -\sin(\theta) & 0 & \cos(\theta) \end{pmatrix}. \tag{5.5}$$

Then applying this rotation matrix we get $(\cos(\theta)(a\cos(\zeta)+b\sin(\zeta))-c\sin(\theta), b\cos(\zeta)+a\sin(\zeta), c\cos(\theta) + \sin(\theta)(a\cos(\zeta) + b\sin(\zeta)))$ which is the crystallographic axes in the ray basis. As there is no component of the electric field along the direction of propagation, that dimension becomes irrelevant and we drop down to a two-dimensional problem (which as we were looking at an $(0,0,L)$ reflection with $(1,0,0)$ along the beam means we lose the first component), $(b\cos(\zeta) + a\sin(\zeta), c\cos(\theta) + \sin(\theta)(a\cos(\zeta)+b\sin(\zeta)))$ then to determine the angles to input into the rotation for the Jones matrix we take the arctan for each crystallographic axis, so taking just the a components in our example we get $\arctan(\sin(\theta)\cos(\zeta)/sin(\zeta)) = \theta_a$ Then using a rotation matrix:

$$R(\theta) = \begin{pmatrix} \cos(\theta) & -\sin(\theta) \\ \sin(\theta) & \cos(\theta) \end{pmatrix}. \tag{5.6}$$

This can be applied to the general Jones matrix 5.3 takes the form where $M(\theta) = R(\theta)MR^{\dagger}(\theta)$. Then summing for each for the crystallographic axes with the appropriate **k**-vector determined from the optical constants gives us the general propagation matrix as:

$$M = e^{(2\pi i \mathbf{k}_a^n \cdot \mathbf{r})} DMt(\theta_a) + e^{(2\pi i \mathbf{k}_b^n \cdot \mathbf{r})} DMt(\theta_b) + e^{(2\pi i \mathbf{k}_c^n \cdot \mathbf{r})} DMt(\theta_c) \qquad (5.7)$$

$$DMt(\theta) = \begin{pmatrix} \cos(\theta)^2 & -\cos(\theta)\sin(\theta) \\ -\cos(\theta)\sin(\theta) & \sin(\theta)^2 \end{pmatrix}. \qquad (5.8)$$

Then for the scattered beam the θ rotation matrix is just the transpose of this. Applying this to the maths for full polarisation analysis we now have a depth dependence on our incident beam, which is inseparable from the scattering process, and as such we must integrate over the depth into the sample, such that:

$$\rho' = \int_0^{r_p} M_{scatt} M_{sam} M_{inc} \rho M_{inc}^{\dagger} M_{sam}^{\dagger} M_{scatt}^{\dagger} dr. \qquad (5.9)$$

Where ρ is the matrix that describes the ray and the M matrices describe the different ray processes, r_p is half the penetration depth at which the ray intensity will fall by $\frac{1}{e}$ (so that the total ray path in the sample is the penetration depth) of the sample where the x-ray intensity drops to $\frac{1}{e}$ which in our case is around 150 nm[7]. Here the incident light is first operated on by the propagation to the scattering point then transformed by the scattering process and then finally operated on by the propagation out of the sample. Including this in our model for the resonant data is only a small correction in this system as shown in figure 5.8, as such will be neglected from now onwards. To check the veracity of this result we can calculate the minimum depth at which a plane polarised ray could be converted to circular. This is given by the equation $r = \frac{\pi}{\delta_1 - \delta_2}$ where δ_1 and δ_2 are the real part of the optical constants along different optical axes. In our case the largest difference in the optical constants is between the a and b axes where $\delta_a = 0.00011$ and $\delta_a = 0.00027$ which gives the shortest path length to completely convert to circular as 4300 nm. Non-linear optical effects which change the optical constants depending on light intensity have also not been considered here.

This result is not unexpected, resonant scattering is postulated under the assumption of a spherical system. For copper in a d^9 state there is only one possible

---

[7]This is given by $\frac{1}{2k\beta}$ with $k = 0.457$ and $\beta = 0.0007$
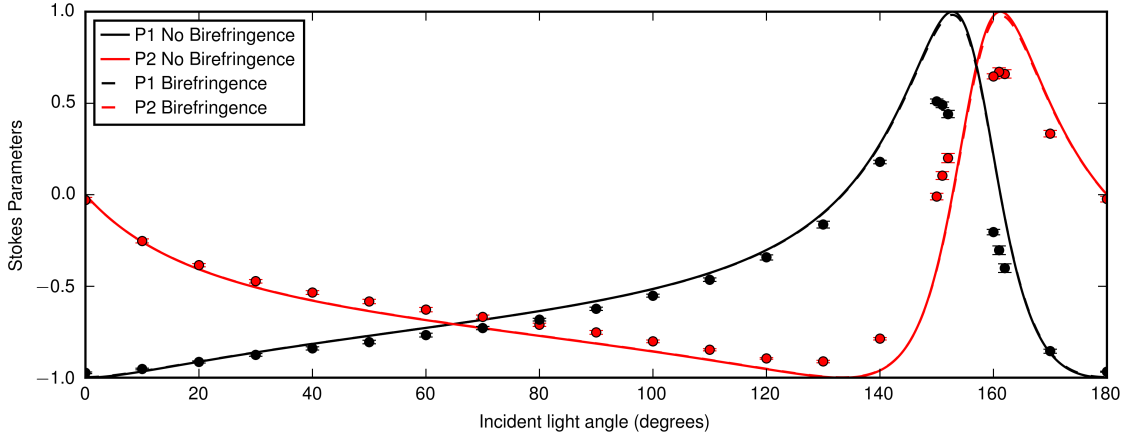
Figure 5.8: Full polarisation analysis of the $(0, 1, 0)$ taken on resonance at 901.8 eV at 14 K. Lines denote the mY_3^- structure at an azimuthal angle of 55.39 away from (0,0,1) in the scattering plane with (dashed line) and without (solid line) birefringence.

absorbing d orbital and this is not a good approximation of a sphere. The scattering processes will therefore be highly dependent upon the orientation of the polarisation compared to the empty d-shell.

Diffuse Moments

Above the edge it can be seen from fitting the resonance line-shape that the M-edge resonance drops to nearly zero at the off-resonant full polarisation analysis, ruling the trail of the resonance out as a contributing factor. However, at these energies we are likely exciting into the conduction band, which is spin-polarised from the RKKY interaction. This is similar to the diffuse moments observed in XMCD [103]. If this is the case we would expect a resonant shape to our full polarisation analysis. The deviation mentioned previously could then be due to charge scattering from the reduction in symmetry to the $Pmnm$ space group. However, if this is the case then these are two separate quantum mechanical processes so the resultant scattered polarisations must be summed and not the scattering matrices (as in equation 4.16). In this case the deviation of P_1 can be modelled but as the processes are separate with sigma incident light we can either get σ scattered from the charge or π scattered from the magnetism and as neither of these have a resultant P_2 neither does their

sum. As such the P_2 would be expected to remain at zero.

Non-Resonant Scattering

From equation 2.24 and following the same method as in section 4.2.1 we get the following scattering matrix for non-resonant scattering:

$$M = \begin{pmatrix} S(K).(k \times k') & -\frac{K^2}{2k^2}\left[\left[\frac{L(K)}{2} + S(K)\right].k' + \frac{L(K)}{2}.k'\right] \\ \frac{K^2}{2k^2}\left[\left[\frac{L(K)}{2} + S(K)\right].k' + \frac{L(K)}{2}.k'\right] & \left[\frac{K^2}{2k^2}\sin(\theta)^2 L(K) + S(K)\right].(k \times k') \end{pmatrix}$$
(5.10)

Just looking at the sigma incident terms both are non-zero, from which we can see that it is possible to produce a non-zero P_2 term at 180°.

5.2.3 Modelling

Resonant Data

By modelling a completely arbitrary scattering matrix with the same form as the first order resonant E1-E1 process:

$$M = \begin{pmatrix} 0 & a \\ b & c \end{pmatrix}.$$
(5.11)

Fitting with a least squares algorithm and imaginary a, b, and c is shown in the top panel of figure 5.9 we can see quite a good agreement to the data, but not perfect. Introducing a fittable parameter in the $\sigma - \sigma'$ channel reproduces an excellent fit (bottom panel of figure 5.9), however, the difference is small and as such we shall use a purely E1-E1 resonant model to fit the data from here onwards. From this we can see that the best possible case for a fit to this data still has a deviation in the peak of the P_2 data at $\sim 160°$ We will now start introducing irreducible representations (Irreps) into the fitting methodology. Using the ISODISTORT online package developed by Branton Campbell *et al.* at Brigham Young University [104] inputting a *cif* file for our structure, choosing magnetic cerium ions, and making no assumptions about the symmetry other than that there is no change in unit cell size we can see that there are twelve Irreps that are consistent with the *Cmcm* space group. These twelve Irreps are displayed in figure 5.10, within the irreducible repre-
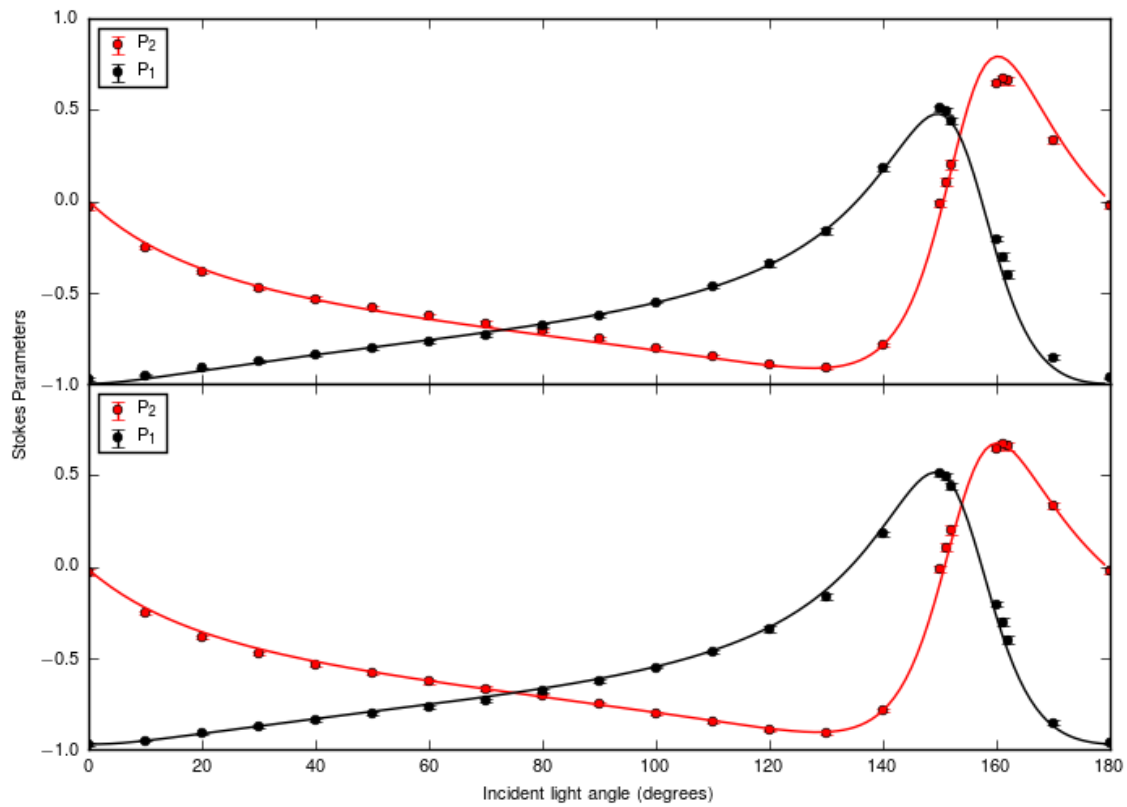
Figure 5.9: Full polarisation analysis of the $(0, 1, 0)$ taken on resonance at 901.8 eV at 14 K. (top) Fitted with an arbitrary scattering matrix (solid lines) with imaginary components and a fixed $\sigma - \sigma' = 0$. (bottom) Fitted with a completely arbitrary scattering matrix (solid lines).
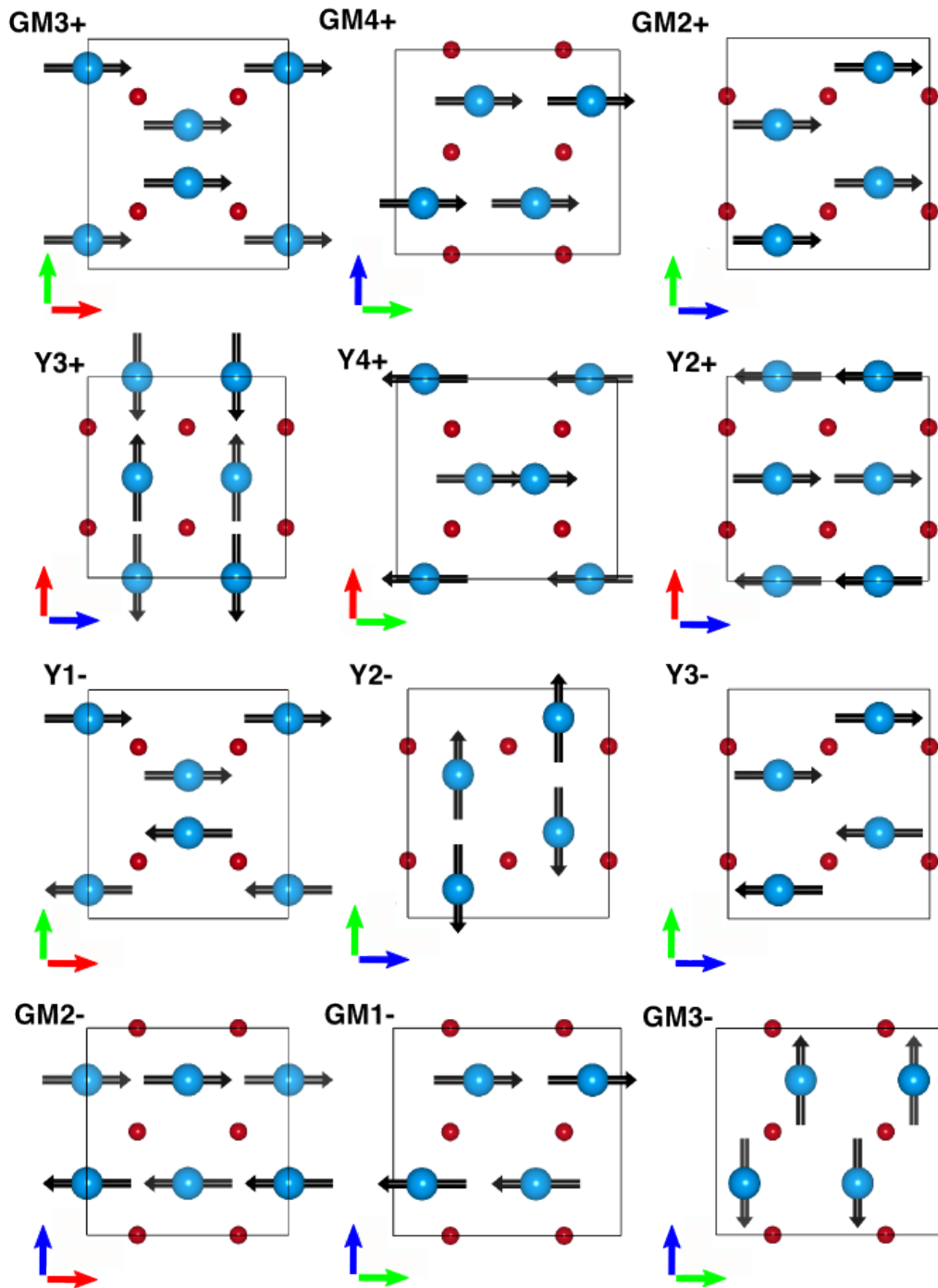
Figure 5.10: The twelve magnetic irreducible representations possible within the system. The cerium atoms are shown in blue with the transition metal atoms shown in red, the aluminium atoms have been removed for clarity. Crystallographic axes are as follows red $= a$ green $= b$ blue $= c$.

sentation parameter space all orientations of magnetic moments are possible. This can easily be seen by the fact that there are four atoms in the unit cell and three spatial dimensions giving a total of twelve parameters. To reproduce the observed deviation from $\sqrt{P_1^2 + P_2^2} = 1$ we require a non-collinear structure, which can only be reproduced by introducing a second Irrep. Just fitting two Irreps with a magnitude difference between the two, as well as a slight variation in the crystal azimuth gives us two fitting parameters (as we are only sensitive to the ratio of the Irreps and not the total magnitude). We are fitting what is essentially a problem with six degrees of freedom as only three of the matrix entries are non-zero but these can be imaginary so the problem is well constrained. Keeping the first Irrep as mY_3^- and fitting these two parameters with the other possible eleven Irreps, immediately reduces the possible magnetic structures to two, as the other Irreps do not form non-collinear structures and cannot reproduce the observed deviation at $\Psi \approx 155°$ the additional Irreps are mY_4^+ and mY_3^+. These two structures correspond to cantings towards the b and a axes respectively and the fits are shown in figure 5.11, the mY_3^+ structure fits better with an $R^2 = 0.975$ compared to $R^2 = 0.929$ for with Y_4^+.

Both of these cantings produce reasonable fits to the data with relatively small differences in the R^2 parameter. As well as having a better R^2 value the canting towards the a-axis more closely resembles that of the fitting of an arbitrary scattering matrix in figure 5.9 with the main deviation from the data being at $160°$. Although both models fit the data to different degrees at different parts the main deviation from $\sqrt{P_1^2 + P_2^2} = 1$ is seen to be at the peak of the P_1 curve. It is this deviation that is indicative of the non-collinear structure, so this curve should be considered more strongly when considering the two fits. The canting towards the a-axis clearly fits much better to the peak in the P_1 data than that of the canting towards the b-axis. A spin canting towards the a-axis also fits with the moment switching upon doping. The presence of a spin canting is most likely introduced by an anisotropic exchange from the Dzyaloshinskii-Moriya interaction.
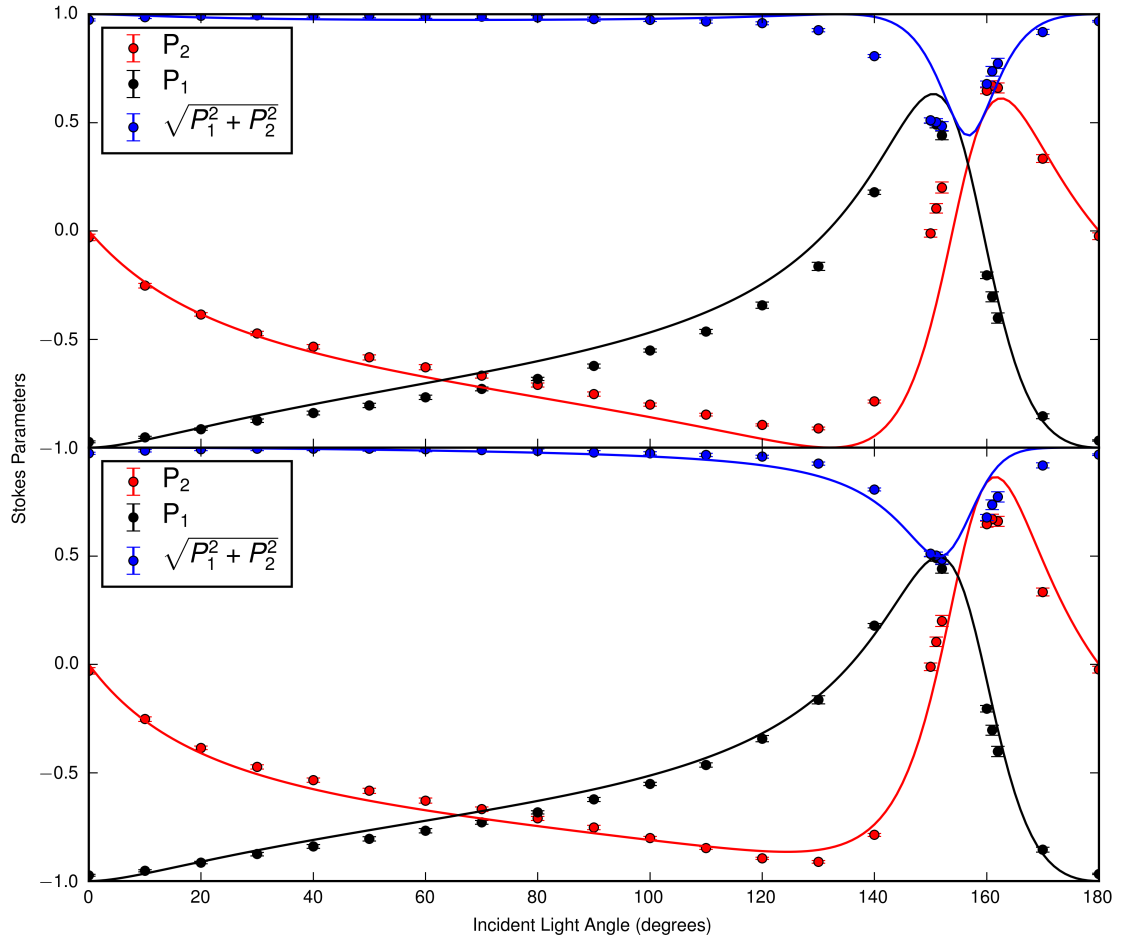
Figure 5.11: Full polarisation analysis of the $(0, 1, 0)$ taken on resonance at 901.8 eV at 14 K. (top) Solid lines represent fits with Irreps mY_3^- and 0.15 ± 0.007 mY_4^+, at an azimuth of 55.01 ± 0.35, $R^2 = 0.929$. (bottom) Solid lines represent fits with Irreps mY_3^- and 0.17 ± 0.02 mY_3^+, at an azimuth of 54.1 ± 0.6, $R^2 = 0.975$.

Magnetic Structure Factors

We will now calculate the magnetic structure factors for the models considered above. The magnetic structure factor can be written as follows:

$$\mathbf{F}^M \propto \sum_{l,m,n} \sum_i^I e^{i\mathbf{q}\cdot\mathbf{r}_{i,l,m,n}} \mathbf{z}(\mathbf{r}_{i,l,m,n}) . \tag{5.12}$$

Where, as before, the sum runs over only the magnetic atoms in the unit cell (i) and the unit cell positions (l,m,n), where $\mathbf{z}(\mathbf{r}_{i,l,m,n})$ is a function describing the magnetic moment. We shall start by calculating the magnetic structure factor for the a-canted moment as this can easily be adapted for the cases of no canting and b-canting. The magnetic structure for the a-canting will take the form:

$$\mathbf{z}(\mathbf{r}_{i,l,m,n}) = (0.17\cos(\boldsymbol{\tau}.\mathbf{r}_{i,l,m,n}), 0, \sin(\boldsymbol{\tau}.\mathbf{r}_{i,l,m,n})) . \tag{5.13}$$

Which can be rewritten in exponential form as follows:

$$\mathbf{z}(\mathbf{r}_{i,l,m,n}) = \frac{1}{2}e^{i(\boldsymbol{\tau}.\mathbf{r}_{i,l,m,n})}\mathbf{Z} + \frac{1}{2}e^{-i(\boldsymbol{\tau}.\mathbf{r}_{i,l,m,n})}\mathbf{Z}^* . \tag{5.14}$$

Where $\mathbf{Z} = (0.17, 0, i)$, we can now substitute this back into the structure factor as follows:

$$\mathbf{F}^M \propto \sum_{l,m,n} \sum_i^I \frac{1}{2}e^{i\mathbf{q}\cdot\mathbf{r}_{i,l,m,n}} \left(e^{i(\boldsymbol{\tau}.\mathbf{r}_{i,l,m,n})}\mathbf{Z} + e^{-i(\boldsymbol{\tau}.\mathbf{r}_{i,l,m,n})}\mathbf{Z}^*\right) \tag{5.15}$$

$$\propto \sum_{l,m,n} \sum_i^I \frac{1}{2}\left(e^{i(\mathbf{q}+\boldsymbol{\tau})\cdot\mathbf{r}_{i,l,m,n}}\mathbf{Z} + e^{i(\mathbf{q}-\boldsymbol{\tau})\cdot\mathbf{r}_{i,l,m,n}}\mathbf{Z}^*\right) \tag{5.16}$$

$$\propto \frac{1}{2}\sum_{l,m,n} e^{i(\mathbf{q}+\boldsymbol{\tau})\cdot\mathbf{R}_{l,m,n}} \sum_i^I e^{i(\mathbf{q}+\boldsymbol{\tau})\cdot\mathbf{r}_i}\mathbf{Z} \tag{5.17}$$

$$+ \frac{1}{2}\sum_{l,m,n} e^{i(\mathbf{q}-\boldsymbol{\tau})\cdot\mathbf{R}_{l,m,n}} \sum_i^I e^{i(\mathbf{q}-\boldsymbol{\tau})\cdot\mathbf{r}_i}\mathbf{Z}^* . \tag{5.18}$$

We can now see that in the presence of a magnetic structure, $\mathbf{q}$ is transformed and this will also transform the Laué condition. The Laué condition will then become, $(\mathbf{q} \pm \boldsymbol{\tau}).\mathbf{R}_{l,m,n} = 2\pi n$ as the sum over l,m,n will be zero otherwise and $\mathbf{G}.\mathbf{R}_{l,m,n} = 2\pi n$ then we get $\mathbf{q} = \mathbf{G} \mp \boldsymbol{\tau} = (h,k,l) \mp \boldsymbol{\tau}$. Then this can be substituted into the structure factor and the τ's will cancel such that we are left with the

following:

$$\mathbf{F}^M \propto \frac{1}{2}\mathbf{Z}\sum_n^I e^{i2\pi(h,k,l)\cdot\mathbf{r}_n}\Bigg|_{\mathbf{q}+\boldsymbol{\tau}}$$

$$+ \frac{1}{2}\mathbf{Z}^*\sum_n^I e^{i2\pi(h,k,l)\cdot\mathbf{r}_n}\Bigg|_{\mathbf{q}-\boldsymbol{\tau}}. \tag{5.19}$$

We are now left with the sum over the atom positions giving the structure factor for the parent Bragg peaks, which we can calculate for the $(0,2,0)-\boldsymbol{\tau}$ and $(0,0,0)+\boldsymbol{\tau}$ peaks simultaneously as they overlap to give us the magnetic structure factor at the $(0,1,0)$. There are 4 atoms within the unit cell with the atom positions $(0,0.1257,0.25), (0,0.8743,0.75), (0.5,0.6257,0.25), (0.5,0.3743,0.75)$. These can be simplified to $(0,y,z), (0,1-y,z+\frac{1}{2}), (\frac{1}{2},y+\frac{1}{2},z), (\frac{1}{2},\frac{1}{2}-y,z+\frac{1}{2})$ where $y = 0.1257$ and $z = 0.25$. Inputting all this into equation 6.20 allows us to calculate the general magnetic structure factor for the $(0,1,0)$ in the following way:

$$\begin{aligned}\mathbf{F}^M_{010} =&\frac{1}{2}\mathbf{Z}\left(e^{2\pi i(0,0,0)\cdot(0,y,z)} + e^{2\pi i(0,0,0)\cdot(0,1-y,z+\frac{1}{2})}\right.\\ &\left.+e^{2\pi i(0,0,0)\cdot(\frac{1}{2},y+\frac{1}{2},z)} + e^{2\pi i(0,0,0)\cdot(\frac{1}{2},\frac{1}{2}-y,z+\frac{1}{2})}\right)\\ &+\frac{1}{2}\mathbf{Z}^*\left(e^{2\pi i(0,2,0)\cdot(0,y,z)} + e^{2\pi i(0,2,0)\cdot(0,1-y,z+\frac{1}{2})}\right.\\ &\left.+e^{2\pi i(0,2,0)\cdot(\frac{1}{2},y+\frac{1}{2},z)} + e^{2\pi i(0,2,0)\cdot(\frac{1}{2},\frac{1}{2}-y,z+\frac{1}{2})}\right)\\ =&2\mathbf{Z}+\frac{1}{2}\mathbf{Z}^*\left(e^{2\pi i(2y)} + e^{2\pi i(2-2y)} + e^{2\pi i(2y+1)} + e^{2\pi i(1-2y)}\right)\\ =&2\mathbf{Z}+2\mathbf{Z}^*\frac{1}{2}\left(e^{2\pi i(2y)} + e^{2\pi i(-2y)}\right)\\ =&2\mathbf{Z}+2\mathbf{Z}^*\cos 4\pi y\,. \tag{5.20}\end{aligned}$$

We can then input our various $\mathbf{Z}$ matrices for the different magnetic structures to retrieve the magnetic structure factors. For the a-canted structure this was $(0.17,0,i)$ giving us $2(0.17(1+\cos 4\pi y),0,i(1-\cos 4\pi y))$. Then we can use the trigonometric identity $\cos 2x = 1 - 2\sin^2 x = 1 + 2\cos^2 x$ to retrieve the following magnetic structure factor:

$$\begin{aligned}\mathbf{F}^M_{010} =&2(0.17(2\cos^2 2\pi y),0,i(2\sin^2 2\pi y))\\ =&(0.68\cos^2 2\pi y,0,4i\sin^2 2\pi y)\,. \tag{5.21}\end{aligned}$$

For the non-canted moment with $\mathbf{Z} = (0,0,i)$ this will result in the following magnetic structure factor:

$$\mathbf{F}^M_{010} = (0,0,4i\sin^2 2\pi y)\,. \tag{5.22}$$

For the b-axis canting with $\mathbf{Z} = (0, 0.15, i)$ the magnetic structure factor will be as follows:

$$\mathbf{F}_{010}^{M} = \left(0, 0.6 \cos^2 2\pi y, 4i \sin^2 2\pi y\right). \tag{5.23}$$

Dzyaloshinskii-Moriya interaction

We shall now consider the basic symmetry arguments for the Dzyaloshinskii-Moriya interaction as set out by Moriya [33]. For ions located at A and B, with C being the midpoint between the ions and the vector $\mathbf{D}$ points parallel to $\mathbf{s}_1 \times \mathbf{s}_2$. The symmetry arguments are as follows.

1. When a centre of inversion is located at C,

   $\mathbf{D} = 0.$

2. When a mirror plane perpendicular to AB passes through C,

   $\mathbf{D} \parallel$ mirror plane or $\mathbf{D} \perp AB$.

3. When there is a mirror plane including A and B,

   $\mathbf{D} \perp$ mirror plane.

4. When a two-fold rotation axis perpendicular to AB passes through C,

   $\mathbf{D} \perp$ two-fold axis.

5. When there is an n-fold axis ($n \geq 2$) along AB,

   $\mathbf{D} \parallel AB$.

For our system there are two possible routes for the Dzyaloshinskii-Moriya interaction depicted in figure 5.12. The coupling could occur between ceriums 1 and 2 *via* the intervening ruthenium or between ions 2 and 3 *via* the intervening aluminiums. Within the $Cmcm$ space group the ruthenium sits on an inversion site meaning that there can be no antisymmetric exchange between cerium 1 and 2. Coupling between ceriums 2 and 3 can occur but is subject to the third symmetry argument as there is a mirror plane in the *c-b* plane, $\mathbf{D}$ would therefore be expected to point along a and the canting to be along the b-axis. If there is a symmetry lowering to either of the space groups $Pmnm$ or $Cm2m$ [99] the mirror plane remains, however, coupling between ceriums 1 and 2 may now occur as there is no longer an inversion site on the ruthenium. In this case there is no symmetry constraint on the direction of $\mathbf{D}$ and therefore the canting. The improved fit to the data combined with the
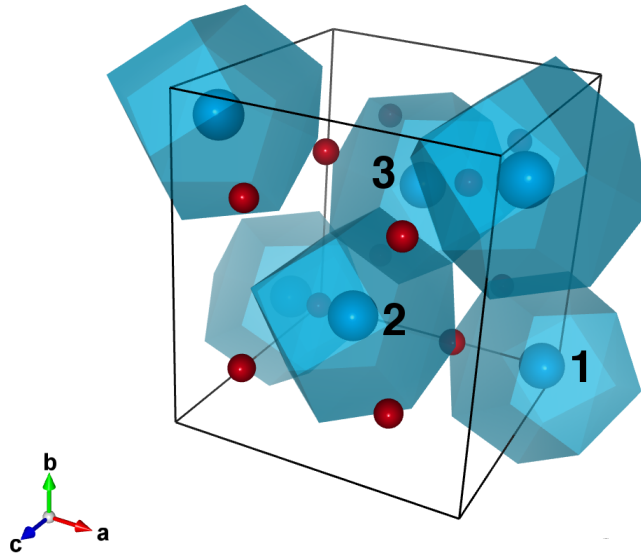
Figure 5.12: Crystal structure of CeRu$_2$Al$_{10}$. Cerium ions 1 and 2 or cerium ions 2 and 3 may display antisymmetric exchange.

doping information leads us to the conclusion that the moment is canted in the a-direction. This is further evidence of a symmetry lowering which was suggested from highly sensitive aluminium NQR (nuclear quadrupolar resonance) measurements. This structural change would be expected to be a very small change to the system and not affect the system other than to allow the possibility of a canting towards the a-axis. The resultant structure has moments canted in the a-direction by an angle of $9.6° \pm 1.1$ and is shown in figure 5.13. The inclusion of a second Irrep is not expected from Landau theory for a second order phase transition, however, other Irreps can sometimes be included from a higher-order Landau expansion of a phase transition [105].

The spin canting measured here is small and is likely consistent with the previous neutron refinement as only a small number of magnetic reflections were observed. Further the refined structure for CeRu$_2$Al$_{10}$ in within the error margin for the measurements taken on CeOs$_2$Al$_{10}$ and a similar model cannot be discounted for that system and may be expected as the systems are isostructural and the antisymmetric exchange could take the same pathway. The canting may be expected to be reduced in this system, however, as there is a stronger conduction band f-electron coupling,
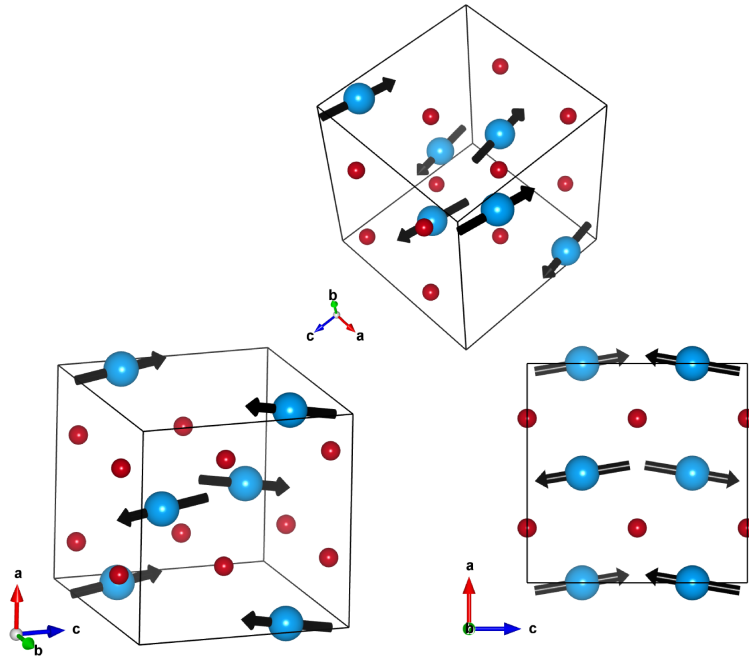
Figure 5.13: Refined magnetic structure of $CeRu_2Al_{10}$ showing the cerium atoms in blue and the ruthenium atoms in red. The aluminium atoms have been removed for clarity.

this will strengthen the RKKY interaction. The near-resonant data has been shown to be completely unrelated to non-resonant scattering. The canting could also be present in the other isostructural compounds. The presence of a spin canting in this system regardless of the direction provides more evidence as to the nature of the coupling mechanism between the cerium ions. If the unusually high transition temperature is related in some way to the canting this should be observable by similar measurements being taken on the doped systems (*e.g.* $CeRu_{0.95}Rh_{0.05}Al_{10}$) which display reduced transition temperatures and rotated moments. If the canting is due to an antisymmetric exchange interaction it might therefore be expected to also occur in other compounds in the series (*e.g.* $GdRu_2Al_{10}$) and possible spin canting in these compounds should be investigated. As these other compounds are well explained by the RKKY interaction it might be expected that this would dominate over any antisymmetric exchange-induced spin canting. If the requirement for a symmetry lowering induced by a small structural change to allow the canting along the *a*-axis plays an important role in the increased transition temperature then the structural change may be specific to the compounds CeT_2Al_{10} ($T =$Ru,Os)
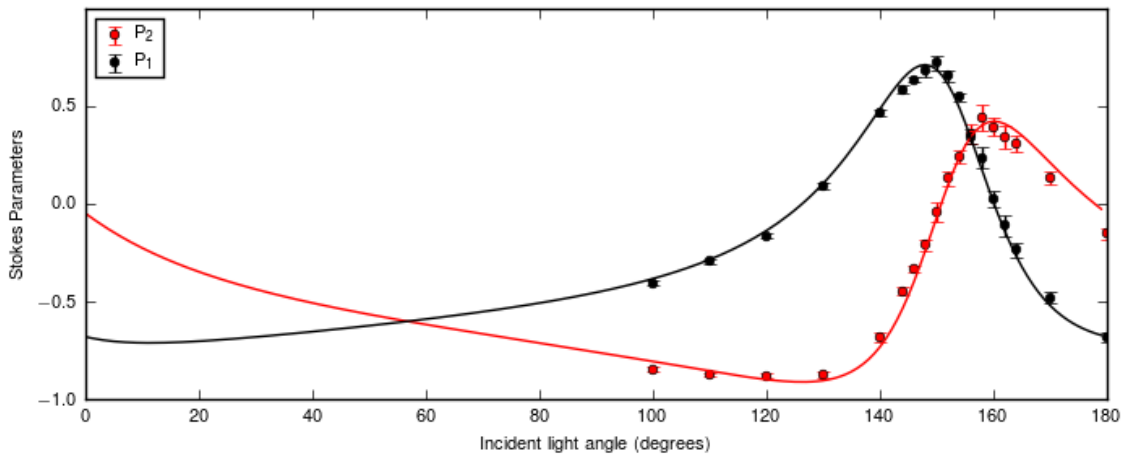
Figure 5.14: Full polarisation analysis of the $(0, 1, 0)$ taken off-resonance at 915 eV at 14 K fitted with an arbitrary scattering matrix (solid lines).

and therefore a similar canting would not be observed in other compounds.

Off-Resonance Data

Fitting again with a completely arbitrary scattering matrix the resultant fit is shown in figure 5.14. We cannot fit the off-resonant data to a high extent around the σ incident data at 180°. There is also little deviation of the best fit model from $P_2 = 0$ at σ incident light, it is a deviation here that would confirm the data is truly non-resonant. Even though the form of the non-resonant scattering matrix 5.10 is quite different from that of the resonant and would be expected to produce a highly different polarisation dependence, we will consider the non-resonant case further for completeness. Making the assumption that the spin and orbital magnetic structures are identical and linked by the spin-orbit coupling with just a magnitude difference between the spin and orbital moments[8]. Using the fit to the resonant data with orbital moment fixed and the spin moment aligned antiparallel with a magnitude of

---

[8]The possibility of different spin and orbital moment directions has been considered in transition metal oxides [106], however, as exchange mechanisms will only couple the spin moment, the ordering of the orbital moment must be enforced by the spin-orbit coupling. If the spin-orbit coupling is weak then the orbital structure could be supposed to point more strongly along high-symmetry crystallographic directions but with the overall direction the same as the spin moment. However, the spin-orbit coupling in cerium is not weak.

Figure 5.15: (top) Full polarisation analysis of the $(0, 1, 0)$ taken on resonance at 901.8 eV at 14 K model as in figure 5.11. (bottom) Full polarisation analysis of the $(0, 1, 0)$ taken off resonance at 915 eV at 14 K (solid lines) simulation of non-resonant polarisation analysis for the resonant structure shown in the top panel.

0.6 (from calculations in collaboration with Strigari [95]). This is shown in figure 5.15, this model cannot reproduce the experimental data well. So it can safely be assumed that the signal is not from a non-resonant source.

We can see that the peak intensity for the off-resonant data is higher than expected for a non-resonant magnetic peak by determining a rough maximum expected ratio for resonant and non-resonant magnetic reflections. To do this we first calculate the ratio for non-resonant magnetic scattering compared to charge scattering. This can then be compared to data from the literature for cerium edge resonances where the ratio of charge peaks and resonant magnetic peaks have been measured.

The cross-section for charge scattering has the prefactor, $r_0^2 = \frac{e^4}{m^2 c^4}$. The non-resonant magnetic scattering cross section has the prefactors, $r_0^2 \left(\frac{\hbar \omega_{\mathbf{k}}}{mc^2} \right)^2 s_j^2$. Given that, $s_j = 0.29 \ \mu_B$, $mc^2 = 511$ keV, and $\hbar \omega = E = 920$ eV, we get that, $\left(\frac{\hbar \omega}{mc^2} \right)^2 s_j^2 \simeq 2.7 \times 10^{-7}$, which is the ratio of charge to non-resonant peaks.
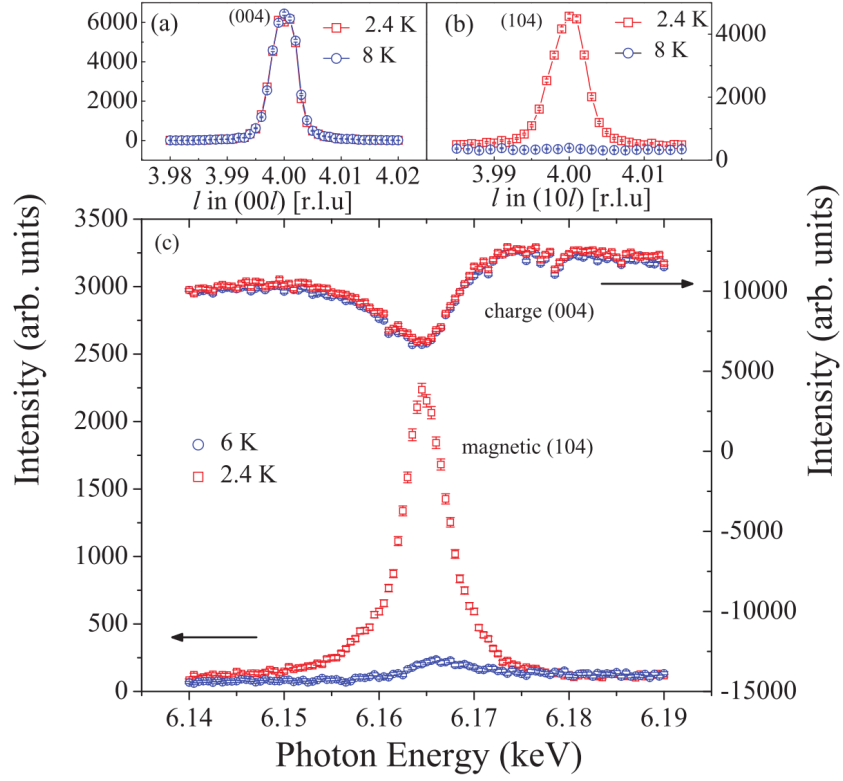
Figure 5.16: Resonant x-ray magnetic scattering from CeFeAsO at the Ce-L_{II} edge l-scans through (a) charge reflection (0,0,4) Bragg reflection and (b) magnetic reflection (1,0,4) at 2.4 and 8 K. (c) Photon energy scan at constant-$\mathbf{q}$ values through the Ce L_{II} resonance at T = 2.4 and 6 K for the strictly charge (0,0,4) Bragg reflection and the (1,0,4) magnetic Bragg reflection. From [107].

Comparing to data from Zhang *et al.* [107], resonant magnetic scattering from Ce-FeAsO was observed at the L-edges and compared to charge peaks, this is reproduced in figure 5.16. From this data the ratio for a L-edge magnetic resonance to a charge peak can be determined and is of the order of $2250/6250 = 0.36$. This should be comparable to our data on $CeRu_2Al_{10}$ as both contain Ce 3+ ions.

This gives the resulting ratio of non-resonant to resonant peaks of 7.5×10^{-7}. This calculation is for the L-edges where our data was taken at the M-edges which might be expected to give a roughly order of magnitude difference in the resonance [108]. This is still much smaller than the roughly 100 times weaker peak observed away from the resonance, giving further evidence that the peak is not a non-resonant magnetic peak.
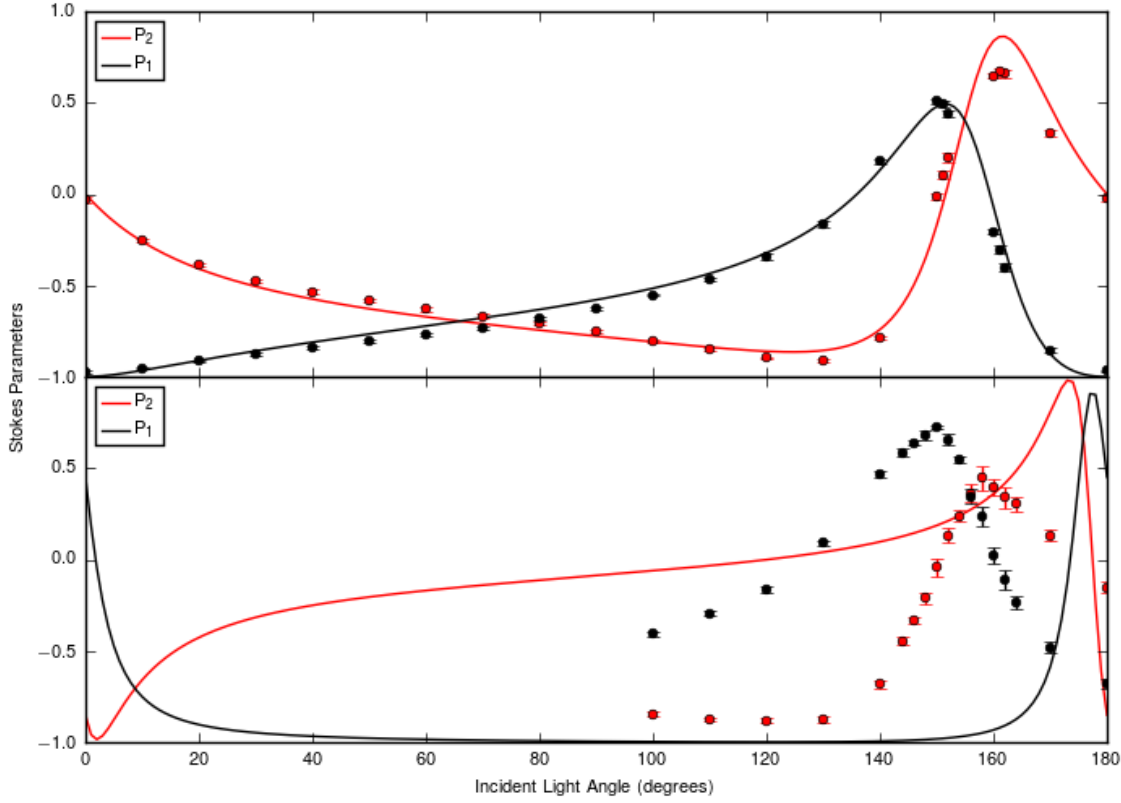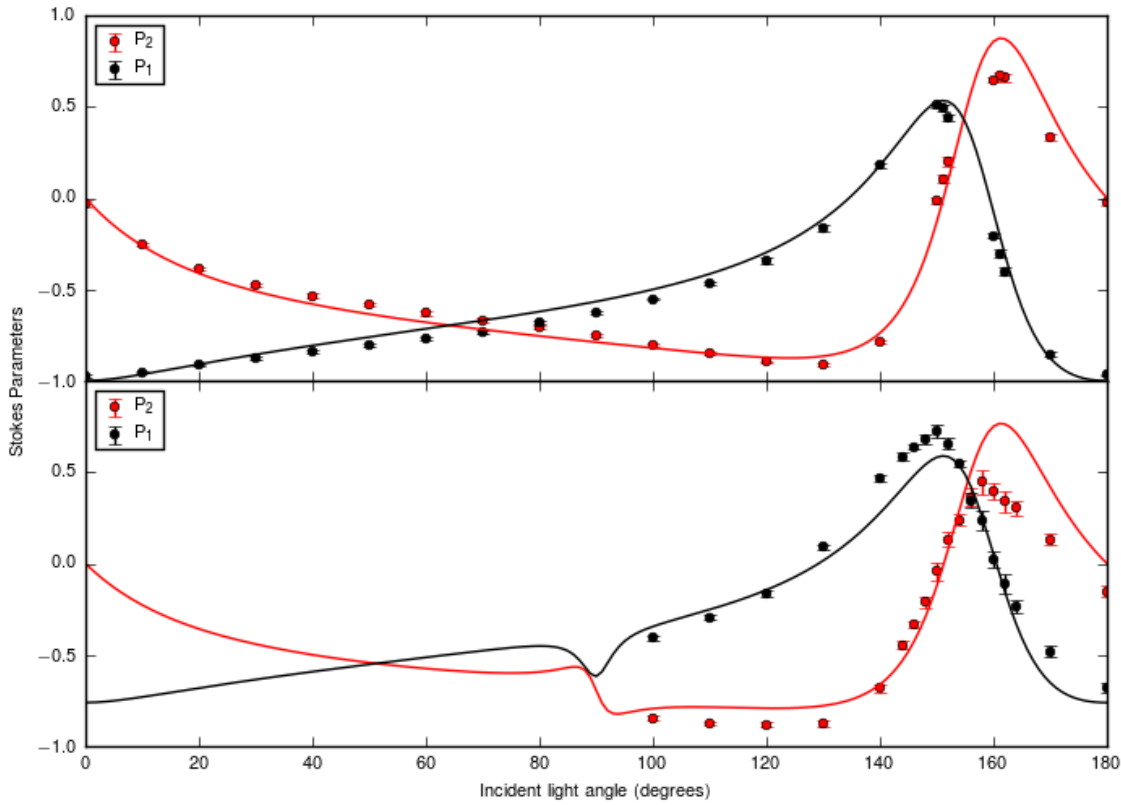
Figure 5.17: (top) Full polarisation analysis of the $(0,1,0)$ taken on resonance at 901.8 eV at 14 K model as in figure 5.11. (bottom) Full polarisation analysis of the $(0,1,0)$ taken off resonance at 915 eV at 14 K (solid lines) simulation of resonant data plus contribution from a weak charge peak.

Moving to the second option that the feature is a product of resonant plus charge scattering which looks more likely from the general matrix fit. Simultaneously fitting the resonant and near resonant data where the near resonant data is modified by a charge background and the scattered polarisation matrices are summed as these are separate scattering processes (as in equation 4.16) this gives a reasonably good fit to the data compared to the resonant data and is shown in figure 5.17. There is a large deviation from the resonant full polarisation analysis line shape just below the collected data, more data would be required to confirm if this model is true. Additional measurements should also be taken further from the resonant feature preferably below the absorption edge to confirm whether of not a charge peak is present. This data strengthens the argument for a symmetry lowering to the space group *Pmnm* allowing the possibility for spin canting in the *a*-direction.

There is some evidence that the near resonant data is mixed with a charge

peak, supporting the evidence that there is a structural change from $Cmcm$ to the subgroup $Pmnm$. However, the evidence for the origin of the near resonant feature is not fully understood and remains largely unexplained.

5.3   Conclusions

The ordered moment in $CeRu_2Al_{10}$ is not as simple as previously thought and requires two irreducible representations mY_3^- and mY_3^+ to model, corresponding to a moment canted towards the a-axis by $9.6° \pm 1.1$ in what is technically a very elliptical short-range helical magnetic structure as the moment is described by $\mathbf{z}_n = (0.17\cos(\boldsymbol{\tau}.\mathbf{r}_n), 0, \sin(\boldsymbol{\tau}.\mathbf{r}_n))$. This is in contrast to what would be expected from Landau theory for a second order magnetic transition where the structure would be expected to be described by a single Irrep, however, a higher order term of the Landau expansion could introduce the second Irrep. The canting is small and highlights the high sensitivity of polarised x-rays to magnetic structures. The canting is towards the magnetic easy axis from the paramagnetic state expected from magnetisation measurements and is evidence to the underlying cause for the instability of the magnetic ordering to doping effects. The coupling mechanism for these moments is still not well understood and this canting of the moments suggests that an antisymmetric exchange from the strong spin-orbit coupling in this system plays an important role in the magnetic ordering. The antisymmetric exchange interaction requires a symmetry lowering to one of the space groups $Pmnm$ or $Cm2m$ for a canting to be possible towards the a-axis and has been previously reported [99]. Symmetry lowering to $Pmnm$ is further backed up by the presence of a peak off resonance. Other effects which could produce a similar polarisation dependence such as x-ray birefringence, have been investigated and can be ruled out as significant effects. Further, the refined structure for $CeRu_2Al_{10}$ is within the error margin for the measurements taken on $CeOs_2Al_{10}$ and a similar model cannot be discounted for that system and may be expected as the systems are isostructural and the antisymmetric exchange could take the same pathway. The canting may be expected to be reduced in this system, however, as there is a stronger conduction band f-electron coupling, this will strengthen the RKKY interaction. The

near-resonant data has been shown to be completely unrelated to non-resonant scattering. There is some evidence that the near resonant data is mixed with a charge peak, supporting the evidence that there is a structural change from $Cmcm$ to the subgroup $Pmnm$. However, the evidence for the origin of the near resonant feature is not fully understood and remains largely unexplained.

Further Work

Further measurements are required on samples of $CeOs_2Al_{10}$ at a similar azimuthal angle to the measurements taken on $CeRu_2Al_{10}$ to confirm if it has a similar canted magnetic structure. Measurements of the off resonant peak are also required further from resonance and across the full range of incident polarisation angles to confirm or deny the presence of a charge peak and subsequent symmetry lowering. As the peak was measured to be weak even with synchrotron radiation, synchrotron based powder x-ray diffraction may be required to confirm this. If the canting is due to an antisymmetric exchange interaction it might therefore be expected to also occur in other compounds in the series (*e.g.* $GdRu_2Al_{10}$) and possible spin canting in these compounds should be investigated. As these other compounds are well explained by the RKKY interaction it might be expected that this would dominate over any antisymmetric exchange-induced spin canting. Measurements of the doped compounds would also be important to see if the canting persists. If the canting is also destroyed with the *c*-axis ordering, the canting may then be important for the unusually high transition temperature.

Chapter 6

New Magnetic Ground State in the Multiferroic Skyrmion System Cu_2OSeO_3

In this chapter we investigate the magnetic structure of the helical, conical, and skyrmion phases of Cu_2OSeO_3. Helical magnetic structures when viewed along the rotation axis are not always circular and can display complex properties becoming elliptical and the major axis of the ellipse can align due to local symmetries [109]. We will therefore investigate the nature of the magnetic structure using the polarisation dependence of magnetic x-ray scattering to determine the magnetic structure and whether it has any intricacies that could promote the formation of skyrmion lattices or if the helix is distorted upon entering the skyrmion phase. We will also investigate the nature of the recently observed $(1, 0, 0)$ reflection [110] which is disallowed in the cubic $P2_13$ to which Cu_2OSeO_3 belongs. Neutron powder diffraction will be used to refine the ground state magnetic structure. The original magnetic structure was unable to resolve the magnetic helices and the ground state was thought to be ferrimagnetic [111]. Helices have since been observed [112] and there is a somewhat open question as to whether the ground state helix is a ferrimagnetic helix or not. We have used long wavelength neutron powder diffraction and single crystal data to attempt to resolve the magnetic satellites and refine the true magnetic ground state.

Firstly though, a broad introduction to the very rich topic of skyrmions will be

given.

6.1 Introduction

A skyrmion is a hypothetical particle which emerges from the Skyrme model developed (by Tony Skyrme) to describe nucleons and nuclei [113]. The Skyrme model bridges classical descriptions of point charges and fields, with quantum chromodynamical theory with quarks and gauge bosons[1]. The Skyrme model consists of a nucleus in a medium formed by three pion fields. Skyrmions are then minimum energy solutions consisting of smooth, topologically stable field configurations. The observation of skyrmion-like objects in materials is not uncommon and has been known about for a number of years, for example in blue liquid crystals [114], with theoretical predictions of their existence in magnetic systems in the same year, 1989 [115]. The topological equivalent of skyrmions in magnetic systems, is a planar vortex-like structure with the moments pointing up on the outside and down in the middle. The theoretical predictions however, found that the formation of skyrmions as a magnetic ground state was impossible. It was not until 2006 that skyrmions were theoretically predicted as a ground state [116], it was this prediction which in 2009 lead to the discovery of skyrmions in MnSi by Mühlbauer *et al.* [117][2]. Skyrmions are a hot topic with the paper presenting their first observation being cited over 500 times in the seven years since its publication. This interest is due to the possible advancements they offer in increasing memory density as well as lower energy, and spintronic devices.

6.1.1 Magnetic Bubbles and Skyrmions

Magnetic bubbles, the smallest possible magnetic domains, are topologically similar to skyrmions. Magnetic bubble memory was an emergent technology of the 1970s and 80s and had increased data storage density and faster read-write times than

---

[1]The Skyrme model was developed before quantum chromodynamics.

[2]The elucidation of skyrmions as a magnetic ground state was prompted by experimental studies on MnSi. This prediction then led to further investigation of MnSi and the connection between a previously anomalous area of the phase diagram known as the A-phase and skyrmions.

conventional hard disk drives [118–120]. However, problems with scaleability and the advent of flash memory devices saw the end of bubble memory. Magnetic bubble memory used small magnetic domains as data storage in a fixed device similar in some respects to racetrack memory [121]. Racetrack memory is the modern-day equivalent of bubble memory and offers possible improvements on current non-volatile computer memory.

In a ferromagnetic material the region between domains of differently oriented magnetisation is called a domain wall. There are two main types of domain wall where the moment rotates in the plane of the domain wall and when the moment rotates in the plane of the moments. These are known as Bloch and Néel walls respectively and are shown in figure 6.1. A magnetic bubble can be thought of as the smallest possible domain which in a plane would be circular in shape with a single moment in the domain. A magnetic bubble described like this is a type of skyrmion, however, it is the magnetic interactions which cause them that are different to the skyrmions in MnSi. These bubble skyrmions are formed from long-range dipolar interactions, whereas the skyrmions in MnSi are chiral skyrmions which form in systems with magnetic helices from a much shorter-range spin-orbit interaction known as the Dzyaloshinskii-Moriya (DM) interaction [122]. Chiral skyrmions are generally smaller than bubble skyrmions so offer a higher possible areal density for memory storage applications. There is also the possibility of lower energy devices as chiral skyrmions are coupled to the conduction electrons and so can be moved with very low currents [123]. Magnetic bubbles are much more diverse forming doubly wound skyrmions and other more exotic objects [124, 125].

The areal density of state-of-the-art hard disk devices is 1.34 Tbit/inch^2 which corresponds to domains which are roughly 25 nm across, although smaller than many current skyrmions it is bigger than the minimum possible from chiral interactions.

6.1.2 Skyrmion Theory

This section largely follows from an excellent review paper by Nagaosa [122]. Skyrmion particles can be pictured as simply the field surrounding a point positive or negative charge. In a magnetic picture we then have a sphere, or moments aligned with the field from the point charge. Preserving the topology these can be azimuthally
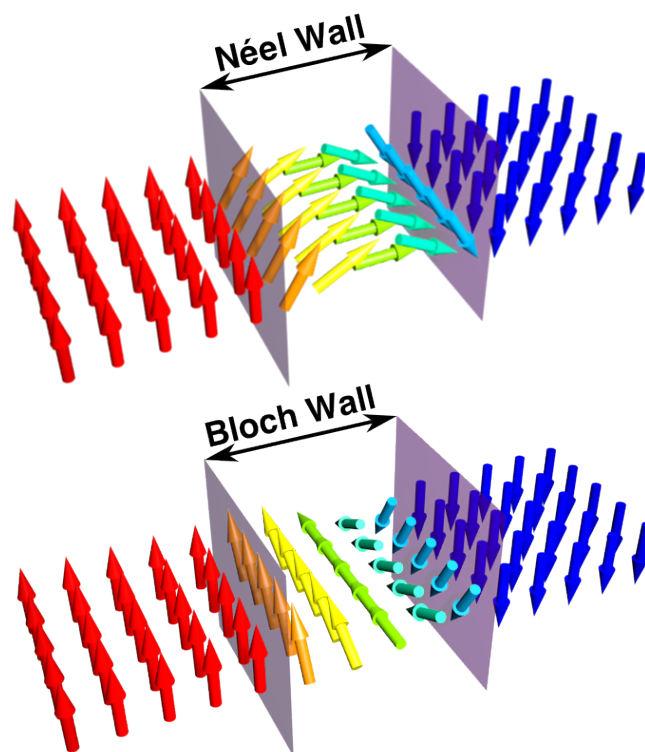
Figure 6.1: (top) Néel domain wall where the moments rotate in the plane perpendicular to the domain wall. (bottom) Bloch domain wall where the moments rotate in the plane of the domain wall.

projected onto a plane with the moment at the north pole being mapped to the circumference of a circle and the south pole being mapped to the centre. There are a number of different types of skyrmion which are depicted in figure 6.2, with their azimuthal projections shown to their right. It is these topologically similar projected skyrmions that are found in condensed matter systems.

Skyrmion particles are interesting due to their topology. They are topologically protected, making them stable in terms of field theory and stops them decaying, a continuous deformation of the field cannot destroy them. This property is preserved with the azimuthal projection making magnetic skyrmions also stable.

There are a number of different stable configurations of spherical skyrmions that can be described by different topological skyrmion numbers N_{sk}, which is given by the following equation:

$$N_{sk} = \frac{1}{4\pi} \int \int \left(\frac{\delta \mathbf{n}}{\delta x} \times \frac{\delta \mathbf{n}}{\delta y} \right) d\mathbf{r} d\mathbf{n} \,. \tag{6.1}$$

Where $\mathbf{n}$ is the moment direction, in polar coordinates this becomes:

$$N_{sk} = \frac{1}{4\pi} \int_0^\infty \int_0^{2\pi} \frac{\delta \Theta(r)}{\delta r} \frac{\delta \Phi(\phi)}{\delta \phi} \sin(\Theta(r)) d\phi dr = [\cos(\Theta(r))]_0^\infty [\Phi(\phi)]_0^{2\pi} \,. \tag{6.2}$$

For all the skyrmions that we are interested in the radial component ($\Theta(r)$) points down in the middle and up at the outside. This means that the radial component is always 2 (1-(-1)) so our only variable then becomes $\Phi(\phi)$. This can take a number of values, but it is well described in terms of the vorticity $m = [\Phi(\phi)]_0^{2\pi}/2\pi$. This number can be ± 1 and denotes the sense of rotation of the moment about the z-axis as you traverse in a right hand sense around the equator. If it is positive the rotation is the same direction as travel around the circle and skyrmions are produced (like the examples in figure 6.2). If $m = -1$ the rotation is the opposite and anti-skyrmions are produced, as shown in figure 6.3.

Another term can be introduced, called the helicity γ, which is an additional phase term in $\Phi(\phi)$ and produces an additional rotation around the z-axis. This transforms between different skyrmions, however, the topology of the anti-skyrmions is invariant to this phase and γ just produces a rotation of the same azimuthally projected structure.

Investigating the energy of these different skyrmions in terms of the DM interaction (which causes the chiral skyrmions) the skyrmions described by $m = 1$ and
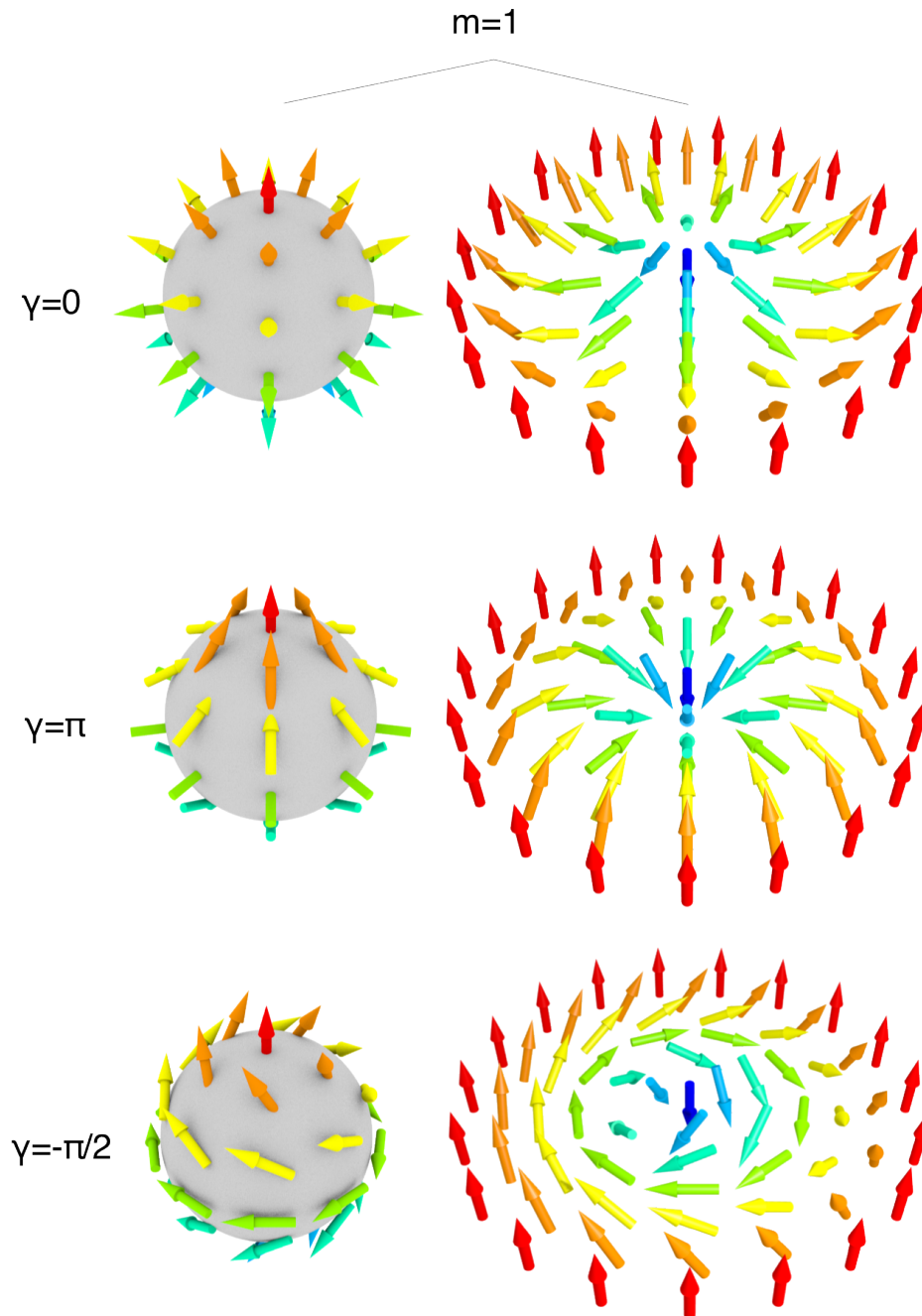
Figure 6.2: On the left are visualisations of different skyrmions and on the right is their azimuthal projection onto a plane. The first case is equivalent to the field surrounding a point charge. The second case is similar but the moment rotates in the opposite sense with the polar angle. The third case is similar to the first but all the moments are rotated by $\pi/2$ about the zenith.
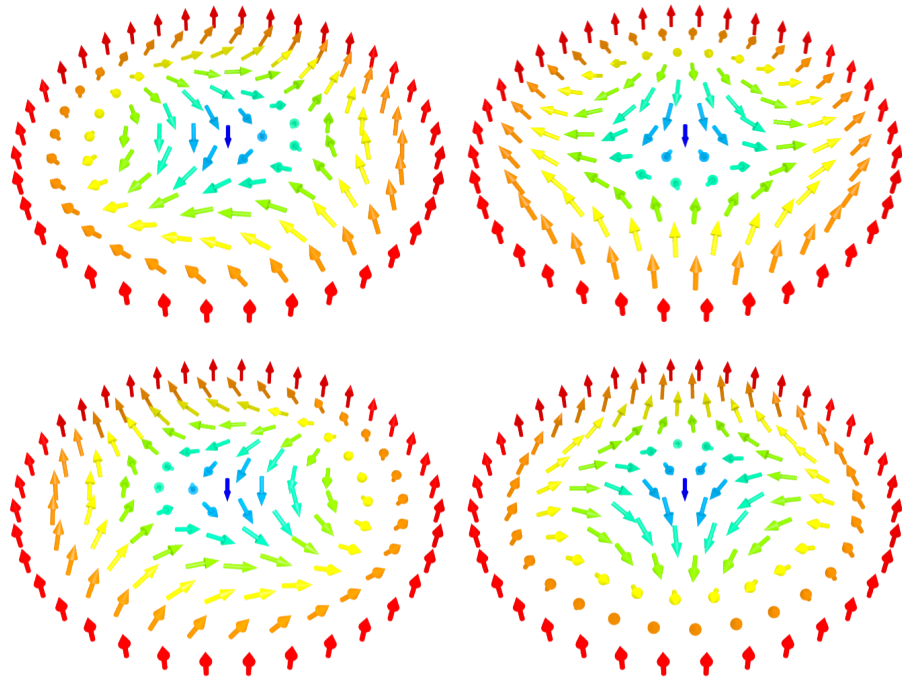
Figure 6.3: Depictions of the azimuthal projections of different anti-skyrmions where the moments rotate about z in the opposite sense to the rotation around each ring.

$\gamma = \pm\pi/2$ are of the lowest energy and are degenerate. Which type is present is then dependent upon the chirality of the system.

Skyrmion Stability

One of the problems with the stability of skyrmions as magnetic objects is that the energy density increases with the radius from the centre. This can be seen in figure 6.4**a** from reference [116]. The energy density reaches a maximum at the outer edge and increases to a level above that of a helix. This destabilises the skyrmion and thus a helix is energetically favourable. On the application of a field the fixed moment skyrmion can become energetically favourable over a helix. A skyrmion with a varying moment, where the moment size reduces to zero at the perimeter, has a reduced energy density at larger radii and could allow a skyrmion to form as a magnetic ground state. Theoretical predictions showed that for skyrmions to exist, systems require an easy-axis ferromagnetism and DM interactions [115, 126]. This is only possible if certain symmetry requirements are met, and systems must belong to symmetry groups with Schönflies notation C_{nv} and $D_n(n = 3, 4, 6)$ or tetragonal classes S_4 and D_{2d}. It was particularly noted that the B20 systems where DM
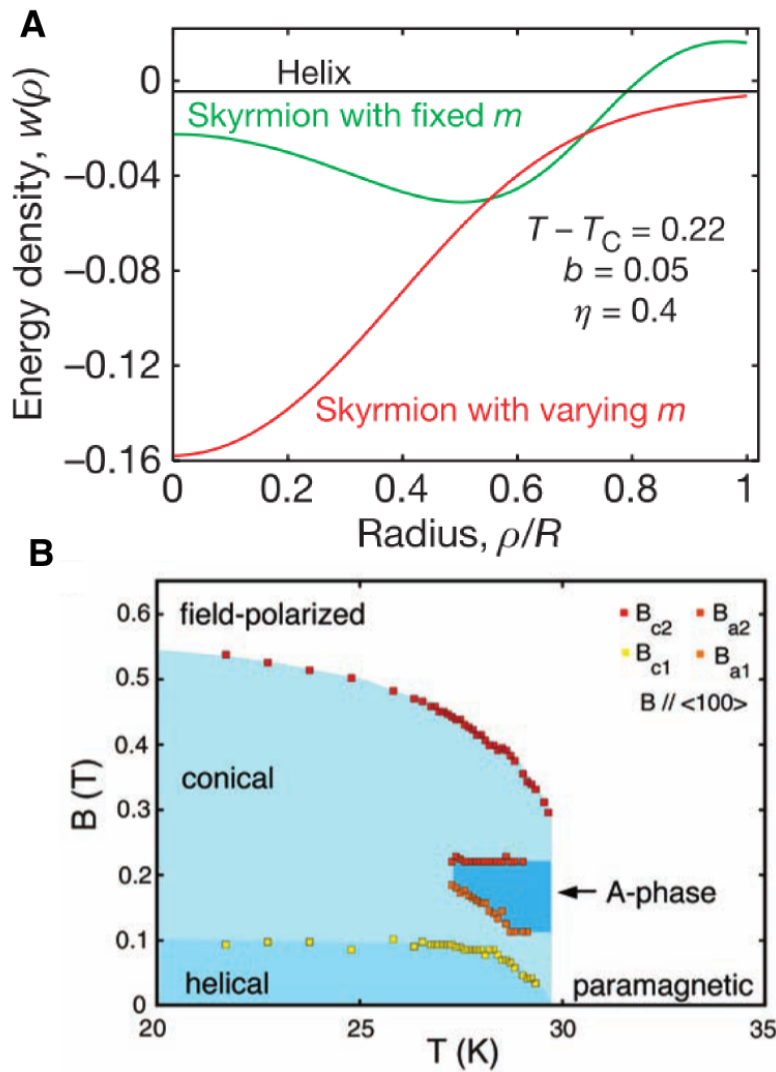
Figure 6.4: **A** Comparison for the local energy density per unit volume for the helical modulation and skyrmions with fixed and varying magnetic moment m, along a radial direction ρ. **B** Magnetic phase diagram of MnSi. For B = 0, helimagnetic order develops below T_c = 29.5 K. Under magnetic field, the helical order unpins and aligns along the field above B_{c1}; above B_{c2}, the helical modulation collapses. In the conical phase, the helix is aligned parallel to the magnetic field. The transition fields shown here have been inferred from the AC susceptibility, where the DC and AC fields were parallel to 100 (10). The A-phase denotes the region where skyrmions were found.

helical structures are well known could be a potential site for skyrmion formation. However, to stabilise skyrmions, an additional uniaxial anisotropy must be present from external stresses or growth anisotropies. This would then reduce the symmetry class to D_n from T[3].

These prediction suggest that skyrmions (and helices) should be possible in other tetragonal systems, Tb_3Al_2 and Dy_3Al_2. Both crystals belong to the space group $P4_2nm$ and have been observed with canted magnetic structures, but no evidence of helical or skyrmion phases has been found.

6.1.3 Observation of Skyrmions

The first observation of a skyrmion in a real system was by way of small angle neutron scattering in MnSi in a small range of field and temperature [117]. MnSi belongs to the B20 crystal systems which are a subset of the $P2_13$ space group, with the previously mentioned anisotropy given by an external magnetic field. The phase diagram presented in their work is reproduced in figure 6.4 B.

Here neutron diffraction was used, and a sixfold diffraction pattern was observed, which is consistent with the hexagonal close packing of skyrmions in a plane[4]. The sixfold pattern was observed to persist unchanged with movement of the sample. The obvious decoupling from the atomic lattice leads to the assumption that the structure is multi-$\mathbf{k}$ in nature and forms a lattice of skyrmions.

Skyrmions are very close in energy to a conical structure, it is thought that critical fluctuations near the magnetic transition temperature help stabilise the skyrmion structure over that of the conical phase. This is due to its topological stability, and explains the position of the skyrmion phase close to the transition, skyrmions have since been observed in other B20 systems such as FeGe and $Fe_xCo_{1-x}Si$. Experimentally observed skyrmion systems were exclusively B20, until 2012 with the discovery

---

[3]Until recently with the discovery of skyrmions in GaV_4S_8 [127] all ordered skyrmion systems had been discovered within the $P2_13$ space group which is cubic and does not belong to any of these symmetry groups.

[4]Previous studies had all looked with the field perpendicular to the beam direction and so were unable to see the sixfold pattern, the phase had been called the A-phase and was thought to be describable by a single wavevector.

of skyrmions in Cu_2OSeO_3 [112] which also belongs to the $P2_13$ space group but is not a B20 system[5]. All of the systems that skyrmions have been discovered in to date are cubic.

Real Space Images of Skyrmions

The multi-**k** nature of these skyrmion systems was not confirmed until Lorentz transmission electron microscopy (TEM) images were able to observe skyrmions in real space in $Fe_{0.5}Co_{0.5}Si$ [128]. Lorentz TEM utilises the Lorentz force which causes electrons to follow curved paths in magnetic fields. The internal magnetisation of the sample then produces light and darks spots as the electrons are deflected. Only fields transverse to the electron motion can be detected. A number of images are taken in under and over focussed setups and these can then be post analysed using the transport-of-intensity equation to determine the magnetisation directions and produce the colour maps pictured in figure 6.5. This constitutes the first incontrovertible evidence of the existence of skyrmions and the skyrmion lattice.

Lorentz TEM requires thinned samples and it has been observed that the skyrmion phase extends over much larger temperature and field range in thin samples, extending into the conical phase [129]. This is likely due to the conical phase becoming less favourable, especially when the sample thickness is reduced below the helical wavevector, as the skyrmions form in a plane perpendicular to the field direction, they remain unaffected.

Skyrmion flow

Skyrmions have been observed to move with current densities around 10^6 times lower than those required to move ferromagnetic domain walls. Although to achieve a similar speed to domain wall motion in skyrmions, a comparable current is still required [123, 130].

Skyrmion motion has also been theoretically predicted with temperature gradients [131] and has been attributed to some effects seen in experimental studies. Skyrmions have also been seen to rotate in a recent resonant x-ray study by

---

[5]B20 systems belong to the $P2_13$ space group.
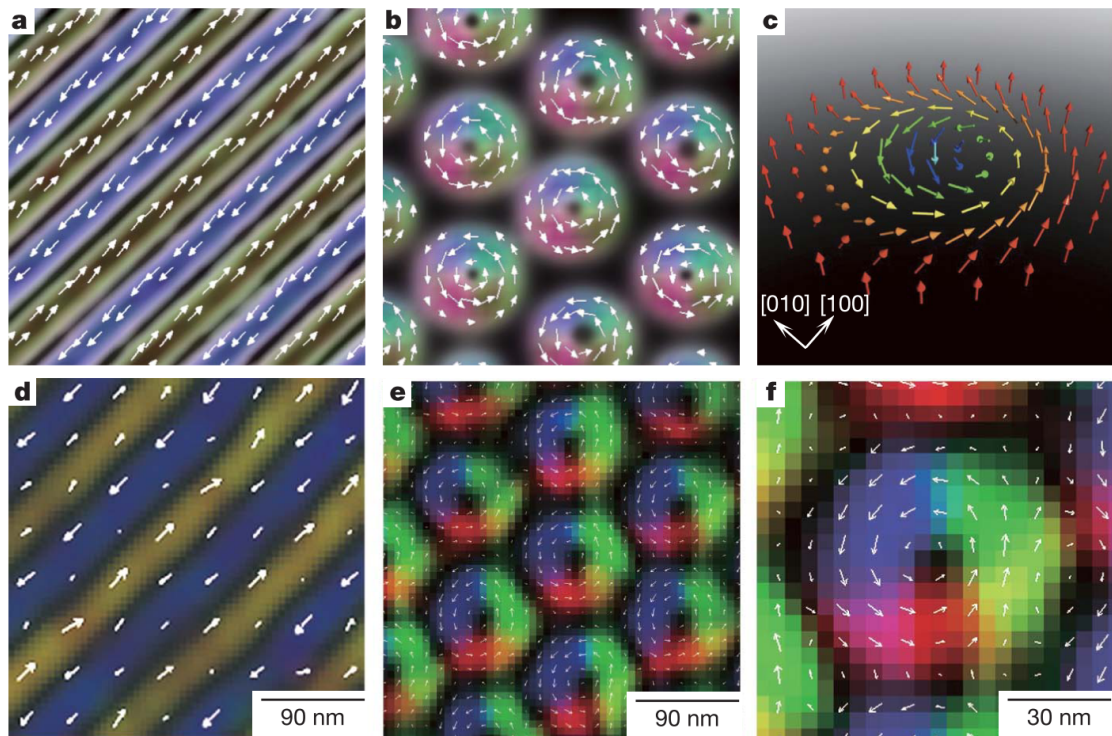
Figure 6.5: Topological spin textures in the helical magnet $Fe_{0.5}Co_{0.5}Si$. (a) Helical and (b) skyrmion structures predicted by Monte Carlo simulation. (c) Schematic of the spin configuration in a skyrmion. (d-f) The experimentally observed real-space images of the spin texture, represented by the lateral magnetisation distribution as obtained by transport-of-intensity analysis of the Lorentz TEM data: (d) helical structure at zero magnetic field, (e) the skyrmion crystal (SkX) structure for a weak magnetic field (50 mT) applied normal to the thin plate and (f) a magnified view of e. The colour map and white arrows represent the magnetisation direction at each point [128].

Langner [110] on Cu_2OSeO_3 which could be due to thermal effects from beam heating or small currents induced due to Auger emission.

Reading and Writing of Single Skyrmions

The reading and writing of single skyrmions has been shown to be possible in a sample consisting of an iron-palladium bilayer deposited on an iridium (1,1,1) substrate [132]. This is still a long way from real applications but shows the basic principals. The sample displays a similar phase diagram to other systems with helical, conical, skyrmion, and ferromagnetic phases, however, the fields required are much higher, with the skyrmion phase around 1.4 T. The reading and writing of skyrmions was shown to be possible around defects which pin the skyrmions. The sample was prepared by increasing the field through the skyrmion phase to the point where only a few skyrmions persist around point defects. Spin-polarised scanning tunnelling microscopy was used to measure the skyrmions It was also shown that they could be created and destroyed by placing the STM tip above the skyrmion and sweeping the voltage by $\pm$ 0.6 V.

6.1.4   Long Period Magnetic Structures

Helical[6], conical, and cycloid structures are all long period magnetic structures which are depicted in figure 6.6. Helical and cycloidal structures can be thought of as being similar to Bloch and Néel domain walls where there are multiple domains each containing one magnetic moment. Upon applying a magnetic field to a helical structure a conical structure is normally formed where there is now a ferromagnetic component along the rotation axis of the helix. The conical structure exists over a range of field with the cone angle decreasing upon increasing the field until it is reduced to zero and a ferromagnetic structure aligned with the field is formed. These structures are long range and can be thought of as being built up by a largely ferromagnetic interaction but with a weak antiferromagnetic coupling. This coupling can come in a number of forms from either the dipolar interaction or the Dzyaloshinskii-Moriya

---

[6]helices are sometimes referred to as spin spirals, however, a spiral and a helix are not synonymous and the term spiral should not be used.

interaction[7].

Long Range Dipole-Dipole Interactions

The strength of the exchange interaction falls exponentially with distance, as it is related to overlap integrals of atomic orbitals which have a similar exponentially decaying spatial dependence. The strength of the dipole-dipole interactions falls as a function of the distance cubed and so can become dominant at large distances. When in competition with the exchange interaction this can lead to long period helical structures. The dipole-dipole interaction can be thought of as a classical interaction where a demagnetising field causes long range antiferromagnetism in the shape of a helix. Long period magnetic structures formed by these interactions are generally larger than 100 nm.

6.1.5 Multi-k Magnetic Structures

The diffraction pattern produced by a skyrmion is a sixfold hexagon and cannot be thought of as being composed of a single wavevector. It is therefore prudent to discuss multi-$\mathbf{k}$ magnetic structures.

Multi-$\mathbf{k}$ or multi-$\mathbf{q}$ structures are a feature of high-symmetry crystal systems. Where some crystals form crystallographic or magnetic domains with spatially separated regions of rotated crystal or magnetic structures, in multi-$\mathbf{k}$ systems a number of different magnetic structures are coincident and form a superposition in the same spatial domain. That is not to say magnetic domains do not exist in multi-$\mathbf{k}$ structures as the structure could have propagation vectors along for example h and k, then domains could form with k and l, and h and l propagation vectors. Some prominent examples of systems such as these are a large number of rare-earth compounds which crystallise in the $AuCu_3$ cubic structure, NdZn [135], Nd metal [136], and disordered $(Fe,Ni)_3Mn$ compounds [137].

The discrimination between domains of single-$\mathbf{k}$ and a true multi-$\mathbf{k}$ structure is non-trivial. If anisotropies introduced by, for example, external magnetic field or

---

[7]Other interactions can cause similar effects but on an atomic scale such as frustrated exchange interactions [133] or four-spin exchange interactions [134]. These interactions can actually produce degenerate states of skyrmions and anti-skyrmions.
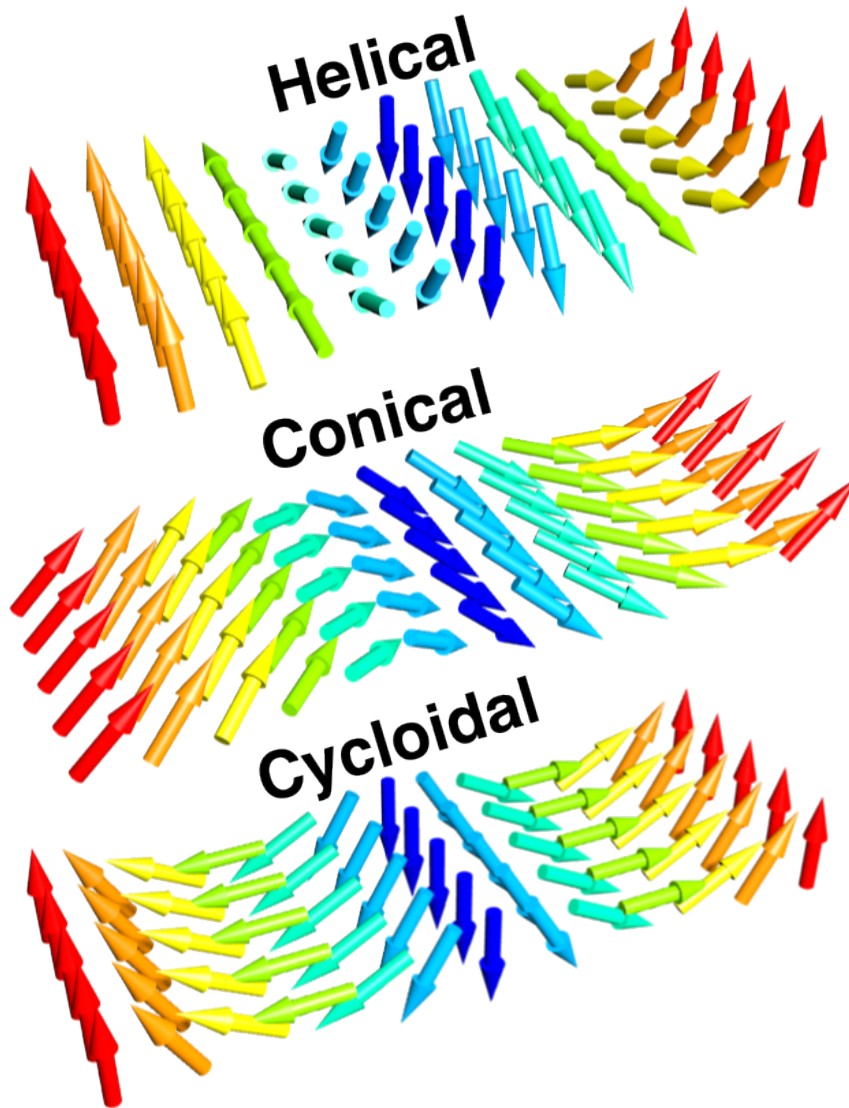
Figure 6.6: (top) Helical magnetic structure where the moment rotates around the propagation direction. (middle) Conical, similar to the helical but with a ferro-magnetic component along the propagation direction. (bottom) Cycloidal structure where the moments rotate around an axis perpendicular to the propagation direction.

the application of strain can unbalance the domain population then this is evidence of a single-**k** structure. However, the lack of any noticeable difference in domain population does not preclude a single-**k** structure[8]. Further the presence of $(k, k, 0)$ peaks in a system with wavevectors $(k, 0, 0)$ and $(0, k, 0)$ again does not necessarily preclude a single-**k** structure. It has however, been shown that resonant scattering from such $(k, k, 0)$ peaks can be used to unambiguously determine the nature of the magnetic structure by their polarisation dependences [138].

There is no doubt in the case of skyrmion systems as to their multi/single-**k** nature as this can be observed, as previously mentioned, with real space imaging techniques such as Lorentz TEM. If a skyrmion in these systems is just a composition of three helical structures it would have the form shown in figure 6.7. This produces a skyrmion with higher moments at the centre (as mentioned previously this could potentially stabilise the skyrmion phase). This object clearly has a very similar topology to a skyrmion, however, it is somewhat distorted. In this case we have a lattice of skyrmions formed by helices, not a close packing of separable objects.

Skyrmion Lattice

A skyrmion lattice would be expected to be composed of hexagonally close packed skyrmions where all the moments not in the skyrmions are ferromagnetic. This is distinct from a skyrmion as a composition of three superimposed helices from figure 6.7 as in this case the regions between the skyrmions are not simply ferromagnetic. Another point to note is that hexagonally close packed skyrmions from theoretical calculations at least would be expected to retain their circular nature. However, this is not what is observed with Lorentz TEM as distinctly hexagonal structures are observed.

---

[8]The skyrmion lattice is a prime example of this where the structure aligns in the plane perpendicular to the field.
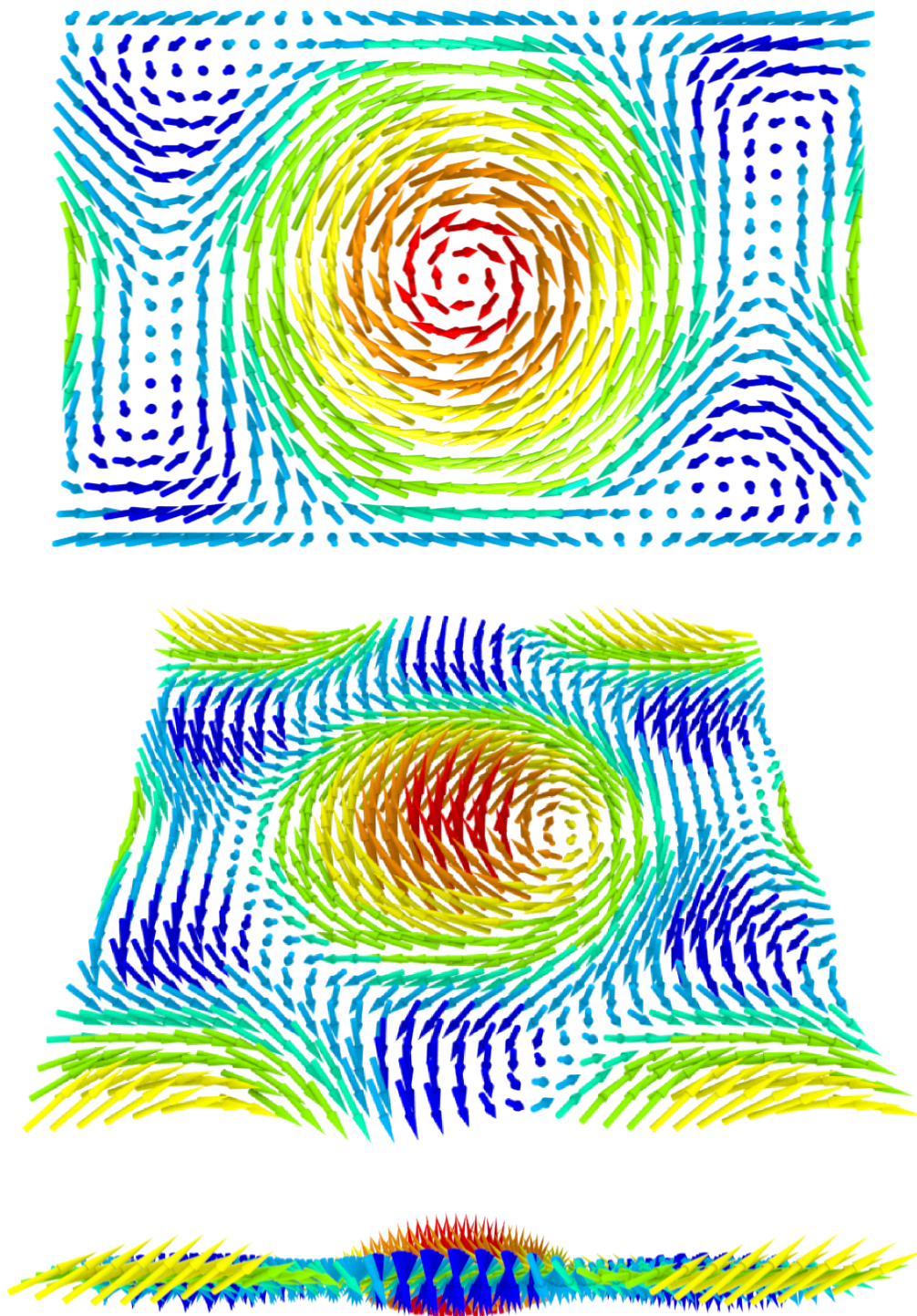
Figure 6.7: The magnetic structure produced by a superposition of three helices with wavevectors rotated by 120° in the plane. The colours denote the z-component of the moments with a maximum of 3 and a minimum of -1.

6.2   Cu$_2$OSeO$_3$

Copper oxyselenide, Cu$_2$OSeO$_3$[9] was first synthesised in 1976 [139]. Measurements using a vibrating sample magnetometer concluded that it was ferrimagnetic due to a reduced saturation magnetisation over what might normally be expected for copper ions [140]. A ferrimagnetic model also appeared to fit well with the determined space group P2$_1$3 where the sixteen coppers in the unit cell sit on two different Wyckoff sites, four on the $4a$ and twelve on the $12b$ site. The ferrimagnetic structure then comes from the moments on one site being anti-aligned with the moments at the other site, this was later confirmed with neutron powder diffraction measurements [111]. The crystal structure for Cu$_2$OSeO$_3$ is somewhat complex and contains highly distorted CuO$_5$ square based pyramids at the $12b$ sites and almost undistorted trigonal bi-pyramids at the $4a$ sites. The structure is depicted in figure 6.8.

Recently using Lorentz TEM, Cu$_2$OSeO$_3$ has been found to contain helical, conical, and skyrmion phases [112], with a similar phase diagram to other skyrmion systems (reproduced in figure 6.9). This was also the first paper to report a helical ground state of the system which had previously been unresolved by the neutron powder diffraction study [111] due to its long wavelength of roughly 50 nm.

Multiferroic Properties

Before the discovery of skyrmions in this system a number of papers were published on its possible magnetoelectric/ferroelectric properties. The P2$_1$3 space group lacks inversion symmetry and must therefore be inherently piezoelectric, however, ferroelectric properties would not be expected within the P2$_1$3 space group even with a uniaxial anisotropy which as previously mentioned could induce a symmetry capable of supporting skyrmions. This does not preclude the possibility of magnetoelectricity (a coupling of the magnetic and electric degrees of freedom where an applied magnetic field can induce an electric polarisation in the sample or visa versa), which has been observed *via* magnetocapacitance (a change in capacitance with an applied magnetic field) measurements on powdered samples by Bos *et al.* [111]. The magne-

---

[9]This is the currently widely used formula, it has however, previously been denoted Cu$_2$SeO$_4$.
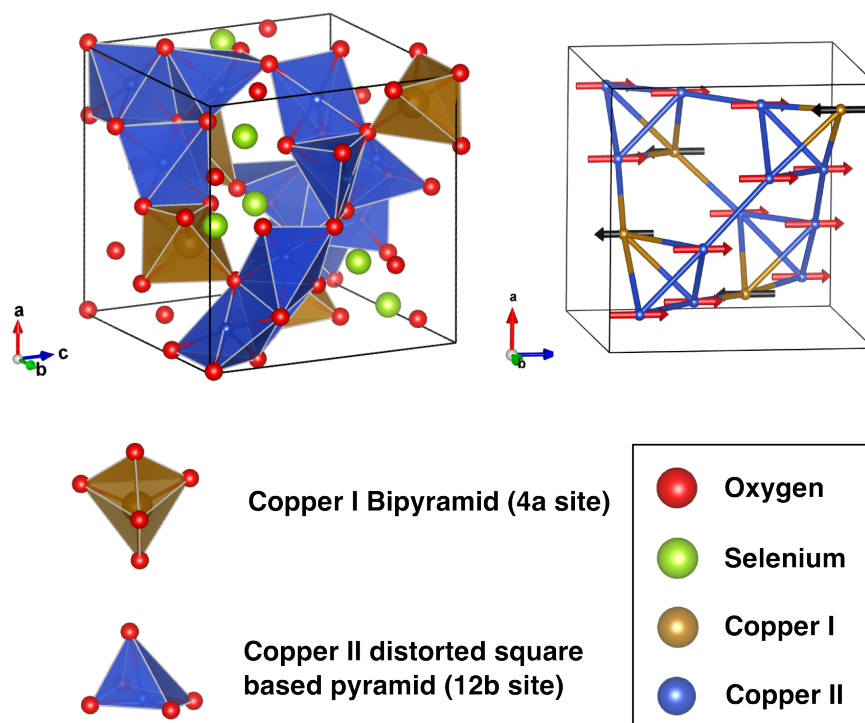
Figure 6.8: Structure of cubic Cu_2OSeO_3. (top left) Full crystal structure. (top right) The arrangement of the copper atoms. (bottom left) polyhedra shapes for the different copper sites.
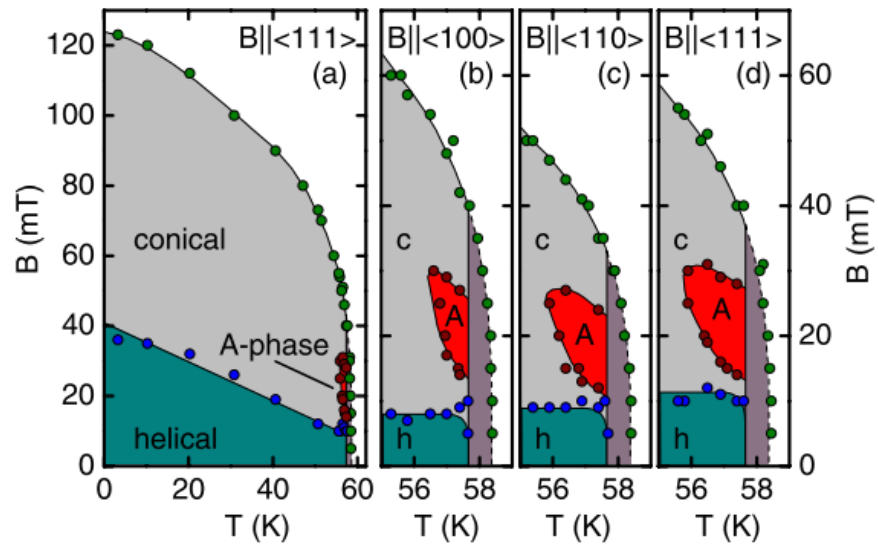
Figure 6.9: Field temperature phase diagram for Cu$_2$OSeO$_3$ determined by magnetisation measurements from [141]. The red region labelled A denotes where skyrmions are observed at equilibrium. The panels b, c, and d show zoomed in regions around the skyrmion phase for different field orientations with the conical phase labelled c and the helical phase labelled h.

tocapacitance signal was observed below the magnetic transition but also only above 500 Oe, consistent with the then unknown, transition from helical to conical magnetic structures. A further study using Raman spectroscopy by Gnezdilov *et al.* [142] found there could be no spontaneous electric polarisation if the net magnetic moment is oriented along the crystallographic axes. Magnetocapacitance measurements have since been completed on single crystals and corroborate these results, finding an electric polarisation when a field is applied (large enough to enter the conical phase), and only when that field is not along a crystallographic axis [112, 143, 144].

Magnetism

The phase diagram determined from Lorentz TEM has been confirmed by small angle neutron scattering (SANS) which finds that the ground state helices are oriented along the $[1, 0, 0]$ type directions [141]. Due to the recent discovery of the helical structure the literature will be reviewed in a chronological manner but attributing conclusions to the current phase diagram. Bos *et al.* completed temperature dependent magnetic susceptibility measurements fitting a Curie constant to the lin-

ear paramagnetic phase and extracting an experimental effective moment of 1.36 μ_B/Cu. At 5K the sample saturates at 0.5 μ_B/Cu agreeing with the three up, one down ferrimagnetic structure. A helical structure would not be expected to show any magnetisation as it has no net moment. This was confirmed by measurements on single crystals by Seki *et al.* [112] where magnetisation versus applied magnetic field (M-H) curves show an increase in magnetisation with applied fields along the $[1,1,1]$ direction with fields less than the helical-conical transition. The cause of this is likely distortions of the helices to give a net magnetisation without altering their wavevector. However, the lack of a magnetocapacitance signal in this phase means that the magnetisation must be along the crystallographic axes, and the helical structure would therefore become conical. The observed helical conical transition is likely then just a transition from conical structures along crystallographic directions to an alignment with the field. This is consistent with SANS measurements [141] which cannot easily differentiate between a cone and a helix.

Bos *et al.* also completed a Rietveld refinement of the magnetic structure using neutron powder diffraction. The ferrimagnetic structure was refined with the moments pointing along the $[1,1,1]$ direction. This is consistent with the Goodenough-Kanamori rules with antiferromagnetic coupling between atoms on the $4a$ and $12b$ sites. The magnetisation measurements were taken at a sufficiently high field to polarise the sample and achieve the ferrimagnetic state, however, the powder diffraction was measured in zero field. There is then the open question of whether the ground state helical structure is also ferrimagnetic.

The refined structure with moments pointing along the $[1,1,1]$ direction is in clear contradiction to the more recent helical domain structure. As well as a combination of the magnetocapacitance measurements taken by Seki *et al.* [112] showing no spontaneous polarisation at low fields and the interpretation by Gnezdilov *et al.* [142] that there will be no magnetocapacitance for a net moment along a crystallographic direction. We therefore take the magnetic structure as having the same three up one down structure from Bos *et al.* but with the moments pointing perpendicular to the crystallographic axes.

In this chapter we describe results obtained from magnetisation measurements and neutron diffraction data collected on Wish, a long-wavelength neutron diffrac-

tometer which should be able to resolve the helical satellites from the parent Bragg peaks. The use of polarised x-rays to investigate the magnetic structure in the helical, conical, and skyrmion phases is further described.

Coupled Skyrmion Sublattices

In 2014 the first resonant x-ray study on any skyrmion system was published on Cu$_2$OSeO$_3$ by Langner *et al.* [110]. A clear sixfold pattern was observed on resonance at the copper *L*-edges. There are a number of possibly interesting observations in this paper. The satellites were observed around a $(1, 0, 0)$ reflection, which is structurally forbidden in the P2$_1$3 space group, however, no explanation as to its origin is given. Two sets of skyrmion peaks were observed at slightly different rotations. These were observed to resonate at slightly different energies and were attributed to the two different copper sites. The peaks were also observed to rotate with time.

Objectives

To reiterate our objectives after a long introduction, we aimed to extend the work of Langner *et al.* using polarised x-rays to investigate both the origin of the $(1, 0, 0)$ reflection and the magnetic nature of its satellites. Helical magnetic structures can display complex properties and become elliptical where the major axis of the ellipse can align due to local symmetries [109]. We therefore investigated the helical, conical, and skyrmion phases to determine the nature of the magnetic structure and whether it has any intricacies that could promote the formation of skyrmion lattices or produce distorted skyrmions which could be more stable.

Neutron powder diffraction was then used to refine the magnetic structure. The original magnetic structure analysis was unable to resolve the magnetic helices and the ground state was thought to be ferrimagnetic. Helices have since been observed and there is a somewhat open question as to whether the ground state helix is a ferrimagnetic helix or not. We used long wavelength neutron powder diffraction and single crystal data to attempt to resolve the magnetic satellites and refine the true magnetic ground state.

6.3   Experimental Methods

Single crystals of Cu_2OSeO_3 were grown by Monica Hatnean and Geetha Balakrishnan at the University of Warwick using the chemical vapour transport method [145]. Powders of CuO and SeO were heated slowly in a sealed tube over a number weeks. Samples were aligned on the lab-based rotating anode x-ray source where the lattice parameters were confirmed to be consistent with previous measurements with cubic parameter of $a = 8.925$ [146]. Neutron single crystal and powder diffraction measurements were taken at the Wish beamline of target station 2 at ISIS (a pulsed neutron spallation source). Soft x-ray measurements were taken on the RASOR end station of the I10:BLADE beam-line at the Diamond Light Source Ltd. A permanent magnet stage provides a variable magnetic field in the range 7-35 mT. A Princeton Instruments model 2048B PI-MTE area detector with 2048 x 2048 pixels and a pixel size of 13.5 x 13.5 μm was used to check the phase diagram before polarisation analysis measurements were taken. A $(1, 0, 0)$ aligned sample was used as the $(1, 0, 0)$ reflection is the only reflection inside the Ewald sphere. Wish was used for both powder and single crystal neutron scattering. As Wish is a time of flight neutron source the data is effectively collected in 3 dimensions, two on the detector and the third being time. The resolution is greatest in the energy of the neutrons related to the time of flight and the field was therefore aligned vertically to project the skyrmion pattern into this plane. The sample was aligned with $(1, 1, 1)$ along the field direction as this gives the largest possible skyrmion phase. Magnetisation data was collected using a Quantum Designs Superconducting QUantum Interference Device (SQUID) magnetometer, with an AC-susceptibility module.

6.4   Results

6.4.1   Magnetisation Data

The sample was aligned with the field along the $(1, 0, 0)$ direction. Magnetisation vs. applied field scans at 20 K are shown in figure 6.10.

The transition between multi-domain helical and conical structures is expected to be around 300 Oe at 20 K and this can be seen by a change in gradient of the
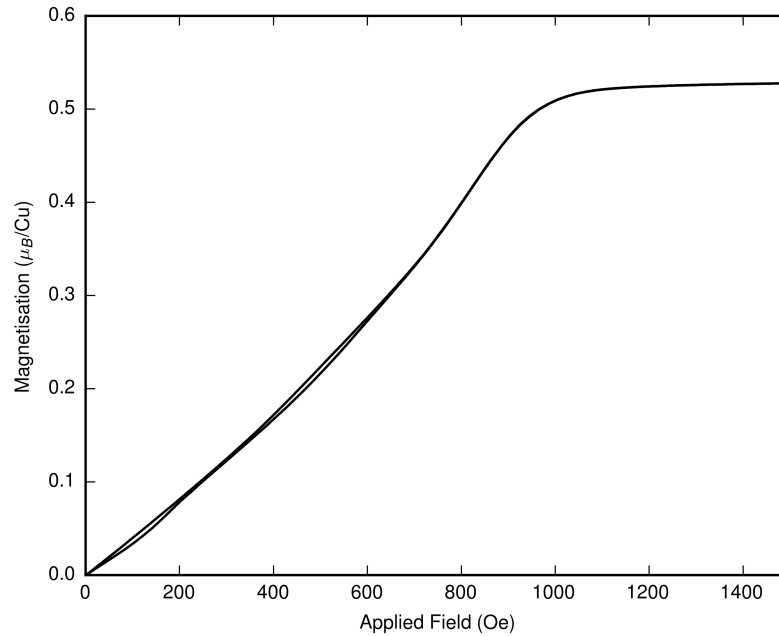
Figure 6.10: Magnetisation as a function of applied magnetic field at 20 K. The field was applied along the $(1, 0, 0)$ direction. With a sample mass of 85.7 mg ± 0.5.

lower, increasing field curve. Some hysteresis can be observed around this transition. This hysteresis is expected and is a result of helical domains preferentially forming along the field direction which is a crystallographic direction when reducing the field from the conical to the helical phase, as such, no change in gradient is observed. Some hysteresis is also observed between 400 and 700 Oe, which is not expected for a single domain conical structure. The saturation magnetisation is 0.527 μ_B/Cu $\pm$ 0.003. This is similar to the value of 0.5 μ_B/Cu (measured at 5 K, with unstated sample orientation) determined in the paper by Bos *et al.* [111].

Temperature dependent magnetisation measurements were taken in the paramagnetic phase with an applied field of 1 T (10,000 Oe). From the following equation the moment size can then be determined:

$$\mu = \sqrt{\frac{3k}{Ax}} . \tag{6.3}$$

Where A is the atomic mass, k is Boltzmann's constant, and x is the gradient of the linear region of the inverse susceptibility, all parameters are in CGS units. The temperature dependence is shown in figure 6.11. This gives the copper moments as 1.50 μ_B $\pm$ 0.009. This is larger than the value of 1.36 μ_B from the Bos paper.
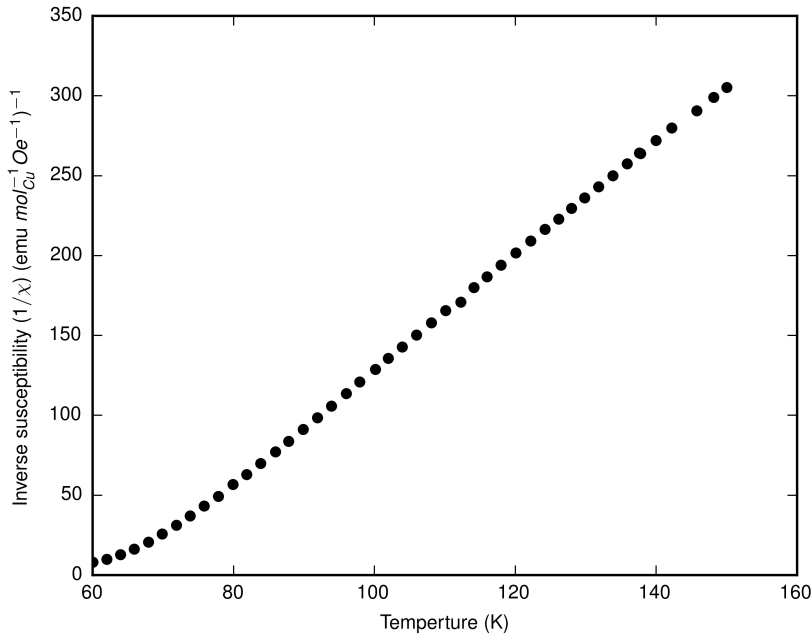
Figure 6.11: Inverse susceptibility vs. temperature in the paramagnetic region in a 10,000 Oe applied field. The linear region is fitted with a straight line with a gradient (x) of 3.58 ± 0.04.

Diamagnetic corrections have been calculated and accounted for with diamagnetic constants from reference [147].

AC-susceptibility scans have been used to map the phase diagram in the region of the skyrmion phase, the results of this are shown in figure 6.12 . The skyrmion phase can be seen as a dip in the region 56.5 - 57.25 K and 150 - 250 Oe. This is roughly similar to the region observed by Adams *et al.* [141]. The magnetisation measurements are largely consistent with those previously reported. The reduced ordered saturation moment suggesting a ferrimagnetic structure.

6.4.2 Resonant X-ray Scattering Results

As previously mentioned the $(1, 0, 0)$ Bragg peak is disallowed in the $P2_13$ space group, the observation of scattering intensity at this position then suggests that the space group may be wrong. Upon further investigation the peak was found to rotate the polarisation of incident light and resonate at the copper L-edges, figure 6.13. The rotation of the polarisation and the copper resonance are usually indicative of
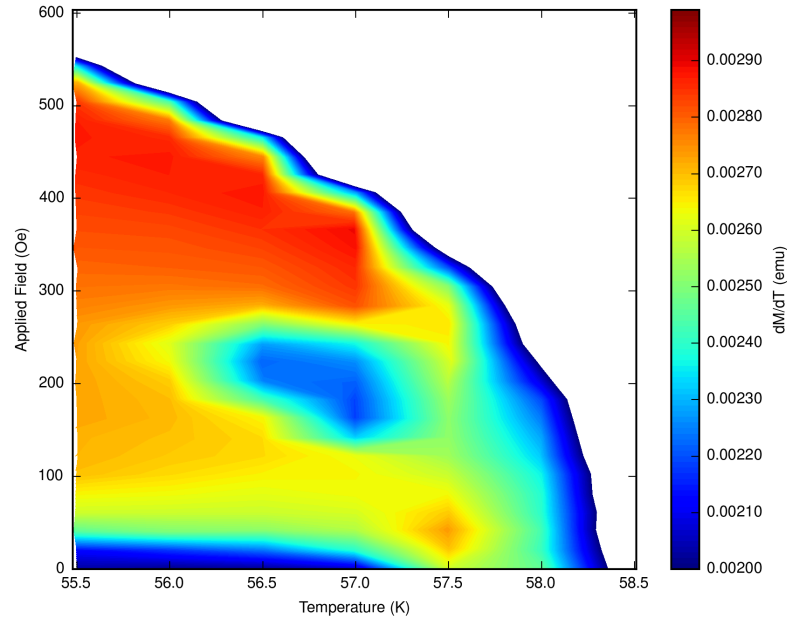
Figure 6.12: AC susceptibility between 0 and 600 Oe applied field at 0.5 K steps. The field was oscillated at a frequency of 700 Hz and an amplitude of 2 Oe. The field was applied along the $(1, 0, 0)$ direction.

magnetic scattering, this can be ruled out by the fact that the peak is observed at room temperature, well above the magnetic transition. Alternatively a scattering process which derives from the anisotropy of the tensor of x-ray susceptibility, so called ATS or Templeton-Templeton scattering, can also produce scattered light of a rotated polarisation [148–150].
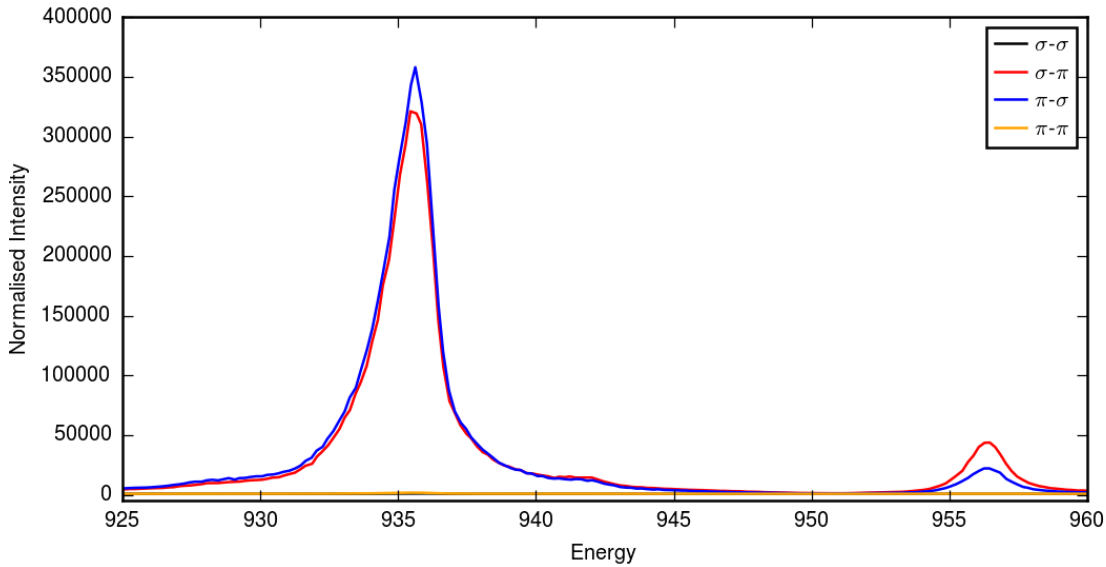
Figure 6.13: Energy scan in the four scattering channels taken at room temperature on the $(1, 0, 0)$ peak. Intensity is only observed in the channels with a rotated polarisation.

6.5 ATS

6.5.1 Anisotropy of the Tensor of X-ray Susceptibility

The information in this section largely follows chapter 8 Resonant X-Ray Scattering and Absorption in the book Magnetism and Synchrotron Radiation [49]. In a tensorial description of scattering, where scattering can be described by a rank two tensor, any tensor can be decomposed into a scalar, a vector, and a symmetric tensor. The scalar part describes isotropic processes such as Thomson scattering, the vector part can be described as a time odd axial vector and describes magnetic scattering. The tensor component is also anisotropic and can produce scattering at positions where there are forbidden reflections due to screw axis and glide plane extinctions. The scattering is produced due to the symmetry of the measurement effectively breaking the symmetry of the space group.

The nature of x-ray scattering with polarised x-rays is that they can be sensitive to the local point group symmetry and thus the symmetry of the measurement breaks the symmetry of the crystal generally breaking glide plane or screw axis extinctions. For Cu_2OSeO_3 the $(1, 0, 0)$ reflections are screw-axis forbidden, so their presence could be expected to be due to ATS.
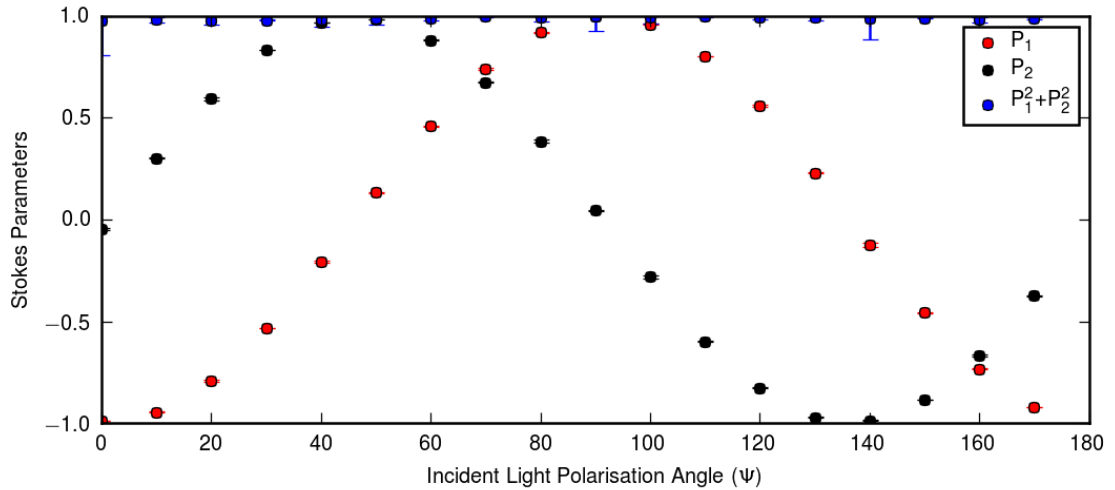
Figure 6.14: Full polarisation analysis measurements of the $(1, 0, 0)$ peak at room temperature.

ATS can be useful for determining small changes in local symmetries. To determine the nature of any ATS scattering we look at the local site symmetries and incorporate these into the structure factor as:

$$\mathbf{F} = \sum_i \mathbf{S}_i \mathbf{T} \mathbf{S}_i^\dagger e^{i\mathbf{q} \cdot \mathbf{r}_i} \, . \tag{6.4}$$

Where $\mathbf{T}$ is a general scattering tensor, $\mathbf{F}$ is the structure factor tensor and $\mathbf{S}_i$ is the site symmetry at the position $\mathbf{r}_i$.

6.5.2 The $(1, 0, 0)$ Peak

A full polarisation analysis measurement was taken of the $(1, 0, 0)$ peak at room temperature, the resultant P_1 and P_2 parameters are shown in figure 6.14. As the peak is resonant at the copper L-edges we consider only the copper atoms when calculating the ATS. There are two symmetry inequivalent copper atoms in the unit cell, and they sit on the Wyckoff positions denoted $4a$, and $12b$. The Wyckoff positions with the associated transforms are shown in table 6.1. These show the symmetry equivalent positions within the unit cell. We can see from this that the equivalent positions for the $4a$ site are just a special case of the general position $12b$ where $x = y = z$. As we are only interested in the site symmetry we can effectively ignore the $+\frac{1}{2}$ from the screw axis as a translation will not change the symmetry, however the rotation from the screw still persists. We can then look at how to transform between the different

Wyckoff position	symmetry	equivalent positions
12b	1	$(x, y, z)(\text{-}x+\frac{1}{2},\text{-}y, z+\frac{1}{2})(x+\frac{1}{2},\text{-}y+\frac{1}{2},\text{-}z)(\text{-}x, y+\frac{1}{2},\text{-}z+\frac{1}{2})$ $(z, x, y)(\text{-}z+\frac{1}{2},\text{-}x, y+\frac{1}{2})(z+\frac{1}{2},\text{-}x+\frac{1}{2},\text{-}y)(\text{-}z, x+\frac{1}{2},\text{-}y+\frac{1}{2})$ $(y, z, x)(\text{-}y+\frac{1}{2},\text{-}z, x+\frac{1}{2})(y+\frac{1}{2},\text{-}z+\frac{1}{2},\text{-}x)(\text{-}y, z+\frac{1}{2},\text{-}x+\frac{1}{2})$
4a	.3.	$(x, x, x)(\text{-}x+\frac{1}{2},\text{-}x, x+\frac{1}{2})(x+\frac{1}{2},\text{-}x+\frac{1}{2},\text{-}x)(\text{-}x, x+\frac{1}{2},\text{-}x+\frac{1}{2})$

Table 6.1: Wyckoff positions and symmetry for the copper atoms in Cu_2OSeO_3.

equivalent positions. Just looking at the $4a$ site, labelling the atom positions in terms of their descending x coordinate; $1, (x, x, x)$; $2, (\text{-}x+\frac{1}{2},\text{-}x, x+\frac{1}{2})$; $3, (x+\frac{1}{2},\text{-}x+\frac{1}{2},\text{-}x)$; $4, (\text{-}x, x+\frac{1}{2},\text{-}x+\frac{1}{2})$. We can easily devise the following transform matrices:

$$\mathbf{S}_1 = \begin{pmatrix} 1 & 0 & 0 \\ 0 & 1 & 0 \\ 0 & 0 & 1 \end{pmatrix}, \mathbf{S}_2 = \begin{pmatrix} -1 & 0 & 0 \\ 0 & -1 & 0 \\ 0 & 0 & 1 \end{pmatrix}, \mathbf{S}_3 = \begin{pmatrix} 1 & 0 & 0 \\ 0 & -1 & 0 \\ 0 & 0 & -1 \end{pmatrix}, \mathbf{S}_4 = \begin{pmatrix} -1 & 0 & 0 \\ 0 & 1 & 0 \\ 0 & 0 & -1 \end{pmatrix}. \tag{6.5}$$

Denoting $\mathbf{f}_i = \mathbf{S}_i \mathbf{T} \mathbf{S}_i^\dagger$ and taking the general matrix, $\mathbf{T} = \begin{pmatrix} a & b & b \\ b & a & b \\ b & b & a \end{pmatrix}$, to describe the local symmetry at a certain atom position after propagating through the symmetry matrices we get the following matrices:

$$\mathbf{f}_1 = \begin{pmatrix} a & b & b \\ b & a & b \\ b & b & a \end{pmatrix}, \mathbf{f}_2 = \begin{pmatrix} a & b & -b \\ b & a & -b \\ -b & -b & a \end{pmatrix}, \mathbf{f}_3 = \begin{pmatrix} a & -b & -b \\ -b & a & b \\ -b & b & a \end{pmatrix}, \mathbf{f}_4 = \begin{pmatrix} a & -b & b \\ -b & a & -b \\ b & -b & a \end{pmatrix}. \tag{6.6}$$

Then the structure factor can be written as:

$$\begin{aligned} \mathbf{F} &= \mathbf{f}_1 e^{2\pi i x} + \mathbf{f}_2 e^{2\pi i(-x+\frac{1}{2})} + \mathbf{f}_3 e^{2\pi i(x+\frac{1}{2})} + \mathbf{f}_4 e^{-2\pi i x} \\ &= \mathbf{f}_1 e^{2\pi i x} - \mathbf{f}_2 e^{-2\pi i x} - \mathbf{f}_3 e^{2\pi i x} + \mathbf{f}_4 e^{-2\pi i x} \\ &= (\mathbf{f}_1 - \mathbf{f}_3)e^{2\pi i x} + (\mathbf{f}_4 - \mathbf{f}_2)e^{-2\pi i x}. \end{aligned} \tag{6.7}$$

Substituting in the $\mathbf{f}$ matrices we get the following result:

$$\begin{aligned} \mathbf{F}_{100}^{4a} &= \begin{pmatrix} 0 & 2b & 2b \\ 2b & 0 & 0 \\ 2b & 0 & 0 \end{pmatrix} e^{2\pi i x} + \begin{pmatrix} 0 & 2b & -2b \\ 2b & 0 & 0 \\ -2b & 0 & 0 \end{pmatrix} e^{-2\pi i x} \\ &= 2b \begin{pmatrix} 0 & e^{2\pi i x} + e^{-2\pi i x} & e^{2\pi i x} - e^{-2\pi i x} \\ e^{2\pi i x} + e^{-2\pi i x} & 0 & 0 \\ e^{2\pi i x} - e^{-2\pi i x} & 0 & 0 \end{pmatrix} \\ &= 4b \begin{pmatrix} 0 & \cos 2\pi x & i \sin 2\pi x \\ \cos 2\pi x & 0 & 0 \\ i \sin 2\pi x & 0 & 0 \end{pmatrix}. \end{aligned} \tag{6.8}$$

Where for the $4a$ site, $x = 0.886$. Computing a similar operation for the general position $12b$[10] we get:

$$\mathbf{F}^{12b}_{100} = 4b \begin{pmatrix} 0 & A & iB \\ A & 0 & 0 \\ iB & 0 & 0 \end{pmatrix}.$$ (6.9)

Where $A = \cos 2\pi x + \cos 2\pi y + \cos 2\pi z$ and $B = \sin 2\pi x + \sin 2\pi y + \sin 2\pi z$ with the coordinates $x = 0.1335$, $y = 0.1221$, and $z = 0.8719$.

To determine a scattering matrix $\mathbf{M}$ we use the equation $\mathbf{M} = \hat{\varepsilon}.\mathbf{F}.\hat{\varepsilon}'$ where the incident polarisation $\hat{\varepsilon}$ is described as a row vector and the scattered polarisation $\hat{\varepsilon}'$ is described as a column vector. The polarisation vectors are as follows in this geometry:

$$\hat{\varepsilon}_\sigma = (0, 0, 1),$$

$$\hat{\varepsilon}'_\sigma = \begin{pmatrix} 0 \\ 0 \\ 1 \end{pmatrix},$$

$$\hat{\varepsilon}_\pi = (\cos\theta, -\sin\theta, 0),$$

$$\hat{\varepsilon}'_\pi = \begin{pmatrix} \cos\theta \\ \sin\theta \\ 0 \end{pmatrix}.$$

As the basic shape is the same for each of the two copper sites they will produce similar scattering matrices:

$$\mathbf{M} = \begin{pmatrix} 0 & 4b\cos\theta(iB + A) \\ 4b\cos\theta(iB + A) & 0 \end{pmatrix} = 4b\cos\theta(iB + A) \begin{pmatrix} 0 & 1 \\ 1 & 0 \end{pmatrix}.$$ (6.10)

The $4b\cos\theta(iB + A)$ term is then just a constant and irrelevant to the polarisation dependence which will just rotate the incident linear polarisation by $90°$ regardless of the incoming polarisation angle. The resulting full polarisation analysis for this model is plotted alongside the data in figure 6.15 and reproduces the data well. Unfortunately due to the large number of parameters involved nothing can be said about the local site symmetries from these results.

---

[10]Where the $\mathbf{S}$ matrices are now $\begin{pmatrix} 1 & 0 & 0 \\ 0 & 1 & 0 \\ 0 & 0 & 1 \end{pmatrix}$, $\begin{pmatrix} -1 & 0 & 0 \\ 0 & -1 & 0 \\ 0 & 0 & 1 \end{pmatrix}$, $\begin{pmatrix} 1 & 0 & 0 \\ 0 & -1 & 0 \\ 0 & 0 & -1 \end{pmatrix}$, $\begin{pmatrix} -1 & 0 & 0 \\ 0 & 1 & 0 \\ 0 & 0 & -1 \end{pmatrix}$, $\begin{pmatrix} 0 & 0 & 1 \\ 1 & 0 & 0 \\ 0 & 1 & 0 \end{pmatrix}$, $\begin{pmatrix} 0 & 0 & -1 \\ -1 & 0 & 0 \\ 0 & 1 & 0 \end{pmatrix}$, $\begin{pmatrix} 0 & 0 & 1 \\ -1 & 0 & 0 \\ 0 & -1 & 0 \end{pmatrix}$, $\begin{pmatrix} 0 & 0 & -1 \\ 1 & 0 & 0 \\ 0 & -1 & 0 \end{pmatrix}$, $\begin{pmatrix} 0 & 1 & 0 \\ 0 & 0 & 1 \\ 1 & 0 & 0 \end{pmatrix}$, $\begin{pmatrix} 0 & -1 & 0 \\ 0 & 0 & -1 \\ 1 & 0 & 0 \end{pmatrix}$, $\begin{pmatrix} 0 & 1 & 0 \\ 0 & 0 & -1 \\ -1 & 0 & 0 \end{pmatrix}$, $\begin{pmatrix} 0 & -1 & 0 \\ 0 & 0 & 1 \\ -1 & 0 & 0 \end{pmatrix}$.

Figure 6.15: Full polarisation analysis measurements of the $(1, 0, 0)$ Bragg peak. With the solid lines representing the model to ATS scattering.

6.5.3 Magnetic Satellite Reflections

Magnetic satellites were observed to exist around the $(1, 0, 0)$ reflection below 57.5 K. A schematic of the experimental set up is shown in figure 6.16, in zero field helical satellites form along the crystallographic directions a, b, and c as $(1 \pm \tau, 0, 0), (1, \pm\tau, 0), (1, 0, \pm\tau)$. In the conical phase satellites form along the field direction (in this case a) $(1 \pm \tau, 0, 0)$. In the skyrmion phase satellites form in a hexagonal pattern in the plane perpendicular to the field (the bc-plane) as $(1, \pm\tau, 0)$, $(1, \pm\frac{2}{3}\tau, \pm\frac{1}{3}\tau)$, $(1, \pm\frac{2}{3}\tau, \mp\frac{1}{3}\tau)$. Using $\theta - 2\theta$ scans with the area detector, a rough phase diagram was constructed. The skyrmion phase was found to exist over only a very small range in temperature and magnetic field. This was slightly smaller than that determined by the AC-susceptibility measurements. Here the skyrmion phase was only found in the darkest blue region of the phase diagram in figure 6.12.

The pattern produced when entering the skyrmion phase is often not a simple hexagon as reported in the literature. Usually a ring of intensity was seen aligned perpendicular to the field with the correct wavevector, an example of this is shown in the left hand side of figure 6.17. This suggests the formation of many domains within the sample all with different orientations aligned with the field. The more intense regions often form along a principal crystallographic direction, however, this is not always the case and shows that there is a relatively weak coupling between the
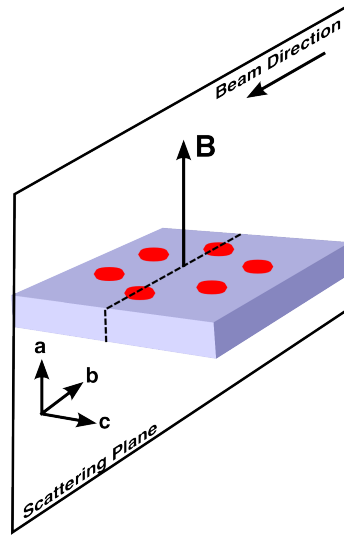
Figure 6.16: Schematic of the experimental geometry. Showing the field direction which was usually along the *a*-axis but can rotate in the *ab*-plane. The red spots are a representation of the skyrmion reflections in reciprocal space.

magnetic structure and the underlying crystal lattice. A single 6-fold pattern was found to be achievable by rotating the field to essentially give a preferred direction of alignment in the plane with one set of reflections aligning along the axis about which the field was rotated. An example of the pattern achieved by such a method is shown in the right hand side of figure 6.17.

6.5.4 Magnetic Structure Factor Calculations

As magnetic peaks were not observed at the $(1, 0, 0)$ position in the previous neutron powder study [111] we shall now calculate the magnetic structure factors for the ferrimagnetic and helical models.

Magnetic Structure Factor of the $(1, 0, 0)$ reflection within the Ferrimagnetic model

No magnetic scattering was observed in the neutron powder data collected by Bos *et al.* [111]. We shall confirm this by calculating the magnetic structure factor for this reflection.

We will now calculate the magnetic structure factor for the $(1, 0, 0)$ reflection with the original ferrimagnetic model. Following the same method as in the previous
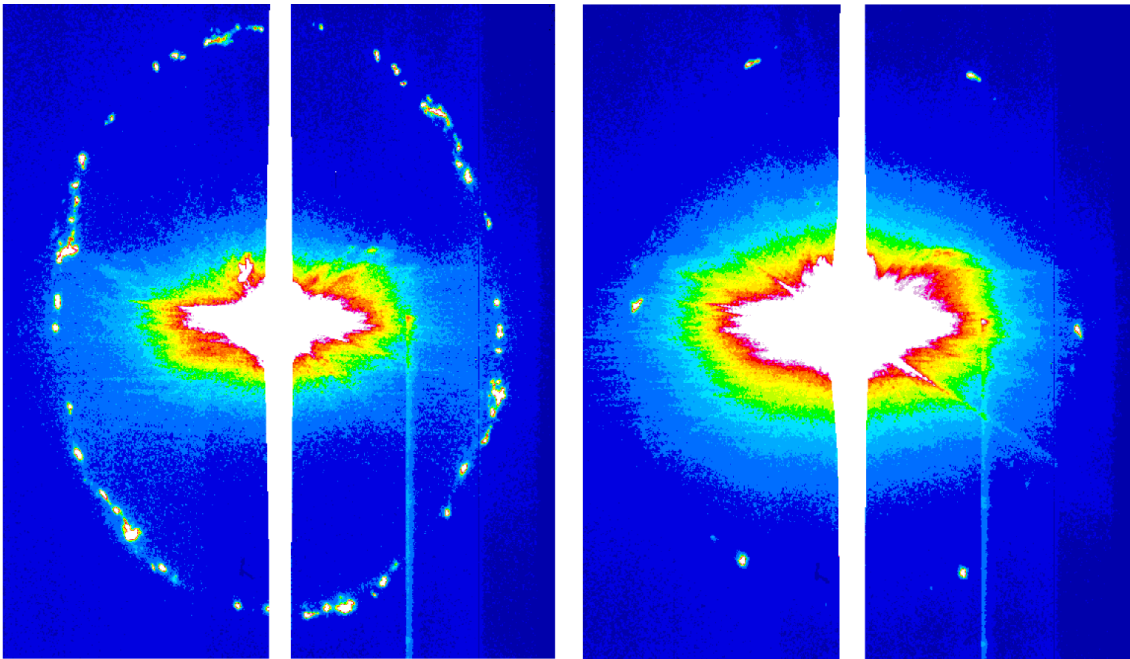
Figure 6.17: Integrated intensity $\theta - 2\theta$ curve scans around the $(1, 0, 0)$ with the area detector. The white streak in the middle of the image is a consequence of the ATS peak overloading the central pixels. The left image shows a typical pattern observed upon cooling into the skyrmion phase. The right image shows an aligned pattern achieved by rotating the magnetic field to align the magnetic domains.

chapter the magnetic structure factor can be written as follows:

$$\mathbf{F}^M \propto \sum_{l,m,n} \sum_i^I e^{i\mathbf{q}\cdot\mathbf{r}_{i,l,m,n}} \mathbf{z}(\mathbf{r}_{i,l,m,n}) \,. \tag{6.11}$$

Where, as before, the sum runs over only the magnetic atoms in the unit cell (i) and the unit cell positions (l, m, n), where $\mathbf{z}(\mathbf{r}_{i,l,m,n})$ is a function describing the magnetic moment. As the ferrimagnetic structure is ferromagnetic within the different Wyckoff sites it can be described with the following vector:

$$\mathbf{z}(\mathbf{r}_{i,l,m,n}) = (1,0,0) \,. \tag{6.12}$$

As there is now no periodicity to the structure, the magnetic structure factor simplifies and intensity is no longer produced at satellites at $\boldsymbol{\tau}$ positions and only at fundamental Bragg peak positions. We begin by just calculating the magnetic structure factor for the $4a$ site and then extending this to the $12b$ site. At the $4a$ site there are 4 atoms within the unit cell at positions; (x,x,x), $(-x+\frac{1}{2},-x,x+\frac{1}{2})$, $(x+\frac{1}{2},-x+\frac{1}{2},-x)$, $(-x,x+\frac{1}{2},-x+\frac{1}{2})$ where $x = 0.886$, resulting in the following calculation for the structure factor:

$$\begin{aligned}
\mathbf{F}^M_{100} =& \frac{1}{2}\mathbf{Z}\left(e^{2\pi i(1,0,0)\cdot(x,x,x)} + e^{2\pi i(1,0,0)\cdot(x+\frac{1}{2},-x+\frac{1}{2},-x)}\right. \\
&\left. + e^{2\pi i(1,0,0)\cdot(-x,x+\frac{1}{2},-x+\frac{1}{2})} + e^{2\pi i(1,0,0)\cdot(-x+\frac{1}{2},-x,x+\frac{1}{2})}\right) \\
=& \frac{1}{2}\mathbf{Z}\left(e^{2\pi ix} + e^{\pi i}e^{2\pi ix} + e^{-2\pi ix} + e^{\pi i}e^{-2\pi ix}\right) \\
=& \frac{1}{2}\mathbf{Z}\left(e^{2\pi ix} - e^{2\pi ix} + e^{-2\pi ix} - e^{-2\pi ix}\right) \\
=& 0 \,. \tag{6.13}
\end{aligned}$$

As this is independent of x we can easily see that the atoms on the $12b$ sites; (x,y,z), $(-x+\frac{1}{2},-y,z+\frac{1}{2})$, $(x+\frac{1}{2},-y+\frac{1}{2},-z)$, $(-x,y+\frac{1}{2},-z+\frac{1}{2})$, (z,x,y), $(-z+\frac{1}{2},-x,y+\frac{1}{2})$, $(z+\frac{1}{2},-x+\frac{1}{2},-y)$, $(-z,x+\frac{1}{2},-y+\frac{1}{2})$, (y,z,x), $(-y+\frac{1}{2},-z,x+\frac{1}{2})$, $(y+\frac{1}{2},-z+\frac{1}{2},-x)$, $(-y,z+\frac{1}{2},-x+\frac{1}{2})$ can be split into 3 groups of four atoms similar to the $4a$ site, e.g. (y,z,x), $(-y+\frac{1}{2},-z,x+\frac{1}{2})$, $(y+\frac{1}{2},-z+\frac{1}{2},-x)$, $(-y,z+\frac{1}{2},-x+\frac{1}{2})$, which will each produce the same zero structure factor as the $4a$ site[11]. This confirms that the structure factor for the ferrimagnetic structure is zero at the $(1,0,0)$ reflection.

---

[11] for the $12b$ site $\mathbf{Z}$ will have the opposite sign.

Magnetic Structure Factor of the $(1 + \tau, 0, 0)$ satellite reflection within the Ferrimagnetic-Helical model

We will now calculate the magnetic structure factor for the magnetic satellite reflections around the forbidden $(1, 0, 0)$ peak. We shall start by calculating the magnetic structure factor for the simple case of a helical structure propagating along a with the moment direction in the bc-plane. This structure can be described as follows:

$$\mathbf{z}(\mathbf{r}_{i,l,m,n}) = (0, \cos(\boldsymbol{\tau}.\mathbf{r}_{i,l,m,n}), \sin(\boldsymbol{\tau}.\mathbf{r}_{i,l,m,n})). \tag{6.14}$$

Which in this case can be rewritten in exponential form as follows:

$$\mathbf{z}(\mathbf{r}_{i,l,m,n}) = \frac{1}{2}e^{i(\boldsymbol{\tau}.\mathbf{r}_{i,l,m,n})}\mathbf{Z} + \frac{1}{2}e^{-i(\boldsymbol{\tau}.\mathbf{r}_{i,l,m,n})}\mathbf{Z}^*. \tag{6.15}$$

Where $\mathbf{Z} = (0, 1, i)$, as in the previous chapter we can now substitute this back into the structure factor as follows:

$$\mathbf{F}^M \propto \sum_{l,m,n} \sum_i^I \frac{1}{2}e^{i\mathbf{q}.\mathbf{r}_{i,l,m,n}} \left(e^{i(\boldsymbol{\tau}.\mathbf{r}_{i,l,m,n})}\mathbf{Z} + e^{-i(\boldsymbol{\tau}.\mathbf{r}_{i,l,m,n})}\mathbf{Z}^*\right) \tag{6.16}$$

$$\propto \sum_{l,m,n} \sum_i^I \frac{1}{2} \left(e^{i(\mathbf{q}+\boldsymbol{\tau}).\mathbf{r}_{i,l,m,n}}\mathbf{Z} + e^{i(\mathbf{q}-\boldsymbol{\tau}).\mathbf{r}_{i,l,m,n}}\mathbf{Z}^*\right) \tag{6.17}$$

$$\propto \frac{1}{2}\sum_{l,m,n} e^{i(\mathbf{q}+\boldsymbol{\tau}).\mathbf{R}_{l,m,n}} \sum_i^I e^{i(\mathbf{q}+\boldsymbol{\tau}).\mathbf{r}_i}\mathbf{Z} \tag{6.18}$$

$$+ \frac{1}{2}\sum_{l,m,n} e^{i(\mathbf{q}-\boldsymbol{\tau}).\mathbf{R}_{l,m,n}} \sum_i^I e^{i(\mathbf{q}-\boldsymbol{\tau}).\mathbf{r}_i}\mathbf{Z}^*. \tag{6.19}$$

So now in the presence of a magnetic structure $\mathbf{q}$ is transformed and this will also transform the Laué condition. The Laué condition will then become, $(\mathbf{q}\pm\boldsymbol{\tau}).\mathbf{R}_{l,m,n} = 2\pi n$ as the sum over l, m, n will be zero otherwise and $\mathbf{G}.\mathbf{R}_{l,m,n} = 2\pi n$ then we get $\mathbf{q} = \mathbf{G} \mp \boldsymbol{\tau} = (h, k, l) \mp \boldsymbol{\tau}$. Then this can be substituted into the structure factor and the τ's will cancel such that we are left with the following:

$$\mathbf{F}^M \propto \frac{1}{2}\mathbf{Z}\sum_n^I e^{i2\pi(h,k,l).\mathbf{r}_n}\bigg|_{\mathbf{q}+\boldsymbol{\tau}}$$

$$+ \frac{1}{2}\mathbf{Z}^*\sum_n^I e^{i2\pi(h,k,l).\mathbf{r}_n}\bigg|_{\mathbf{q}-\boldsymbol{\tau}}. \tag{6.20}$$

We are now left with the sum over the atom positions giving the structure factor for the parent Bragg peaks, which we can calculate for the $(1+\boldsymbol{\tau}, 0, 0)$ peak. As

with the ferrimagnetic structure factor for ease we shall consider the different atom Wyckoff positions separately, starting with the $4a$ site:

$$
\begin{aligned}
\mathbf{F}_{100}^{M} =& \frac{1}{2}\mathbf{Z}\left(e^{2\pi i(1,0,0).(x,x,x)} + e^{2\pi i(1,0,0).(x+\frac{1}{2},-x+\frac{1}{2},-x)} \right.\\
&\left. + e^{2\pi i(1,0,0).(-x,x+\frac{1}{2},-x+\frac{1}{2})} + e^{2\pi i(1,0,0).(-x+\frac{1}{2},-x,x+\frac{1}{2})}\right)\\
=& \frac{1}{2}\mathbf{Z}\left(e^{2\pi ix} + e^{\pi i}e^{2\pi ix} + e^{-2\pi ix} + e^{\pi i}e^{-2\pi ix}\right)\\
=& \frac{1}{2}\mathbf{Z}\left(e^{2\pi ix} - e^{2\pi ix} + e^{-2\pi ix} - e^{-2\pi ix}\right)\\
=& 0\,.
\end{aligned}
\tag{6.21}
$$

As this is again independent of x we can see that following the same logic as before for the atoms on the $12b$ sites, the magnetic structure factors for the satellites around the $(1,0,0)$ reflection are also zero.

The lack of a magnetic structure factor is consistent with the neutron powder diffraction data from Bos *et al.* [111]. However, there is the presence of the ATS reflection at the $(1,0,0)$ to consider. This complicates the situation and could allow for magnetic intensity to still be observed at the $(1,0,0)\pm\boldsymbol{\tau}$ positions without a magnetic contribution being observable with neutron scattering.

Magnetic satellite reflections have been observed around forbidden reflections in BiFeO$_3$ [151]. In this example reflections around a glide plane forbidden reflection (which was also ATS forbidden) are observed as the magnetic structure displays antiferromagnetic coupling between atoms on the same site.

Applying a similar structure from BiFeO$_3$ to Cu$_2$OSeO$_3$ will result in a structure where the tetrahedral arrangements of copper atoms are all aligned ferromagnetically but one of the tetrahedra has moments aligned antiferromagnetically with the other three. This structure is shown in figure 6.18. The magnetic structure factor in this case will no longer be zero and is calculated below:
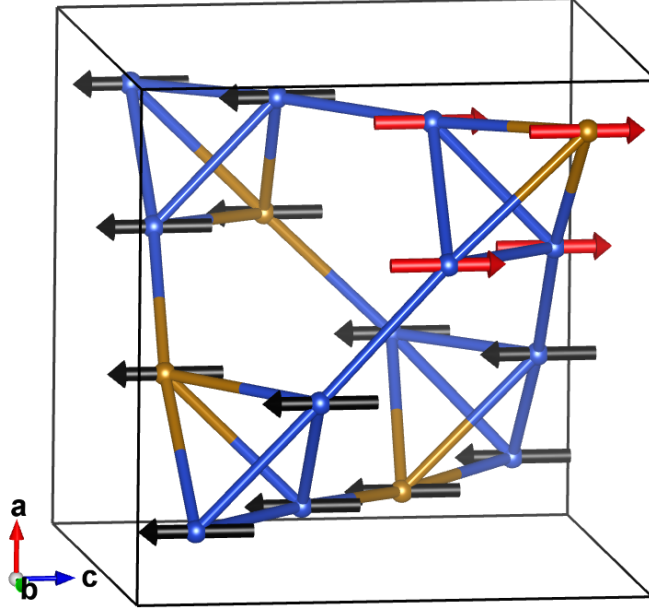
Figure 6.18: Structure of cubic Cu_2OSeO_3, with only copper atoms shown for clarity. Brown atoms denote coppers at the $4a$ site, blue atoms denote coppers at the $12b$ site. Magnetic moments directed along the c-axis.

$$\mathbf{F}_{100}^{M} = \frac{1}{2}\mathbf{Z} \left(e^{2\pi i(1,0,0).(x,x,x)} - e^{2\pi i(1,0,0).(x+\frac{1}{2},-x-\frac{1}{2},-x)} \right.$$
$$\left. - e^{2\pi i(1,0,0).(-x,x+\frac{1}{2},-x+\frac{1}{2})} - e^{2\pi i(1,0,0).(-x+\frac{1}{2},-x,x+\frac{1}{2})} \right)$$
$$= \frac{1}{2}\mathbf{Z} \left(e^{2\pi ix} - e^{\pi i}e^{2\pi ix} - e^{-2\pi ix} - e^{\pi i}e^{-2\pi ix} \right)$$
$$= \frac{1}{2}\mathbf{Z} \left(e^{2\pi ix} + e^{2\pi ix} - e^{-2\pi ix} + e^{-2\pi ix} \right)$$
$$= \mathbf{Z}e^{2\pi ix} . \tag{6.22}$$

Redefining x as x_1 and extending this to encompass the $12b$ site, with atom position (x_2, y, z), gives:

$$\mathbf{F}_{100}^{M} = \mathbf{Z} \left(e^{2\pi ix_1} - e^{2\pi ix_2} - e^{2\pi iy} - e^{2\pi iz} \right)$$
$$= (0, \cos 2\pi x_1 + i\sin 2\pi x_1 - \cos 2\pi x_2 - i\sin 2\pi x_2 - \cos 2\pi y - i\sin 2\pi y$$
$$- \cos 2\pi z - i\sin 2\pi z, i\cos 2\pi x_1 - \sin 2\pi x_1 - i\cos 2\pi x_2 + \sin 2\pi x_2$$
$$- i\cos 2\pi y + \sin 2\pi y - i\cos 2\pi z + \sin 2\pi z) . \tag{6.23}$$
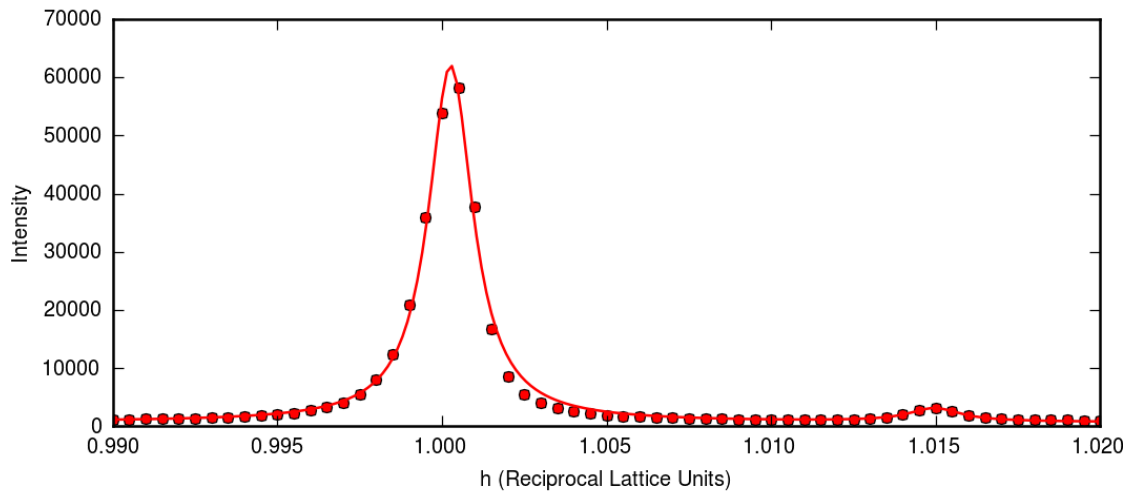
Figure 6.19: h-scan at 14 K in zero field around the $(1,0,0)$ Bragg peak showing the helical satellite reflection. The line corresponds to Lorentzian peakshapes with a linear background from which the wavevector of $\tau = 0.0147 \pm 0.00025$ r.l.u.

Where x_1, x_2, y, z come from the atom positions and are as follows $x_1 = 0.886, x_2 = 0.1335, y = 0.1211, z = 0.8719$.

This structure maintains the one up three down moment structure and will therefore be consistent with magnetisation measurements. It would however, be expected to show intensity at the $(1,0,0)$ position in neutron powder diffraction.

The difference between the two structures is independent of the $\boldsymbol{\tau}$ periodicity and would therefore not be expected to be observable in the polarisation dependence of the satellite peaks.

Satellite Peak Characterisation

Using the polarisation analyser a theta two-theta (h) scan was performed in the σ-π channel showing the strong intensity still present at the $(1,0,0)$ position and the $(1+\tau,\ 0,\ 0)$ satellite. The peaks have been fitted to Lorentzian lineshapes to accurately determine their centres. The wavevector was found to agree with previous measurements to be $\tau = 0.0147 \pm 0.00025$ r.l.u corresponding to a helical wavelength of 60.7 nm $\pm$ 1 (figure 6.19). Energy scans of the satellites were taken in the three phases, as shown in figure 6.20, and are relatively uncomplicated with only a single peak at both the L_{II} & L_{III} edges, mirroring that seen with the forbidden ATS reflection. These results are somewhat in opposition to those observed by Langner

et al. [110] reproduced in figure 6.21. The Langner paper attributed these different resonances and peaks to the two different copper sites and are the result of a moiré pattern. However, we only observed one set of peaks in the skyrmion phase and only a single resonance feature. A recent paper by Zhang *et al.* [152] has thoroughly discounted the data of Langner *et al.* as they were able to observe one, two, or three sets of peaks, further the Fourier transform of a moiré pattern would produce a six-fold pattern of secondary satellites around the primary ones. The peak splitting is shown to be a function of the magnet poles not being aligned creating a field gradient at the sample position, this is supported by the fact that in the Langner paper the field was fixed in the experimental frame and not in the sample frame as in our experiment. The attribution of the peaks to the two copper sites obviously no longer holds when it is noted that three peaks can also be observed. It was also noted in the Zhang paper that the peak splitting cannot be explained by the different copper sites considering that both valence bond sum and DFT calculations [111,153] show very little difference in the oxidation states between the two sites. We expect that the discrepancy between the energy resonance is as a result of using an area detector and that both peaks could not be aligned properly at the same time[12].

Further work by Zhang *et al.* which has yet to be published has found that an offset in the permanent magnets produce a pattern that rotates with time suggesting that an inhomogeneous field produces the rotating pattern. This is similar to that observed by Langner *et al.*

As we have seen the structure factor for the currently accepted ferrimagnetic structure cannot explain the magnetic satellites observed around the $(1, 0, 0)$ position. We shall therefore turn to the neutron scattering results to attempt to explain this before returning to the polarisation analysis results.

---

[12]This could be counteracted by doing a full theta-two theta scan at each energy, but would not be possible with the noted rotation of the pattern reported in the paper.
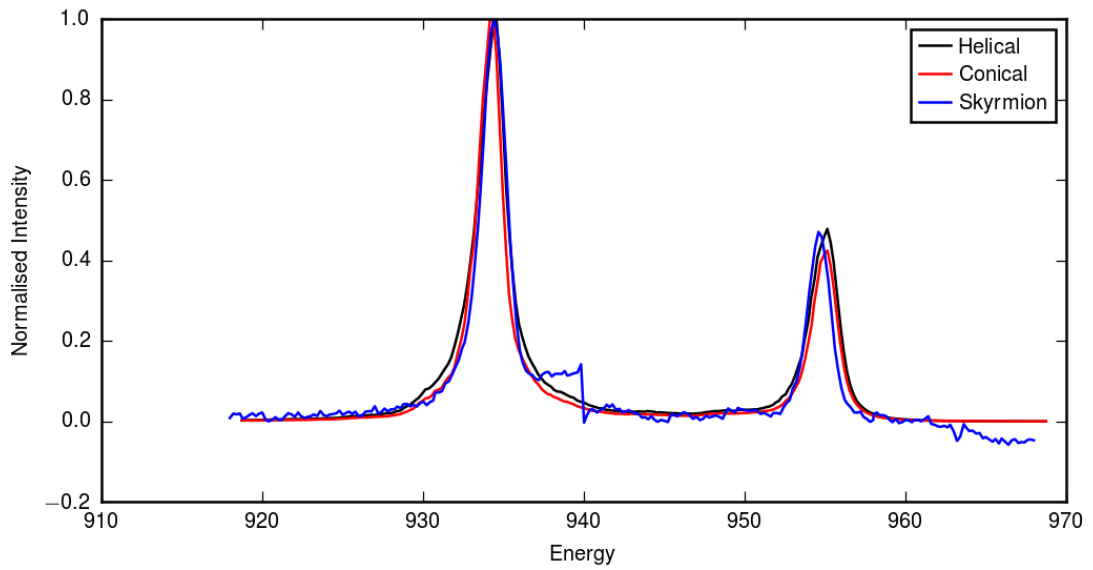
Figure 6.20: Energy scans of the magnetic satellites in the three different phases with σ incident light. The step at 940 eV in the data for the skyrmion peak is an artefact from normalising the background which showed a strong change in gradient after the L_{III} edge. This was notable as the skyrmion phase satellites were much weaker than in the other phases.
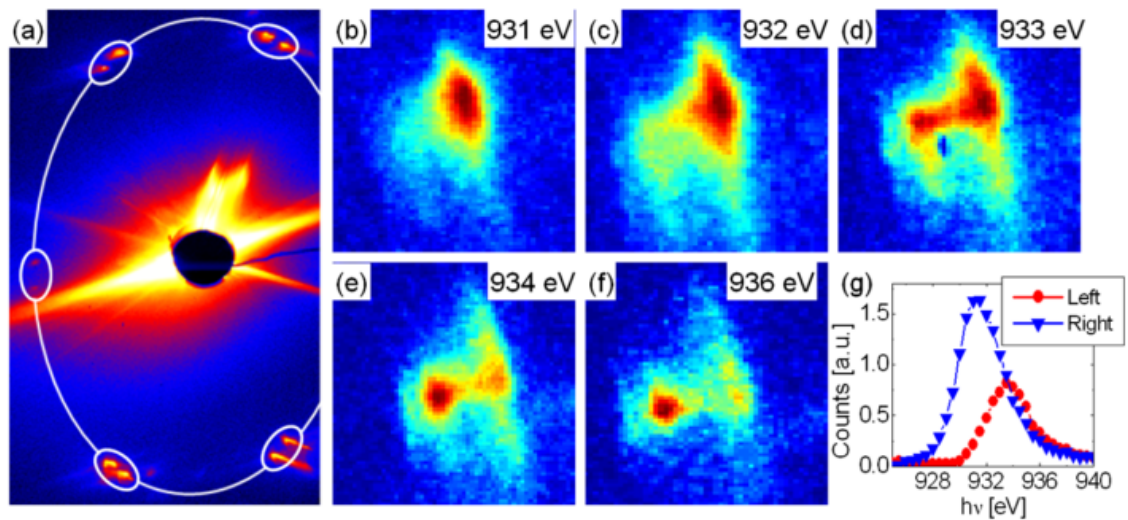
Figure 6.21: (a) Skyrmion peaks at 933 eV (b)-(f) Evolution of the double peak as a function of the incident photon energy. (g) Integrated peak intensities as a function of photon energy, showing different resonances for each peak, from [110].

6.5.5   Neutron scattering

Single Crystal

Figure 6.22 shows results from single crystal measurements taken on Wish. As expected in the helical phase figure 6.22 (a-c) six satellite peaks were observed and are oriented along $[1, 0, 0]$ type directions. No central peak is observed which indicates that there is no net moment as expected for a helix. On the application of a magnetic field the domains preferentially align to the field direction, figure 6.22(d), a further increase of the magnetic field, figure 6.22(e), induces a spin canting and the structure becomes conical, as evidenced by the intensity now present at the central position. There is also a slight movement of the satellite peaks suggesting that the wavevector becomes shorter with the application of the field, this is consistent with the slight hysteresis observed in the magnetisation data. This conical structure results in a net moment and some remnant intensity at the parent peak position. When the field is increased further, the canting effectively becomes 90 degrees and all the moments align with the field. Subfigures 6.22(g) and (h) show a one degree temperature difference from below and in the skyrmion phases respectively. The resolution is too low to distinguish separate peaks in the skyrmion phase, however, a transfer of intensity from aligned along the field to in the plane perpendicular to the field is evident. It also appears that the intensity on the parent Bragg peak persists and it is therefore likely that there is a coexistence of the skyrmion and ferrimagnetic phases. If there were domains where there were not skyrmions these would be expected to be conical as the skyrmion phase is completely surrounded by the conical phase, however, the lack of intensity below and above the parent peak precludes this situation.

6.5.6   Powder Diffraction

Following the successful resolution of the satellite peaks using single crystal measurements, powder diffraction was used to attempt to refine the magnetic structure with a helical model instead of a ferrimagnetic one and investigate the presence of a $(1, 0, 0)$ reflection. We will consider a combination of the different possible models where helical satellites are allowed.
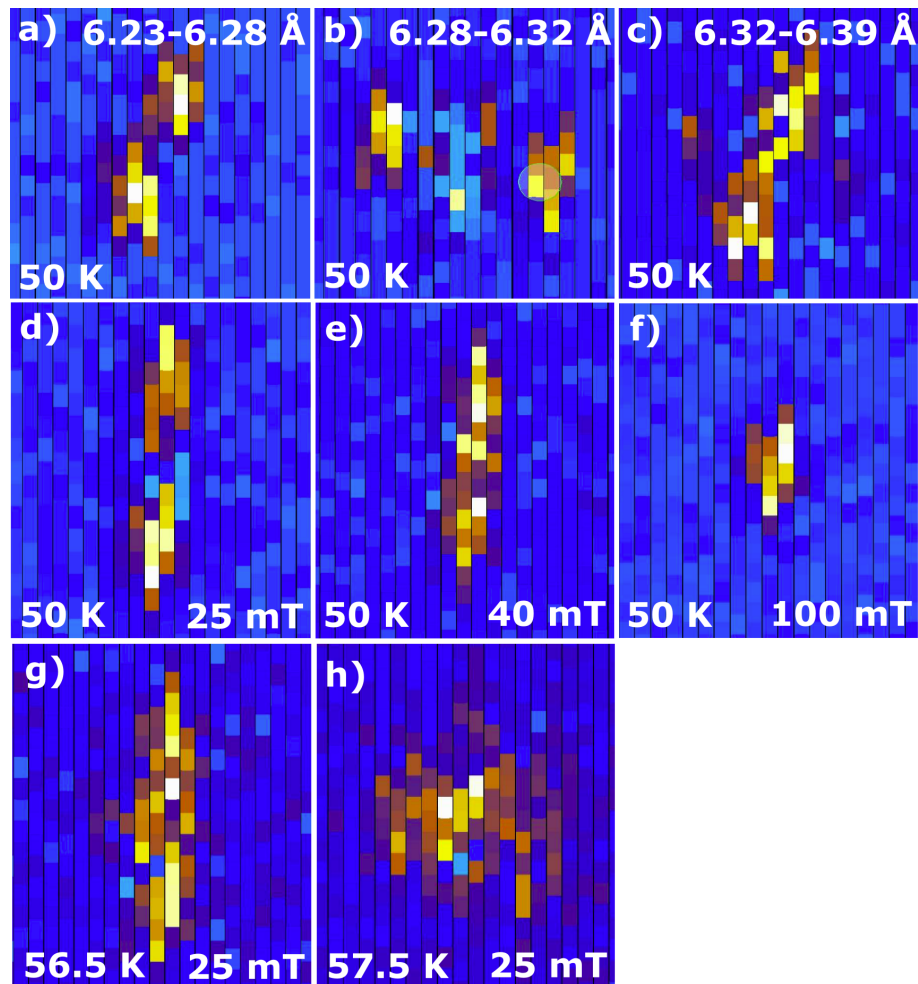
Figure 6.22: Single crystal diffraction patterns on Wish. Images are around the $(1, 1, 0)$ Bragg peak and the Bragg peak is removed by subtraction of images above and below the magnetic transition. Images a-c are separated in d-spacing and show the three pairs of helical domains, no remnant peak is observed at the $(1, 1, 0)$ position. subfigures d-f show successive increases in field from the conical to the ferrimagnetic phases. The final images, g and h show what should be the conical and skyrmion phases respectively.

Table 6.2: Atomic parameters for Cu_2OSeO_3 at 60 K. Goodness of fit statistics: $R_p = 18.6\%$, $wR_p = 9.4\%$, $R_{exp} = 3.0\%$, $\chi^2 = 9.7$. Space-group $P2_13$ and $a = 8.97639(7)$ Å.

atom	Wyckoff site	x	y	z
Cu1	$4a$	0.8870(8)	-	-
Cu2	$12b$	0.1315(7)	0.1189(7)	-0.1293(8)
Se1	$4a$	0.2025(6)	-	-
Se2	$4a$	0.4636(5)	-	-
O1	$4a$	0.7575(6)	-	-
O2	$4a$	0.018(1)	-	-
O3	$12b$	0.2686(6)	0.1829(7)	0.0324(7)
O4	$12b$	-0.0164(9)	0.0415(8)	-0.2677(8)

6.5.7   Nuclear Model

Data for the nuclear model was taken at 60 K in zero applied magnetic field. The Rietveld refined model was consistent with the measurements of Bos *et al.* [111] with a lattice parameter of $a = 8.980$. The atom positions are in table 6.2 with data and refinement shown in figure 6.23.

6.5.8   Ferrimagnetic Phase

For the magnetic structure refinement we begin with the simplest case of the ferrimagnetic phase. A field of 0.12 mT was applied to the sample at 20 K and collected for 3 hours. Differences in the powder pattern were observed between this and the 60 K data, as shown in figure 6.24. The difference patterns are shown in figure 6.25. While many of the peaks do show a difference, this is a product of thermal contraction of the sample and can be seen by the positive and negative nature of the peak differences. It should be noted that no intensity is observed in the difference patterns (figure 6.25) at 8.925 corresponding to the $(1, 0, 0)$ reflection, consistent with the magnetic structure factor calculated previously and the three up one down ferrimagnetic structure proposed by Bos *et al.*. The pattern was Rietveld refined using Fullprof [53] with the nuclear model remaining the same, apart from the lattice,
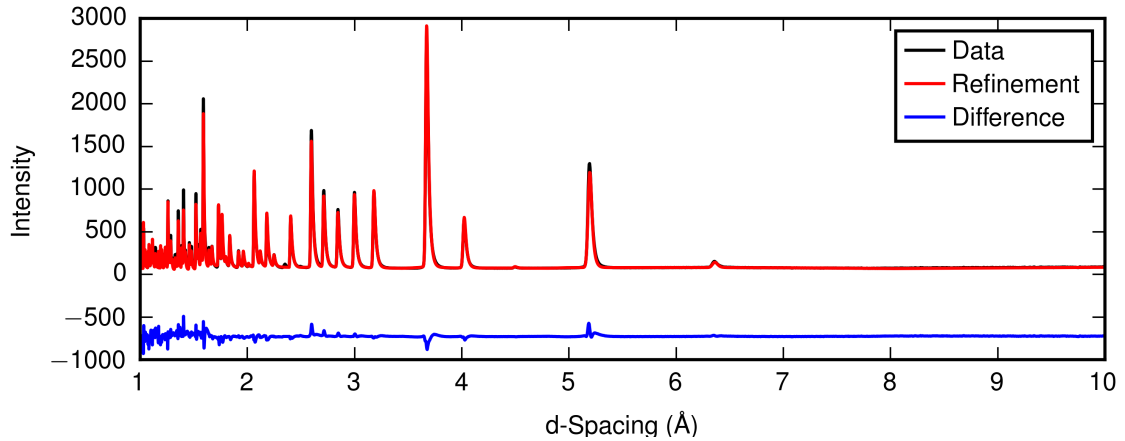
Figure 6.23: Neutron powder diffraction from Cu_2OSeO_3 taken on Wish at 60 K in zero field, $tth = 90°$. The crystallographic parameters from this model are shown in table 6.2.

thermal, and background parameters.

The result of this is shown in figure 6.26 with a fitted copper moment of 0.924 $\mu_B/Cu \pm 0.025$. This is larger than the value of 0.615 μ_B/Cu derived by Bos *et al.*. Our value is more consistent with the magnetisation data which predicts a moment of 1.06 $\mu_B/Cu \pm 0.006$ with the ferrimagnetic structure.

6.5.9 The Magnetic Ground State

A 20 K pattern was then taken in zero field to investigate the helical phase. Differences in the powder pattern were observed between this and the 60 K data, as shown in figure 6.27. The difference patterns are shown in figure 6.28. There are clear differences between these patterns and the ferrimagnetic phase. The magnetic reflections are much weaker than in the ferrimagnetic phase and a peak can be observed at the $(1, 0, 0)$ position corresponding to a d-spacing of ~ 8.9 Å that was not observed in the other phases, as shown in figure 6.29. At the $(1, 1, 1)$ position (~ 5.2 Å) the satellite peaks are clearly resolved in the difference pattern. The presence of a magnetic peak at the $(1, 0, 0)$ position is not consistent with a simple helical rotation of the moments of the ferrimagnetic structure as the structure factor for this remains zero. This suggests that the magnetic structure is more complicated in the helical phase than previously thought. Further it rules out that the $(1, 0, 0)$ satellites observed in the x-ray data are an anomaly originating due to the ATS

Figure 6.24: Neutron powder diffraction from Cu_2OSeO_3 taken on Wish. The black line is the data taken at 60 K in zero field and the red line is data taken at 20 K and 0.12 mT.

Figure 6.25: Neutron powder diffraction from Cu_2OSeO_3 taken on Wish. The black line is the difference between data taken at 60 K in zero field and 20 K and 0.12 mT.

Figure 6.26: Neutron powder diffraction from Cu_2OSeO_3 taken on Wish in the ferrimagnetic phase at 20 K and 0.12 mT, $tth = 27.1°$.

scattering. A small structural change would not produce the observed result of a $(1, 0, 0)$ peak in the helical but no peak in the ferrimagnetic phase.

One possible candidate structure was introduced in figure 6.18. These two structures are shown again in figure 6.30, the structures are labelled with the coupling between moments on the $4a$ and $12b$ sites respectively and are labelled F/F and AF/AF. The magnetic structures shown in these figures display only the local coupling and the moments are still long period helical.

We shall now compare these models with the neutron powder data. The optimal detector banks for determining the magnetic structure are at $2\theta = 27, 58, 90°$ where the main magnetic reflections are still visible and the highest resolution is offered.

Fullprof was used to fit the nuclear and ferrimagnetic patterns, however, it encountered problems fitting the very short wavevector magnetic models. Patterns can still be predicted but require a sub-optimal peak-shape. As a result the Rietveld refinement is sub-optimal and results should be considered somewhat qualitatively.

Data compared to refined models are shown in figures 6.31 and 6.32 with the refinements in figure 6.31 having a freely varying moment magnitude and the moments in figure 6.32 having a moment size of 0.924 μ_B/Cu from the refinement in the ferrimagnetic phase. Refinement parameters for each model are shown in table 6.3. Model (1) of the F/F structure proposed by Bos *et al.* produces very similar results to theirs with a reduced refined moment. The refined moment of 0.772 μ_B/Cu is below that refined in the ferrimagnetic phase and is not consistent with
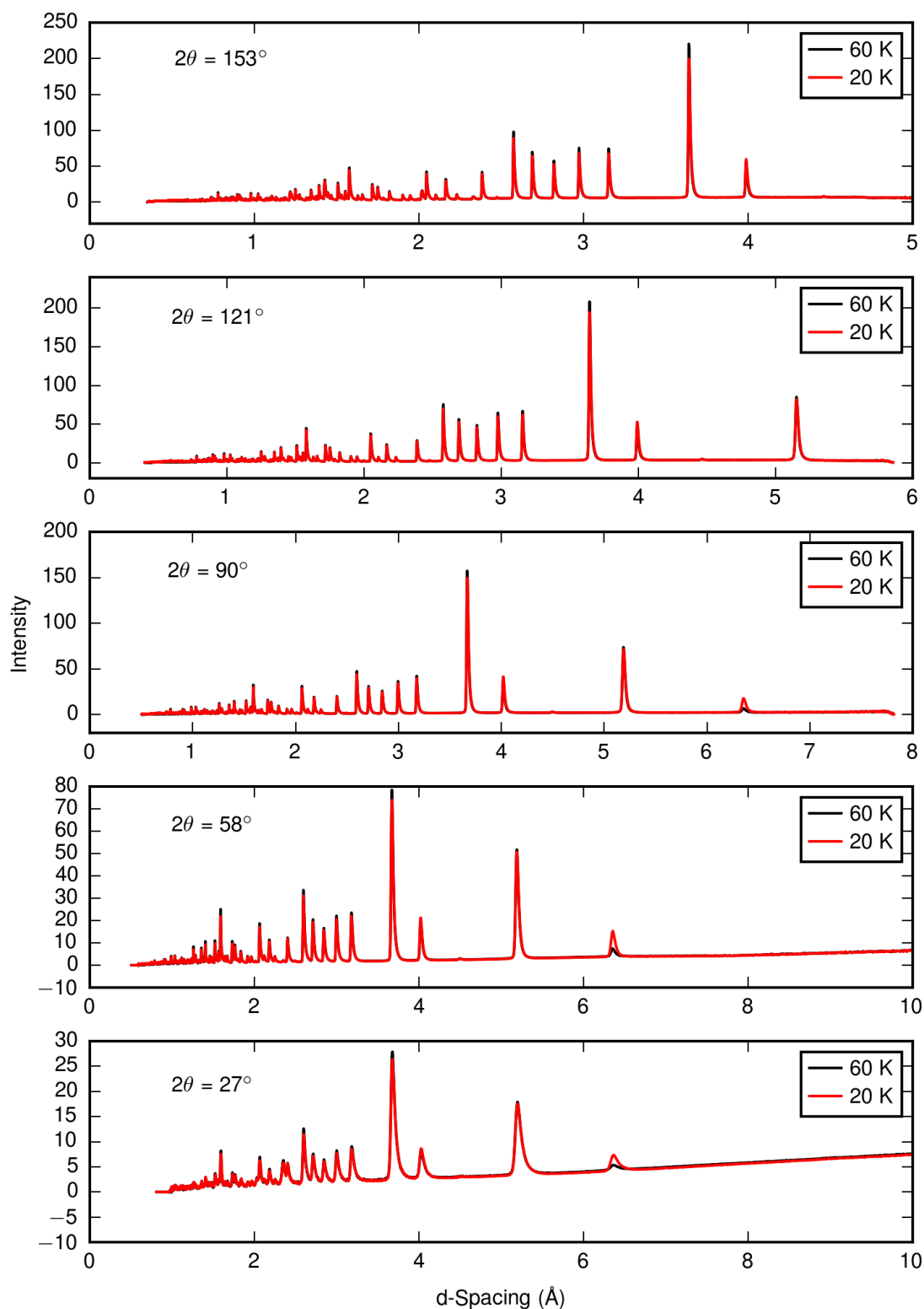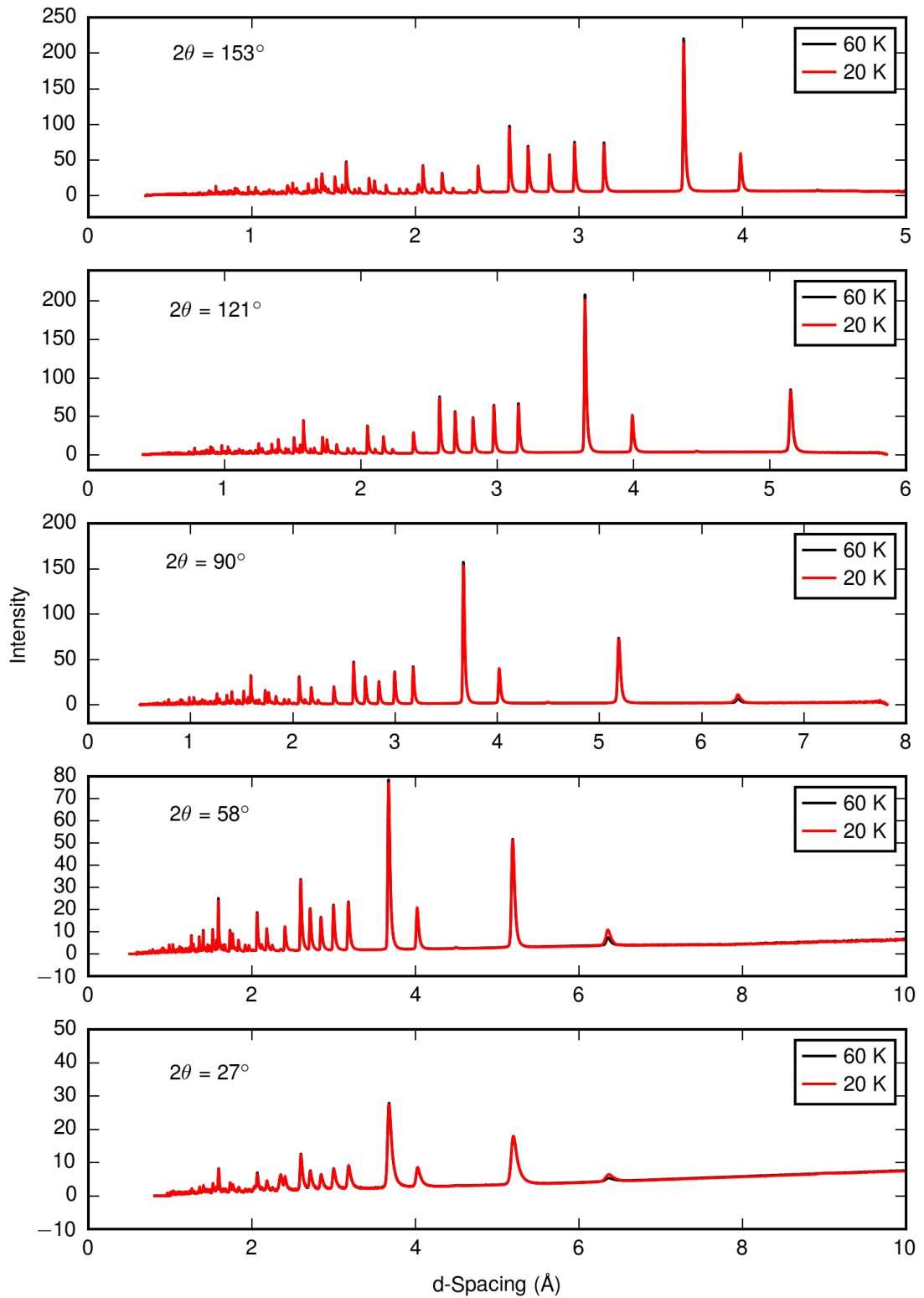
Figure 6.27: Neutron powder diffraction from Cu_2OSeO_3 taken on Wish. The black line is the data taken at 60 K and the red line is data taken at 20 K in zero field.
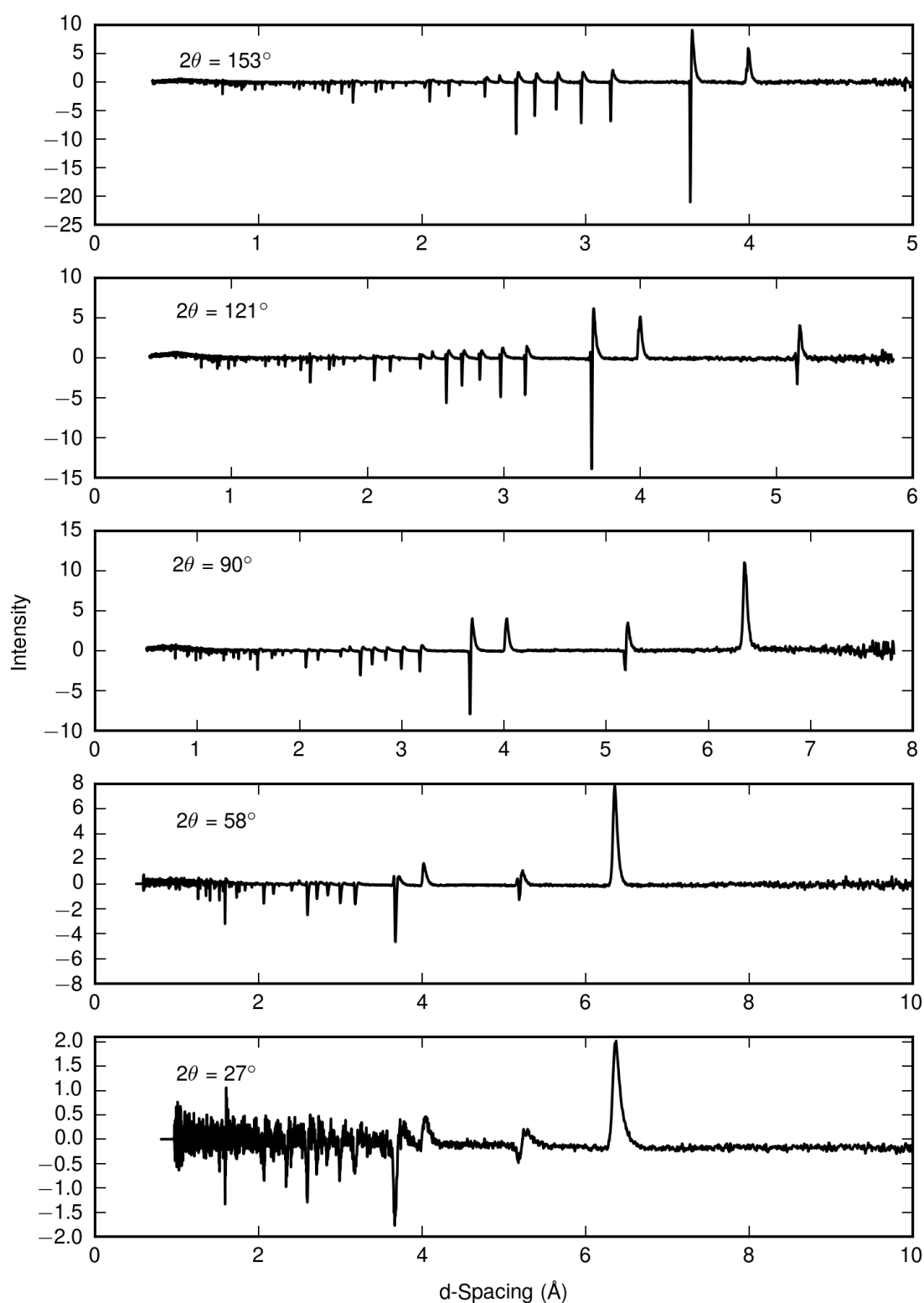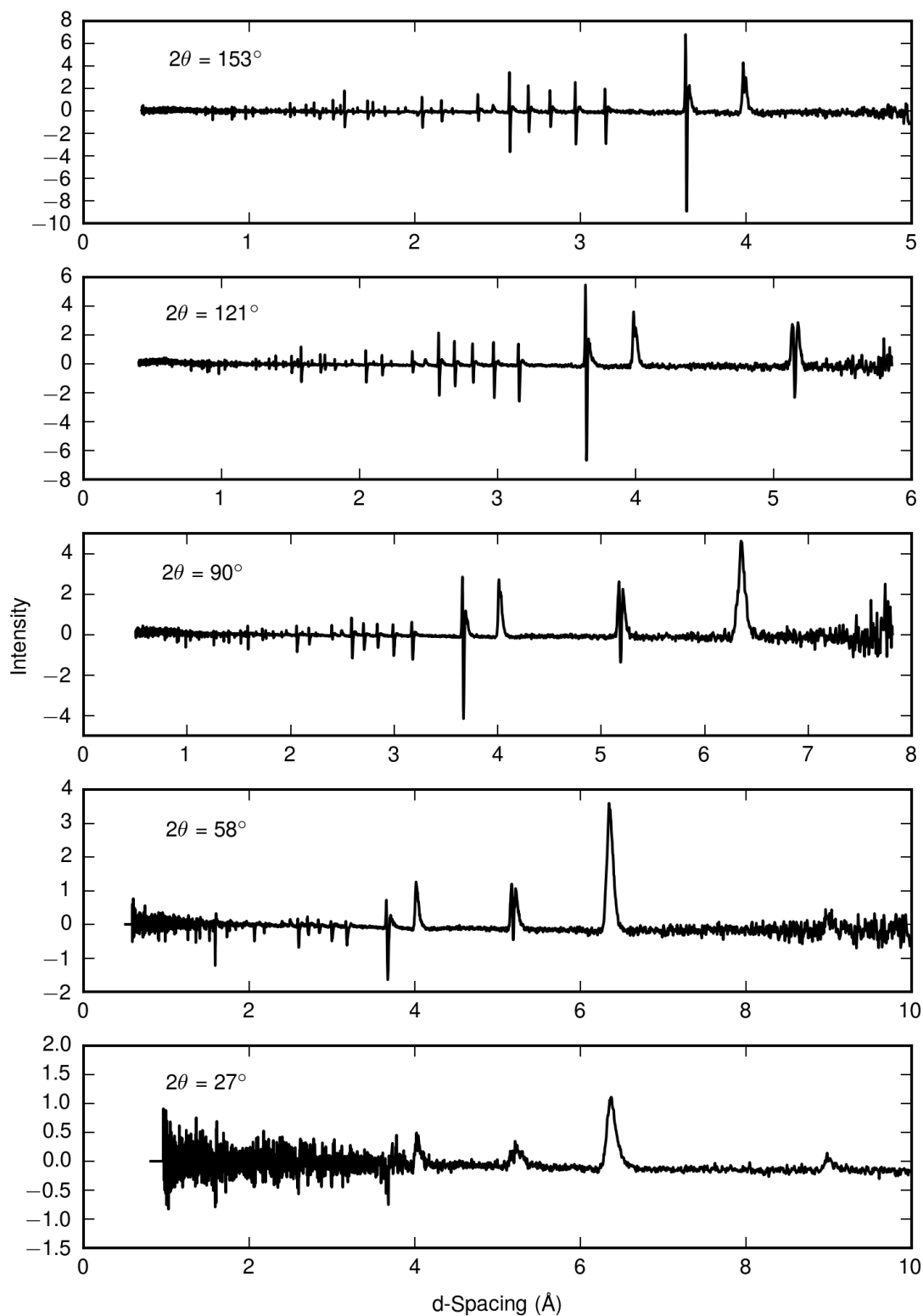
Figure 6.28: Neutron powder diffraction from Cu_2OSeO_3 taken on Wish. The black line is the difference between data taken at 60 K and 20 K in zero field.
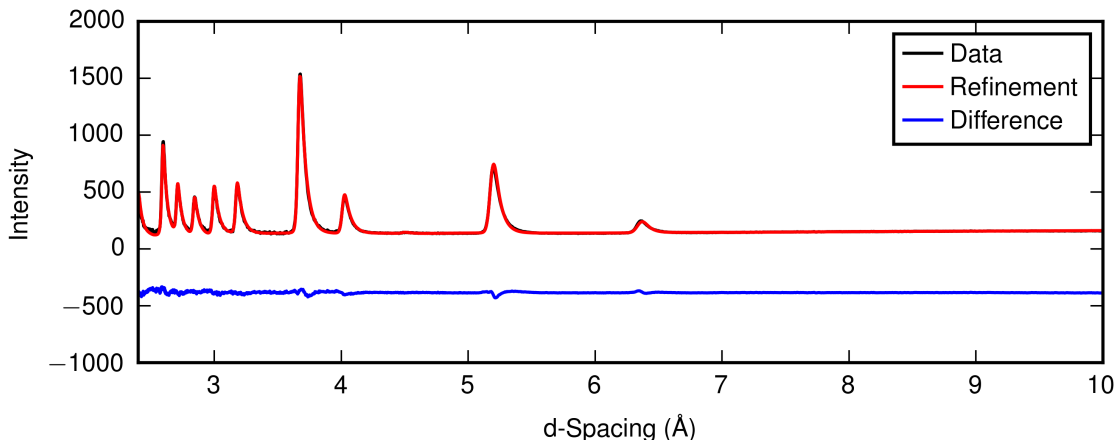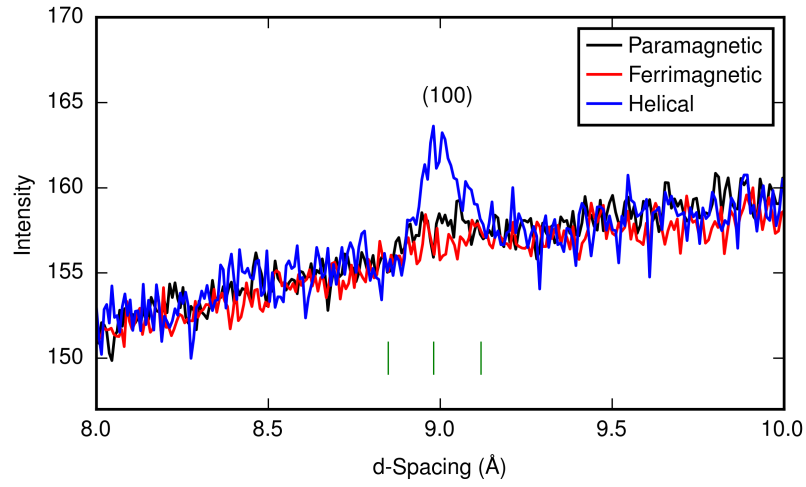
Figure 6.29: Neutron powder diffraction from Cu_2OSeO_3 taken on Wish in the paramagnetic, ferrimagnetic, and helical phases. A peak at the $(1,0,0)$ position is only observed in the helical phase.

Table 6.3: Goodness of fit parameters for different magnetic models for the ground state. A * denotes that the moment is fixed.

Model No.	Model	Moment	$R_p\%$	$wR_p\%$	$R_{exp}\%$	χ^2
(1)	F/F	0.772	10.2	9.4	3.9	5.8
(2)	F/F	0.924*	10.9	10.5	3.9	7.2
(3)	AF/AF	0.519	11.4	12.6	4.0	10.1
(4)	AF/AF	0.924*	14.3	28.1	3.9	50.7
(5)	F/AF-	0.933	9.5	8.4	3.9	4.6
(6)	F/AF-	0.924*	9.5	8.4	3.9	4.6
(7)	F/AF+	1.002	8.7	7.6	3.9	3.7
(8)	F/AF+	0.924*	8.7	7.6	3.9	3.7
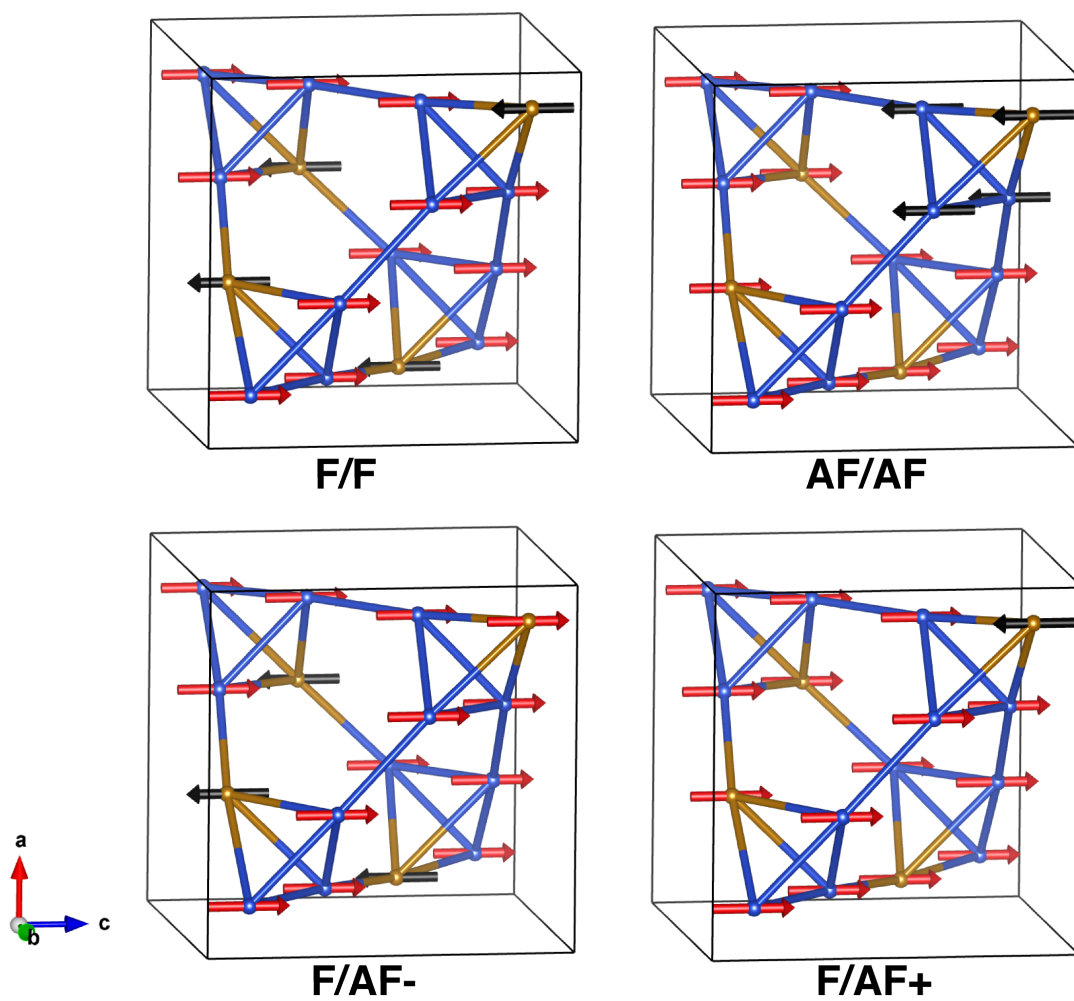
Figure 6.30: Nuclear unit cell arrangement with different magnetic structures refined using the Neutron Powder pattern from the helical phase.
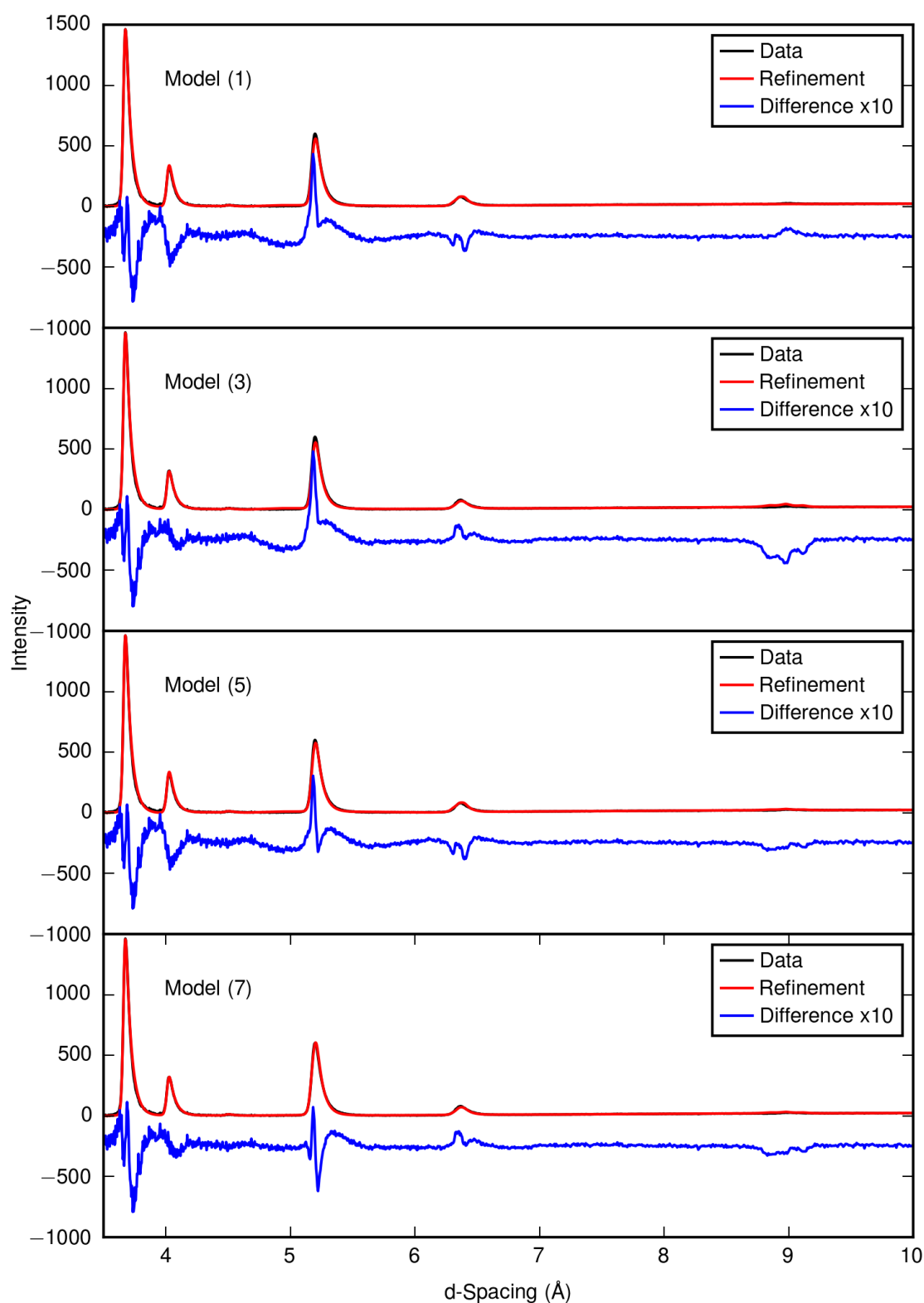
Figure 6.31: Neutron powder diffraction from Cu_2OSeO_3 taken on Wish at 20 K in zero field. Each panel displays refinements for different models with model parameters shown in table 6.3.
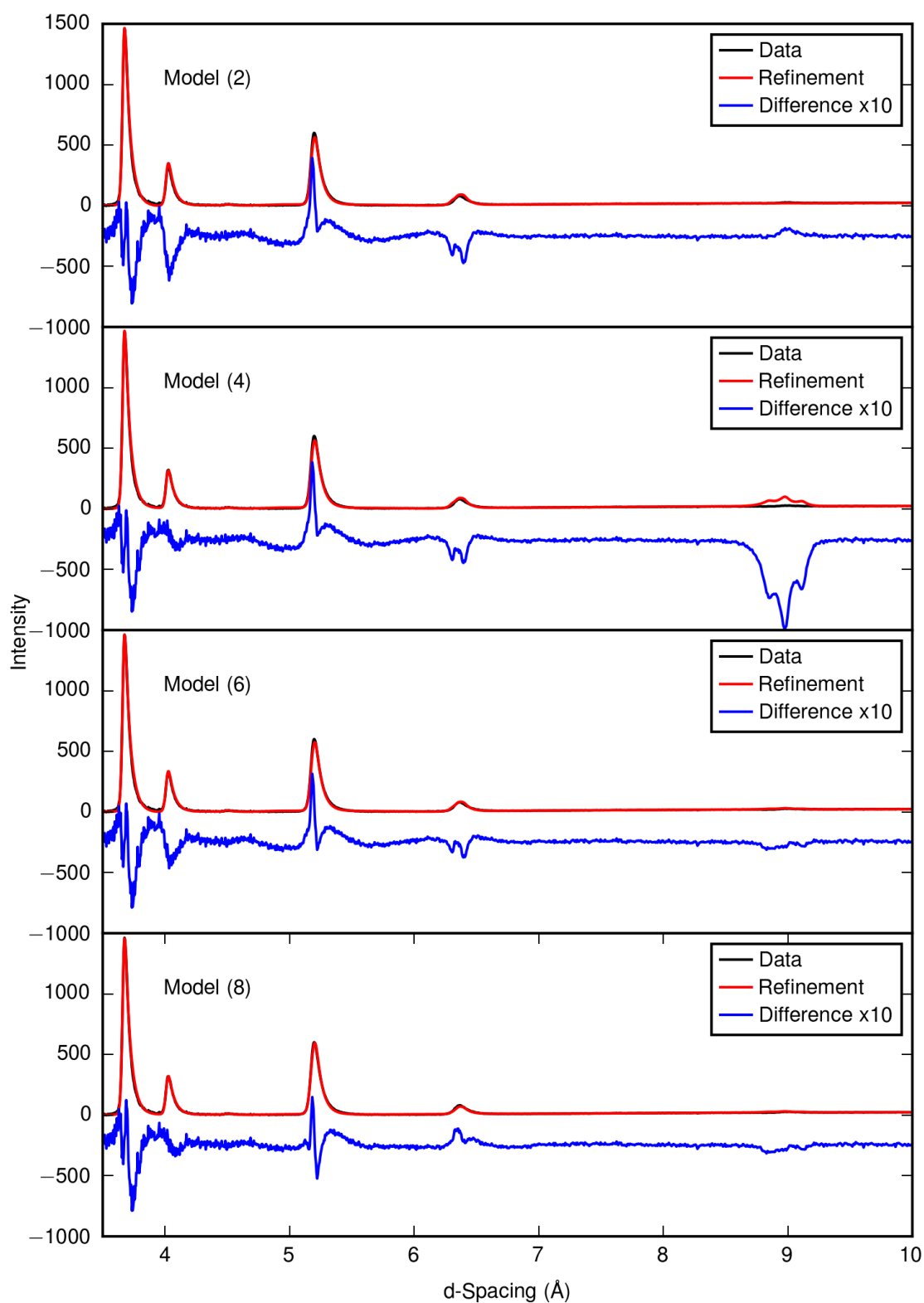
Figure 6.32: Neutron powder diffraction from Cu_2OSeO_3 taken on Wish at 20 K in zero field. Each panel displays refinements for different models with model parameters shown in table 6.3. In these refinements the moment size is fixed to that refined in the ferrimagnetic phase.

the magnetisation measurements. The F/AF models (3) and (4) produce too much intensity at the $(1, 0, 0)$ position and inferior fits to the original F/F ferrimagnetic model. Two more reduced ferrimagnetic models were considered, labelled F/AF- and F/AF+, and show in the bottom half of figure 6.30. These models have no antiferromagnetic moments on the $12b$ site, the fewer antiferromagnetic moments in these models will reduce the intensity at the $(1, 0, 0)$ position from the AF/AF structure. The - and + in the labels denote whether the majority of the moments on the $4a$ site are aligned (+) or anti-aligned (-) with those of the $12b$ site.

With freely varying moment sizes in models (5) and (7) the refined moment sizes are much more comparable to the magnetisation data and the refined moment from the ferrimagnetic phase. Both models display significant improvements over the F/F fixed moment model. With moment values fixed to the ferrimagnetic phase refined value of $0.924\ \mu_B/Cu$ the refinements are not significantly affected.

Model (8), the F/AF+ model best fits the results. It is not consistent with the saturation magnetisation and the three up one down structure expected. This structure requires a change in the local magnetic coupling, however, as all the copper moments are actually magnetically frustrated this change is therefore not unfeasible, a spin flop transition is now required between the helical and ferrimagnetic phases. The magnetic frustration is realised as each Cu I has six Cu II nearest neighbours, three with expected antiferromagnetic, and three with expected ferromagnetic coupling (from the Kanamori-Goodenough rules[13]). Further, each Cu II has two Cu I nearest neighbours, one with expected antiferromagnetic, and one with expected ferromagnetic coupling, as well as four Cu II nearest neighbours, two with expected ferromagnetic, and two with expected antiferromagnetic coupling.

Therefore the reduced ferrimagnetic arrangement observed may be minimised in energy when an external field is applied. This change of structure from the helical to the ferrimagnetic phase may be another cause for the hysteresis observed through the conical phase in the magnetisation data.

---

[13]Ferromagnetic coupling is expected where there are edge sharing polyhedra and antiferromagnetic coupling is expected with corner sharing polyhedra.

6.5.10   Polarisation Analysis of X-ray Satellite Peaks

Full polarisation analysis measurements were then taken in the helical, conical, and skyrmion phases. All polarisation dependences were measured at the same position so that a direct comparison between the different phases can be drawn. This required a rotation of the field by 90° between the conical and skyrmion measurements. The $(1, -\tau, 0)$ peak (with $(0, -1, 0)$ in the beam direction) was chosen to be measured largely due to technical constraints[14].

Helical Phase

In addition to the $(1, -\tau, 0)$ reflection the $(1 + \tau, 0, 0)$ peak was also measured in the helical phase at 0 T and 14 K. All of the satellite peaks are in close proximity to the ATS peak. This is especially relevant for the $(1 + \tau, 0, 0)$ peak as it sits on the crystal truncation rod from the ATS peak. As such measurements were also taken initially either side of the peak to account for the background from the crystal transaction rod, these were stopped when it became apparent that the polarisation dependence of the background and the peak were identical. The polarisation dependence for the helical phase at these two reflections is shown in figure 6.33, the solid lines represent the expected polarisation dependences for a helical model. The polarisation dependence of the $(1, -\tau, 0)$ satellite has a roughly similar P_1 dependence to the $(1 + \tau, 0, 0)$ and the ATS peak, however, the P_2 dependence is flipped confirming that there is no contamination from the ATS peak. There is little to no correlation between the helical model and the data for either peak. Possibly the most notable feature is the complete lack of any P_3 dependence in the data which as explained in chapter 4 is inherent in all non-collinear structures as it is produced on a mathematical level by the introduction of imaginary elements in the scattering

---

[14]Due to the close proximity of the satellites to the $(1, 0, 0)$ peak the slit width allowed intensity from the central peak into the detector when peaks at $(1, 0, \tau)$ are measured. $(1 \pm \tau, 0, 0)$ peaks are on a background from the crystal truncation rod. A technical detail of the experimental equipment allows intensity from the central peak to the detector when $(1, \tau, 0)$ peaks are measured. This is because the slits are a fixed piece of metal with different sized slots cut in them which can be moved vertically through the beam. When the $(1, \tau, 0)$ peak goes through the main slits the $(1, 0, 0)$ peak is able to get through another set of slits and be incident on the detector.

Figure 6.33: Full polarisation analysis measurements of the (top) $(1 + \tau, 0, 0)$ and (bottom) $(1, -\tau, 0)$ superlattice reflections. Solid lines show simulations for a helical magnetic structure.

matrix. The imaginary numbers come about due to a phase shift in the moments which will produce a non-collinear structure. There is very strong evidence for a helical structure in the related systems such as MnSi [154, 155]. There is direct evidence of the helical structure from Lorentz transmission electron microscopy [112] with further direct observations from spin-polarised tunnelling electron microscopy in related systems [156]. The direct observations with LTEM, it could be argued, are not representative due to the sample having to be thinned before measurement and this has been shown to have a large effect on the phase diagram. The SP-STM does not require the thinning of the sample, however, to date these measurements have not been carried out on the Cu_2OSeO_3 system.

One novel possibility that would allow for magnetic intensity is that the rotation

Figure 6.34: Full polarisation analysis measurements of the (top) $(1 + \tau, 0, 0)$ and (bottom) $(1, -\tau, 0)$ superlattice reflections. Solid lines show simulations for a helical magnetic structure with counter rotating spins.

sense of the helix is opposite for the moments found to be antiferromagnetic from the neutron data. These counter rotating helices are described (for the $(1 + \tau, 0, 0)$ reflection) by the vectors $(0, 1, i)$, and $(0, -1, i)$, the imaginary parts will then cancel with the structure factor and the polarisation dependence would appear to be collinear[15], this will result in no P_3 dependence, as observed in the data. The results of these models are shown in figure 6.34. As expected there is no P_3 dependence to this model, however, it does not reproduce the data. Second order electric dipole (E1) scattering, electric quadrupole scattering (E2) and birefringence are other factors which we will now consider. Second-order dipole scattering could play a role if there is a ferromagnetic component to the helices and so they are, in-fact, con-

---

[15]This will only occur due to the forbidden nature of the $(1, 0, 0)$ reflection.

ical structures. The matrix for this will only produce intensity at the τ satellite instead of the 2τ position when the ferromagnetic component is multiplied by an antiferromagnetic component. The second order matrix can therefore immediately be reduced to:

$$\mathbf{M} = \begin{pmatrix} 0 & -z_2(z_1 sin\theta - z_3 cos\theta) \\ z_2(z_1 sin\theta + z_3 cos\theta) & 0 \end{pmatrix}. \qquad (6.24)$$

For the $(1 + \tau, 0, 0)$ and $(1, \tau, 0)$ reflections these are further reduced to:

$$\mathbf{M} = \begin{pmatrix} 0 & z_2 z_3 cos\theta \\ z_2 z_3 cos\theta & 0 \end{pmatrix}, \text{ and } \mathbf{M} = \begin{pmatrix} 0 & -z_2 z_1 sin\theta \\ z_2 z_1 sin\theta & 0 \end{pmatrix}. \qquad (6.25)$$

The results of this are shown in figure 6.35. It can be seen that this model fits the $(1 + \tau, 0, 0)$ data well but does not fit the $(1, \tau, 0)$ perfectly although the shapes are somewhat similar. A deviation like this might be expected to relate to the azimuth, however, this will only affect the intensity of the reflections and not the shape of the polarisation dependence, as the matrices involved will retain the same basic shape. Although this does reproduce the data reasonably and a conical nature of the structure could be explained by the external magnetic field which on I10 is produced by permanent magnets where the minimum field is around 6.5 mT. Further this polarisation dependence would require a large disparity in the resonant scattering pre-factors such that the second order matrix dominates.

Quadrupolar scattering has been observed in non-centrosymmetric systems at positions where E1 scattering is disallowed [157], it is usually coexistent with a double peak feature in the energy resonance. This is not observed so a quadrupolar effect can be disregarded, further the sigma-sigma channel from quadrupolar scattering is non-zero and a deviation from 0 and -1 at $\psi = 0$ is expected for quadrupolar scattering. The σ-σ channel has a $\tan 2\theta$ term which as the scattering angle is close to 90 would be expected to dominate for this process.

The case for x-ray birefringence playing a role is potentially much stronger. The seminal paper on x-ray birefringence was on copper oxide [100] which is expected to have a large birefringence as Cu^{2+} is in the d^9 state so only has one hole. In an octahedral crystal field this would either reside in the $3z^2 - r^2$ or the $x^2 - y^2$ orbital and limit the absorption of the x-rays to certain polarisations aligned with these orbital shapes. The theory for the polarisation dependence of resonant x-ray
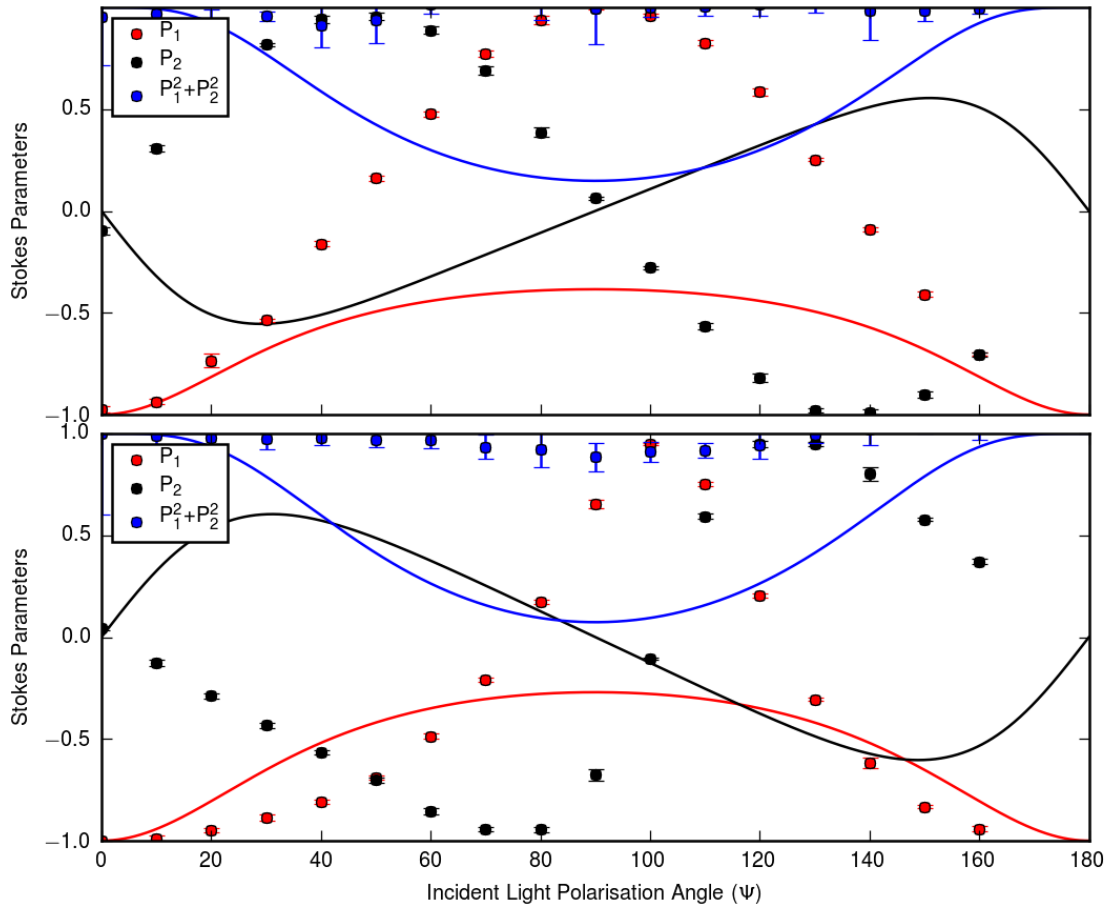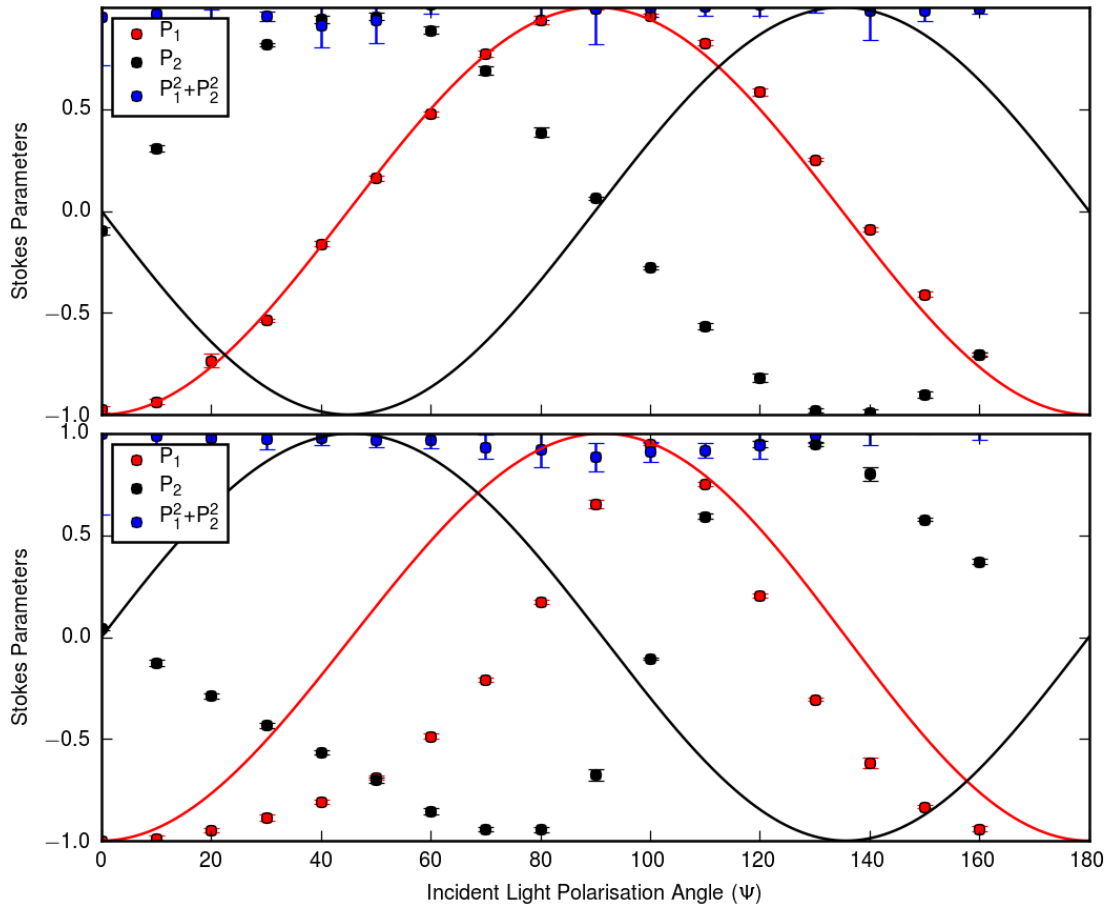
Figure 6.35: Full polarisation analysis measurements of the (top) $(1 + \tau, 0, 0)$ and (bottom) $(1, -\tau, 0)$ superlattice reflections. Solid lines show simulations for a conical magnetic structure with a second order scattering matrix.
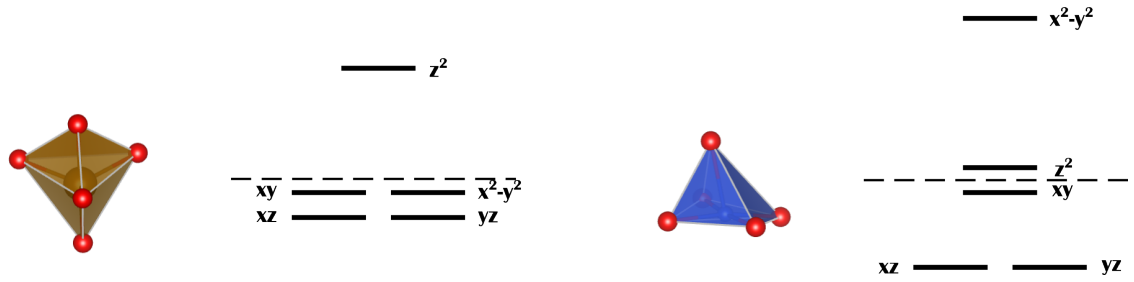
Figure 6.36: Ligand arrangements for the different copper sites. The energy level diagrams correspond to undistorted trigonal bipyramidal and square based pyramid structures

scattering requires that the intermediate state be able to absorb all polarisations of x-rays. This would complicate the calculations somewhat as the two copper sites have different ligand fields. An energy level diagram for the different arrangements is shown in figure 6.36.

One major argument that there is a lack of birefringent effects is that the ATS peak fits perfectly with theory, with the incident polarisation always being rotated by 90 degrees. The satellite peaks which are in very close proximity would be expected to show similar but not identical birefringent effects[16]. Again considering the polarisation dependences the problem really is much more deep rooted as any inclusion of the helical model will produce an imaginary component within the scattering matrix which will produce a deviation from $P_1^2 + P_2^2 = 1$ which is not observed (other than with the already considered counter rotating helical model).

We will fit the data with a general model to see what moment would be expected from this full polarisation analysis. It is found that the data can be reproduced with a simple matrix with real components as follows:

$$\mathbf{M} = \begin{pmatrix} 0 & 1 \\ 1 & 0 \end{pmatrix}, \tag{6.26}$$

$$\mathbf{M} = \begin{pmatrix} 0 & -0.46 \\ 1 & 0.204 \end{pmatrix}. \tag{6.27}$$

---

[16]The birefringent effects would not be the same on the scattered ray as for the different peaks these would have different polarisations. So any birefringence could transform the scattered beam differently.
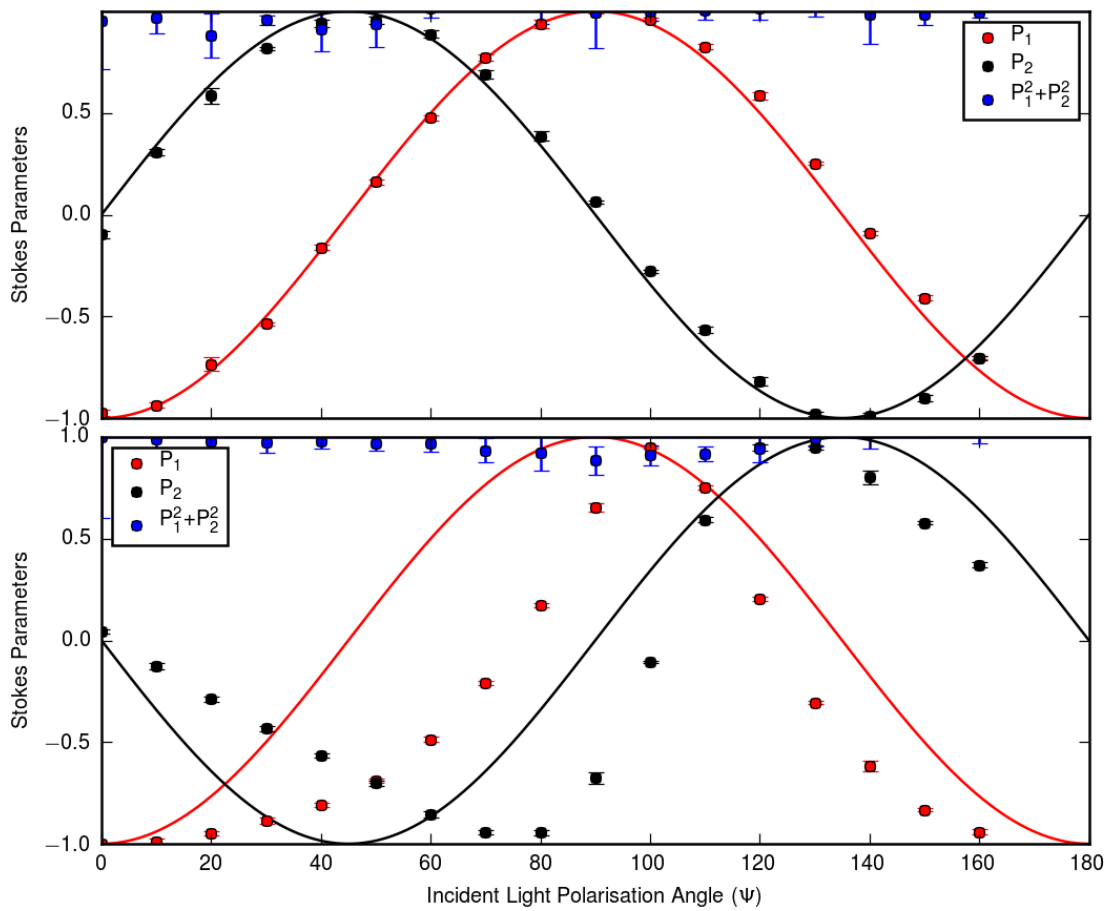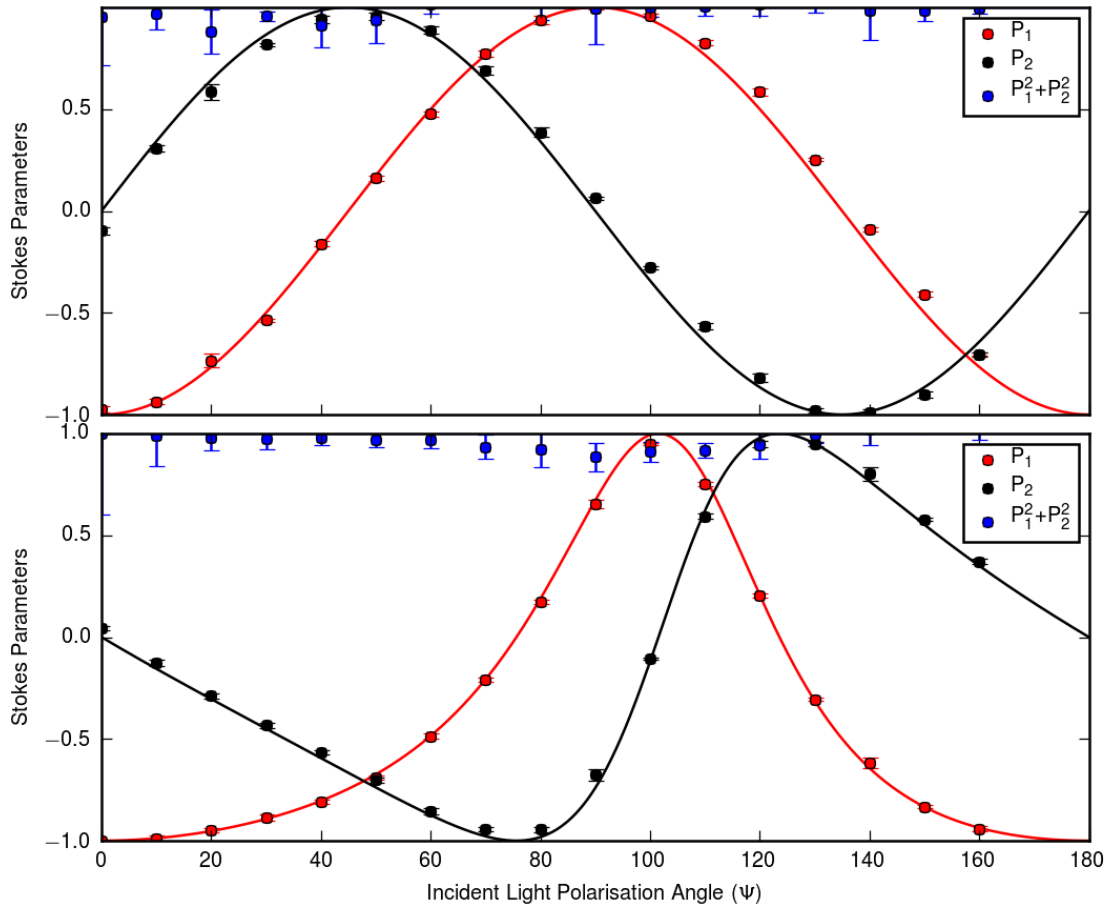
Figure 6.37: Full polarisation analysis measurements at 901.8 eV and 12 K of the (top) $(1+\tau, 0, 0)$ and (bottom) $(1, -\tau, 0)$ superlattice reflections. Solid lines in top and bottom graphs show simulations from the scattering matrices $\mathbf{M} = \begin{pmatrix} 0 & 1 \\ 1 & 0 \end{pmatrix}$, and $\mathbf{M} = \begin{pmatrix} 0 & -0.46 \\ 1 & 0.204 \end{pmatrix}$ respectively.
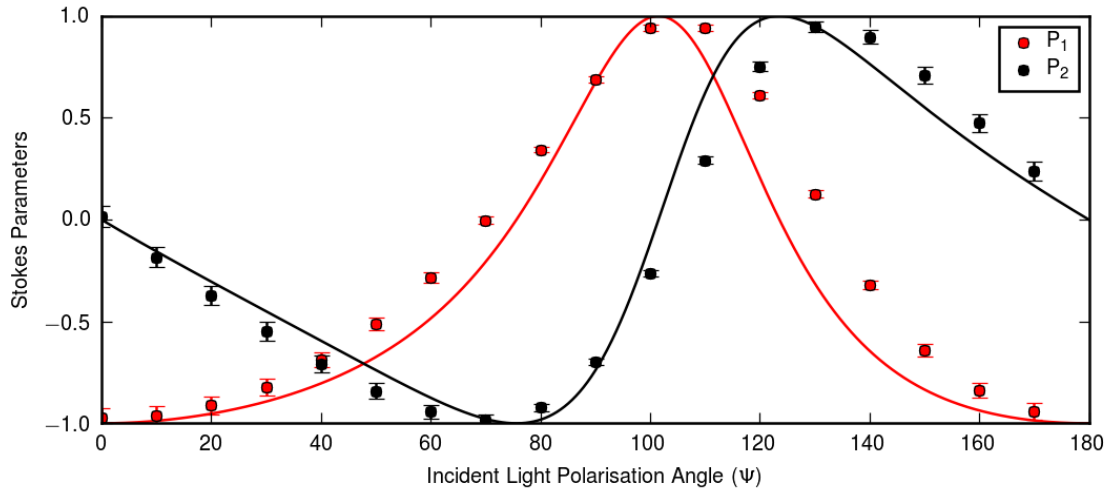
Figure 6.38: Full polarisation analysis measurements of the $(1, -\tau, 0)$ superlattice reflection in the conical phase at 901.5 eV, 50 K, and 21.5 mT. Solid lines again show simulations from the scattering matrix $\mathbf{M} = \begin{pmatrix} 0 & -0.46 \\ 1 & 0.204 \end{pmatrix}$.

These matrices correspond to moments pointing roughly along the propagation vectors $(1, 0, 0)$ and $(0, 1, 0)$.

The component in the $\pi - \pi$ channel comes from the $(1, 0, 0)$ peak no longer being along the scattering vector and the inequivalent $\sigma - \pi$ and $\pi - \sigma$ elements are due to a slight azimuthal rotation of the structure. This model corresponds to a long period spin density wave with the moment pointing along the scattering vector.

Conical and Skyrmion Phases

Full polarisation measurements were also taken in the conical phase at 50 K, shown in figure 6.38. The field was rotated to be perpendicular to the sample so that the peak is measured at the same $(1, \tau, 0)$ position for all other magnetic phases. A 21.5 mT field was applied so such that the field did not have to be adjusted between the conical and skyrmion phases. The skyrmion phase was measured in the same field but at 57.5 K. The results of the conical phase shown in figure 6.38 are fitted to the same model as the helical phase. Some deviations can be noted between the model and the data. This is likely due to the peak position changing and the alignment of the field not being perfectly along the $(0, 1, 0)$ direction. There are however, no major deviations from the helical model and a similar pattern is observed. It is
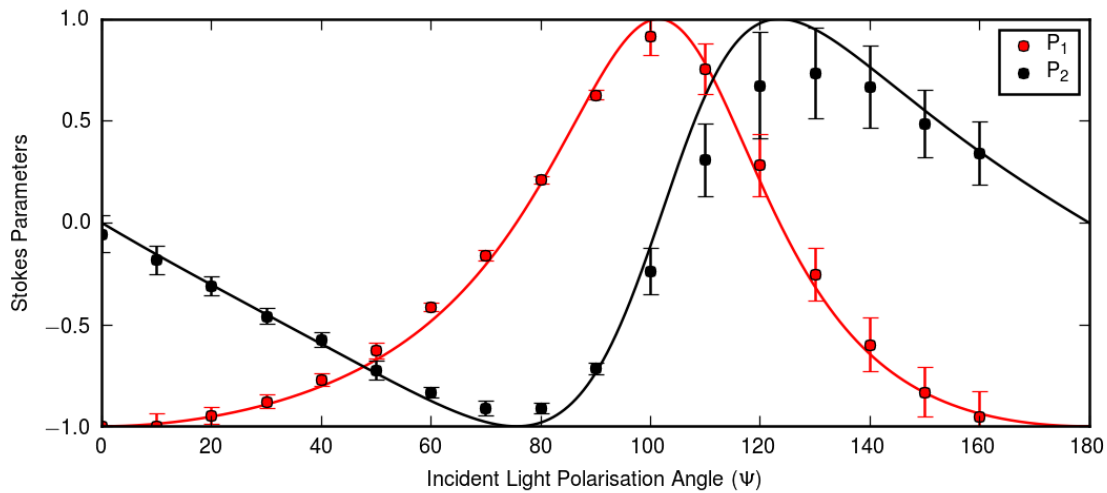
Figure 6.39: Full polarisation analysis measurements of the $(1, -\tau, 0)$ superlattice reflection in the skyrmion phase at 901.5 eV, 57.5 K, and 21.5 mT. Solid lines again show simulations from the scattering matrix $\mathbf{M} = \begin{pmatrix} 0 & -0.46 \\ 1 & 0.204 \end{pmatrix}$.

therefore expected that a similar model of moments oriented along the scattering vector satisfies the data. The skyrmion phase showed a similar result, with data and the same model as the helical phase shown in figure 6.39. The error bars here are quite large as the peak is much weaker than in the other phases, however, the previous model fits well to within the error bars.

These polarisation dependences are far from expected. All the polarisation dependences of the three phases can be fitted to the same model. It can therefore be supposed that the skyrmion phase is very similar to the helical phase, and that the skyrmion phase is similar to the convolution of three of the magnetic structures from the helical phase, it is this that can be approximated to a skyrmion.

6.5.11 Spin Density Wave

We shall now consider the physical possibility of the long spin density wave structure and it's implications. Long spin density waves of this nature are novel but have been observed in other systems such as $Ca_3Co_2O_6$ [158]. This is possible as there are multiple exchange interactions which are present in the crystal which occur *via* different intermediate oxygens. In Cu_2OSeO_3 there are two oxygen ligands between

each of the 12b site copper atoms which will largely cancel the DM interaction, however, a large DM interaction is expected and predicted between the 12b and 4a sites [153]. Currently the only direct evidence for the helical structure is from LTEM measurements. LTEM is only sensitive to moments in the plane and could produce images similar to those observed in the helical and conical regions of the phase diagram. However, the moment is pointing perpendicular to the direction expected for these cases. As only the in-plane moment direction can be measured in the 6-fold region, a pattern that would resemble a Néel wall type skyrmion with $\gamma = 0, \pi$ case from figure 6.2 would be expected for this spin density wave. A vortex like pattern could still be observed but the moments would point towards the centre of the skyrmion and not perpendicular to it.

Magnetisation measurements of a helical structure would be expected to be quite different from that of a long spin density wave. Magnetisation measurements of the long spin density wave structure of $Ca_3Co_2O_6$ show strong step like features where the magnetisation is relatively constant until a magnetic transition is induced and then staying constant again [159]. This is not observed in the magnetisation data collected on this sample, which is consistent with the helical structures.

6.5.12   Satellites Around Forbidden Reflections

This is not the first case where satellite reflections around forbidden reflections have shown unexpected polarisation dependences. The most relevant case is in the thesis of Thomas Frawley [160], and published here [109]. Here FeAs was investigated which adopts an incommensurate helical magnetic structure below 77 K with a propagation vector $(0, 0, 0.389)$ and a similar sized ordered moment to Cu_2OSeO_3 of 0.5 μ_B. In this study full polarisation analysis measurements were taken at $(0, 0, \tau)$ and $(0, 0, 1 - \tau)$ at the Fe L-edges as well as azimuthal measurements at the $(0, 0, 2 - \tau)$ and $(1, 0, 3 - \tau)$ reflections at the Fe K-edge.

The $(1, 0, 3 - \tau)$ azimuthal measurement was not ideal due to a large angle between the surface and the reflection but qualitatively fitted with the same model as the $(0, 0, \tau)$ and $(0, 0, 2 - \tau)$ reflections. The fitted model was a distorted helix, with an elliptical structure which is further rotated so that the major axis points roughly 21° away from the a-axis.
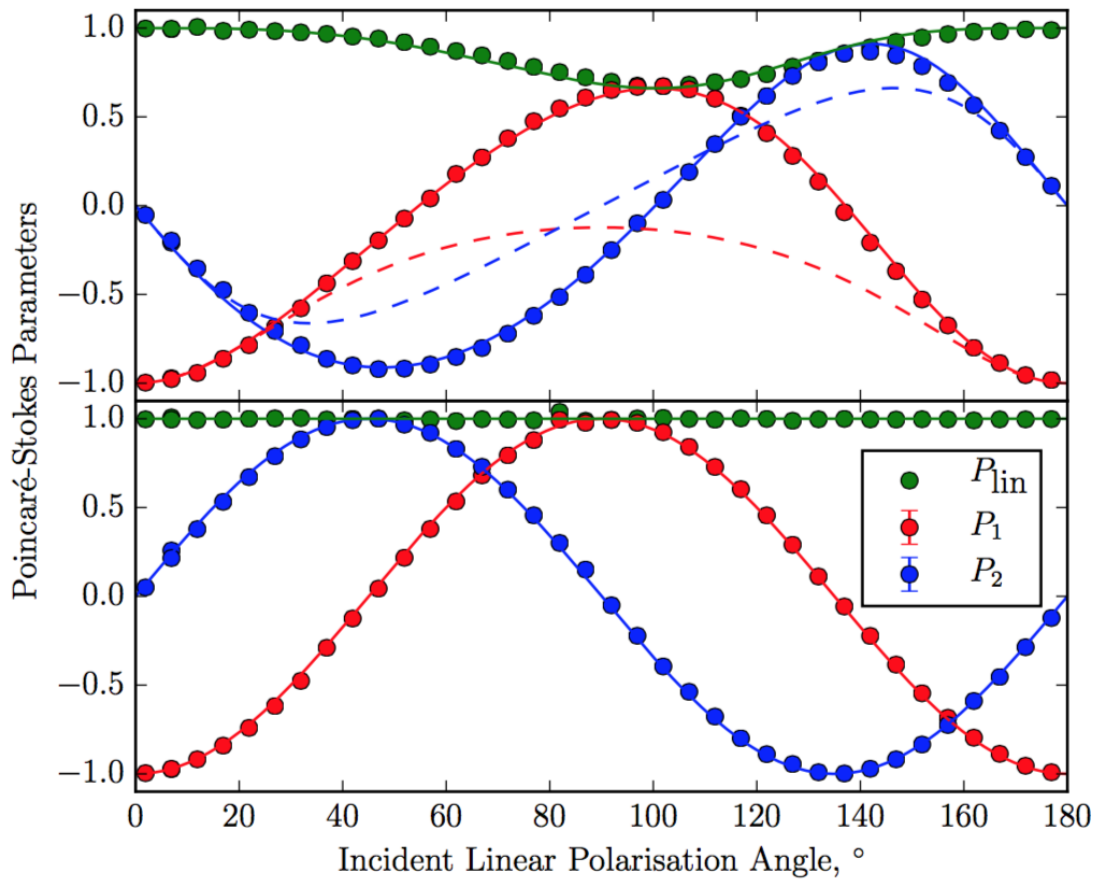
Figure 6.40: (top) Full polarisation analysis measurements of the $(0, 0, \tau)$ reflection in FeAs at the Fe L_{III} edge. (bottom) Full polarisation analysis measurements of the $(0, 0, 1 - \tau)$ reflection in FeAs at the Fe L_{III} edge. Figure taken from [160].

The full polarisation analysis measurements of the $(0, 0, 1 - \tau)$ do not fit with this model. In FeAs the $(0, 0, 1)$ reflection is outside the Ewald sphere at the Fe L-edges, however, it is a forbidden reflection in the $Pnma$ space group but would be expected to exist on resonance as an ATS reflection due to the glide plane extinction in a similar situation to Cu_2OSeO_3. Further the polarisation dependence of this forbidden reflection would be expected to be identical to the $(1, 0, 0)$ in Cu_2OSeO_3 just rotating the incident light by 90°. The polarisation dependence of the $(0, 0, 1 - \tau)$ peak in FeAs and the $(1 + \tau, 0, 0)$ peak in Cu_2OSeO_3 are identical. The full polarisation analysis measurements from FeAs are reproduced in figure 6.40.

6.6   Summary

We have measured samples of Cu_2OSeO_3 using resonant x-ray as well as neutron powder and single crystal diffraction with the aim of determining any peculiarities in the magnetic structure of the helical, conical, and skyrmion phases.

A $(1,0,0)$ reflection has been observed in neutron powder diffraction data in the helical ground state, this is not consistent with the magnetic ground state having the one up three down magnetic structure. The $(1,0,0)$ reflection disappears upon entering the ferrimagnetic phase and Rietveld refinement fits the pattern well with a moment size of 0.924 $\mu_B/Cu \pm 0.05$.

The helical ground state fits best with a structure where all the moments are ferromagnetic apart from one of the $4a$ moments which is antiferromagnetically aligned. The refined moment was consistent with that determined by magnetisation measurements of ~ 1 μ_B. Magnetisation measurements were consistent with those taken previously with a paramagnetic moment determined as 1.50 $\mu_B/Cu \pm 0.009$ but with a saturation moment of 0.527 $\mu_B/Cu \pm 0.003$ below the magnetic transition. This is consistent with the three up one down ferrimagnetic structure and an ordered moment size of 1.06 $\mu_B/Cu \pm 0.006$.

We have determined that the resonant reflection at the structurally forbidden $(1,0,0)$ position visible at all temperatures is allowed due to the anisotropy of the tensor of x-ray susceptibility (ATS). ATS can provide information about the local environment of the resonant atoms, in our case there are too many parameters in the scattering tensor to be able to derive anything more interesting than the cause of the peak.

Magnetic satellites were observed around the ATS reflection below ~ 57 K, the patterns being consistent with the helical, conical, and skyrmion phases. The reflections display scattering only in the σ-π' channel and not in the σ-σ' channel, as expected for magnetic scattering, however, their polarisation dependence is far from that expected for a helix.

There is no deviation from the equation $\sqrt{P_1^2 + P_2^2} = 1$ which is inherent in any non-collinear magnetic structure. One possibility considered was that there are counter rotating helices within the magnetic structure as this would cancel the imaginary parts and the equation $\sqrt{P_1^2 + P_2^2} = 1$ would be retrieved. The simulated

polarisation dependences for the reflections, however, did not match the data.

Other effects such as birefringence [100] can be discounted as the ATS reflection has the expected polarisation dependence. Higher order scattering processes such as quadrupolar scattering [157] would expect a large deviation from $P_1 = -1$ $P_2 = 0$ with sigma incident light and can also be discounted.

Second order dipole scattering could produce a similar polarisation dependence to the data but requires a conical magnetic structure as well as a dominant resonant scattering factor for the second order process. This possibility appears unlikely when comparing to the results of FeAs [109, 160] where a similar second order matrix and conical structure could explain the polarisation dependence but the dominant second order process is not evident in other magnetic reflections.

It is suspected that the polarisation dependence is in some way related to the reflections being satellites around the ATS reflection. Similar results have been observed in FeAs [109, 160] for a satellite reflection around an ATS peak, however, in this example the ATS reflection was outside the Ewald sphere and was not considered in the analysis. The polarisation dependence was therefore attributed to a long period antiferromagnetic structure with the moment oriented along the propagation vector. In FeAs all the azimuthal and polarisation dependences of all other reflections were consistent with a helix with the moment rotating in the plane perpendicular to the propagation vector. We have fitted our data with a similar model of moments aligned along the propagation vector in a long spin density wave and found it consistent with the polarisation dependence. This however, is not consistent with either our magnetisation data from the same sample or any other published data on this system.

We have been unable to determine any details of the magnetic structure from the polarisation measurements other than that they are similar in the helical, conical, and skyrmion phases. This suggests that the magnetic structure is similar in all three phases, however, this could be distorted as in the case of FeAs [109, 160]. The complex nature of the helix was not realised at the ATS satellite in FeAs and the sensitivity to the structure may be lost in such a reflection. It is therefore impossible to draw any conclusions from the polarisation dependence of these peaks without more investigation of satellite reflections around ATS peaks.

6.7 Conclusions

We have used resonant x-ray, as well as neutron powder, and single crystal diffraction to study both the magnetic ground state and the skyrmion phase of Cu_2OSeO_3.

Magnetisation measurements are largely consistent with those measured previously and confirm the presence of the skyrmion phase. The saturation magnetisation of 0.53 $\mu_B/Cu \pm 0.003$ suggests a moment in the ferrimagnetic phase of 1.06 μ_B/Cu $\pm$ 0.006. The paramagnetic susceptibility is fitted to give a Curie constant from a moment of $1.50\mu_B/Cu \pm 0.009$.

We have determined the nature of the $(1, 0, 0)$ reflection by full polarisation analysis to be due to the anisotropy of the tensor of x-ray susceptibility (ATS).

Polarisation analysis of the helical conical and skyrmion satellites have been undertaken. These polarisation dependences fit with a model of a long-range spin density wave with the moments oriented along the scattering vector. This model is very different from the expected polarisation dependence for a helix. This provides evidence along with the measurements in the thesis of Thomas Frawley [160] that the observed polarisation dependence is transformed as a result of being a satellite around an ATS reflection. We have had many discussions with scientists in the field about this data and none can see why, in the current theory, that a satellite reflection should be affected by the parent peak. There are no large modifications in the polarisation dependence between the helical, conical, and skyrmion phases. Although these results do not reproduce the correct magnetic structure, it is an indication that the magnetic structure of the helices remains unchanged between the phases and is not modified in the skyrmion phase.

Wish (a long-wavelength neutron diffractometer) was used for both single crystal and powder neutron measurements. The satellite peaks were resolved in both of these setups. The data however, was not sufficient to easily distinguish the 6-fold skyrmion satellites. The neutron powder measurements confirm the nuclear structure and that the field polarised phase structure is ferrimagnetic in nature, although with a larger moment size of 0.924 $\mu_B/Cu \pm 0.025$.

The presence of a $(1, 0, 0)$ reflection in the helical phase indicates a fundamental change in the magnetic structure. This has been fitted with a structure where all the moments are ferromagnetic apart from one of the $4a$ site copper moments which

is aligned antiparallel in a reduced ferrimagnetic structure.

This is the first direct evidence that the ground state of Cu_2OSeO_3 is different to the ferrimagnetic phase and also the first evidence showing that the skyrmion phase is ferrimagnetic. This reduced ferrimagnetism is not expected to alter the properties of the skyrmion phase and would be expected to behave simply as a skyrmion with a reduced moment. There is therefore a more complex magnetic transition required between the helical and ferrimagnetic phases than previously thought. The nature of this transition may play an important role in the stabilisation of the skyrmion phase. This is also the first confirmed study of a change in the polarisation dependence of a magnetic reflection around an ATS reflection, which requires much more study.

Further Work

To further investigate the skyrmion phase, measurements around the main beam would need to be taken. This would remove any effects from the ATS peak giving more evidence that there is something missing from the theory of resonant x-ray scattering but also hopefully give more of an insight into the magnetic structure in these systems. Further investigations should also be made into satellites around ATS reflections from different magnetic structures. A good starting point might be $Ca_3Co_2O_6$ which displays a long spin density wave with the moment aligned along the propagation vector as this system belongs to the space group $R\bar{3}c$ and has both glide plane and screw axis extinctions which will likely produce ATS reflections [158]. Similar measurements may be possible in other skyrmion systems MnSi, $Fe_{0.5}Co_{0.5}Si$, FeGe, and MnGe. These systems have much smaller unit cells so only measurements around the main beam would be possible, but the satellites would have a larger separation from the main beam than in Cu_2OSeO_3 so contamination would be less likely. Polarisation analysis measurements of the magnetic satellites in $BeFeO_3$ would also provide useful insight as there is no ATS reflection. Although there may be technical constraints with the peak intensity and close proximity of the satellites in this system.

Addendum

Since the submission of this thesis there has been further work published on the polarisation dependence of the magnetic satellites of Cu_2OSeO_3 using soft x-rays [161]. Circularly polarised light was used to distinguish between the different winding numbers of possible skyrmions. The polarisation in this instance appears to follow the expected pattern. Circular polarisation is sensitive to the sense of the helical rotation and the scattering intensity at the positive and negative satellites gives insight to the domain populations of the different helical rotation [162]. As our scattering matrix just induces a rotation of the polarisation, this would not affect helically polarised light, further they did not measure the scattered polarisation only its intensity, making them insensitive to the peculiarities that we have observed. It is, however, evidence that the helical nature of the peaks can be observed at these reflections around the ATS peak.

Anti-skyrmions have also been observed both above room temperature and in a non-cubic tetragonal system [163] with the C_{nv} symmetry predicted by theory.

Part III

The Magnetic Properties of Manganese Oxide Mono- and Bi-layers in Different Charge Environments

Chapter 7

Sample Growth and the Properties of Thin-Film Perovskite Structures

The following two chapters investigate the magnetic properties of manganese in highly unique thin film arrangements, the first chapter consists of measurements on single layers of manganese oxide in heterostructures while the second chapter consists of measurements on bilayers of manganese, where the manganese layers are separated by lanthanum oxide or strontium oxide. Different configurations of strontium titanate $(SrTiO_3)$(STO) and lanthanum aluminium oxide $(LaAlO_3)$(LAO) are used as sandwich layers with the aim of controlling the magnetic properties due to the differing charge environments. The different layers surrounding the manganese layers are expected to donate electrons and begin filling the e_g orbitals. In this way we hope to be able to demonstrate that the magnetism of the manganese layer can be effectively controlled by layering with different materials. These constitute the first samples of their kind. We have used x-ray magnetic circular dichroism (XMCD), a highly sensitive element selective technique which directly probes the orbital specific populations of spin-up and spin-down electrons. XMCD is a resonant x-ray technique and gives element specific information about spin and orbital magnetic properties of systems.

7.1 Introduction

While the fundamental properties of single crystals are interesting, it is the prop-
erties of thin-films of materials that are the most viable option for technological
advancement. When a material is grown as a thin film onto a substrate the dif-
fering properties of the substrate can produce entirely new phenomena. Transition
metal oxides, especially those containing manganese are a continuing field of study
due to them simultaneously displaying spin, charge, and orbital degrees of freedom,
which manifest among other things as, magnetism, charge ordering, and cooperative
Jahn-Teller distortions.

Interfaces already play a crucial role in electronics with the conducting junction
between two different semiconductors forming the basis for modern electronics in
transistors, solar cells, LEDs, etc. Compared to bulk semiconductors, bulk transi-
tion metal oxides display a diverse and interesting array of properties such as high
temperature superconductivity, colossal magneto-resistivity, charge and orbital or-
dering, and Jahn-Teller distortions [164]. These properties arise due to strongly
interacting electrons, the reduced dimensionality present in heterostructures leads
to stronger electron correlations, enabling the possibility for an even more diverse
range of properties.

Manganese oxides are highly functional materials which display properties desir-
able for application in devices. For example giant magneto-resistance is a property of
layered ferromagnetic materials where there is a large change in the resistance when
changing the magnetisation state. This property is used to read the magnetic state
of hard drives. Manganese oxides have the property of colossal magneto-resistance
which is orders of magnitude stronger than giant magneto-resistance [165]. They
also display multiferroic properties which are a coupling of the electronic and mag-
netic degrees of freedom such that the magnetic behaviour can be controlled with
currents and electric fields [166].

7.2 Material Growth

Over the past decade sample growth techniques have developed greatly, where atom-
ically smooth thin-film structures can now be grown a single layer at a time. Pulsed

laser deposition and sputter deposition techniques involve ablating a target of the material desired for deposition, the resultant vapour is then deposited onto a substrate. The substrate is heated to ensure the deposited materials have the required energy to move on the surface and form a good crystal structure. When depositing oxide materials the whole process is often carried out in an oxygen atmosphere to reduce the risk of oxygen vacancies. Molecular beam epitaxy is a similar technique where there are multiple sources of different elements and these react when they are incident on the surface to form the required material. This process is much slower and a good vacuum is required so that the rate of impurity introduction is low enough. The growth of these layers in monitored by *in-situ* RHEED (reflection high energy electron diffraction) to determine when layers have formed before growing the next layer. RHEED is a surface diffraction technique and the intensity of the diffraction spots relate directly to the surface roughness. Therefore, peaks in the intensity of the RHEED pattern correspond directly to the completion of a single layer of growth. This results in unit-cell thick layers with exceptional structural and electronic morphologies.

7.2.1 Pulsed Laser Deposition

Pulsed laser deposition (PLD) is a technique that grows single unit cell layers of materials almost instantaneously at the limit of extreme vapour supersaturation. PLD uses a high intensity pulsed ultraviolet laser light to ablate the target. The most common laser used is a KrF laser which is an excimer laser (excited dimer) sometimes called an exciplex laser (excited complex) where the laser light is produced when the KrF complex decomposes to Kr and F emitting light of 248 nm (in the deep UV region of the spectrum), UV light is used due to its strong absorption. There is a certain amount of dead time to allow the reactants to re-form the excited complex, as a result they can only operate at a maximum of around 50 Hz (which defines the pulses). This can be utilised in the growth as an exact number of pulses required to grow a single layer can be determined.

7.2.2   Sputter Deposition

Sputtering is a similar technique to pulsed laser deposition differing only in the ablation method of the target. In sputter deposition ion beams are used to transfer energy to the atoms on the surface of the material so that they can overcome the surface binding energy. Argon beams are generally used due to argon being inert. In sputter deposition an electric field is used to accelerate the argon ions towards the targets.

7.3   Material Properties

7.3.1   Bulk Transition Metal Oxide Properties

Before looking directly at the properties of thin-film systems it is important to have a general knowledge of the bulk properties of these systems.

The Perovskite Crystal Structure

The perovskite and perovskite-like crystal structures are ubiquitous across many of the transition metal oxides studied currently, with almost 200 publications linked to perovskites in 2015. Perovskites are named after a naturally occurring mineral (perovskite) composed of calcium titanate $CaTiO_3$ which has a cubic structure. The cubic perovskite structure is generalised as ABO_3 where B is a transition metal, the A atoms reside at the apexes of a cube, the B atom at the body centre and the oxygen atoms at the face centres which form an octahedron with the B atom, as depicted in figure 7.1 [167]. This can be thought of as being composed of AO and BO_2 monolayers which is useful when discussing thin-film materials. The name perovskite is now very broad and is usually linked to any systems containing octahedral arrangements of oxygens not limited to cubic systems. Perovskite structures are prevalent in transition metals due to the shapes of the $5d$ orbitals (shown in the introduction in figure 1.3).
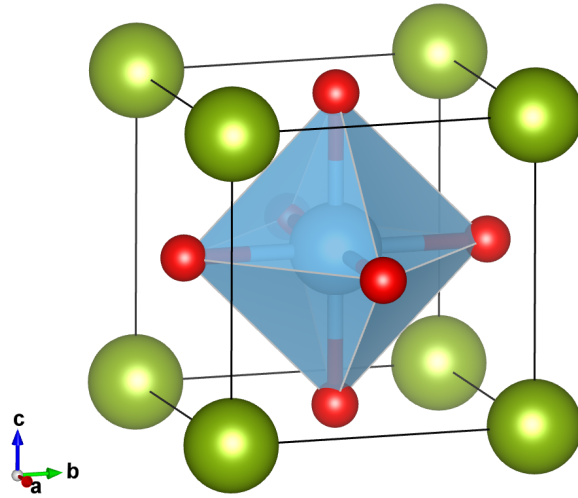
Figure 7.1: Crystal structure of the cubic perovskite $CaTiO_3$. with calcium in green, titanium in blue, and oxygen in red.

Octahedral Rotations

Octahedral rotations are an ordered tilting of the transition metal octahedra and are prevalent in many perovskite systems. They play an important role in the electronic, magnetic and orbital properties as these are all heavily mediated by the B-O-B bond angle. The electron bandwidth and hence the metal insulator transition temperature is also strongly dependent upon the B-O-B bond angle. The electron bandwidth takes the form $W = d^{-3.5} \cos\theta$ [168] where 2θ is the bond angle away from 180°. Octahedral rotations occur when the unit cell size is not compatible with the energy minimum for the B-O bond length. In this case the octahedra can rotate to maintain the octahedral arrangement or distorted octahedra can form, whichever is more energetically favourable. Strain has been used in the past to alter the electronic properties of materials [169, 170], however, applying strain reduces the bond length as well as the bond angle which counteract each other, reducing the effect on the electron bandwidth. The transfer of octahedral rotations from the substrate to the film has been shown to be a much more efficient route to enhancing the electronic properties than strain as the bond lengths and angles can be adjusted cooperatively.
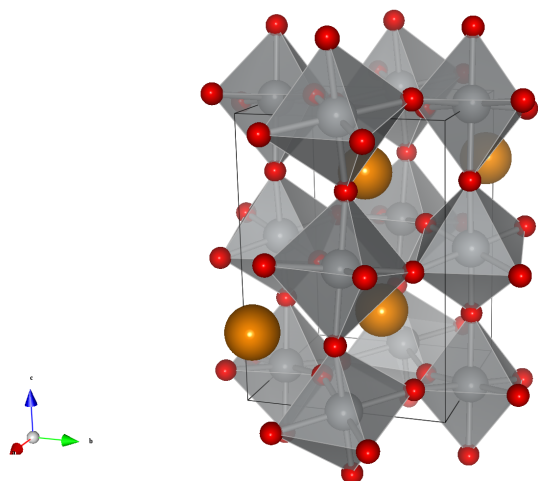
Figure 7.2: Structure of $NdNiO_3$ showing rotations of the NiO_6 octahedra using [172] and data from [173].

Rotation Nomenclature

Octahedral rotations were first characterised and categorised by Glazer *et al.* in 1975 [171]. A rotation in one octahedron induces a rotation of the opposite sense in the neighbouring octahedra occupying the plane perpendicular to the rotation axis. However, subsequent layers out of plane are free to rotate either in the same or the opposite direction. In Glazer notation we denote the rotation about a particular axis with superscript $+$ or $-$ denoting rotations in subsequent planes being in the same or opposite direction. The rotation axis is denoted by the position and tilting by the crystallographic axis (a, b or c). When the magnitude of the tilting is equal to another axis the letter is repeated. For example an **abc** rotation would have different magnitudes of tilts along the three axes but an **aaa** rotation would have the same magnitude of tilt along all three axes. An example of a system with octahedral rotations is shown for the case of $NdNiO_3$ in figures 7.2 and 7.3.

Determination of Rotations

The Glazer notation for the tilt system can be determined through simple extinction rules. The tilting causes a doubling of the unit cell along the pseudo cubic axes, resulting in the reflections shown in table 7.1 [171];
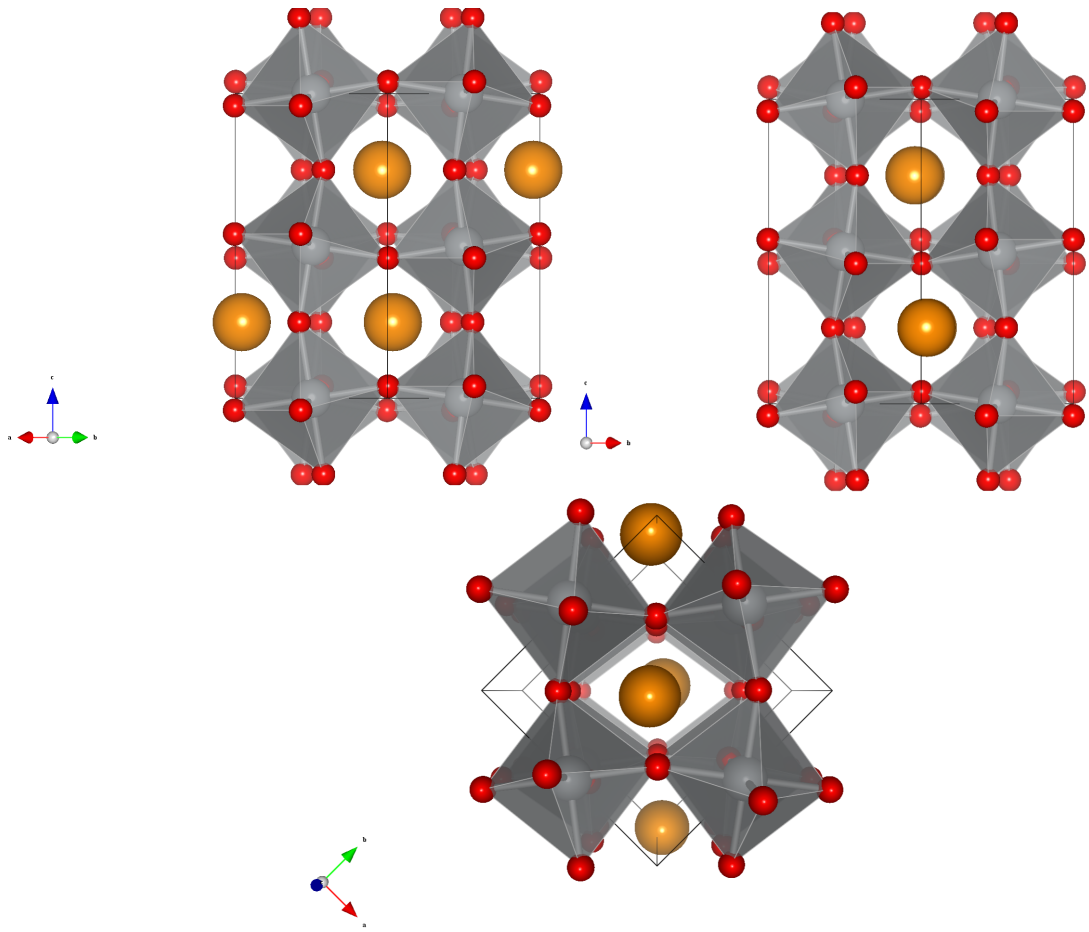
Figure 7.3: Crystal structure of NdNiO$_3$ shown along the pseudocubic axes showing the $\mathbf{a}^-\mathbf{b}^-\mathbf{c}^+$ tilt system.

symbol	h	k	l	conditions
$\mathbf{a}^+$	even	odd	odd	$k \neq l$
$\mathbf{b}^+$	odd	even	odd	$l \neq h$
$\mathbf{c}^+$	odd	odd	even	$h \neq k$
$\mathbf{a}^-$	odd	odd	odd	$k \neq l$
$\mathbf{b}^-$	odd	odd	odd	$l \neq h$
$\mathbf{c}^-$	odd	odd	odd	$h \neq k$

Table 7.1: Reflection conditions for different octahedral rotations

7.3.2   Properties of Thin-Film Oxide Heterostructures

Epitaxial Strain

One of the first problems encountered when attempting to grow thin films is the lattice mismatch between the lattice parameters of the sample and the substrate. For poorly matched materials, defects are introduced in the growth which relieve the strain until after a certain thickness of deposited material the lattice parameters are relaxed back to its unstrained bulk values, the larger the mismatch the more defects are introduced and the quicker strain is relieved. Epitaxially strained films have the property that the material being grown has a very similar lattice parameter to the substrate such that the lattice parameter of the deposited material is the same as that of the substrate throughout the deposited layer.

Interfacial Roughness

In a heterostructured material the roughness between different materials can be important for the growth of subsequent layers. If a large number of layers are needed a rough interface will cause a large intermixing of the materials which can increase in subsequent layers. The interfacial roughness can be improved by a number of growth technique factors such as the substrate temperature, substrate treatment, and control of the growth mode. Further to this there are some more fundamental properties that govern interface roughness which are related to charge transfer and polar interfaces.

Interfacial roughness can most easily be thought of as the interface between two materials being distinct but not localised to a plane. There are two distinct ways interfaces can be rough, one where there is a sharp interface but it is disordered, the other where there is ion intermixing, examples of this are shown in figure 7.4. In both cases there is a finite width to the interface and they can display the same averaged ion distributions across the interface, however, in the case of ion intermixing, roughness will not worsen with subsequent layers.
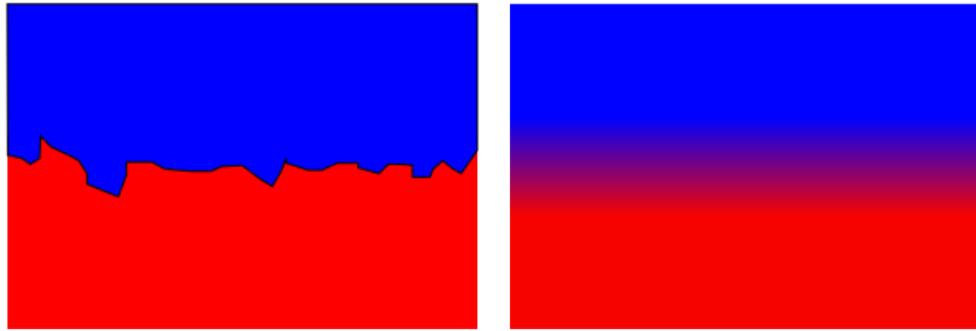
Figure 7.4: (left) Interfacial roughness from disordered interface. (right) Interfacial roughness from ion intermixing.

The Polar Catastrophe, Charge Transfer, and Oxygen Vacancies

Many materials can be thought of as being built up of a number of different mono-layers, in some cases these monolayers are charged forming a polar material. For comparison we shall look at non-polar STO and polar LAO, both take the form of a perovskite structure and can be thought of as being built up of AO and BO_2 layers. In the case of STO both of these layers are charge neutral. In the AO layer the strontium forms 2+ ions paired with the 2− oxygen ions and in the BO_2 layer the titanium forms 4+ ions paired with the two oxygen 2− ions. For the case of LAO the lanthanum forms 3+ ions which gives an overall charge to the LaO layers of +1 and the aluminium forms 3+ ions giving the AlO$_2$ layers an overall charge of −1. The so-called 'polar catastrophe' in oxide heterostructures is the thin-film equiva-lent of the problem of single crystal surface termination, where reconstructions and dangling bonds occur. In a single crystal of LAO the termination layer is charged and this charge is only partially compensated for by the layer below. The surface reconstruction must therefore also incorporate a charge of 0.5e. The polar catas-trophe occurs at the interface between polar and non-polar materials in thin-film structures, where now an interfacial reconstruction is required to compensate the extra charge. In systems used in the semiconductor industry growing GaAs on Si will result in large interfacial roughnesses as the materials compensate for charges at the interface by an intermixing of the ions. In transition metal oxide materials the

transition metal valence state can change so the charge is compensated in a process known as charge transfer. Alternately if no valencies are energetically favourable, oxygen vacancies may occur to compensate the charge.

It has been reported that how an interfacial region is constructed can play an important role in the balance between charge transfer and oxygen vacancies [174]. Fundamental differences have been observed in $SrTiO_3/LaAlO_3$ interfaces depending on the deposition order with strontium interfaces ($AlO_2/SrO/TiO_2$) being around half as rough as lanthanum interfaces ($AlO_2/LaO_2/TiO_2$). Electron energy loss spectroscopy (EELS) measurements pinpoint the difference between the interfaces. Strontium interfaces are compensated by oxygen vacancies resulting in a sharper interface than in the lanthanum case, where the titanium valence changes and a more diffuse electron cloud results in an increased roughness.

There are a number of factors which need to be examined when considering how this will affect magnetism in such systems. While oxygen mediates the magnetic exchange, vacancies at the apical sites will only affect magnetic coupling between subsequent deposited layers. The orbital magnetic moment could be effected to a much larger degree due to orbital quenching of the moment from the crystal field splitting resulting in only a small number of electrons contributing to the orbital moment.

Orbital Reconstruction

Interfacial orbital ordering has been observed in $4\times LaNiO_3/4\times LaAlO_3$ heterostructures [175]. There was found to be an average preferential occupation of the $x^2 - y^2$ over the $3z^2 - r^2$ orbitals by $5.5 \pm 2\%$ in the nickel layers. A further segregation is found between the inner and outer layers (of the stacks of four) with the inner layers having a roughly 3% higher occupation than the outer layers. The errors are not explicitly worked out for this final number but from their previous results we expect an error value of around $\pm$ 3%. However, the results are further corroborated by local density approximation (LDA + U[1]) calculations. These measurements were determined by the fitting of resonant x-ray spectra taken at the superlattice reflection

---

[1]The U stands for an introduction of a strong intra-atomic interaction as LDA calculations often fail to describe systems with strongly correlated d or f electrons

coming from the repeating structure of the thin-film in the x-ray reflectivity.

7.4 Sample Growth

Samples were grown on 5 mm square STO substrates which were treated with hydrogen fluoride to ensure TiO_2 termination and annealed to achieve atomic terraces. To achieve the 'monolayers' single unit cells of either $SrMnO_3$ or $LaMnO_3$ were grown on the substrate and then the capping layers of 6 unit cells of STO or LAO were deposited on top. Reflection high energy electron diffraction measurements were used to calibrate the number of pulses required by giving surface sensitive information with oscillations in intensity peaking at each complete growth layer. The lattice parameters between all these systems are relatively matched (for the small thicknesses of the samples being grown) and are shown in table 7.2.

7.4.1 Theoretical Calculations

Theoretical calculations have been completed on bulk samples of $SrMnO_3$ (SMO), $LaMnO_3$ (LMO), and $LaSrMn_2O_6$ which highlight some interesting properties which may be relevant to our systems [179, 180]. In the case of $LaMnO_3$ it was found that with a reduction in the lattice parameters there is only a small energy difference between configurations with Mn^{4+} and the more favourable Mn^{3+} of between 5 and 15 mRy (less than 0.2eV). These calculations do not extend to how the change in oxidation state comes about or where the extra electron on the manganese is coming from. In the case of $LaSrMn_2O_6$ the ground state is found to be Mn^{4+} but with Jahn-Teller distortions a mixed valence Mn^{3+}/Mn^{4+} state becomes favourable. In

Crystal	Space Group	Lattice parameter	Reference
$SrTiO_3$	$Pm3m$	3.905 Å	[176]
$LaAlO_3$	$R\bar{3}m$	3.792 Å	[176]
$SrMnO_3$	$Pm3m$	3.805 Å	[177]
$LaMnO_3$	$Pbnm$	(Pseudocubic) 3.914 Å	[178]

Table 7.2: Lattice parameters for various cubic perovskites.

Crystal	Magnetism	Transition Temperature	Moment Size	Ref
$SrTiO_3$	-	-	-	-
$LaAlO_3$	-	-	-	-
$SrMnO_3(bulk)$	G-Type AFM	260 K	2.6 μ_B	[181]
$SrMnO_3(film)$	?	40 K	?	[182]
$LaMnO_3(bulk)$	A-Type AFM	125 K	4 μ_B	[183]
$LaMnO_3(film)$	FM	25 K	1.14 μ_B	[183]

Table 7.3: Type transition temperature and moment size for the constituent components of our samples. Non-magnetic samples are shown with a (-) unknown values with a (?).

$SrMnO_3$, Mn^{4+} is calculated to be energetically favourable by over 100 mRy, for all cases the Mn^{4+} was calculated to display ferromagnetic ordering.

It is interesting to note that the mixed valence state is relatively unfavourable in these systems and the effect of strain altering the energy gap between different ground states as small perturbations could easily be induced in the heterostructure. These calculations highlight how sensitive these systems are to small changes in environment.

7.4.2 Magnetic Transition Temperature

The magnetic transition temperatures and moment sizes of all the different constituent components of the systems are displayed in table 7.3. The transition temperatures and moment size for thin films compared to the bulk are much reduced. This is due to the lack of inter-layer coupling in thinner samples and we would therefore expect a similar lowering of the transition temperature in our samples.

7.4.3 Magnetic Properties

A recent paper by Zhai *et al.* [183] has investigated the link between octahedral rotations and magnetism. In this work samples were grown on TiO_2 terminated $SrTiO_3$ substrates with structures $(LaMnO_{3+\delta})_N/(SrTiO_3)_N$. A large increase in transition temperature was observed from 25-75 K from two to three layers with a moment

size increase from 1.2 to 2.2 μ_B. No investigations were carried out on single unit cell layers, however, a similarly large increase in transition temperature between the monolayer and bilayer systems could be expected. Bulk $LaMnO_3$ exhibits A-Type antiferromagnetic ordering[2] with an ordered moment size of 4 μ_B and a transition temperature at 125 K. Thin-films are generally observed to exhibit ferromagnetism with a reduced moment and a composition of $LaMnO_{3+\delta}$ due to cation vacancies and strain effects.

Octahedral Rotations

Bulk $SrTiO_3$ has no octahedral rotations but $LaMnO_3$ displays octahedral rotations depending upon the manganese valence. For Mn^{3+} an orthorhombic structure with $a^-a^-c^+$ rotations is adopted, for higher valencies a rhombohedral structure with $a^-a^-a^-$ rotations becomes prevalent. LAO for nine unit cells has a rotation nomenclature of $a^-a^-a^-$ [184] which is the same as that for LMO but with a different magnitude around the c-axis. This should give a difference in the manganese layers for our samples as the capping layer in the case of LAO will reinforce the octahedral rotations. The reduced Mn-O-Mn bond angle resulting from this would be expected to reduce both the ordered moment size and the transition temperature in these cases.

From the Zhai *et al.* paper [183] the most relevant system to our study is the case of two unit cells of $LaMnO_3$. This system has a much reduced moment of 1.14 μ_B and the transition temperature is reduced to 25 K. The remnant field from the hysteresis in this system is also very reduced to around 0.25 μ_B. X-ray absorption fine structure (XAFS) measurements confirm the valence state of the manganese at around 3.15 for the two unit cell thick sample. This reduction is attributed to the B-O-B bond angle which has the largest deviation in this case. The maximum moment (2.9 μ_B) being observed in the six unit cell system which has a much reduced in-plane rotation angle, with a subsequent increase in the ordering temperature to around 120 K

It has been shown by theoretical calculations that about four unit cells are af-

---

[2]Consisting of ferromagnetic planes stacked antiferromagnetically

fected when $La_{0.75}Sr_{0.25}MnO_3$ which has an $a^-a^-a^-$ rotation pattern is forced to have no rotation [185]. So rotations are expected to be largely effected by the surrounding layers.

Chapter 8

The Magnetic Properties of Manganese Oxide Monolayers in Different Charge Environments

The results presented in this chapter are published here H.-J. Liu, J.-C. Lin, *et al.* 'A Metal-Insulator Transition of the Buried MnO_2 Monolayer in Complex Oxide Heterostructure'. *Advanced Materials*, **28**; pp. 9142-9151 (2016) [186].

The following chapter investigates the magnetic properties of monolayers of manganese when surrounded by different configurations of strontium titanate ($SrTiO_3$) (STO) and lanthanum aluminium oxide ($LaAlO_3$) (LAO). The aim is to control the magnetic properties due to the differing charge environments as LaO layers would be expected to donate electrons to the MnO_2 layers. We have used x-ray magnetic circular dichroism (XMCD) to determine the magnetisation and temperature dependent properties of these films. This chapter focusses on the results, introductory material can be found in the previous chapter Chapter 7 Sample Growth and the Properties of Thin-Film Perovskite Structures.

8.1   Manganese Oxide Monolayers

The monolayer samples grown were $SrO/MnO_2/SrO$ (SMS), $SrO/MnO_2/LaO^+$ (SML) and $LaO^+/MnO_2/LaO^+$ (LML), the structures are shown in figure 8.1. To compen-
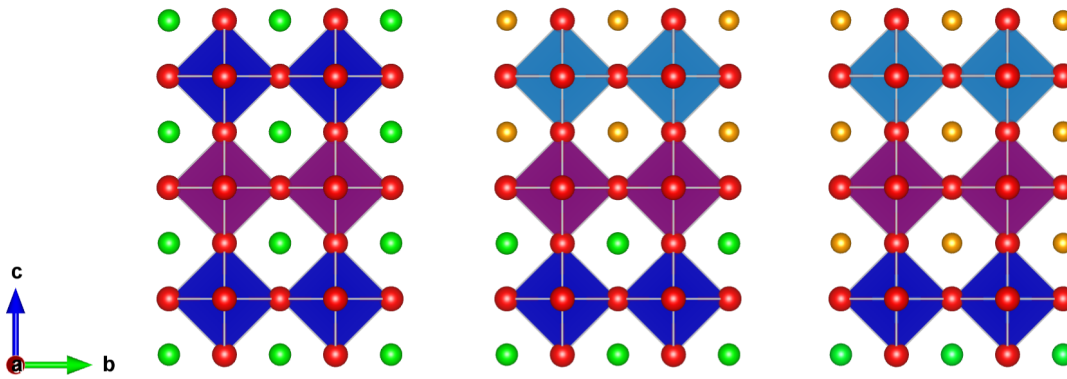
Figure 8.1: Structures around the MnO_2 monolayers with atoms depicted as follows; green strontium, blue titanium, red oxygen, purple manganese, orange lanthanum, and light blue aluminium. Left to right the samples as SMS, SML, and LML.

sate for the positively charged local environment in the SML and LML samples fewer electrons are expected to be given up from the manganese to the conduction band the corresponding oxidation states would then näively be expected to form Mn^{4+}, and $Mn^{3.5+}$ in the SMS, and SML samples. As the LaO layer below the MnO_2 layer in the LML samples is deposited on non-polar STO the whole of the charge compensation for this layer might be expected to be taken on by the manganese layer and oxidation states as low as $Mn^{2.5+}$ could be achieved.

8.1.1 Experimental Techniques

Three samples were grown by pulsed laser deposition with single manganese oxide layers in different charge environments provided by adjacent layers of either LaO or SrO. The three samples were all grown on TiO_2 terminated STO substrates. X-ray absorption measurements including temperature and field dependence XMCD measurements were taken using total electron yield. The high-field magnet end-station of the I06:Nanoscale beam-line at the Diamond Light Source Ltd. was used with energies at the manganese L_{II}/L_{III} edges, more details of the I06 beamline can be found in section . All measurements were taken with the samples oriented at 30° to the main beam to maximise the in-plane magnetisation with the field directed along the beam.

The samples were insulating and as such many effects of charging were observed

before the rate of photoelectrons and the drain current could equilibrate. To counteract this, measurements were taken with an extended pre-edge region and also spectra were taken in the sequence with circular polarisations positive, negative, negative, positive so that time dependent charging effects could easily be recognised.

Structural Analysis by HAADF-STEM

A Cs-corrected STEM (JEM-2100F, JEOL, Co., Tokyo, Japan) operated at 200 kV and equipped with a spherical aberration corrector (CEOS Gmbh, Heidelberg, Germany) were performed with a minimum probe of about 1 Å in diameter. The probe convergence angle and the detection angle were 25 mrad and 92-228 mrad, respectively.

Scanning Tunnelling Microscopy and Spectroscopy (STM/STS)

Topography measurements were taken by scanning the tip at a fixed voltage (-2.0 V) and adjusting the height so the current is constant. Current measurements were taken by scanning the tip at a fixed height and fixed voltage and measuring the tunnel current. By ramping the bias voltage and keeping the tip distance fixed, information regarding the local density of states can be determined. The gradient of the tunnel current is proportional to the density of states with a resolution of 0.4 nm. Before the STM measurements, amorphous $SrRuO_3$ (SRO) capping layers (>500 nm) were deposited on top of all samples to prevent the tip crashing during the measurements. The samples were cleaved in situ in an UHV chamber whose base pressure was approximately 5×10^{-11} torr [187]

8.2 Results and Discussion

8.2.1 Monolayer Sample Quality

All results in the following section were collected by our collaborators. All figures are either from the published paper [186] or its supplementary material.

TEM Measurements

High-angle annular dark-field scanning transmission electron microscopy (HAADF-STEM) was used to confirm the sample structure quality and interface segregation. Figure 8.2 shows results of HAADF-STEM images for the three samples which are top to bottom, SMS, SML, and LML. The intensity is related to the electron density and the raw images clearly show the difference between the columns of A sites (Sr and La) and B sites (Ti, Mn, and Al). The interface is clear in the SML and LML cases due to the difference in electron density of La and Sr. The manganese ions however, are not easily distinguishable from those of titanium or aluminium as they have similar atomic numbers. Averaging the images improves the distinction. The right hand column shows the intensity plots of the averaged data and shows that the desired structures have been realised. There is still some variation in the background which could be the result of inter-diffusion between the different materials. To further investigate this possibility atomic resolution EDS (energy dispersive x-ray spectroscopy) mapping has been carried out which is shown in figure 8.3. This reveals a large diffusion (two to three unit cells) of the manganese when the capping layer is LAO, and some subsequent diffusion of titanium from the substrate. A similar inter-diffusion was not observed with SMO as a capping layer.

Transport Measurements

As bulk measurements cannot determine the properties of the interface, scanning tunnelling microscopy and spectroscopy (STM/STS) was used to probe the electronic properties across the interface taken at a cleaved cross-section of the sample. The schematic of STM measurements of the SMS and LML samples are illustrated in figure 8.4 (a). STM measurements were then taken on the SMS and LML samples at 110 K (figure 8.4 (b)), apparent height differences are due to different electronic structures of the different materials offering differing tunnel currents. The topography images are sensitive to the conductivity of the different materials. There is a large amount of variation in the SMS sample suggesting that the surface is not well cleaved, which can be expected for pseudo-cubic perovskites.

Figure 8.4 (c) shows the tunnel current profile across the sample surfaces. The tunnel current images of the SMS sample appear to show a diffuse conducting region
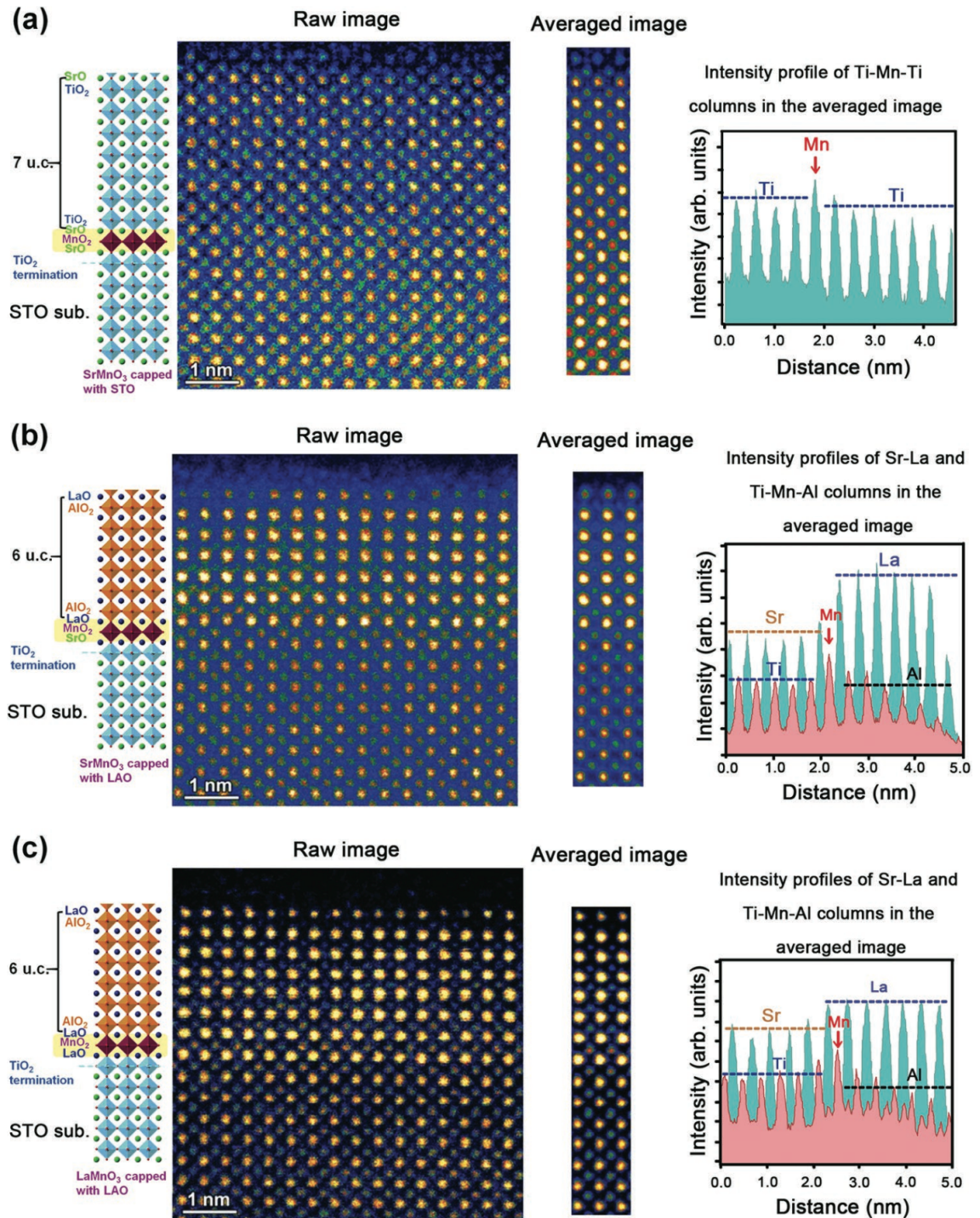
Figure 8.2: High-angle annular dark-field scanning transmission electron microscopy images with growth direction vertical for SMS (top), SML (middle) and LML(bottom). With raw image (left), averaged image (middle) and the intensity profiles (right) from [186].
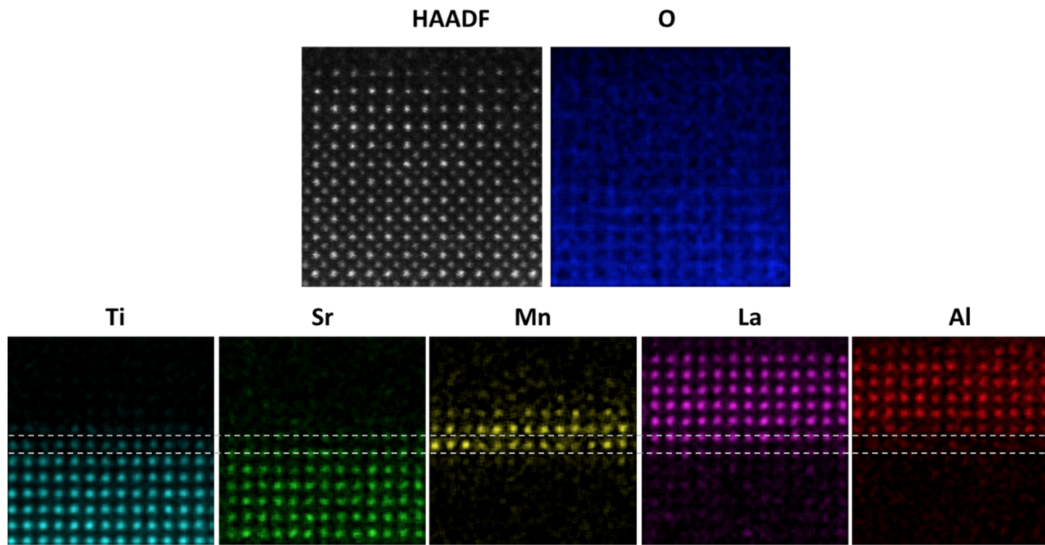
Figure 8.3: Atomic resolution EDS mapping data showing the atomic positions of the different constituents in the SML sample, from the supplementary materials of [186].

around the monolayer position. This may be linked to the roughness of the cleaved surface as there are regions deep within the substrate which also show currents similar to those around the interface.

There is also a roughly 1 nm line of high current in the LML sample. The resolution of the measurement is around one unit cell and this broadening is likely due to the manganese diffusion noted in the EDS maps. There are large variations in the current along the monolayer which may be due to percolation effects from the manganese diffusion as these samples are largely insulating.

The conductivity of the monolayers is unexpected as both $SrMnO_3$ and $LaMnO_3$ are insulating, however, bulk ceramic samples of $La_xSr_{1-x}MnO_3$ have been shown to be conducting. The end members are insulating but with doping of $0.8 > x > 0.2$ the samples become conducting. This has been associated with Jahn-Teller-induced structural distortions which destroy charge ordering and a ferromagnetic metal forms [188]. It is interesting to note that these measurements calculate a roughly 80% manganese 3+ valence for the $x = 0.5$ case. The deviation from the expected ratio mirrors the conductivity increase across the x range. The presence of a conducting interface in both cases therefore suggests a similar process and a higher proportion of Mn^{3+} may be expected in the LML and SML cases.
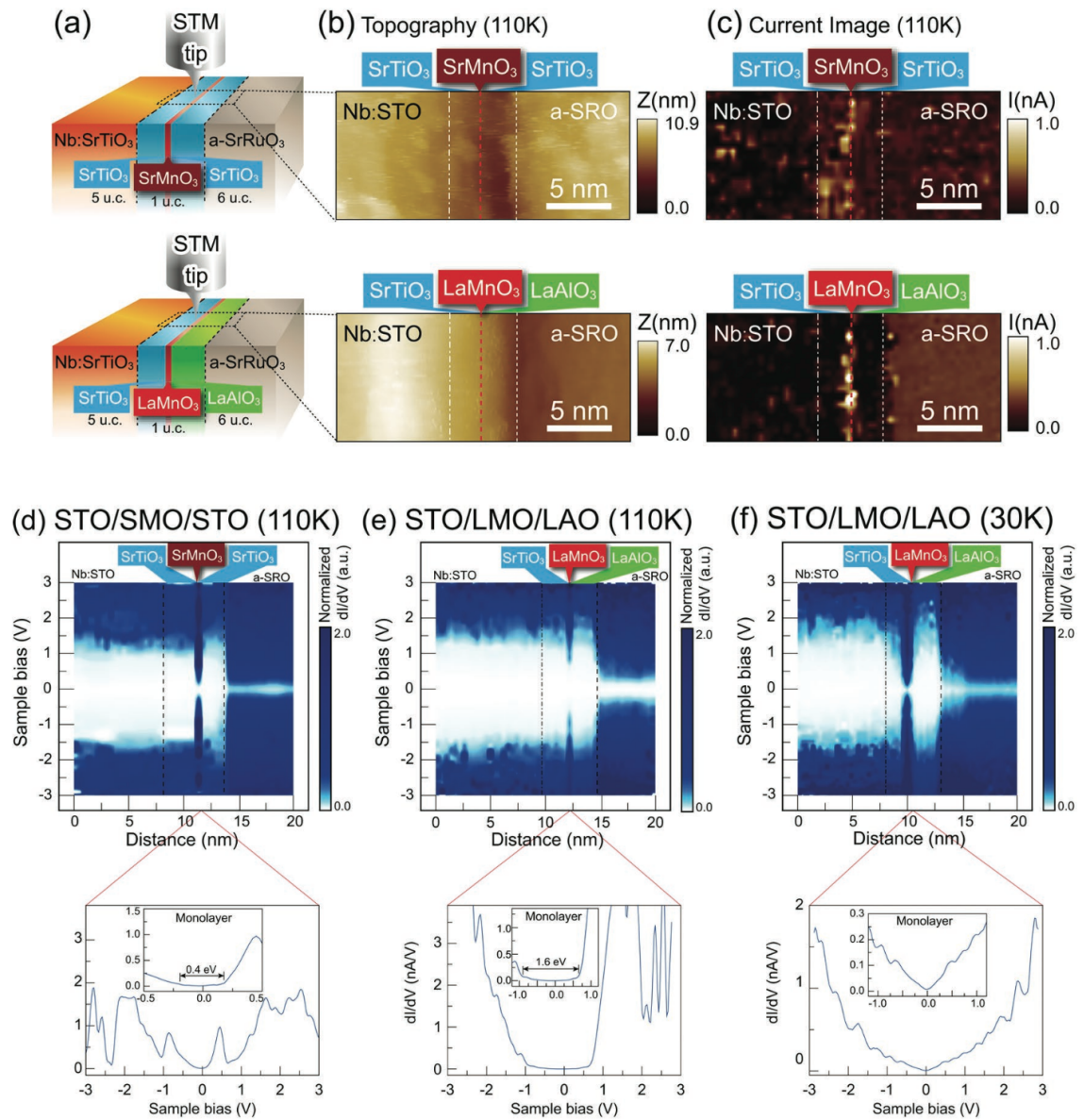
Figure 8.4: (a) Schematics of cross-sectional STM employed to investigate the properties of the MnO_2 monolayers. (b) Typical cross-sectional topography images of the SMS and LML samples with a tip bias of -2.0 V. (c) Tunnel current images of the SMS and LML samples at tip bias of -2.0 V. The red dashed lines in the images can be assigned as the position of the MnO_2 monolayers, which show brighter contrast compared to other region. (d) Differential of the tunnel current providing density of states information across the MnO_2 monolayers in SMS are measured at 110 K. (e-f) The same analyses of the LML sample measured at 110 K and 30 K, respectively from [186].

For the SMS sample, conductivity could occur due to oxygen vacancies which have been shown to be linked to growth by pulsed laser deposition of STO and a subsequent conductivity in the STO films [189, 190]. Another important effect to consider is the stacking of interfaces. In LAO and STO systems TiO_2 terminated STO produce conducting interfaces but SrO terminated STO interfaces are insulating [191]. This is due to the ability of the titanium to change oxidation state compared to the aluminium. Increased oxygen pressures in the growth was observed to reduce the conductivity again suggesting a link to oxygen vacancies. More recent surface diffraction measurements have confirmed a link to oxygen vacancies [192]. A reduction in apical oxygen occupancy around the interfacial TiO_2 layer and a coincident reduction of the titanium from 4+ to 3+ causes a bending of the conduction band in the STO to below the fermi level and hence conductivity.

The derivative of the tunnel current gives information about the local density of states, this is shown in figures 8.4 (d) and (e). The STO and LAO layers surrounding the monolayer interfacial region all have a large band gap of over 3 eV (as expected for an insulator)[1], the interfacial regions more closely resemble the band gap for a semiconductor with 0.4 and 1.6 eV respectively (silicon has a band gap of 1.14). The reduced band gap in the interfacial regions is consistent with the tunnel current measurements, the density of states is much lower in the SMS sample, supporting the smaller tunnel current observed in the LML sample.

The LML sample shows a sharp transition away from the interface providing more evidence of its locally high quality. The interfacial region is extended to about 1 nm, which is above the instrument resolution and consistent with the observation of manganese inter-diffusion. In the SMS sample the interfacial region is much narrower, consistent with there being less inter-diffusion of the manganese layer. The band gap is very disperse which could be due to the oxygen vacancies providing different charge environments for different manganese ions which smoothes the band gap.

DFT calculation also carried out by our collaborators and published here [186] predicted the LML sample to be metallic. These are predictions of low temperature properties, so to corroborate the calculations a measurement at 30 K was taken,

---

[1]The expected band gaps for STO, and LAO are 3.2 eV, and 5.6 eV respectively [191]

figure 8.4 (f). This shows markedly different results from the 110 K data. The band gap is much more disperse and appears to meet in the middle giving rise to something resembling a semi-metal, more like the high temperature SMS sample. The interface also appears much less sharp suggesting that the monolayer now affects the surrounding layers much more.

The temperature dependences of semiconducting materials can depend on a number of factors. The temperature dependence may be expected to be similar to that of a metal with an increasing conductivity on reducing temperature due to a reduction in scattering of the conduction electrons from the thermal motion of the lattice. The factors which can affect the temperature dependence however, are more numerous as both the band gap and the fermi level will change with temperature. Doping further alters the temperature dependence with doped semiconductors sometimes showing a decrease in conductivity upon cooling. This semiconductor-semi-metal transition occurs between 30 K and 110 K and may be linked to magnetic order within the system.

8.2.2   Monolayer XMCD

Initial measurements were taken using total electron yield as this gives a much stronger signal than fluorescence yield, due to the small sample volume involved. This is largely due to the different interaction volumes of the two measurements reducing the background for the total electron yield. Due to the insulating nature of the samples the Auger electrons cannot be compensated and charge builds up on the sample surface causing a large change in the initial slope of the measurements as well as spikes and steps in the datasets when the surface charge builds up sufficiently to cause a current to flow. An example dataset is shown in figure 8.5. The initial scan of a measurement set also often showed a large decaying tail down to a linear background as the surface charges reach equilibrium. To counter this, new samples were fabricated with a thin layer of titanium coated on the surface to increase the surface conductivity. Titanium was used because of a good surface affinity and the fact that only thin layers need to be grown to form a good conducting surface. Due to the changing charge and chemical environment of the samples, chemical shifts might be expected between the different spectra. The absorption spectra are shown
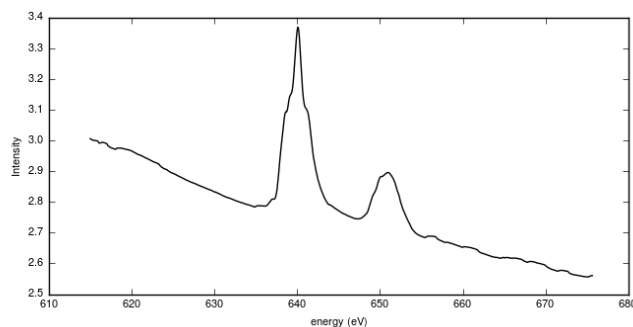
Figure 8.5: Absorption spectra from a non titanium coated sample.

in the top panel of figure 8.6, the edge jump is normalised to 1 in each case. There is no noticeable chemical shift between samples. The maximum chemical shift that might be expected in manganese systems is around 1 eV [193] which would easily be notable with the energy resolution of these measurements.

The SML and LML samples show qualitatively very similar lineshapes with very similar features. The notable exception to this being the pre-edge peak in the LML sample, however, closer inspection of the SML and SMS samples suggests the presence of a similar peak, all be it one that is not experimentally resolved.

Determination of Manganese Valence

The valence state of the manganese is important for accurate determination of the moment using the sum rules. Fitting spectra of a known manganese valence can provide a reasonable method for determining the oxidation state of the manganese present in the absence of full multiplet calculations.

Reference spectra are shown in the middle panel of figure 8.6 and comprise of MnO_2, $SrMnO_3$, and $LaMnO_3$ which have manganese oxidation states of 2+, 3+, and 4+ respectively[2]. The reference spectra are fitted to the experimental data using a least squares algorithm with the parameters of; the reference spectra magnitudes, and an energy shift between the monolayer samples and the reference spectra, which will account for different energy calibrations between the different measurements. Finally a tanh step edge was fitted to the spectra to account for differences in the

---

[2]The reference spectra were collected separately to the monolayer spectra by our collaborators on the dragon beamline at NSRRC, Taiwan
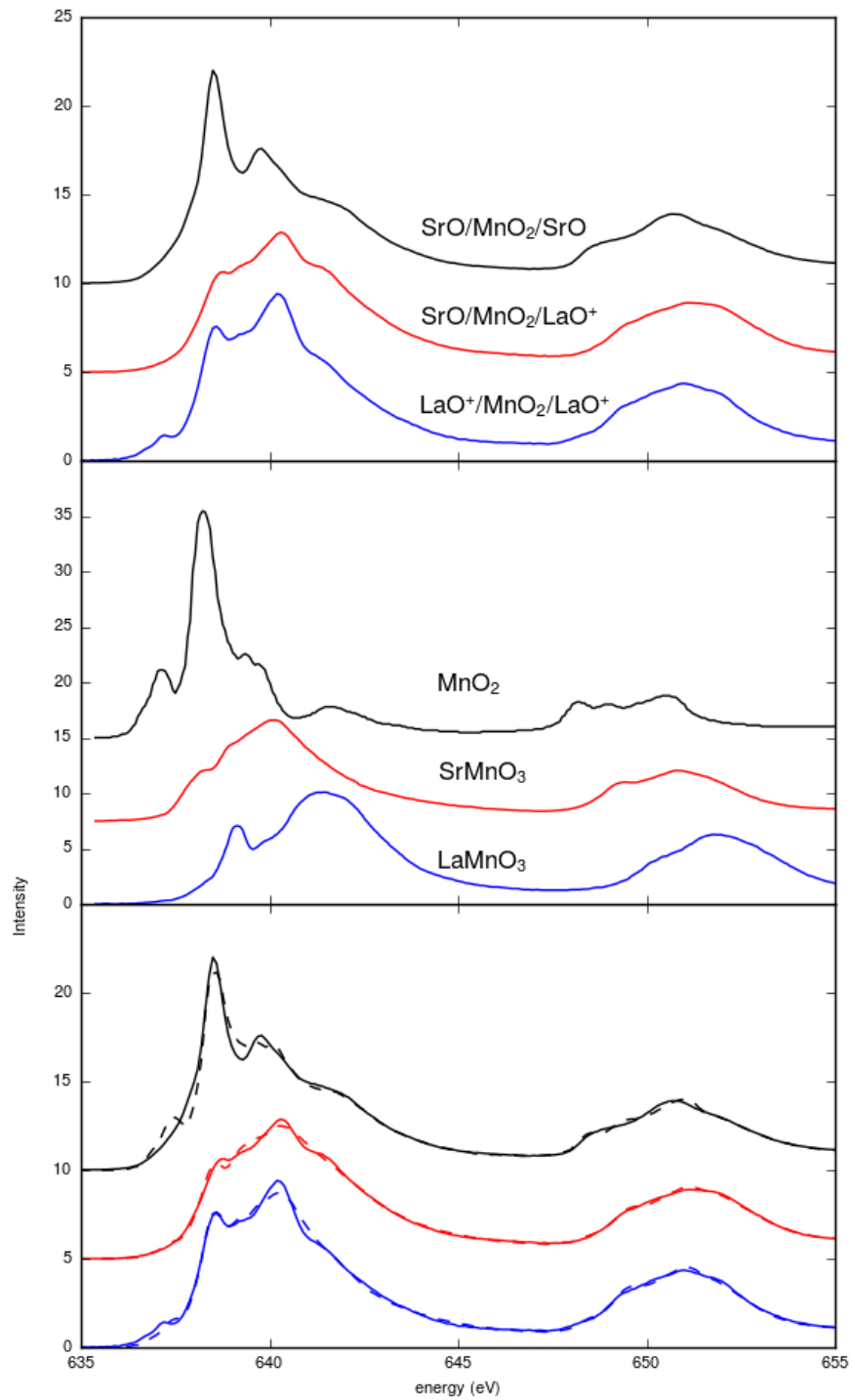
Figure 8.6: (top) Absorption spectra from monolayer samples from the average of circular right and circular left absorption scans. (middle) Absorption scans from reference spectra. (bottom) Fitted (dashed line) and experimental data (solid line) of the sample spectra by summing reference spectra in different ratios. In all panels the edge jump is normalised to 1.

Sample	Spectra ratios			Oxidation State
	MnO(2+)	SMO(3+)	LMO(4+)	
SMS/Ti	0.46 ± 0.02	0.44 ± 0.03	0.10 ± 0.02	2.64 ± 0.13
SML/Ti	0.10 ± 0.01	0.77 ± 0.01	0.13 ± 0.01	3.03 ± 0.05
LML/Ti	0.18 ± 0.01	0.82 ± 0.02	0	2.82 ± 0.06

Table 8.1: The oxidation states determined from least squares fitting of reference spectra shown in figure 8.6. The corresponding number of holes for manganese is three more than the oxidation state.

edge jump. The result of these are convincing fits and are shown in the bottom panel of figure 8.6, the calculated oxidation states and corresponding ratios of the reference spectra are displayed in table 8.1.

There is a significant proportion of manganese 2+ across all the samples. The largest proportion being found in the SMS sample where the manganese would be expected to be in the 4+ state from charge transfer arguments.

The overall oxidation state of the SMS system is calculated at 2.64 which even if it was energetically favourable for only the manganese to change oxidation state and not the surrounding titanium ions would correspond to roughly 80% of the manganese ions having at least one oxygen vacancy. This number of oxygen vacancies might suggest problems with the sample growth.

The SML and LML samples are somewhat similar so will be considered together. The 3+, 4+ ratio in the SML and LML samples are roughly the same as expected from bulk (0.8/0.2 and 1.0/0.0 respectively) [194], the main difference being the addition of manganese 2+ ions, the presence of which could contribute to the conductivity seen in the previous section.

These valencies cannot be explained by charge transfer arguments and are expected to be a result of oxygen vacancies induced by the growth. Nakagawa *et al.* [174] showed that the structure of an interface can be dependent upon the deposition order of different layers between polar and non-polar materials sometimes inducing intermixing and other times introducing oxygen vacancies. They found that $LaO/AlO_2/SrO$ interfaces introduced oxygen vacancies with $LaO/TiO_2/SrO$ interfaces introducing ion intermixing. This kind of oxygen vacancy which is lo-

Sample	Spin (μ_B/Mn)	Orbital (μ_B/Mn)	Total (μ_B/Mn)
SMS/Ti	0.82 ± 0.02	0.29 ± 0.006	1.11 ± 0.05
SML/Ti	0.41 ± 0.003	0.15 ± 0.001	0.56 ± 0.05
LML/Ti	0.50 ± 0.005	-0.10 ± 0.001	0.40 ± 0.05

Table 8.2: Sum rule derived spin and orbital magnetic moment values are derived from the 1.7 K, 6 T data in figure 8.7.

calised at the interface to account for the polarity difference between the materials may be difficult to remove with post growth annealing in an oxygen environment or even by increasing the pressure of the oxygen atmosphere during growth especially if this is an energetically favourable way of accounting for the polar interface.

The reduced proportion of manganese 2+ and therefore oxygen vacancies in the SML and LML samples is accounted for by the ion intermixing observed with the EDS mapping in these samples which will account for the polar interfaces and therefore require fewer oxygen vacancies to equilibrate.

Electron energy loss spectroscopy (EELS) measurements could be useful in determining the cause of the 2+ ions, as in the case of reference [174] by determining the oxidation state of the surrounding ions [195].

XMCD Measurements

XMCD measurements were taken in a 6 T field on all three samples and strong dichroic signals were observed at 1.7 K, as shown in figure 8.7. Sum rule analysis of the dichroic signals are displayed in table 8.2. The overall moment sizes are of the order of magnitude expected for a thin-film. The moment size in the SMS sample is significantly larger than in the LML or SML samples. The moment size roughly follows the proportion of manganese 2+ in each sample. This is due to manganese 2+ having five electrons in the d-orbitals, in a high spin state, with all the spins aligned in the same direction.

It should be noted that the moment derived here is an average over all manganese ions and that any non-magnetic ions will still contribute to the absorption but not the dichroism. These values should therefore be considered as a minimum.
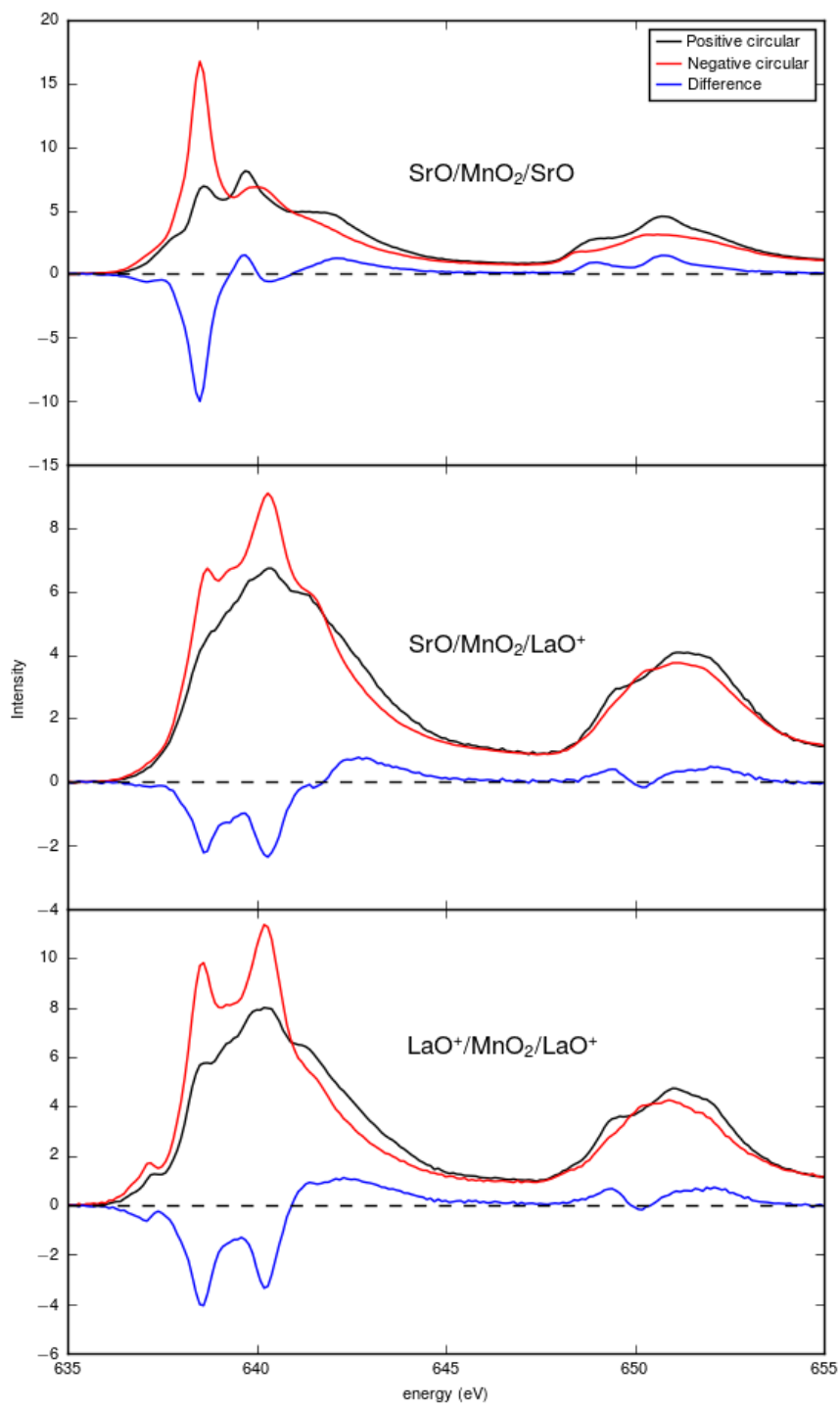
Figure 8.7: Base temperature (1.7 K) XMCD spectra from the SMS (top), SML (middle), and LML (bottom) samples in the maximum field of 6 Tesla.

Comparing these measurements to multiplet calculations carried out on thin films of $MnFe_2O_4$ [196] (figure 8.8), there is a striking resemblance between the dichroism of the SMS sample and calculations for manganese 2+ in a tetrahedral environment.

This would suggest that the apical oxygens around the manganese 2+ ions are both missing and that the in-plane oxygen ions are highly distorted to something resembling a tetrahedral geometry. From the calculations in figure 8.8 [196] it can be seen that there is also an increased dichroism in this case which is reflected in the increased moment size for the SMS sample.

XMCD is not a perfect technique and is useful for comparative measurements between samples but due to the close nature of the manganese L-edges, accurately determining a moment size is difficult, and depends upon the choice of where one peak ends and the next peak begins, explained by Piamonteze *et al.* here [197].

This shows to some extent the ability to control the magnetic moment size with oxidation state. However, the desired effects were not achieved through charge transfer from the surrounding layers but properties introduced by the layer deposition method.

8.2.3 Magnetic Field Dependence

Magnetisation curves were taken by measuring the intensity on and off the peak in the dichroism while varying the field from -6 to $+6$ Tesla and back to -6 Tesla, then repeating with the opposite polarity of the light. The sample magnetisations are shown in figure 8.9, for all three cases a paramagnetic like field dependence with no remnant magnetisation is observed. All the curves have a slight positive gradient at the high field values, a paramagnet would be expected to saturate to a constant value at high fields. The field dependence for a paramagnet outside the linear low field Curie constant region is that of a tanh following the equation:

$$M(B) = \mu \tanh \frac{\mu B}{k_B T} \tag{8.1}$$

Where μ is the moment size, B it the applied field, k_B is Boltzmann's constant, and T is the temperature. In nanoparticles a form of magnetism called superparamagnetism can occur [198–202]. Where there are ferromagnetic nanoparticles that are separated spatially and therefore do not interact with each other, forming a system
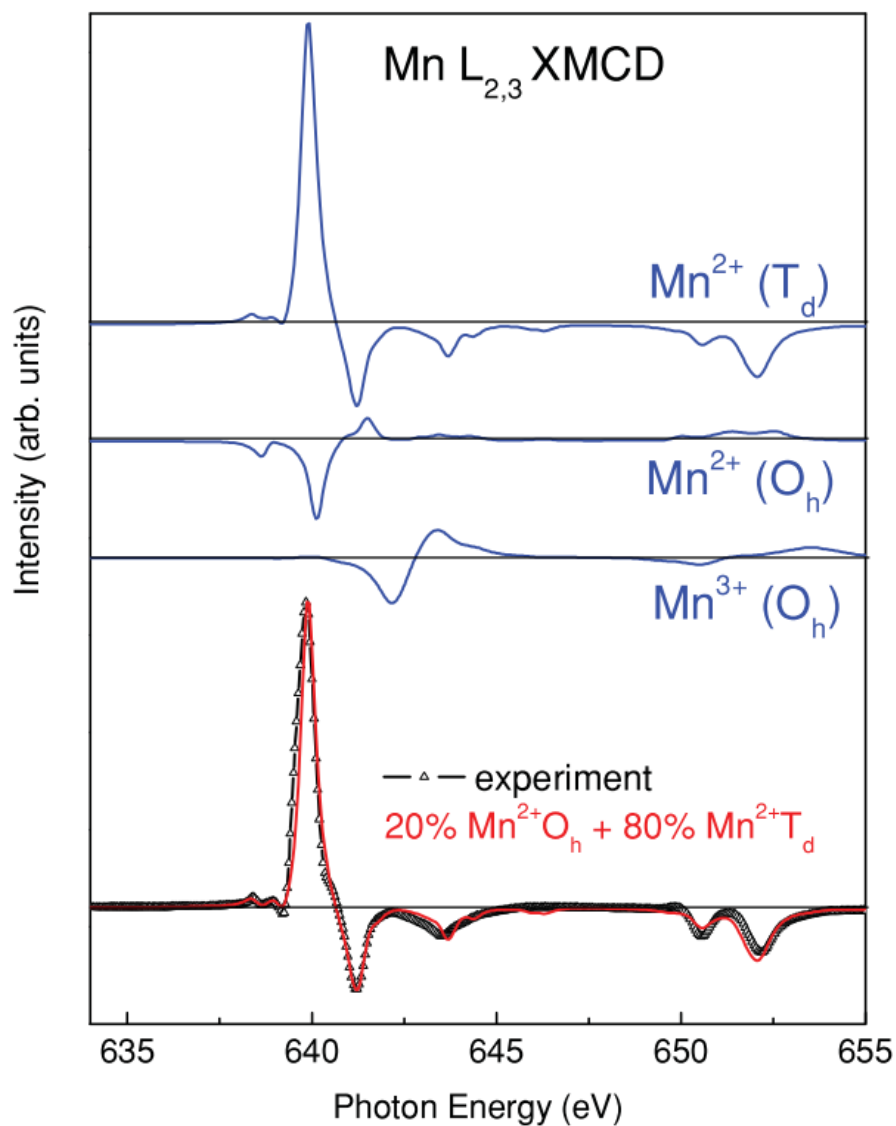
Figure 8.8: Comparison of the Mn $L_{II,III}$-edges' XMCD of $MnFe_2O_4$ (5 nm) to the calculated Mn $L_{II,III}$ edges XMCD for Mn^{2+} (T_d), Mn^{2+} (O_h), and Mn^{3+} (O_h) (blue lines) and their weighted sum (red line) (T = 300 K, H = 5 T) [196].
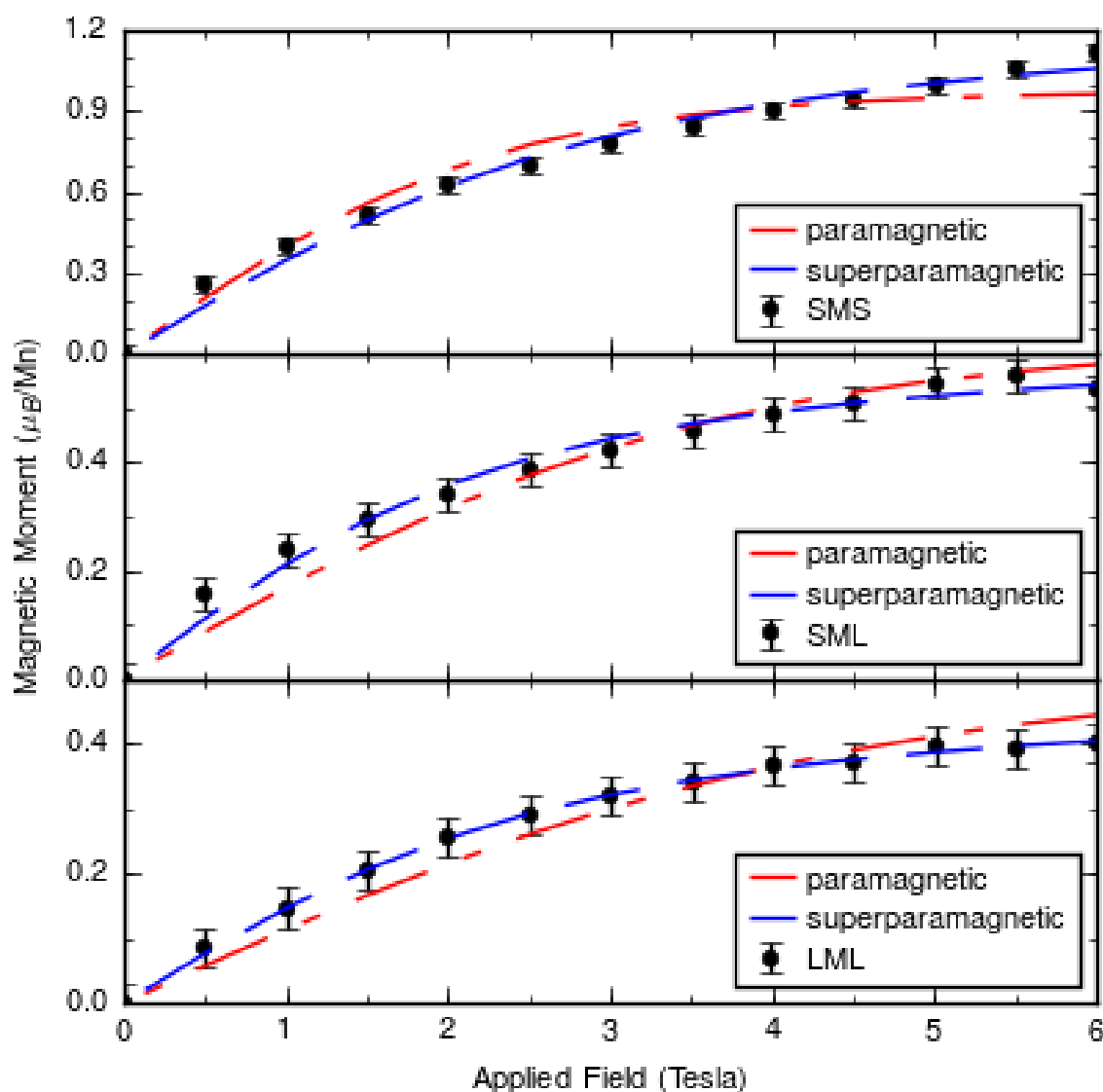
Figure 8.9: Field dependence of the manganese magnetisation, top, middle, bottom; LML, SML, and SMS samples respectively. Experimental data represented by black circles, fits to paramagnetic and superparamagnetic models shown in red and blue dashed lines respectively.
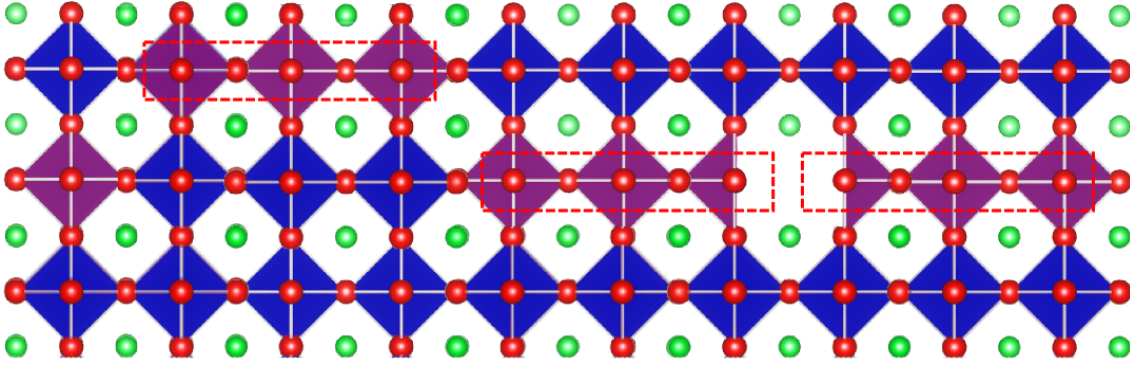
Figure 8.10: Schematic of how both ion interdiffusion and oxygen vacancies can introduce pockets of locally ferromagnetic manganese (surrounded by red dashed boxes) that are not coupled to each other.

which behaves like a paramagnet with large moments. Superparamagnetism is a magnetic effect which comes from the magnetic separation of moments so that they are no longer interacting and is not specific to certain systems [203].

Superparamagnetism has been observed in thin-film samples [204–206], for example $Co_{0.9}Zn_{0.1}Fe_2O_4$ grown by pulsed laser deposition on MgO substrates displays superparamagnetic properties [207]. In these cases nano-crystallites instead of smooth layers were formed which caused the superparamagnetism.

An analogous effect can occur in our thin-film materials where the manganese inter-diffusion will remove the Mn-O-Mn bonds and will interfere with any exchange interactions, also oxygen vacancies will remove the superexchange pathway causing the manganese ions to be non-interacting. An example of how such isolated ferromagnetic 'nanoparticles' may form is shown in figure 8.10. Superparamagnetism is characterised by the Langevin function and the magnetisation follows the relation:

$$M(B) = n\mu \left(\frac{1}{tanh\frac{\mu B}{k_B T}} - \frac{1}{\frac{\mu B}{k_B T}} \right) \tag{8.2}$$

Where now n is the density of nanoparticles in the sample and μ is the magnetic moment of a nanoparticle. All other variables have their usual meaning. The Langevin function has a positive gradient at high x values. Fitting to both the paramagnetic and superparamagnetic functions is shown in figure 8.9 with the results of the fits in table 8.3. The superparamagnetic model has consistently better R^2 values than the paramagnetic model. Although the fits are similar between the paramagnetic and superparamagnetic models and both fit largely within the error bars, the variance of

Sample	Paramagnetism		Superparamagnetism		
	Moment	R^2	Density	Moment	R^2
SMS/Ti	0.97 ± 0.02	0.957	0.720 ± 0.173	1.84 ± 0.16	0.987
SML/Ti	0.62 ± 0.01	0.953	0.274 ± 0.218	2.35 ± 0.22	0.984
LML/Ti	0.51 ± 0.01	0.951	0.232 ± 0.064	2.11 ± 0.06	0.998

Table 8.3: Parameters for the fit to the magnetisation curves with paramagnetic and superparamagnetic models.

the data should also be taken into account. The variance in the datasets are small which suggests that the error bars are overestimates. Just looking at the data points the superparamagnetic model can be seen to fit much better to the data.

From the densities of the superparamagnetic fit 'nanoparticle' sizes can be calculated and contain 1.4, 3.7, and 4.3 manganese ions respectively for the SMS, SML, and LML samples. The values around 4 are consistent with the inter-diffusion for the SML and LML samples noted by EDS mapping in figure 8.3. The value of 1.4 manganese ions per 'nanoparticle' is very small and suggests that the large number of oxygen vacancies are localised to the MnO_2 plane and there are limited vacancies at the apical sites. The tetrahedral distortion could also play an important role as the superexchange strength is dependent to some extent upon bond angle [208]. This could result in strong coupling in pairs of manganese ions where the distortion maintains a bond angle close to 180°.

Superparamagnetism is a widely investigated phenomenon which has potential applications in, for example, hyperthermia. Hyperthermia is a phenomenon where magnetic nanoparticles heat up in varying magnetic fields and has applications in cancer treatment. Increased efficiency of heating in superparamagnetic particles allows safer frequencies of the field to be used [209]. Superparamagnetic nanoparticles also have potential applications as spin filters for spintronics [210]. Thin films may also be useful for such applications, however, there are problems with making small enough grains/nanoparticles [204]. Our samples display very small grains, however, this effect would not be seen in thicker films as (1) it would be localised to the interface and (2) coupling out of the plane from successive layers would link the previously isolated 'nanoparticles'.

8.2.4   Temperature Dependence

The experimental set up on I06 is optimised for low temperature measurements, as a result, higher temperature measurements are technically difficult, especially when the reduced signal requires that a higher number of repeat measurements must be taken to establish a good signal to noise ratio (see the section Section 3.3.3 Diamond I06 on I06 for more details).

As a superparamagnet has very similar behaviour to a paramagnet it will also display a similar temperature dependence. There are however, a few notable exceptions. Superparamagnets display a property called the blocking temperature[3]. The effect arrises due to different time scales of the moments compared to the measurement method. If the measurement time is faster than the time taken for the moments to switch, the sample can be described as being in a blocked state, which would result in the observation of ferromagnetic behaviour. The switching speed of the moments will change with temperature so there is therefore a set blocking temperature for a measurement method with a fixed measurement time. The x-ray measurements taken here are slow (a number of minutes) and are expected to be longer than the moment switching time (usually in the order of nanoseconds). This is further verified by the lack of any ferromagnetic behaviour in the field dependent data.

We therefore expect the paramagnetic and superparamagnetic temperature dependences to follow very similar decays and both described are by the Langevin function. The shapes of the temperature dependences can be fitted with the Langevin function, however, a y-offset is required to achieve a good fit to the data. The results and fit are shown in figure 8.11 with the fit parameters shown in table 8.4. The physical interpretation of the y-offset is an ordered ferromagnetic moment which persists with a negligible temperature dependence up to 200 K.

This interpretation of the results seems unlikely, even though bulk SMO has a transition temperature of 260 K. This is significantly higher than previously observed transition temperatures in thin film samples of only 40 K. For an ordered system the

---

[3]The effect should also be present in a paramagnet, however, it is in reality not observable due to the smaller moment size.
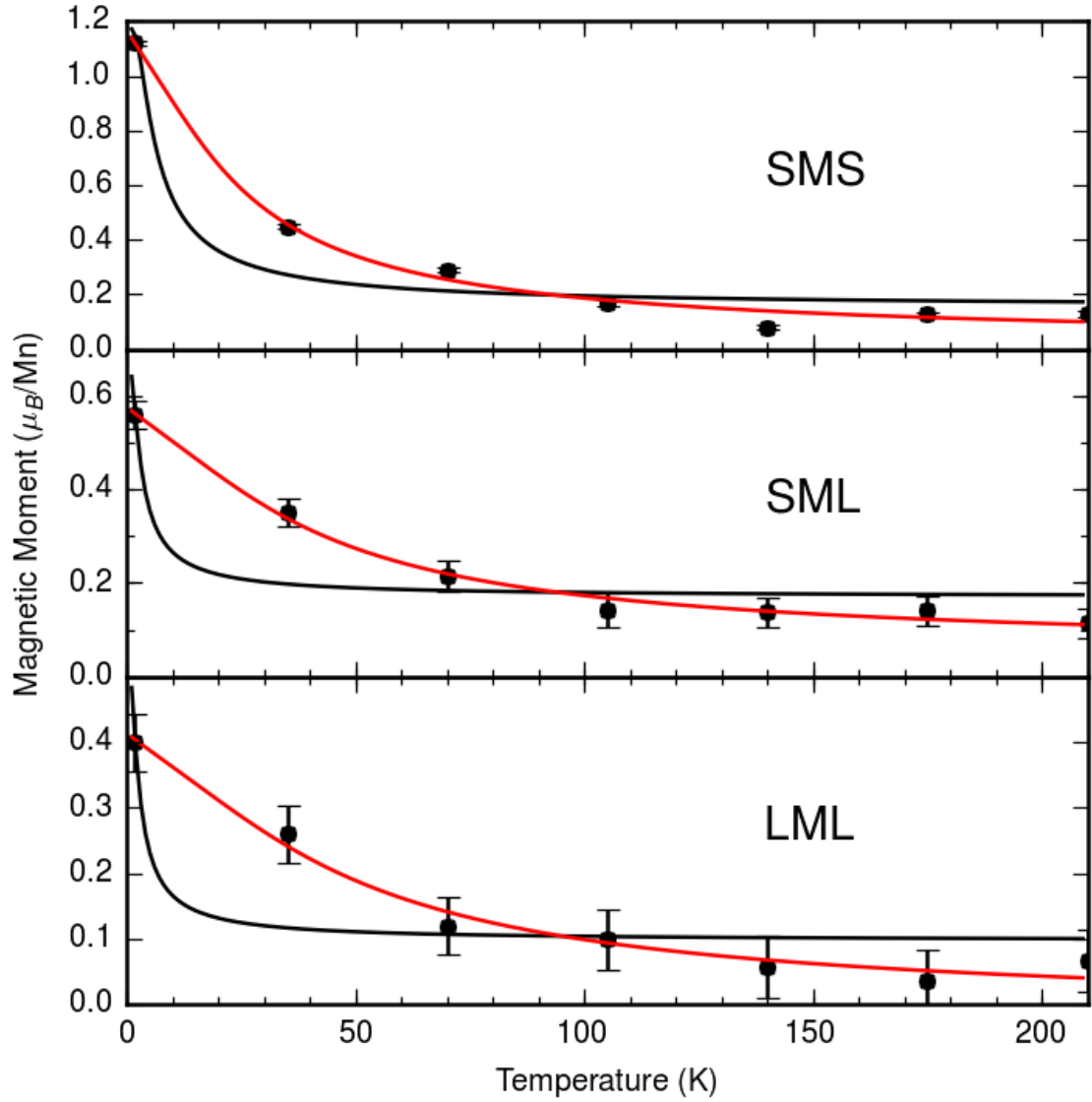
Figure 8.11: Temperature dependences of the manganese magnetic moment. Top middle and bottom show dependences from the SMS, SML, and LML samples respectively. The black and red lines show fits to paramagnetic and superparamagnetic models respectively.

Sample	Paramagnetism		Superparamagnetism		
	Moment	Offset	Moment	Density	Offset
SMS/Ti	1.02 ± 0.11	0.15 ± 0.05	11 ± 1.6	0.104 ± 0.01	0.019 ± 0.03
SML/Ti	0.49 ± 0.07	0.17 ± 0.03	18 ± 2.2	0.029 ± 0.004	0.05 ± 0.02
LML/Ti	0.42 ± 0.07	0.097 ± 0.03	21 ± 4	0.021 ± 0.004	-0.017 ± 0.03

Table 8.4: Parameters for the fit to the temperature curves with paramagnetic and superparamagnetic models.
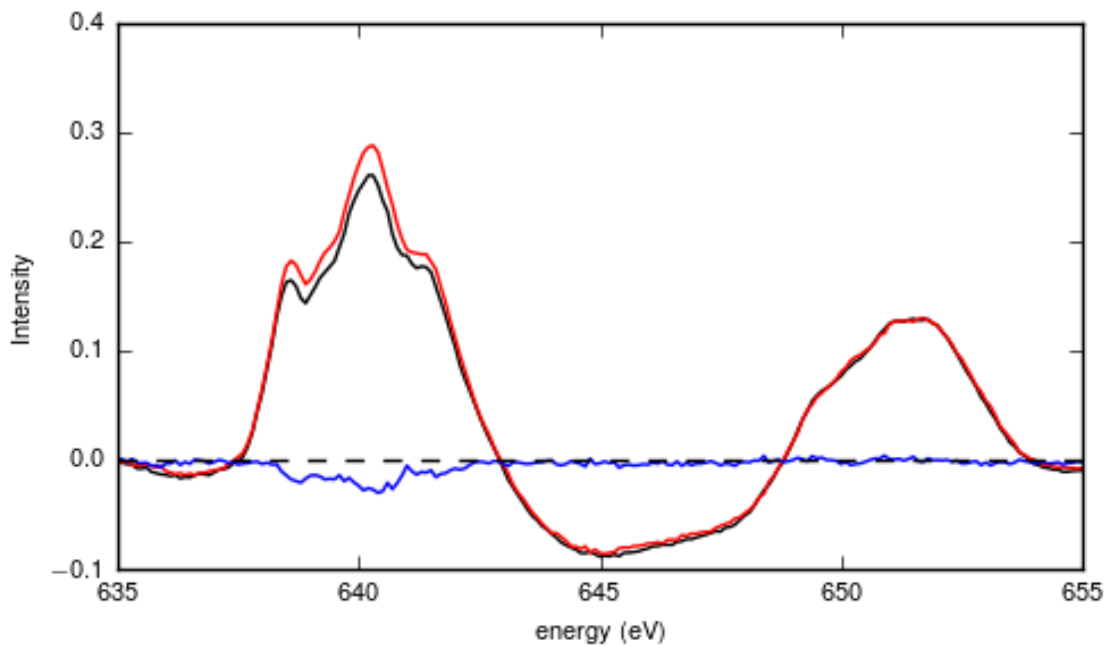
Figure 8.12: Spectra with circular right, circular left, and the difference, shown for the SML sample at 210 K in a 6 T field.

removal of nearest neighbours by layering a material in a heterostructure reduces the ordering temperature as evidenced by the reduction in ordering temperature noted in SMO. The remnant moment is small but appears real as shown by the 210 K data from the SML sample (figure 8.12). Although the baseline is atypical it is well matched between the two spectra. Further, a ferromagnetic moment of this size would be observable in the low-temperature field dependent data. The superparamagnetic model fits the data to a high degree but the fit parameters are not consistent with those from the field dependent data. Fitting both the field and temperature dependent data simultaneously (figure 8.13 and table 8.5) further verifies that the model cannot fit the temperature data[4].

In some situations the temperature dependences of ferrimagnetic samples can display relatively flat temperature dependences which could be an explanation for the constant moment above 100 K, however, this is due to the moments changing size in an unequal way until they become antiferromagnetic and is usually present in

---

[4]The data is fitted with a least squares algorithm, as such all the data points are treated equally. As a result the field dependent data dominates the fit
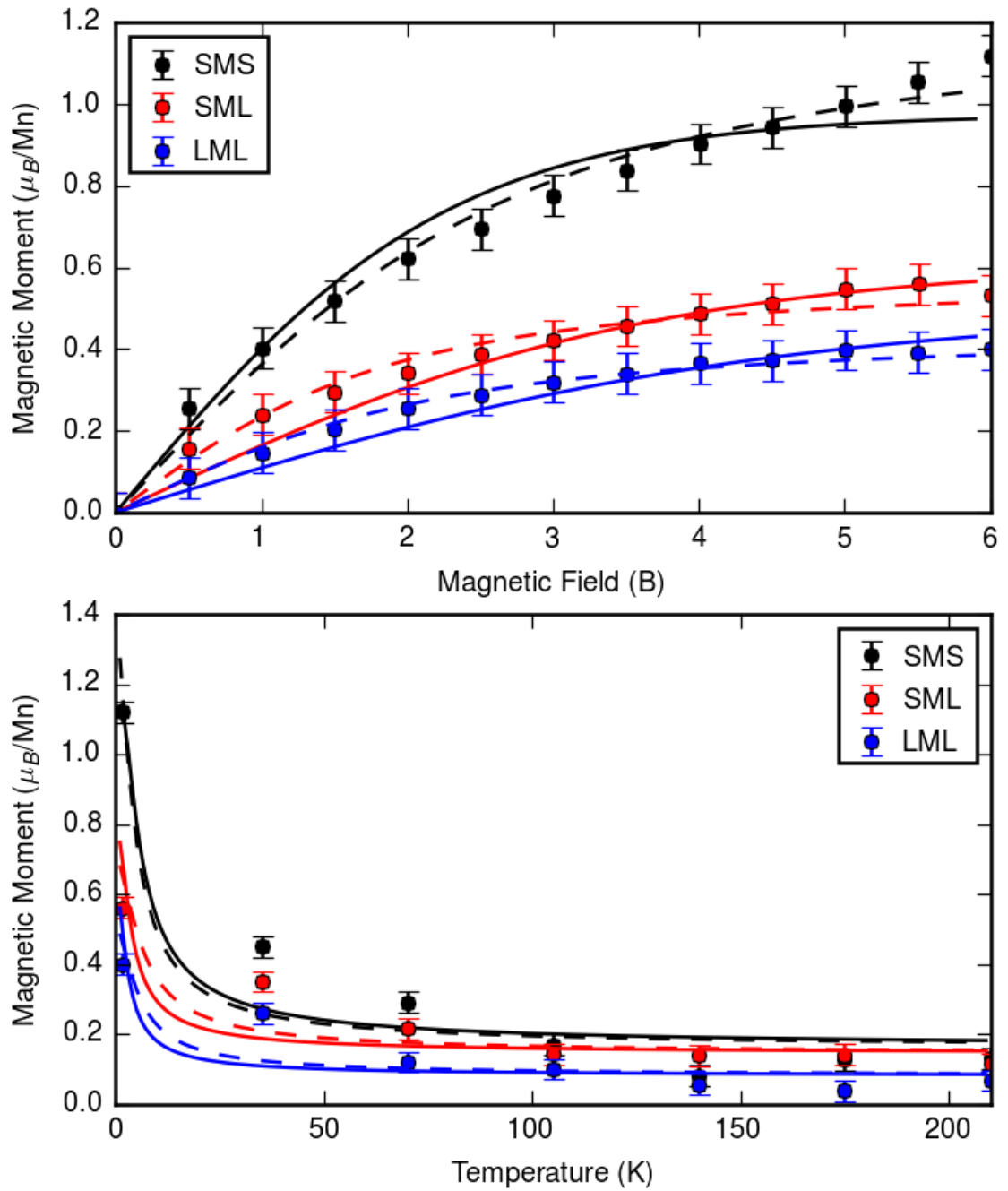
Figure 8.13: Simultaneous fitting of both the temperature and field dependent datasets using the same model. Solid lines show a paramagnetic model and dashed lines show the superparamagnetic model.

Sample	Paramagnetism		Superparamagnetism		
	Moment	Offset	Moment	Density	Offset
SMS/Ti	0.98 ± 0.02	0.16 ± 0.03	2.01 ± 0.28	0.60 ± 0.09	0.16 ± 0.03
SML/Ti	0.61 ± 0.02	0.14 ± 0.02	2.96 ± 0.56	0.20 ± 0.04	0.14 ± 0.02
LML/Ti	0.50 ± 0.01	0.08 ± 0.02	2.56 ± 0.54	0.18 ± 0.04	0.08 ± 0.01

Table 8.5: Parameters from simultaneous fitting of temperature and field data.

systems where there are two different magnetic elements. Ferrimagnetism has been observed in purely manganese systems, albeit rarely. Ferrimagnetic manganese has most commonly been found in molecular magnets [211, 212], although the system $YBaMn_2O_5$ is ferrimagnetic [213], where there is a reduced dimensionality of the manganese similar to the CuO planes in YBCO. In this case the ferrimagnetism is due to a combination of antiferromagnetism and charge ordering. There is a chequerboard pattern of manganese 2 and 3 plus ions which have different size moments and antiferromagnetic coupling between the two. A similar effect would be possible in these samples with the different oxidation states found from the valence calculations. A change in ferrimagnetic moment sizes would be evidenced by a change in the dichroic lineshape with temperature. The normalised dichroism spectra for the SMS sample is therefore shown in figure 8.14. The dichroic lineshape is constant with temperature with the lowest temperature, 1.7 K, data being anomalous. The shift in the dichroism cannot account for the low temperature increase in the magnetisation over the other samples as this shift would actually constitute a reduction in the total moment, it could however, explain to some extent the increased orbital moment. These results do not rule out ferrimagnetism, just that any ferrimagnetism that may exist has a fixed moment ratio with temperature and therefore cannot explain the higher temperature linear dependence observed. A ferrimagnetic arrangement would however, cause a linear high-field field-dependence as the moments begin a spin flop transition.

Temperature dependences qualitatively similar to those observed here have been observed in magnetic nanoparticles due to size effects [214, 215]. At low temperatures there is a significant deviation from the expected $T^{3/2}$ Bloch law for a ferromagnet. This is explained by the nanoparticle size altering the magnon spectrum as
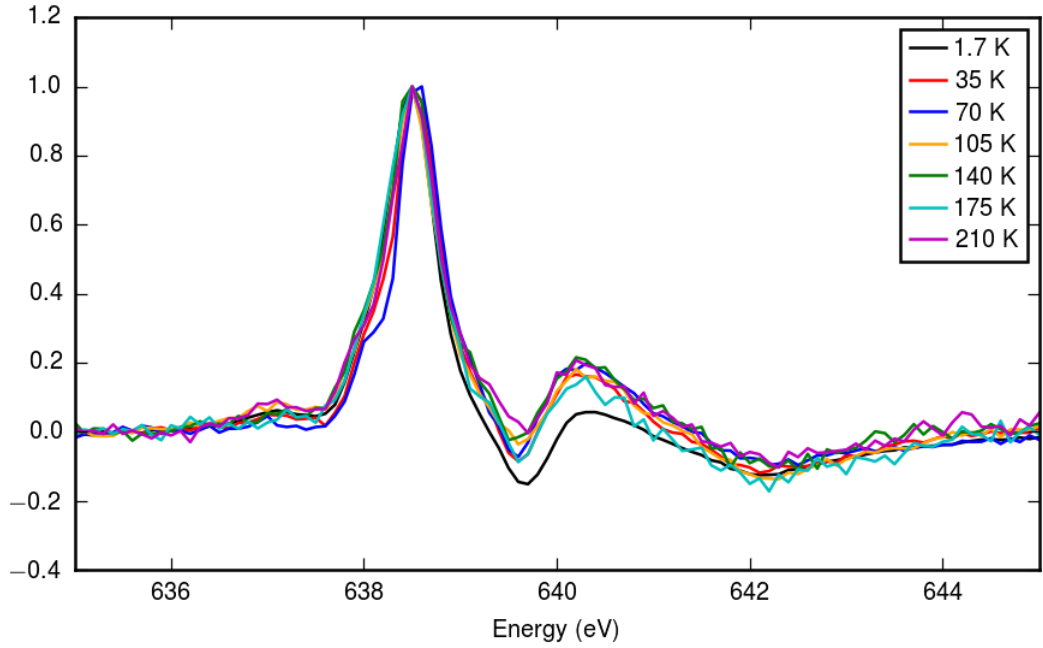
Figure 8.14: Normalised dichroic signals at different temperatures for the Mn L_{III} edge of the SMS sample.

long wavelength magnons can no longer propagate. Long wavelength magnons are responsible for demagnetisation at low temperatures and the suppression of these magnons results in an increase in the sample magnetisation. The functional form of this increase is exponential of the form $M_s = Ce^{-E/k_BT}$ and has been shown to be prevalent below around 100 K. Above this temperature there is a crossover back to the normal Bloch temperature dependence. M_0 is the saturation magnetisation, C is related to the spin wave number and occupancy and relates to the linear region at high temperatures, the E/k_B value relates to the shape of the exponential decay and is dependent upon the spin wave energy levels.

The result of such a fit is shown in figure 8.15. The low temperature spin-wave adjusted Bloch function fits all three datasets without the need for a transition to the high temperature Bloch law. The fitted parameters for E/k_B are 18.0±2.7, 30±3, and 35±6. These values are within the ranges from the previous measurements [214, 215]. As there is no real magnetic transition observed, a different explanation for the change in the transport measurements of the LML sample is required. The change in conductivity of the sample at low temperatures could also be related to the curtailing of the magnon spectrum.
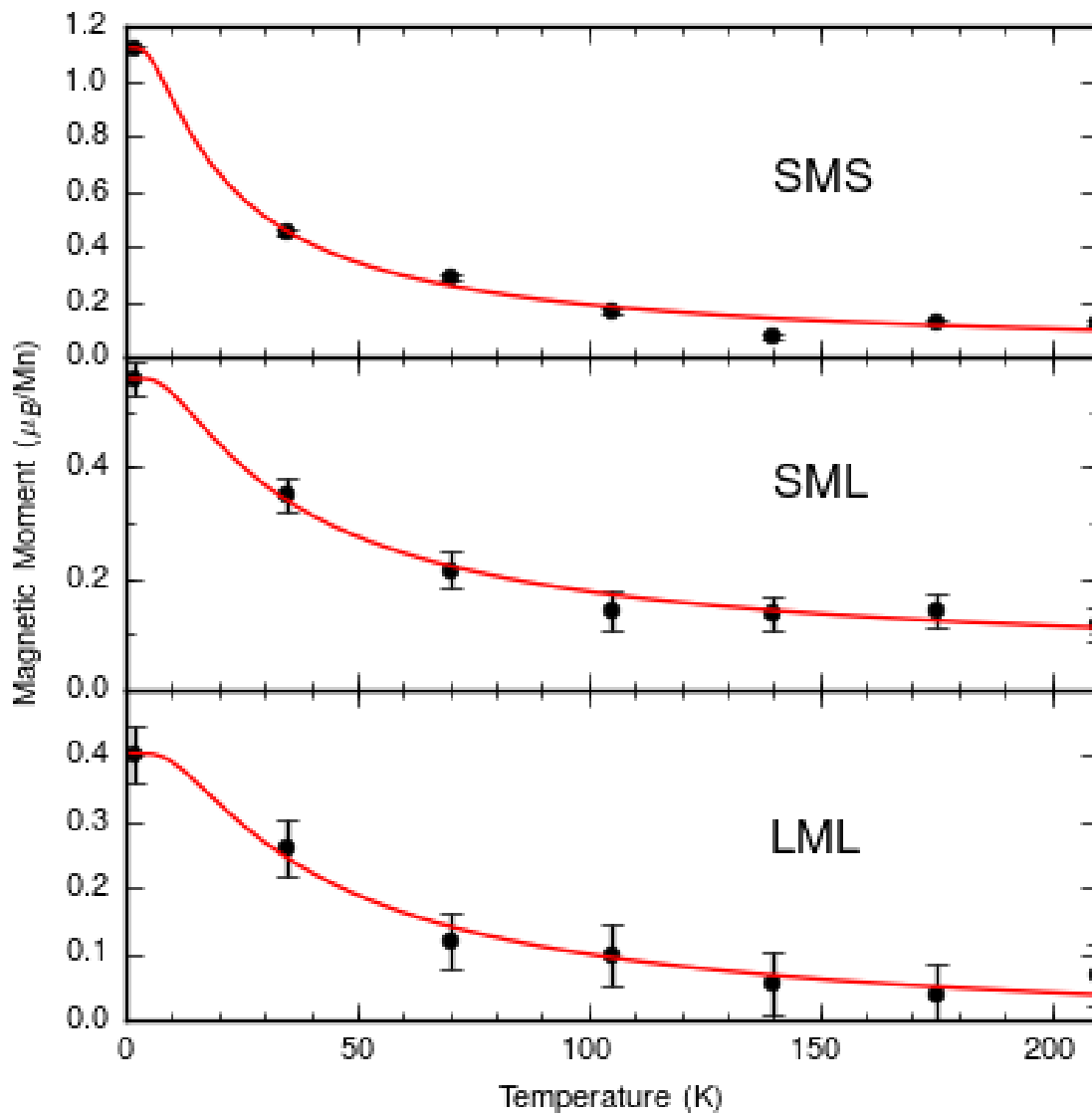
Figure 8.15: Fitting of the temperature dependent data to a modified low temperature Bloch model described by $M_s - Ce^{-E/k_B T}$.

8.3 Summary

The electronic and magnetic properties of manganese oxide monolayers in heterostructures between $LaAlO_3$ and $SrTiO_3$ have been measured. Three samples were measured with structures $LaO/MnO_2/LaO$ (LML), $SrO/MnO_2/LaO$ (SML), and $SrO/MnO_2/SrO$ (SMS). Magnetic and electronic measurements were given by x-ray absorption techniques with sample quality and conductivity given by electron microscopy. The differing charge environments induced by the neutral SrO layers and the positively charged LaO layers were expected to alter the magnetic properties of the manganese *via* charge transfer.

Scanning transmission electron microscopy measurements showed apparently high quality interfaces and the desired sample structures across the three samples with epitaxial growth and no defects. Further investigation using an energy sensitive electron detector allowed the determination of different chemical elements. This showed that the manganese layer does not form a single layer in the SML sample and that some intermixing is occurring of around three unit cells when the capping layer is $LaAlO_3$. Ion intermixing was not observed in the SMS sample. Ion intermixing has been shown to be a prevalent effect in heterostructured systems and can occur to compensate for a polar interface [174].

Scanning tunnelling microscopy was then used to give local conductivity information around the manganese layer, not possible from bulk measurements. This showed that the samples display conducting interfaces. The presence of conducting regions in $SrTiO_3$ deposited by pulsed laser deposition is not uncommon and can occur due to a reduction in the oxygen composition so that it becomes non-stoichiometric, $SrTiO_{3-\delta}$ [189, 190]. This conduction is then attributed to the presence of titanium 3+ ions. These conducting regions are often localised to interfaces and it is therefore difficult to determine what exactly is causing the conduction in these samples. These conductivity effects have been shown to be reduced in other samples by growth in an oxygen environment and post growth annealing [189].

X-ray absorption measurements were fitted to reference samples to determine a rough manganese oxidation state for the samples. The x-ray absorption spectra are very different from that expected from purely charge transfer from the surrounding layers. Significant quantities of manganese 2+ are detected across all the samples.

The manganese 2+ concentration cannot be explained by charge transfer and is expected to be a result of oxygen vacancies induced by the growth method. Nakagawa *et al.* [174] showed that the structure of an interface can be dependent upon the deposition order of different layers between polar and non-polar materials, sometimes inducing intermixing, and other times introducing oxygen vacancies. They found that $LaO/AlO_2/SrO$ interfaces introduced oxygen vacancies with $LaO/TiO_2/SrO$ interfaces resulting in ion intermixing. Even by increasing the pressure of the oxygen atmosphere during growth these vacancies may be difficult to remove especially if this is an energetically favourable way of accounting for the polar interface. Our two cases for the top layer are MnO_2/LaO and MnO_2/SrO which appear to induce ion intermixing and oxygen vacancies respectively, although the reverse effects are still expected to exist to some extent in all the samples. The presence of oxygen vacancies explains the large proportion of manganese 2+ in the SMS sample and the intermixing observed by EDS mapping in the SML sample. The overall oxidation states of the ion intermixing dominated SML and LML samples (3.03+, 2.82+) are somewhat close to those expected from pure charge transfer (3.5+, 3+). The SMS sample showed a large deviation from the charge transfer expected value (4+) due to the presence of a large quantity of oxygen vacancies (2.64+).

XMCD measurements were then taken on all the samples at 1.7 K and 6 T. The SMS sample has the largest moment as determined by the XMCD sum rules. This is due to the large manganese 2+ proportion as manganese 2+ will have 5 electrons in the *d*-orbitals all aligned in the same direction. By comparison of the shape of the XMCD spectra to calculations by Matzen *et al.* [196] the SMS sample appears to show that the manganese 2+ ions are in a tetrahedral environment suggesting the oxygen vacancies cause a large distortion of the remaining oxygen ligands away from the usual octahedral arrangement. The calculated moment sizes are 1.11, 0.56, 0.4 μ_B for the SMS, SML, and LML samples respectively, these values are very reasonable compared to other thin film samples of similar thicknesses. XMCD is not a perfect technique and is useful for comparative measurements between samples but due to the close nature of the manganese *L*-edges accurately determining a moment size is difficult, as explained by Piamonteze *et al.* here [197]. These results show to some extent the ability to control the magnetic moment size with oxidation state,

however, the desired effects were not achieved through charge transfer from the surrounding layers, but introduced by the layer deposition.

The magnetic field dependences of all three samples were then measured again by XMCD. The magnetisation did not show any remnant field, showing that the samples are not ferromagnetic, however, the shape of the magnetisation curve indicates that they are superparamagnetic. Superparamagnetism is an effect which is prevalent in magnetic nanoparticles [198–203] and the system behaves in a similar way to a paramagnet with a very large moment size. This suggests that our samples consist of ferromagnetic domains which do not interact strongly. Both ion intermixing and oxygen vacancies will remove the magnetic interactions with the nearest neighbours to the manganese ions, oxygen vacancies remove the intervening oxygen required for the superexchange mechanism while ion intermixing will separate them spatially. Fitting of the magnetisation curves suggests that manganese ions are clustered in groups of only a handful of interaction manganese ions, this is consistent with the intermixing observed from the EDS mapping as well as the proportion of oxygen vacancies.

Superparamagnetic properties have been observed in thin films previously [207], here again the deposition method was pulsed laser deposition and $Co_{0.9}Zn_{0.1}Fe_2O_4$ was deposited. In this case nano-crystallites instead of smooth layers were formed which result in the superparamagnetism There are many examples of superparamagnetism in thin films of nano-crystalline material [204–207]. We believe this is the first example of such a feature in an epitaxial film.

Further evidence of the superparamagnetic behaviour is given in the temperature dependence of the moments which doesn't follow the standard Bloch law. In superparamagnets the magnon spectrum is curtailed by the nanoparticle size, which modifies the Bloch law temperature dependence which then takes on an exponential form [214, 215].

Superparamagnetism is not expected to be observed in thicker films as coupling with ions out of the plane will reconnect ions which would not previously interact.

8.4   Conclusions

We have measured samples of manganese oxide monolayers in differing charge environments provided by heterostructures between $LaAlO_3$ and $SrTiO_3$. The differing charge environments due to the neutral SrO layers and the positively charged LaO layers being expected to alter the magnetic properties of the manganese *via* charge transfer. The samples structural quality and conductivity were measured with electron microscopy techniques. Further analysis using x-ray absorption techniques were used to determine the magnetic and electronic properties of the manganese.

Electron microscopy shows a good epitaxial structure with no dislocations. Further investigation using energy dependent mapping shows that the manganese layer is diffused into the surrounding layers by around 3 unit cells when the capping layer is $LaAlO_3$.

Transport measurements with scanning tunnelling electron microscopy show a conducting interface in all samples. The presence of a conducting interface in the non-polar $SrO/MnO_2/SrO$ (SMS) sample suggests oxygen vacancies introduced in the growth induce the conductivity. This is backed up by the presence of manganese 2+ ions, determined by fitting the manganese absorption spectra with reference spectra of samples with different manganese oxidation states.

X-ray absorption measurements were then taken, these show that the samples broadly fall into two categories, dependent upon the capping layer. Comparison to reference spectra shows significant quantities of manganese 2+ across all the samples. This is expected to be induced by oxygen vacancies in the samples. Lower oxidation states observed in the LML and SML samples is compensated for by ion intermixing

X-ray magnetic circular dichroism (XMCD) measurements at 1.7 K and 6 T show strong a signal in all the samples, with calculated moment sizes of 1.11, 0.56, 0.4 μ_B for the $SrO/MnO_2/SrO$ (SMS), $SrO/MnO_2/LaO$ (SML), and $LaO/MnO_2/LaO$ (LML) samples respectively. These values are consistent with the magnitudes of moments observed in other thin film samples. The varying moments show to some extent that the magnetic properties of the manganese can be controlled by thin film deposition with different surrounding layers. Comparisons to other multiplet calculations suggest that the $SrTiO_3$ capped samples absorption signal is a result of

manganese 2+ in a tetrahedral environment giving evidence that there are oxygen vacancies and a distortion of the remaining in-plane oxygen ligands.

The magnetic field dependences of all three samples do not display any remnant field, revealing that they are not ferromagnetic, however, the shape of the magnetisation curves indicate that they are superparamagnetic and the sample consists of ferromagnetic domains which are separated spatially so that they do not interact strongly. The diffusion of the manganese layer into the surrounding layers and oxygen vacancies would both produce such an effect, stopping the formation of long-range magnetic interactions. The fitted nanoparticle sizes are 1.4, 3.7, and 4.3 manganese ions respectively for the SMS, SML, and LML samples.

The temperature dependent data, although not fitting with the Langevin function, does fit with a modified Bloch law which is again consistent with nanoparticle like objects.

We believe this is the first example of superparamagnetic behaviour in an epitaxial film as opposed to polycrystalline thin films.

We have also shown that although the surrounding layers do not contribute to the manganese layers oxidation state as expected. The magnetic properties of the manganese layers can be controlled by growing samples with different capping layers.

Further Work

As this and the following chapter are investigating very similar samples, details on further work will be given at the end of the conclusions of the next chapter in section

Chapter 9

The Magnetic Properties of Manganese Oxide Bilayers in Different Charge Environments

The following chapter investigates the magnetic properties of bilayers of manganese oxide when surrounded by different configurations of strontium titanate ($SrTiO_3$) (STO) and lanthanum aluminium oxide ($LaAlO_3$)(LAO). The aim is to control the magnetic properties due to the differing charge environments as LaO layers would be expected to donate electrons to the MnO_2 layers. Now in addition to the previous chapter's investigation of the monolayers, an increased coupling between manganese layers out-of-the-plane is expected to strengthen the magnetic coupling and allow for larger ordered moments and higher transition temperatures. We have used x-ray magnetic circular dichroism (XMCD) to determine the magnetisation and temperature dependent properties of these films. This chapter focusses on the results, introductory material can be found in the previous chapter Chapter 7 Sample Growth and the Properties of Thin-Film Perovskite Structures.

9.1   Manganese Oxide Bilayers

To further investigate these systems, bilayer samples were grown, where two MnO_2 layers are separated by a single atomic layer. Now there is an added degree of freedom of what the intervening AO layer is between the two manganese monolayers,

Structure					short label
SrO	/MnO$_2$	/SrO	/MnO$_2$	/SrO	(SSS)
SrO	/MnO$_2$	/SrO	/MnO$_2$	/LaO$^+$	(SSL)
SrO	/MnO$_2$	/LaO$^+$	/MnO$_2$	/LaO$^+$	(SLL)
SrO	/MnO$_2$	/LaO$^+$	/MnO$_2$	/SrO$^+$	(SLS)
LaO$^+$	/MnO$_2$	/LaO$^+$	/MnO$_2$	/LaO$^+$	(LLL)
LaO$^+$	/MnO$_2$	/LaO$^+$	/MnO$_2$	/SrO	(LLS)
LaO$^+$	/MnO$_2$	/SrO	/MnO$_2$	/SrO	(LSS)
LaO$^+$	/MnO$_2$	/SrO	/MnO$_2$	/LaO$^+$	(LSL)

Table 9.1: Growth direction is left to right and the right hand column shows the shorthand notation.

in these samples an increased ordered moment is expected due to increased coupling between the manganese ions out of the plane. The additional manganese layer should also limit the effects of inter-diffusion and fill in the gaps allowing for magnetic exchange between what would have previously been separated regions. The samples are again topped with a titanium layer to reduce charging effects. Samples are described in table 9.1 where a short notation for the sample structures is introduced, and visualised in the same order in figure 9.1. This chapter only contains the results from the XMCD measurements as this is part of an extended project with many collaborators. The other measurements taken on the monolayer samples remain to be taken.

9.1.1 Experimental Technique

Eight samples were grown with two manganese oxide layers in different charge environments surrounded by either LaO or SrO. The samples were all grown on TiO$_2$ terminated STO substrates. X-ray absorption measurements including temperature and field dependence XMCD measurements were taken using total electron yield. The high field magnet end-station of the I06:Nanoscale beam-line at the Diamond Light Source Ltd was used with energies at the manganese L_{II}/L_{III} edges. More details of the I06 beamline can be found in section Section 3.3.3 Diamond I06. All
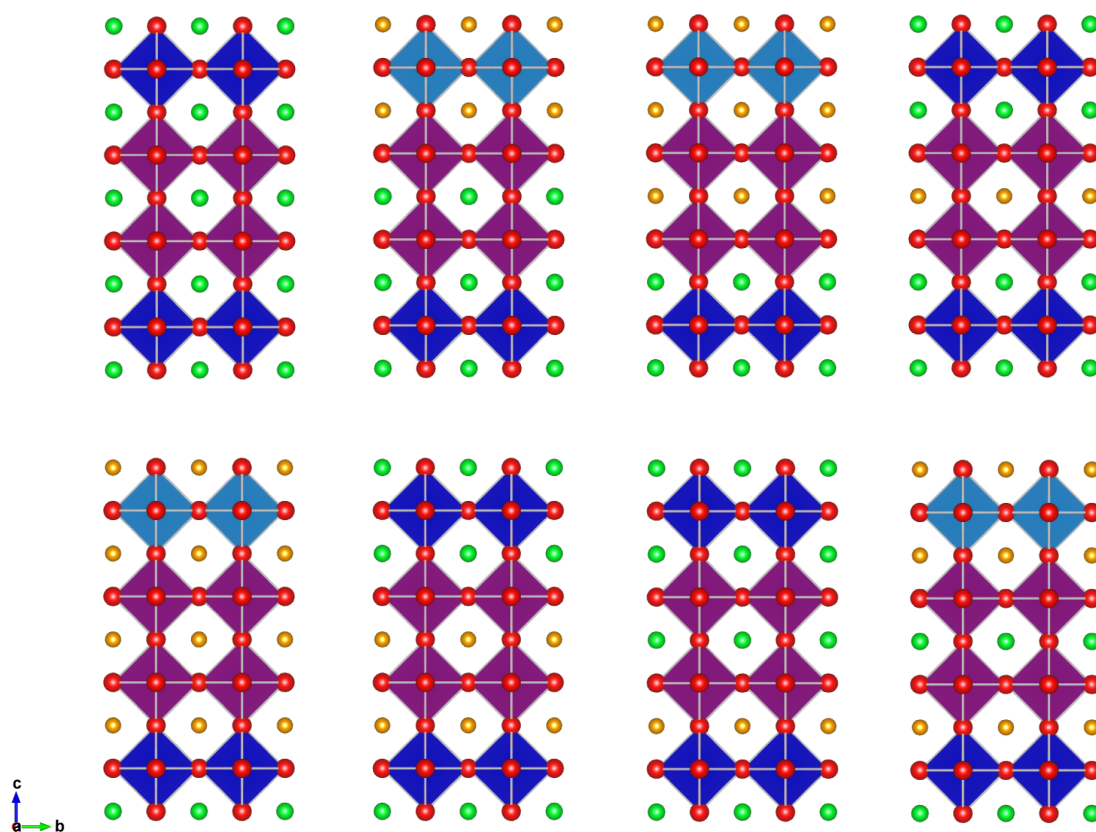
Figure 9.1: Structures around the MnO$_2$ monolayers with atoms depicted as follows green strontium, blue titanium, red oxygen, purple manganese, orange lanthanum, and light blue aluminium. Sample labels from top left to bottom right are as follows, SSS, SSL, SLL, SLS, LLL, LLS ,LSS, LSL.

measurements were taken with the samples oriented at 30° to the main beam to maximise the in-plane magnetisation with the field directed along the beam.

The samples were insulating and as such many effects of charging were observed before the rate of photoelectrons and the drain current could equilibrate. To counteract this, measurements were taken with an extended pre-edge region and also spectra were taken in the sequence with circular polarisations positive, negative, negative, positive so that time dependent charging effects could easily be recognised.

9.2   Results and Discussion

As with the monolayer samples, absorption measurements were taken using total electron yield due to the small sample volume. The lineshapes can broadly be split into two groups and appear to be strongly linked to the capping layer. The samples with a lanthanum oxide capping layer (- - L) resemble the lineshape of the SML monolayer sample and samples with a strontium oxide capping layer (- - S) resemble the lineshape of the SMS monolayer with a dominant Mn^{2+} peak, this is shown in figure 9.2. Analogous to the monolayer samples very little chemical shift is noticeable. The exception to this is in the SSL sample where an apparent positive shift is observed, however, little to no shift in the position of the central peak at the L_{III} edge is observed. The positive shift is therefore likely to indicate the presence of manganese 4+ ions which from the reference spectra (figure 8.6) can be seen to have a higher energy.

9.2.1   Determination of Manganese Valence

Fitting the reference spectra from the middle panel of figure 8.6[1] provides convincing fits and are shown in figure 9.3, with the calculated oxidation states and corresponding ratios of the reference spectra displayed in table 9.2.

---

[1]The reference spectra are fitted to the experimental data using a least squares algorithm with the parameters of the reference spectra magnitudes and a general shift between the monolayer samples and the reference spectra which will account for different energy calibrations between the different measurements. Finally a tanh step edge was fitted to the spectra to account for differences in the edge jump

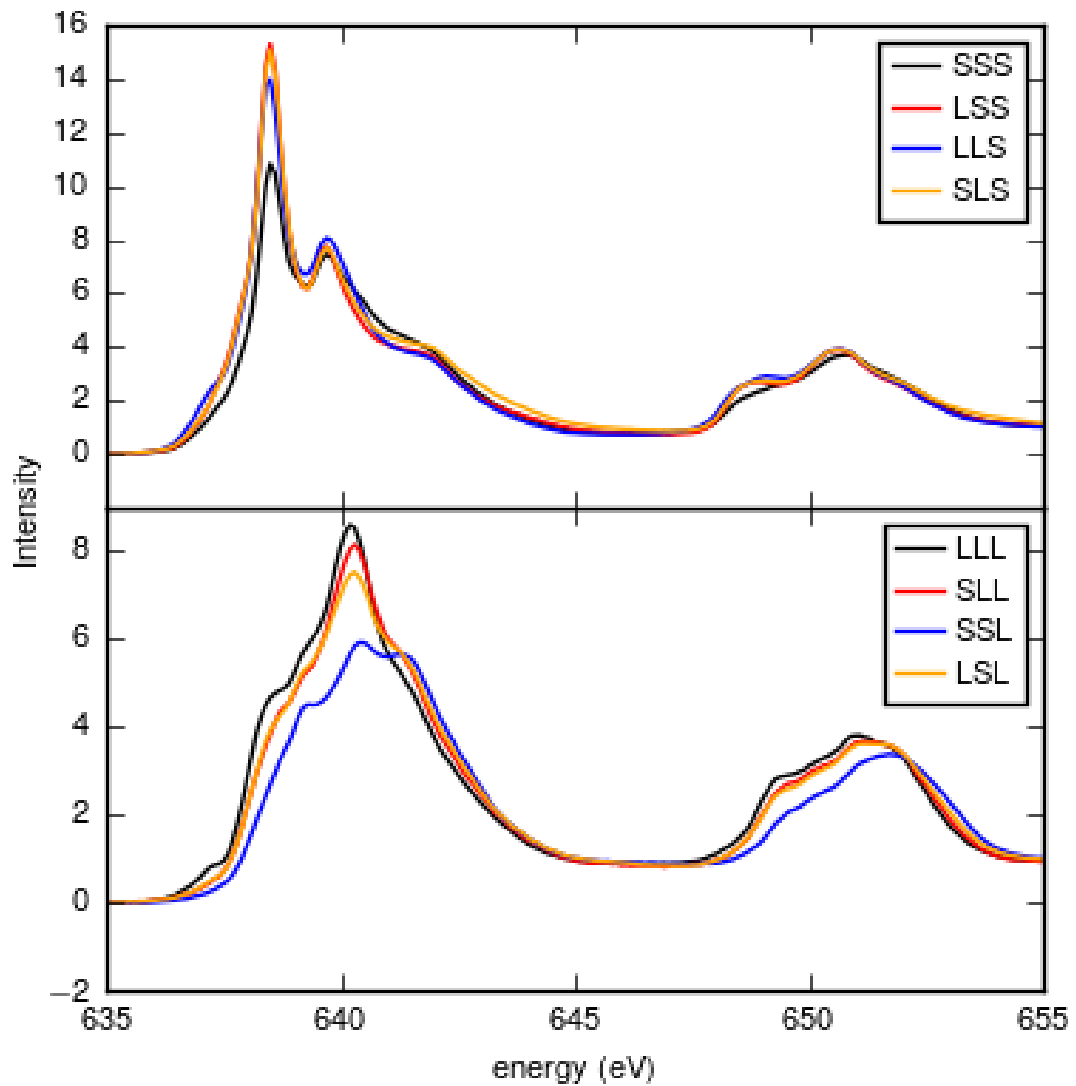Figure 9.2: Absorption spectra from bilayer samples from the average of circular right and circular left absorption scans. (top) L - - samples with lanthanum oxide below the manganese bilayer. (bottom) S - - samples with strontium oxide below the manganese bilayer.
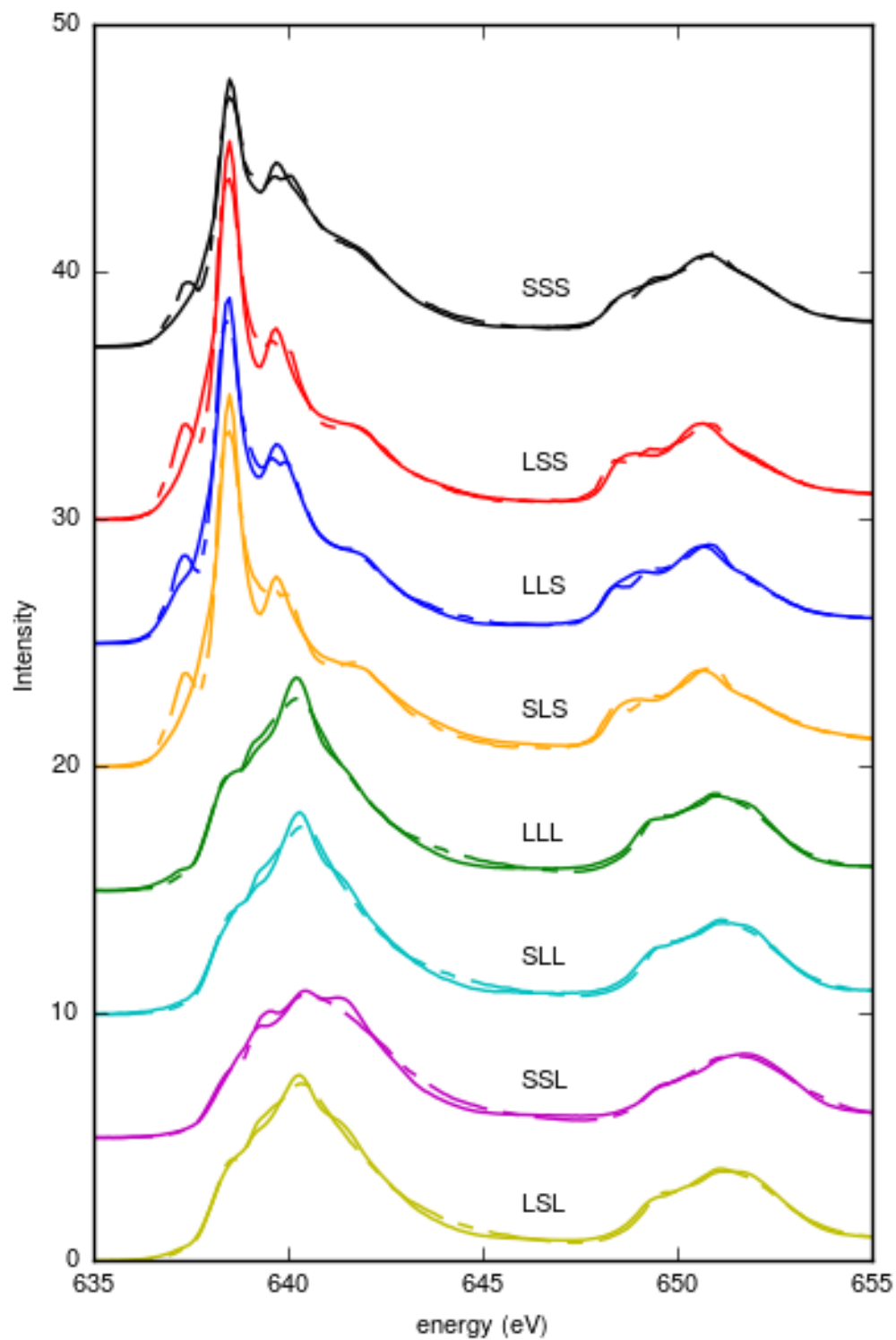
Figure 9.3: (solid lines) Averaged absorption spectra from bilayer samples. (dashed lines) Fitted line from summing reference spectra in different ratios.

| Sample | Spectra ratios | | | Oxidation |
	MnO(2+)	SMO(3+)	LMO(4+)	State
SSS	0.42 ± 0.01	0.54 ± 0.01	0.04 ± 0.01	2.62 ± 0.05
LSS	0.62 ± 0.01	0.33 ± 0.03	0.05 ± 0.03	2.43 ± 0.15
LLS	0.55 ± 0.01	0.45 ± 0.01	0	2.45 ± 0.04
SLS	0.60 ± 0.01	0.30 ± 0.03	0.10 ± 0.03	2.50 ± 0.15
LLL	0.05 ± 0.01	0.95 ± 0.01	0	2.95 ± 0.04
SLL	0.02 ± 0.01	0.98 ± 0.01	0.00 ± 0.01	2.98 ± 0.05
SSL	0.01 ± 0.01	0.69 ± 0.02	0.30 ± 0.01	3.29 ± 0.07
LSL	0.04 ± 0.01	0.88 ± 0.01	0.08 ± 0.01	3.04 ± 0.05

Table 9.2: The oxidation states determined from least squares fitting of reference spectra shown in figure 9.3. The corresponding number of holes for manganese is just three more than the oxidation state.

It is no surprise that the spectra again fall into two broad categories with - - S samples all showing similar oxidation states of around 2.5+ and the - - L samples all showing oxidation states of around 3+. The exception to this is the SSL sample which has the highest oxidation state of any of the monolayer or bilayer samples measured with an oxidation state of 3.29 and is the only sample with an appreciable Mn^{4+} concentration. This accounts for the positive energy shift noted in the previous section. The - - S samples have roughly proportionate values of manganese 2+ and 3+ resulting in oxidations states around 2.5+.

The high quantities of manganese 2+ in the - - S samples provide evidence that the 2+ moments observed in the SMS monolayer sample was not anomalous and is reproducible. This is further evidence that the oxygen vacancies are a byproduct of the deposition of the STO capping layer similar to references [189, 190].

Unlike in the monolayers where manganese 2+ is present in all the samples the - - L bilayer samples only contain small proportions of manganese 2+ and other than the SSL sample (which has already been noted to be somewhat anomalous) small or negligible proportions of 4+. As a result the fitted oxidation states for the LLL, LSL, and SLL samples are found to be predominantly 3+. These are consistent with the monolayer samples with LAO capping layers.

Even though the samples' properties appear to be dominated by the capping layer there is still some variation within the different capping layers. The - - S samples do not follow the expected oxidation states from simplistic charge transfer calculations, however, the SSS sample does have the highest oxidation state which is expected. The other samples SLS and LSS are expected to have similar oxidation states and LLS would be expected to be lower, all are within the calculated errors.

In the absence of the oxygen vacancies produced by the STO capping layer the SSL sample is expected to have the highest oxidation state and this is the case. Even with smaller error bars the remainder of the - - L samples are still very close in oxidation state showing the strong coupling to the capping layer and little effect of the other layers on the oxidation state.

Again these valencies cannot be explained by charge transfer arguments and are expected to be a result of oxygen vacancies induced by the growth method and capping layer [174].

Theoretical calculations have shown that strain can induce a favourable manganese 3+ in LaMnO$_3$ [179, 180]. As our results show a strong dependence on the capping layer it is expected that this strain is induced by the capping layer. This is unlikely to be the case as the monolayer films were observed to be epitaxial and the capping layer is only 6 unit cells thick. Another possibility is that the titanium is changing oxidation state preferentially over the manganese in the samples governed by ion intermixing. Ion intermixing may also allow for energetically favourable charge transfer horizontally instead of in the growth direction, where the manganese nearest neighbour is replaced by a titanium or aluminium ion. This suggests that more care must be taken to ensure that the charge transfer will happen in the desired direction and theoretical calculations should be carried out first.

A localised probe which is sensitive to the oxidation state such as Electron energy loss spectroscopy (EELS) would be required to determine if the titanium and aluminium ions are playing a role in the manganese oxidation state by determining their oxidation states (as in the case of reference [174]).

Sample (μ_B/Mn)	Spin (μ_B/Mn)	Orbital (μ_B/Mn)	Total
SSS	0.68 ± 0.006	0.24 ± 0.002	0.92 ± 0.006
LSS	1.03 ± 0.028	0.51 ± 0.014	1.54 ± 0.032
LLS	0.94 ± 0.007	0.25 ± 0.002	1.19 ± 0.007
SLS	0.95 ± 0.026	0.19 ± 0.005	1.14 ± 0.026
LLL	0.81 ± 0.005	0.35 ± 0.002	1.15 ± 0.006
SLL	0.56 ± 0.005	0.017 ± 0.0001	0.58 ± 0.005
SSL	0.43 ± 0.005	0.09 ± 0.001	0.52 ± 0.005
LSL	0.61 ± 0.005	0.17 ± 0.001	0.78 ± 0.005

Table 9.3: Sum rule derived spin and orbital magnetic moment, values are derived from 1.7 K, 6 T data in figure 9.4.

9.2.2 XMCD Measurements

The absorption spectra for circular-right and circular-left polarised light and the corresponding difference spectra are shown in figure 9.4, sum rule analysis of these spectra is shown in table 9.3. It is interesting to note that even though the SSL sample has a different spectral lineshape, the dichroic signal has a similar shape to the other - - L samples.

The calculated moment sizes are similar in magnitude to those from the monolayer samples, an increased moment could be expected for an increased manganese coupling due to its higher concentration in these samples, however, this is not observed. The moments of the - - S samples are generally larger than the - - L moments due to the large manganese 2+ concentration. The XMCD signal in all the - - S samples resemble the multiplet calculations for manganese 2+ in a tetrahedral environment from figure 8.8 [196] resembling the monolayer SMS sample. The spin moment sizes of the - - S samples appear to follow a similar trend to the manganese 2+ proportion. The orbital moments do not appear to be linked to any particular feature from the valence calculations. The calculated orbital moments are significant and contribute a large proportion to the overall moment sizes.

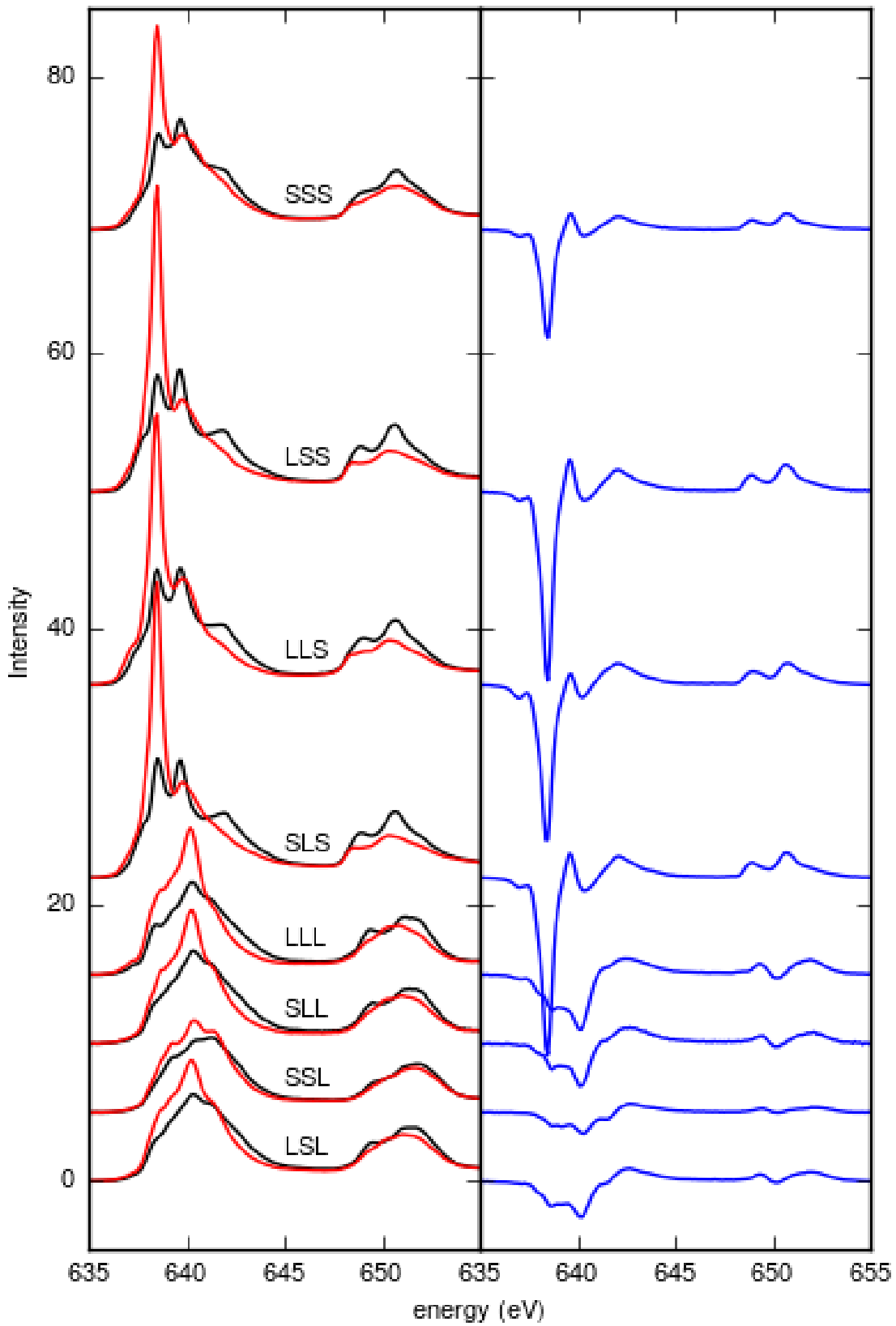The expected moment sizes from the simple valence and only charge transfer

Figure 9.4: Base temperature (1.7 K) spectra in maximum field of 6 Tesla. (left) Circular right (red) and circular left (black) spectra from the bilayer samples. (right) Difference spectra between circular right and circular left.

would be in the order LLL>LSL>SLL>SSL and this order is reproduced. It is also consistent within the - - L samples that the samples containing more LaO layers have larger moments. Which when referring to table 7.3 is consistent with $LaMnO_3$ having a larger moment than $SrMnO_3$.

The lack of increased moment sizes in the bilayers as compared to the monolayer samples is in contradiction to the results of [183] and may be due to a similar inter-diffusion of the manganese into the capping layer as seen with the monolayer samples. Even with inter-diffusion there would still be expected to be more manganese ions stacked vertically than in the monolayer samples and therefore an increased moment size. Apical oxygen vacancies could inhibit the interlayer coupling in the - - S samples, in the - - L samples the valence calculations are also strongly linked to the capping layer and show little variation to the other layers surrounding the manganese oxide. It is therefore again likely that oxygen vacancies are the main contributing factor to the oxidation state and inhibiting the interlayer coupling resulting in the same magnitude of ordered moment.

The tetrahedral distortion could also play an important role as the superexchange strength is dependent to some extent upon bond angle [208]. This could result in strong coupling between pairs of manganese ions where the distortion maintains a bond angle close to 180°. This would maintain a similar moment size to that observed in the monolayer samples even with a similar proportion of oxygen vacancies. As mentioned in the previous chapter XMCD is not a perfect technique due to the close proximity of the manganese L-edges and accurately determining a moment size is difficult, as explained by Piamonteze *et al.* here [197].

Again as in the previous chapter these XMCD measurements further confirm the ability to control the magnetic moment size with oxidation state, not through charge transfer from the surrounding layers but by properties introduced by the layer deposition.

9.2.3   Magnetic Field Dependence

Magnetisation curves were taken by the same method as for the monolayers, measuring the intensity on and off the peak in the dichroism while varying the field from -6 to $+6$ Tesla and back to -6 Tesla, then repeating with the opposite polarity of

| Sample | Paramagnetism | Superparamagnetism | |
	Moment	Moment	Density
SSS	0.86 ± 0.007	1.68 ± 0.01	0.70 ± 0.01
LSS	1.30 ± 0.03	1.86 ± 0.03	1.03 ± 0.03
LLS	1.09 ± 0.01	2.05 ± 0.01	0.72 ± 0.02
SLS	1.04 ± 0.01	2.11 ± 0.01	0.65 ± 0.01
LLL	1.06 ± 0.01	2.70 ± 0.01	0.47 ± 0.03
SLL	0.62 ± 0.01	2.71 ± 0.01	0.23 ± 0.01
SSL	0.58 ± 0.003	1.62 ± 0.003	0.42 ± 0.01
LSL	0.76 ± 0.005	1.98 ± 0.005	0.47 ± 0.02

Table 9.4: Parameters for fits to the magnetisation curves shown in figure 9.5 with paramagnetic and superparamagnetic models.

light.

The magnetisation curves for the bilayer samples show qualitatively a very similar shape to the monolayer samples with an initial curve followed by a linear increase above around three Tesla and no remnant field, suggesting again that these samples are superparamagnetic in nature. The magnetisation curves are shown in figure 9.5 with the results of a fit to a paramagnetic model following equation 8.1 shown by solid lines. As with the previous chapter the paramagnetic model does not reproduce the data and a superparamagnetic model must be considered. The results of a fit to a superparamagnetic model following equation 8.1 are shown by dashed lines again in figure 9.5. The results of fitting to these models are displayed in table 9.4.

Superparamagnetism is usually observed in magnetic nanoparticles , as explained in Section 8.2.3 Magnetic Field Dependence and figure 8.10. Oxygen vacancies and ion intermixing are expected to magnetically isolate small group of manganese ions.

Again the fitted moment sizes per nanoparticle are consistent with nanoparticle sizes of only a few manganese ions. As these densities are related to the coupling of the different 'nanoparticles' the fact that the densities from the superparamagnetic fits is then consistent with oxygen vacancies impeding the interlayer coupling as both the densities and the moment sizes are comparable across the monolayer and bilayer samples.
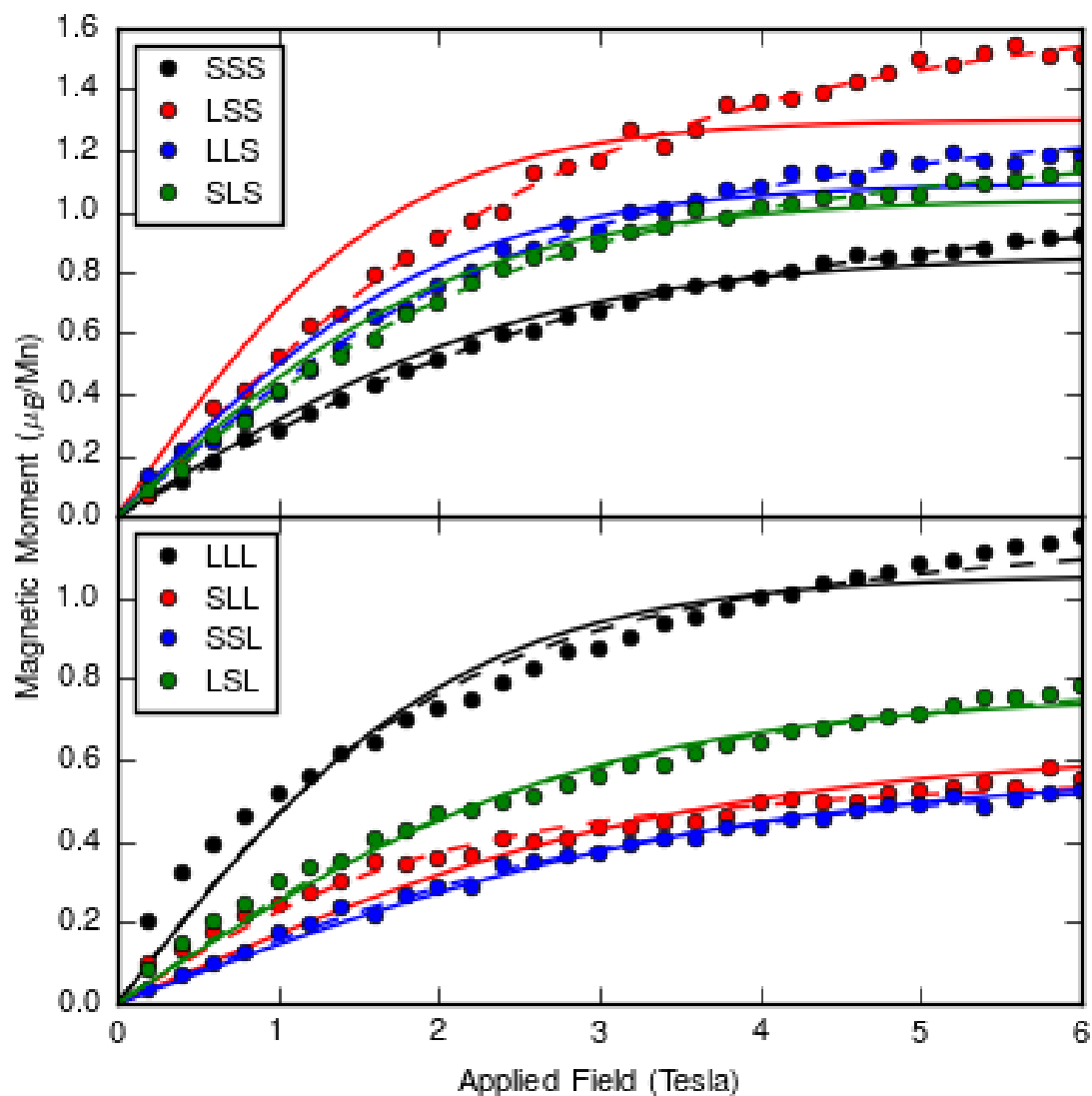
Figure 9.5: Magnetic field dependence of sample magnetisations. Data is represented as filled circles with paramagnetic fits shown by solid lines and superparamagnetic fits shown by dashed lines.

Generally the samples can be split again into the two groups observed from the lineshapes by the shapes of the magnetisation curves. The - - L samples are roughly linear above 2 T while the - - S samples have a more gradual curve. This is mirrored in the fitted nanoparticle densities, which are linked to the shape of the tanh curve.

The LLL sample cannot be fitted well with the superparamagnetic model, this is due to a dominant linear shape at high fields. The Langevin function cannot accommodate the increasing linear region above 2 T. Similar effects have been observed in ferrimagnetic nanoparticles [200, 201, 215, 216] (mainly ferrite) with a linear increasing high field region, which is not observed in the corresponding bulk materials. The linear region can then be attributed to the beginnings of a spin flop transition. Magnetic induction can cause a post-saturation linear region in ferromagnetic hysteresis curves, but as we are only sensitive to the magnetism on the manganese and are investigating an insulating material this can be disregarded.

Superparamagnetism is a widely investigated phenomenon which has potential applications for example in hyperthermia where magnetic nanoparticles heat up in varying fields which has applications in cancer treatment. Increased efficiency of heating in superparamagnetic particles allows safer frequencies of the field to be used [209]. Superparamagnetic nanoparticles also have potential applications as spin filters for spintronics [210]. Thin films may also be useful for such applications, however, there are problems with making small enough grains/nanoparticles [204]. Our samples display very small grains, however, this effect would not be seen in thicker films as (1) it would be localised to the interface and (2) coupling out of the plane from successive layers would link the previously isolated 'nanoparticles'.

9.2.4   Temperature Dependence

The temperature dependences are shown in figure 9.6. The distinction between the - - L and - - S samples here is striking. The - - S samples show an initial drop off in the aligned moment, followed by a somewhat linear trend upon further increasing the temperature above around 70 K. For the - - L samples the moment follows a more linear trend with temperature. The temperature dependences from the SML and LML monolayer samples in figure 8.11 seem to also fit this pattern of a flatter curve when the capping layer is LAO.

Again fitting the temperature dependences with a paramagnetic (solid lines) and superparamagnetic (dashed lines) models (shown in figure 9.6) the superparamagnetic fits are consistently better than the paramagnetic ones and the fit parameters are displayed in table 9.5. As with the monolayer samples a constant offset must be added as the moment does not reduce to zero at high temperatures.

The results of a combined fit for the - - S samples are shown in figure 9.7 with - - L samples in figure 9.8, the results of the fit are shown in table 9.6. The - - S samples fit well to the field-dependent data and at least show the expected shape in the temperature data, although neither of the models fit well. The temperature dependent data for the - - L samples does not follow the expected trend and cannot be explained by this model. The temperature dependences are again shown not to fit when a combined model was used for the temperature and field data.

The temperature dependences are shown to fit with a modified Bloch law at low temperatures, as shown in figure 9.9. The results of the temperature dependences are well reproduced, mirroring the monolayer samples. The fits are similar to those of the Langevin function without consideration for the field dependent data. The functional form between the Langevin function and the modified Bloch law are different and more data points would be required to distinguish between them. The modified Bloch function is dependent upon the spin wave spectrum which is linked to the nanoparticle sizes. One explanation for the differences between the - - S and - - L samples is then that differing manganese inter-diffusion between the two sample sets results in different effective nanoparticle sizes.

The difference in two groups of temperature dependences could arise from the oxygen symmetry as the - - S samples from the XMCD measurements are in a tetrahedral environment compared to the - - L octahedral environment. The distorted tetrahedral arrangement would result in a reduced electron bandwidth which will inhibit the superexchange interaction and therefore weakening the coupling giving the reduced temperature stability observed.

The transfer of octahedral rotations from the capping layer might also have a similar effect, however, as only the LAO and not the STO capping layers will exhibit octahedral rotations, this effect may only be small when compared to the distortion of the oxygen ligands in the - - S samples.
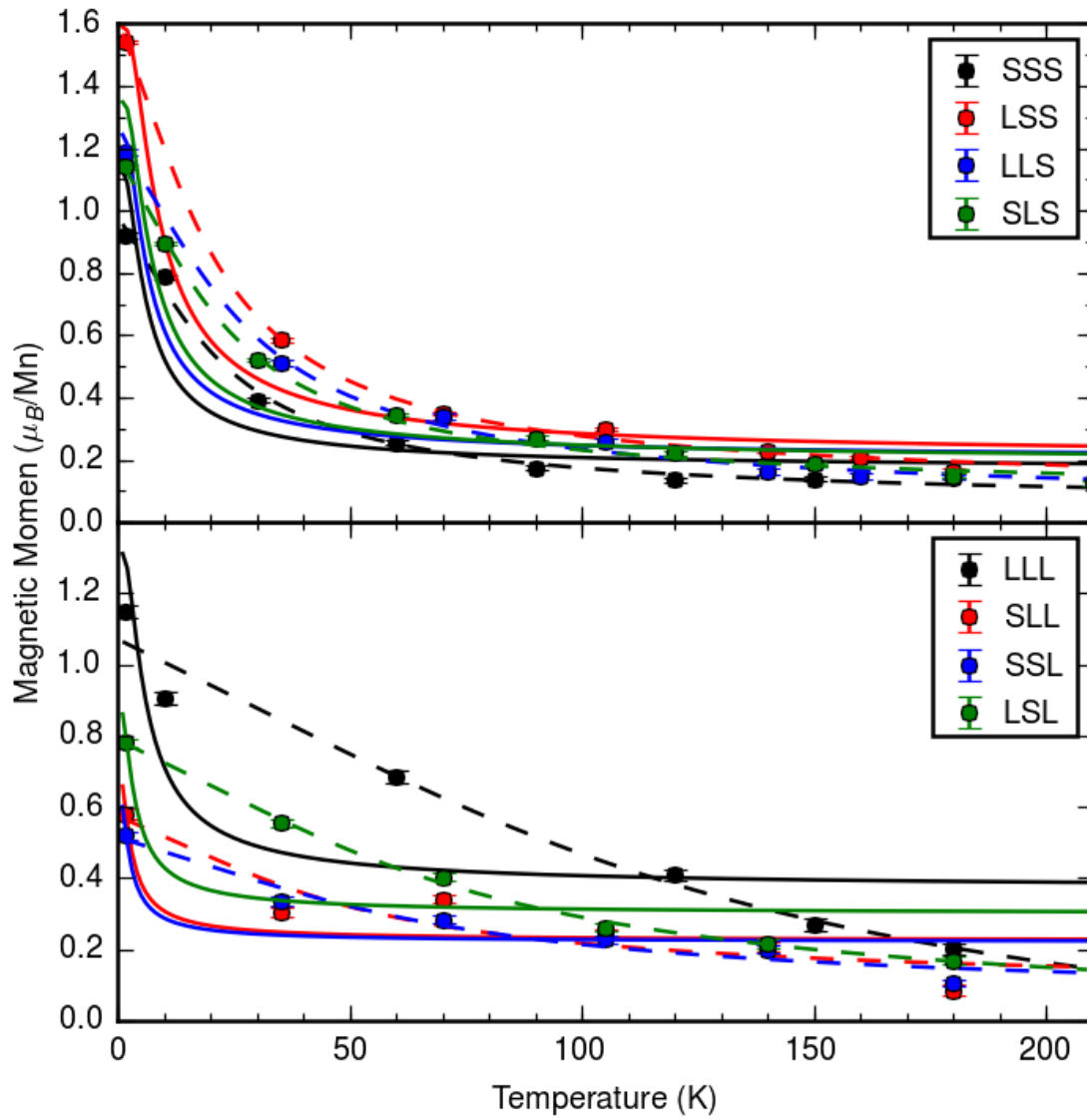
Figure 9.6: Temperature dependence of sample magnetisations from XMCD measurements. Data is represented by filled circles, the solid lines represent paramagnetic fits and the dashed lines represent superparamagnetic fits.

Sample	Superparamagnetism		
	Moment Size	Density	Size
SSS	9.79 ± 1.22	0.10 ± 0.01	2.6 ± 0.1
LSS	9.18 ± 0.68	0.17 ± 0.01	2.4 ± 0.2
LLS	11.89 ± 1.22	0.10 ± 0.01	2.5 ± 0.1
SLS	10.24 ± 0.74	0.11 ± 0.01	2.5 ± 0.2
LLL	51.54 ± 24.07	0.026 ± 0.014	3.0 ± 0.1
SLL	21.07 ± 14.51	0.017 ± 0.023	3.0 ± 0.1
SSL	28.20 ± 11.28	0.016 ± 0.01	3.3 ± 0.1
LSL	30.94 ± 2.89	0.026 ± 0.003	3.0 ± 0.1

Table 9.5: Parameters for superparamagnetic fits to the temperature dependence data shown in figure 9.6.

Sample	Superparamagnetism		
	Moment Size	Density	Offset
SSS	1.98 ± 0.20	0.55 ± 0.06	0.20 ± 0.02
LSS	1.95 ± 0.10	0.96 ± 0.05	0.22 ± 0.02
LLS	2.16 ± 0.14	0.66 ± 0.04	0.19 ± 0.02
SLS	2.42 ± 0.20	0.54 ± 0.05	0.22 ± 0.02
LLL	3.12 ± 0.32	0.39 ± 0.04	0.32 ± 0.03
SLL	3.00 ± 0.33	0.20 ± 0.02	0.18 ± 0.02
SSL	1.81 ± 0.21	0.35 ± 0.04	0.18 ± 0.02
LSL	2.23 ± 0.26	0.39 ± 0.05	0.25 ± 0.03

Table 9.6: Parameters for simultaneous fitting of temperature and field dependent data to superparamagnetic functions shown in figures 9.7 and 9.8.
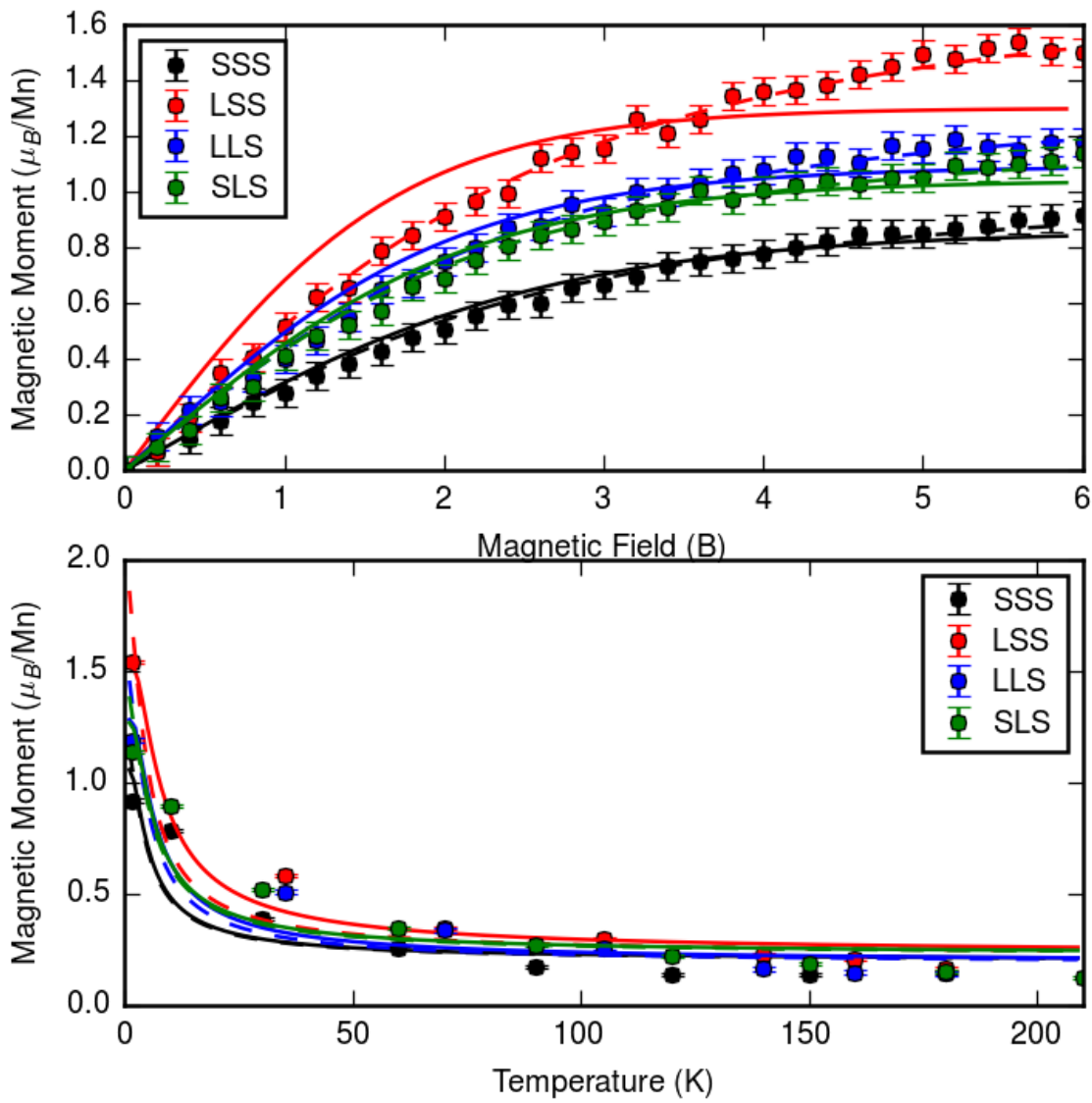
Figure 9.7: Simultaneous fitting of the temperature and field dependent data for the - - S samples to a superparamagnetic Langevin function.
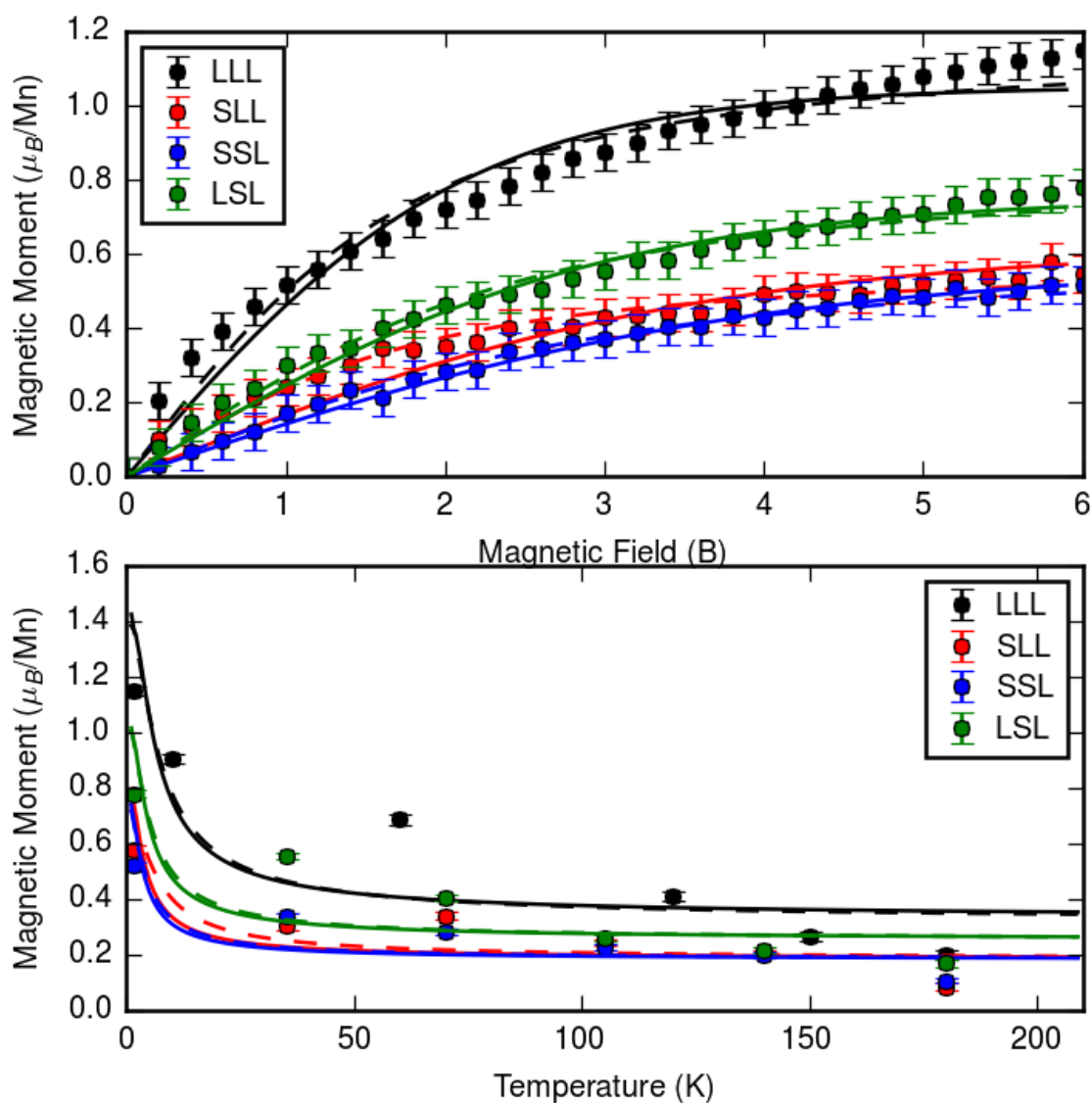
Figure 9.8: Simultaneous fitting of the temperature and field dependent data for the - - L samples to a superparamagnetic Langevin function.
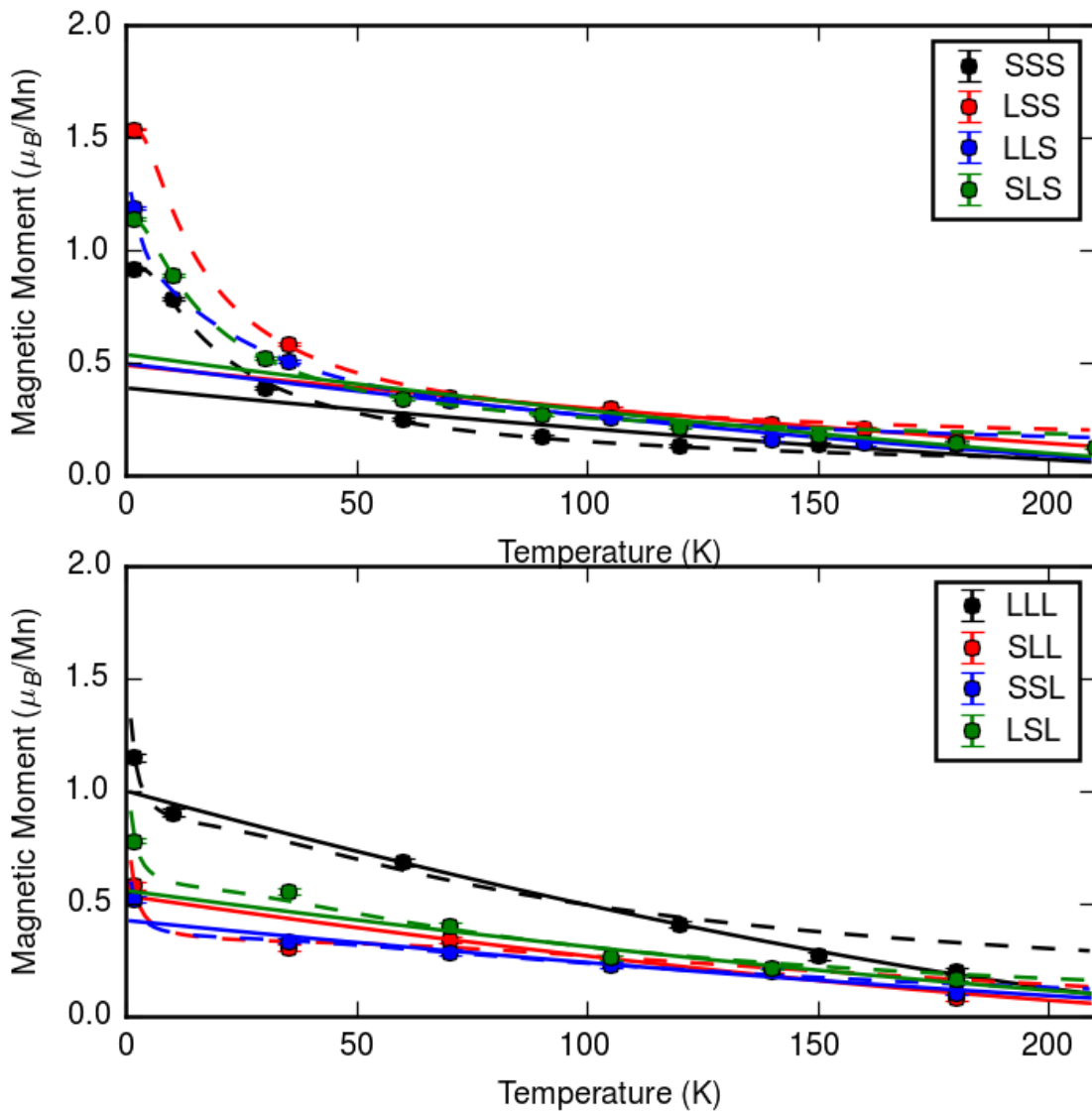
Figure 9.9: Temperature dependent data fitted with a modified Bloch function.

9.3   Summary

We have measured the electronic and magnetic properties of manganese oxide bilayers in heterostructures between $LaAlO_3$ and $SrTiO_3$. The differing charge environments due to the neutral SrO layers and the positively charged LaO layers being expected to alter the magnetic properties of the manganese *via* charge transfer. Now with manganese coupling out-of-the-plane stronger magnetic coupling is expected and concurrent increases in the ordered moment size, and transition temperature, over the previous chapters monolayer samples. X-ray absorption techniques were used to determine the magnetic and electronic properties of eight different manganese bilayer samples.

X-ray absorption measurements have been fitted to reference samples to determine a rough manganese oxidation state for the samples. This reference spectra fitting shows very different results than expected purely from charge transfer from the surrounding layers. The lineshapes and resultant oxidation states were found to be mainly dependent on the capping layer. Samples which would nominally be expected to be the same for example $LaO/MnO_2/SrO/MnO_2/SrO$ (LSS) and $SrO/MnO_2/SrO/MnO_2/LaO$ (SSL) therefore display very different properties.

Significant quantities of manganese 2+ are detected across all the $SrTiO_3$ capped (- - S) samples. The manganese 2+ cannot be explained by charge transfer and is expected to be a result of oxygen vacancies induced by the growth of the capping layer. The $LaAlO_3$ capped (- - L) sample valencies are all around 3+ which is consistent with the monolayer samples. It is expected that the titanium is changing oxidation state preferentially over the manganese in the - - L samples, which, as in the monolayer samples, are expected to be governed by ion intermixing.

The unexpected oxidation states and strong links to the capping layer suggest that more care must be taken to ensure that the charge transfer occurs in the desired way and theoretical calculations should be carried out first. A localised probe which is sensitive to the oxidation state such as Electron energy loss spectroscopy (EELS) [195] would be required to determine if the titanium and aluminium ions are playing a role in the manganese oxidation state by determining their oxidation states (as in the case of reference [174]). The dependence of interfacial properties on the growth order is not new and has been previously observed in $LaAlO_3/SrTiO_3$

heterostructures [174].

X-ray magnetic circular dichroism (XMCD) measurements were then taken on all the samples at 1.7 K and 6 T. Sum rule analysis of XMCD spectra show larger moments in the - - S samples than the - - L samples, consistent with the monolayer results. The larger - - S moment is due to the manganese 2+ proportion as manganese 2+ will have 5 electrons in the d-orbitals all aligned in the same direction. By comparison of the shape of the XMCD spectra to calculations by Matzen *et al.* [196], the - - S samples appear to show that the manganese 2+ ions are in a tetrahedral environment, suggesting the oxygen vacancies cause a large distortion of the remaining oxygen ligands away from the usual octahedral arrangement.

As with the monolayer samples, the calculated moment sizes are consistent with those expected for thin film samples. XMCD is not a perfect technique and is useful for comparative measurements between samples but due to the close nature of the manganese L-edges, accurately determining a moment size is difficult, as explained by Piamonteze *et al.* [197]. These results show to some extent the ability to control the magnetic moment size with oxidation state, however, the desired effects were not achieved through charge transfer from the surrounding layers, but properties introduced by the layer deposition of the capping layer.

The magnetic field dependence of all the samples was then measured, again by XMCD. The magnetisation curves do not show any remnant field, showing that they are not ferromagnetic, however, the shape of the magnetisation curve indicates that they are superparamagnetic and that the samples consist of ferromagnetic domains, which do not interact strongly. Superparamagnetism is an effect which is prevalent in magnetic nanoparticles [198–203] where the system behaves in a similar way to a paramagnet with a very large moment size. Both ion intermixing and oxygen vacancies will remove the magnetic interactions making superparamagnetism possible, oxygen vacancies remove the intervening oxygen required for the superexchange mechanism, while ion intermixing will separate them spatially.

The field dependent curves largely fit a superparamagnetic model, however, the LLL and LSL samples, although producing fits close to the error bars appear to follow a dependence more like that of a ferrimagnet, with a linear magnetisation dependence at high fields. To distinguish between these models higher-field data

would be required to determine if the linear region continues or saturation is reached.

Fitting the magnetisation curves suggests that manganese ions are clustered in groups of only a handful of interacting manganese ions. This is consistent with the intermixing observed from the EDS mapping of the monolayer samples as well as the proportion of oxygen vacancies.

Superparamagnetic properties have been observed in thin films before [207], here again the deposition method was pulsed laser deposition and $Co_{0.9}Zn_{0.1}Fe_2O_4$ was deposited. In this case, nano-crystallites instead of smooth layers were formed, which result in the superparamagnetism. There are many examples of superparamagnetism in thin films of nano-crystalline material [204–207]. We believe this is the first example of such a feature in an epitaxial film.

Further evidence of the superparamagnetic behaviour is given in the temperature dependence of the moments. For superparamagnetism the magnon spectrum is curtailed by the nanoparticle size, which modifies the expected Bloch law temperature dependence, as a result the temperature dependence takes on an exponential form [214, 215].

If superparamagnetism is purely a result of charge equilibration at the capping layer it would not be expected to be observed in thicker films as coupling with ions out-of-the-plane will reconnect ions that were not previously interacting.

The capping layer has proven to be the dominant factor in the magnetic properties of the thin films. It has also shown to be highly robust, overriding other potential influences such as charge transfer, especially in thin film samples. It is a highly important and somewhat overlooked factor when considering thin film properties. This leaves the question of how far into a film the effects of the first deposited layer penetrate and therefore dominate in determining the thin-film properties.

9.4 Conclusions

We have measured samples of manganese oxide monolayers in differing charge environments provided by heterostructures between $LaAlO_3$ and $SrTiO_3$. Charge transfer from the positively charged LaO layers was expected to alter the magnetic properties of the manganese. Compared to the previous chapter manganese coupling

out-of-the-plane is expected to result in stronger magnetic coupling and concurrent increases in the ordered moment size, and transition temperature. X-ray absorption techniques were used to determine the magnetic and electronic properties of the manganese.

X-ray absorption measurements show that the samples broadly fall into two categories dependent upon the capping layer. Comparison of the absorption spectra to literature values shows that the samples capped with $SrTiO_3$ (- - S) have a large amount of manganese 2+ present and this is consistent with the shape of the x-ray magnetic circular dichroism (XMCD). The dichroic lineshapes resemble that of a tetrahedrally coordinated manganese ion [196] suggesting that the apical oxygens are missing (consistent with the valence state) and that the remaining in-plane oxygen atoms are highly distorted. The moment sizes calculated by the XMCD sum rules are in the region of 1 μ_B, consistent with other thin film samples. The $LaAlO_3$ (- - L) capped samples are found to be dominated by manganese 3+ which taking account of the results from the previous chapter and Nakagawa *et al.* [174] is expected to introduce ion intermixing at the interfaces. The XMCD sum rule derived moment sizes are reduced compared to the - - S samples due to the decrease in unpaired electrons from manganese 2+ to 3+.

The field dependent curves for both capping layers largely fit to a superparamagnetic model, however, the high field regions for the $LaO/MnO_2/LaO/MnO_2/LaO$ (LLL), and $LaO/MnO_2/SrO/MnO_2/LaO$ (LSL) samples, although producing good fits close to the error bars, appear to follow a dependence more like that of a ferrimagnet, with a linear increase in magnetisation at high fields. Superparamagnetism, usually observed in magnetic nanoparticles, occurs in these samples through the decoupling of manganese ions from both ion intermixing and oxygen vacancies.

Temperature dependences are best described by a modified Bloch function consistent with measurements on magnetic nanoparticles. These measurements are again consistent with the nanoparticle like nature of the samples and evidence the intervention of the oxygen vacancies, and diffusion of the manganese layers, to the magnetic coupling.

Oxygen vacancies and the oxygen environment in growth are very important factors for the final properties of the sample. These results show that the control

of the oxygen environment cannot be generalised and although the samples capped with $LaAlO_3$ (- - L) appear to have a stoichiometric oxygen ratio, the - - S samples grown under the same conditions do not. This highlights the care that must be taken to ensure the correct oxygen pressure even across nominally similar samples.

We have shown that the magnetic properties of the manganese oxide layer can be effectively controlled by the heterostructuring of different materials. However, the dominant processes are limited to structural changes in ion intermixing and oxygen vacancies and not charge transfer due to the polarity of the surrounding materials.

In future a more careful analysis to characterise the structure of the sample is required to determine ion intermixing oxygen vacancies before magnetic measurements are taken.

Further Work

Further samples should be grown under increased oxygen pressures to reduce the oxygen vacancies of the samples with $SrTiO_3$ capping layers. This may allow the control of the magnetic properties of the manganese through charge transfer.

Some of the samples did not follow the expected field dependence for a super-paramagnetic system at higher fields, suggesting that the samples may have some ferrimagnetic properties. Higher field measurements should be carried out on these samples. The continuation of the high field linear regions in the magnetisation or a discontinuous increase in the moment indicative of a spin-flop transition would confirm that the manganese is ferrimagnetic.

The suggested mechanism for decoupling of the manganese moments of ion intermixing and oxygen vacancies are expected to be localised at interfacial regions. A more focussed study should therefore be carried out with samples with $SrTiO_3$ and $LaAlO_3$ capping layers with increasing manganese layer thicknesses to confirm that a remnant field is set up and that the manganese ions become coupled and display ferromagnetic properties. This would also allow the determination of how far reaching the effects of the capping layer are in controlling the material properties.

Electron energy loss spectroscopy (EELS) measurements should be undertaken to confirm the oxidation states of the atoms surrounding the manganese layers. In the case of the $LaAlO_3$ capping layer this could confirm if charge transfer is indeed

occurring, but with charges preferentially localising on the titanium ions.

Chapter 10

Overall Conclusions and Future Work

This thesis has highlighted the sensitivity of soft x-rays to small changes in magnetism, with both the polarisation dependence of magnetic scattering, and x-ray magnetic circular dichroism.

This work has improved upon the metrology of how to take full polarisation analysis measurements. This improvement allows data on much weaker reflections to be collected as longer count times can be used which can be applied to measuring weak non-resonant scattering. This will also allow full polarisation analysis measurements to be collected on multiple stronger peaks to give a more robust picture of the nature of magnetic systems.

The sensitivity of the polarisation of magnetic x-ray scattering has been highlighted with the small canting of the magnetic moments observed in the system $CeRu_2Al_{10}$. A canting of 9.6 degrees was observed towards the a-axis in this system. This spin canting is likely caused by the Dzyaloshinskii-Moriya interaction, however, taking the symmetry arguments for the possible interaction pathways into account there must be a symmetry lowering for the canting to exist. The structural arguments for a symmetry lowering imply the possibility for spin canting in isostructural compounds, which require further investigation to observe if a canting is present in these systems.

The $(1, 0, 0)$ reflection in Cu_2OSeO_3 was found to be due to the anisotropy of the tensor of x-ray susceptibility (ATS). X-ray intensity was observed at the $(1, 0, 0)$

position when entering the helical magnetic state, indicating a fundamental change in the magnetic structure from the ferrimagnetic state (where no $(1, 0, 0)$ intensity is observed). Rietveld analysis is consistent with a helical magnetic structure where one moment is aligned antiparallel to the other fifteen, in a reduced ferrimagnetic structure. A novel polarisation dependence was observed in the magnetic satellites around the ATS reflection, the polarisation dependence of which does not follow that of a helical magnetic structure that is expected in these systems. There is a suggestion that the polarisation dependence is altered due to the ATS reflection. To check this the polarisation dependence of the magnetic satellites should be measured around the main beam.

Unique samples of manganese oxide mono- and bi-layers were investigated using x-ray magnetic circular dichroism. Different layers were grown surrounding the manganese to create different charge environments so that charge transfer between the surrounding layers could change the oxidation state of the manganese and hence the magnetic properties. The magnetic properties and the oxidation state of the manganese was found to be strongly linked to the capping layer used which was either $SrTiO_3$ (STO) or $LaAlO_3$ (LAO). The STO-capped samples displayed large quantities of manganese 2+ and larger magnetic moments than the LAO-capped samples which displayed ion intermixing. Both types of samples display apparently superparamagnetic properties, which, although a property that has been observed in thin films has until now only been observed in polycrystalline samples, and not in buried heterostructures. Further investigation of these systems is required to rule out the possibility of ferrimagnetism. Further samples should also be grown in increased oxygen pressures to try to limit the oxygen vacancies seen in the STO capped samples. The range of effects of the capping layer requires further investigation. Samples of different thicknesses would be needed to be grown with different capping layers. When/if the properties of the films with different capping layers converge this would suggest that the capping layer is no longer the dominant factor of the thin film properties. The ability to control magnetic properties in thin films has been confirmed to some extent, however, it is strongly linked to the capping layer and not the surrounding layers. It has been shown to be a highly robust method with very similar properties being observed for many different sample architectures.

Part IV

Appendices

Appendix A

Relation Between Polarisation and Electric Field

By considering the electron clouds around the atoms to be bound classically in a varying applied electric field we have a system that resembles a forced harmonic oscillator, obeying the equation of motion shown below:

$$F(t) = m(\ddot{x} + \gamma\dot{x} + \omega_0^2 x) = \boldsymbol{q}E \tag{A.1}$$

Where γ is a damping term, ω_0 is the natural frequency of the system, and $\mathbf{q}$ is the polarisation vector. The driving force is light, described by the equation for the plane wave equation as follows:

$$E = E_0 e^{i(kx - wt)} \tag{A.2}$$

Where k is the wavevector, x is the propagation direction ,w is the angular frequency, t is time, and E_0 is the wave amplitude. The displacement of the electron cloud will oscillate at the same frequency as the light, therefore we can write.

$$x = x_0 e^{i(kz - wt)} \tag{A.3}$$

Then the time derivates become, $\gamma\dot{x} = -i\gamma wt$, and $\ddot{x} = -w^2 x$, solving equation A.1 for x gives:

$$x = \frac{\boldsymbol{q}/m}{-i\gamma wt + w^2 - w_0^2}E \tag{A.4}$$

Using $\mathbf{p} = \boldsymbol{q}x$ we arrive at:

$$\mathbf{p} = \frac{\boldsymbol{q}^2/m}{-i\gamma wt + w^2 - w_0^2}E \tag{A.5}$$

Appendix B

Particles in an External Field

Using Lagrangian Mechanics $L = V - T$ becomes:

$$L = \frac{1}{2}m\dot{x}^2 + \frac{e}{c}\dot{x}\mathbf{A} \tag{B.1}$$

For a particle of mass m with charge e moving in an external field with vector potential $\mathbf{A}$, the canonical momentum is then:

$$\mathbf{p} = \frac{\delta L}{\delta \dot{x}} = m\dot{x} + \frac{e}{c}\mathbf{A} \tag{B.2}$$

The Hamiltonian is then:

$$H = \sum \dot{x}p - L = m\dot{x}^2 + \frac{e}{c}\dot{x}\mathbf{A} - \frac{1}{2}m\dot{x}^2 - \frac{e}{c}\dot{x}\mathbf{A} = \frac{m\dot{x}^2}{2} \tag{B.3}$$

Rearranging the equation B.2 for the normal momentum $\dot{x}m$ we get:

$$\dot{x}m = \mathbf{p} - \frac{e}{c}\mathbf{A} \tag{B.4}$$

Substituting this into the equation for the Hamiltonian we can see that in an external field the momentum is just transformed thus $\mathbf{p} \rightarrow \mathbf{p} - \frac{e}{c}\mathbf{A}$:

$$H = \frac{\left(\mathbf{p} - \frac{e}{c}\mathbf{A}\right)^2}{2m} \tag{B.5}$$

For the momentum squared the transform becomes more complicated:

$$\mathbf{p}^2 \rightarrow \left[\boldsymbol{\sigma}\left(\mathbf{p} - \frac{e}{c}\mathbf{A}\right)\right]^2 \tag{B.6}$$

Which can be evaluated by using relationships for the commutators and anti-commutators of the Pauli matrices:

$$\sigma_a\sigma_b = 1/2([\sigma_a, \sigma_b] + \{\sigma_a, \sigma_b\}) = 1/2(\sigma_a\sigma_b - \sigma_b\sigma_a + \sigma_a\sigma_b + \sigma b\sigma_a) \tag{B.7}$$

Examples of the commutator and the anti-commutator are shown below:

$$[\sigma_a, \sigma_b] = \begin{pmatrix} 0 & 1 \\ 1 & 0 \end{pmatrix} \times \begin{pmatrix} 0 & -i \\ i & 0 \end{pmatrix} - \begin{pmatrix} 0 & -i \\ i & 0 \end{pmatrix} \times \begin{pmatrix} 0 & 1 \\ 1 & 0 \end{pmatrix}$$

$$= \begin{pmatrix} i & 0 \\ 0 & -i \end{pmatrix} - \begin{pmatrix} -i & 0 \\ 0 & i \end{pmatrix}$$

$$= 2i\sigma_c \tag{B.8}$$

Therefore:

$$[\sigma_b, \sigma_a] = \begin{pmatrix} -i & 0 \\ 0 & i \end{pmatrix} - \begin{pmatrix} i & 0 \\ 0 & -i \end{pmatrix} = -2i\sigma_c \tag{B.9}$$

$$\{\sigma_a, \sigma_b\} = \begin{pmatrix} 0 & 1 \\ 1 & 0 \end{pmatrix} \times \begin{pmatrix} 0 & -i \\ i & 0 \end{pmatrix} + \begin{pmatrix} 0 & 1 \\ 1 & 0 \end{pmatrix} \times \begin{pmatrix} 0 & -i \\ i & 0 \end{pmatrix}$$

$$= \begin{pmatrix} i & 0 \\ 0 & -i \end{pmatrix} + \begin{pmatrix} -i & 0 \\ 0 & i \end{pmatrix}$$

$$= 0 \tag{B.10}$$

$$[\sigma_b, \sigma_b] = \begin{pmatrix} 0 & -i \\ i & 0 \end{pmatrix} \times \begin{pmatrix} 0 & -i \\ i & 0 \end{pmatrix} - \begin{pmatrix} 0 & -i \\ i & 0 \end{pmatrix} \times \begin{pmatrix} 0 & -i \\ i & 0 \end{pmatrix}$$

$$= \begin{pmatrix} 1 & 0 \\ 0 & 1 \end{pmatrix} - \begin{pmatrix} 1 & 0 \\ 0 & 1 \end{pmatrix}$$

$$= 0 \tag{B.11}$$

$$\{\sigma_b, \sigma_b\} = \begin{pmatrix} 0 & -i \\ i & 0 \end{pmatrix} \times \begin{pmatrix} 0 & -i \\ i & 0 \end{pmatrix} + \begin{pmatrix} 0 & -i \\ i & 0 \end{pmatrix} \times \begin{pmatrix} 0 & -i \\ i & 0 \end{pmatrix}$$

$$= \begin{pmatrix} 1 & 0 \\ 0 & 1 \end{pmatrix} + \begin{pmatrix} 1 & 0 \\ 0 & 1 \end{pmatrix}$$

$$= 2I \tag{B.12}$$

From this we obtain:

$$\boldsymbol{\sigma\sigma} = \delta I + \sum i\boldsymbol{\sigma}\varepsilon_{abc}(a.\sigma)(b.\sigma) = a_i\sigma_i b_i\sigma_i = a_i b_i(\delta I + i\varepsilon_{abc}\sigma_k) \tag{B.13}$$

Where hopefully we can see from above that:

$$i\varepsilon_{abc}\sigma_k a_i b_j = i\sigma_k(a_i b_j - b_i a_j) + i\sigma_j(a_k b_i - b_k a_i) + i\sigma_i(a_j b_k - b_j a_k) = i\sigma.(a \times b)$$

(B.14)

Where $ab\delta I$ becomes abI then using this in the equation above (remembering that the cross product of two parallel vectors is 0, $a \times b = ab\sin(\theta)$) produces :

$$\begin{aligned}
\left[\boldsymbol{\sigma}\left(\mathbf{p} - \frac{e}{c}\mathbf{A}\right)\right]^2 &= \left(\mathbf{p} - \frac{e}{c}\mathbf{A}\right)^2 + i\boldsymbol{\sigma}\left(\mathbf{p} - \frac{e}{c}\mathbf{A}\right) \times \left(\mathbf{p} - \frac{e}{c}\mathbf{A}\right) \\
&= \left(\mathbf{p} - \frac{e}{c}\mathbf{A}\right)^2 + i\boldsymbol{\sigma}\left(\mathbf{p} \times \mathbf{p} + \frac{e^2}{c^2}\mathbf{A} \times \mathbf{A} - \frac{e}{c}\mathbf{p} \times \mathbf{A} - \frac{e}{c}\mathbf{A} \times \mathbf{p}\right) \\
&= \left(\mathbf{p} - \frac{e}{c}\mathbf{A}\right)^2 - i\boldsymbol{\sigma}\left(\frac{e}{c}\mathbf{p} \times \mathbf{A} + \frac{e}{c}\mathbf{A} \times \mathbf{p}\right)
\end{aligned}$$

(B.15)

To make progress we introduce an arbitrary wavefunction (ψ):

$$\begin{aligned}
\left(\frac{e}{c}\mathbf{p} \times \mathbf{A} + \frac{e}{c}\mathbf{A} \times \mathbf{p}\right)\psi &= \frac{e}{c}(\mathbf{p} \times \mathbf{A})\psi + \frac{e}{c}(\mathbf{p}\psi) \times \mathbf{A} + \frac{e}{c}\mathbf{A} \times \mathbf{p}\psi \\
&= -i\hbar\boldsymbol{\sigma}\left(\frac{e}{c}\nabla \times \mathbf{A}\right)\psi \\
&= -i\hbar\frac{e}{c}\boldsymbol{\sigma}\mathbf{B}\psi
\end{aligned}$$

(B.16)

So now the first order approximation becomes:

$$\boldsymbol{\sigma}\mathbf{p}^2 \to \left(\mathbf{p} - \frac{e}{c}\mathbf{A}\right)^2 - \frac{\hbar e}{c}\boldsymbol{\sigma}\mathbf{B}$$

(B.17)

Appendix C

Full Polarisation Analysis Setup

The usual experimental setup involves finding the centre of rotation of the diffractometer and ensuring that the incident beam coincides with this point. For experiments requiring polarisation analysis the determination of the centre of rotation of the analyser stage is also required, and this must also coincide with the beam. This is important as it will ensure that the beam always hits the same part of the polarisation analyser crystal (PA) as analyser crystals are not always uniform across their surface. If this is not the case the peaks in θ_p will move with η and much longer scans in θ_p must be taken, significantly increasing the measurement time. An example of a poorly aligned analyser is shown in figure C.1[1].

Alignment of the PA stage can be non-trivial due to the absence of a pin and camera. It requires the rotation of the diffractometer perpendicular to the scattering plane (α), or at least the motion of the detector perpendicular to the scattering plane. The alignment can be done by having the $2\theta_p$ (the angle of the detector on the PA stage) at zero and half-cutting the PA crystal with the beam at successive η rotations. The alignment of the PA requires at least three measurements of the half-cut at different η angles, preferably at values of 0, 90, and 180 degrees and adjustment of the diffractometer so that these coincide using the detector angle 2θ and the angle of the diffractometer perpendicular to the scattering plane α. It should also be noted that the PA crystal should be flat with respect to the beam at this point as the half-cut position is important for ensuring the diffracted beam is also

---

[1]Only the half-cut position of the PA stage must be on the centre of rotation, and the beam is a useful tool for doing this in the absence of a pin and camera.
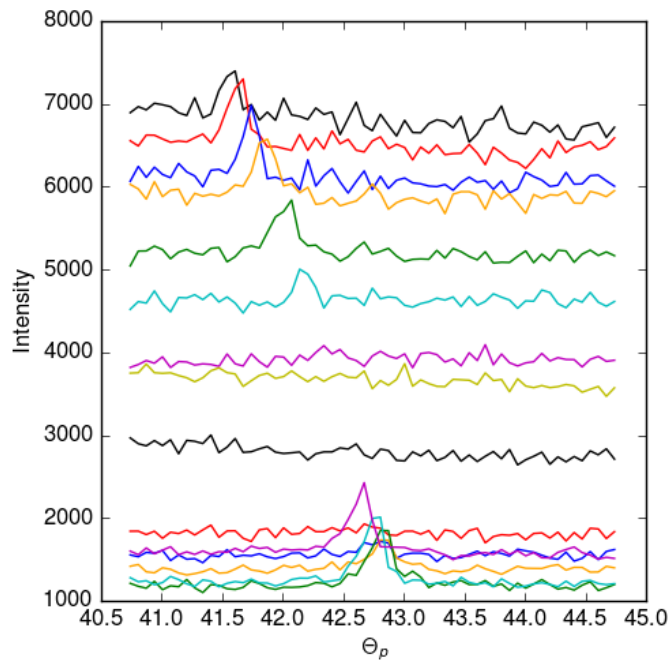
Figure C.1: θ_p scans at different η angles for a poorly aligned analyser.

hitting the centre of rotation of the PA stage. This can be achieved by iteratively rocking the PA crystal in the beam using θ_p going to the peak and the half-cutting the sample. The main aim of this process is to ensure that the surface of the PA crystal coincides with the centre of rotation of the PA stage.

Alignment of Bragg reflections correctly onto the PA crystal is also imperative. This must be done by effectively halfcutting the beam by moving 2θ (with η at 0) and then repeating with χ (and η at 90). This will ensure that the diffracted beam is hitting the centre of rotation of the PA stage. Even with a perfectly aligned diffractometer and PA stage θ_p scans are still required as the background may change depending upon the η rotation.

References

[1] F. DeBergevin and M. Brunel. 'Observation of Magnetic Superlattice Peaks by X-ray-Diffraction on an Antiferromagnetic NiO Crystal'. *Phys. Lett. A*, **A 39**, 2; p. 141 (1972).

[2] M. Blume. 'Magnetic Scattering of X-rays'. *J. Appl. Phys.*, **57**, 8; pp. 3615–3618 (1985).

[3] K. Namikawa, M. Ando, T. Nakajima, and H. Kawata. 'X-ray Resonance Magnetic Scattering'. *J. Phys. Soc. Japan*, **54**, 11; pp. 4099–4102 (1985).

[4] D. Gibbs, D. R. Harshman, *et al.* 'Polarization and Resonance Properties of Magnetic-X-ray Scattering in Holmium'. *Phys. Rev. Lett.*, **61**, 10; pp. 1241–1244 (1988).

[5] J. P. Hannon, G. T. Trammell, M. Blume, and D. Gibbs. 'X-ray Resonance Exchange Scattering'. *Phys Rev. Lett.*, **61**, 10; p. 1245 (1988).

[6] W. C. Rontgen. 'On a new kind of ray'. *Radiology*, **45**, 5; pp. 428–435 (1945).

[7] M. Laue. 'A quantitive examination of the theory for the interference appearances in X-rays'. *Ann. Phys.*, **41**, 10; pp. 989–1002 (1913).

[8] W. Friedrich, P. Knipping, and M. Laue. 'Interference appearances in X-rays'. *Ann. Phys.*, **41**, 10; pp. 971–988 (1913).

[9] W. H. Bragg and W. L. Bragg. 'The Reflection of X-rays by Crystals'. *Proc. R. Soc. London A Math. Phys. Eng. Sci.*, **88**, 605; pp. 428–438 (1913).

[10] F. R. Elder, A. M. Gurewitsch, R. V. Langmuir, and H. C. Pollock. 'Radiation from Electrons in a Synchrotron'. *Phys. Rev.*, **71**, 11; pp. 829–830 (1947).

[11] H. Winick, G. Brown, K. Halbach, and J. Harris. 'Wiggler and undulator magnets'. *Phys. Today*, **34**, 5; pp. 50–63 (1981).

[12] D. H. Bilderback, P. Elleaume, and E. Weckert. 'Review of third and next generation synchrotron light sources'. *J. Phys. B At. Mol. Opt. Phys.*, **38**, 9; p. S773 (2005).

[13] P. F. Lindley. 'The use of synchrotron radiation in protein crystallography'. *Radiat. Phys. Chem.*, **45**, 3; pp. 367–383 (1995).

[14] D. B. McWhan. 'Synchrotron Radiation in the Study of Magnetism'. *J. Synchrotron Radiat.*, **1**, 1; pp. 83–90 (1994).

[15] H. Ohsumi and T.-h. Arima. 'Novel insight into structural magnetism by polarized synchrotron X-ray scattering'. *Adv. Phys. X*, **1**, 1; pp. 128–145 (2016).

[16] J. H. Kinney and M. C. Nichols. 'X-ray Tomographic Microscopy (XTM) Using Synchrotron Radiation'. *Annu. Rev. Mater. Sci.*, **22**; pp. 121–152 (1992).

[17] R. P. Feynman. *QED: The Strange Theory of Light and Matter*, (Princeton University Press2014). ISBN 9781400847464.

[18] D. Kaiser. 'Physics and Feynman's Diagrams'. *Am. Sci.*, **93**; p. 156 (2005).

[19] E. Hecht. *Optics*, (Addison-Wesley2002). ISBN 9780805385663.

[20] J. S. Toll. 'Causality and the Dispersion Relation: Logical Foundations'. *Phys. Rev.*, **104**, 6; pp. 1760–1770 (1956).

[21] E. J. W. Verwey. 'Electronic Conduction of Magnetite (Fe_3O_4) and its Transition Point at Low Temperatures'. *Nature*, **144**, 3642; pp. 327–328 (1939).

[22] J. B. Goodenough. 'Theory of the Role of Covalence in the Perovskite-Type Manganites [La, M (II)] MnO_3'. *Phys. Rev. B*, **100**, 2; pp. 564–573 (1955).

[23] Y. Tokura and N. Nagaosa. 'Orbital Physics in Transition-Metal Oxides'. *Science*, **288**, 5465; pp. 462–468 (2000).

[24] H. A. Jahn and E. Teller. 'Stability of Polyatomic Molecules in Degenerate Electronic States. I. Orbital Degeneracy'. *Proc. R. Soc. A*, **16t1**, 906; pp. 220–235 (1937).

[25] M. V. Berry and A. K. Geim. 'Of flying frogs and levitrons'. *Eur. J. Phys.*, **18**; pp. 307–313 (1997).

[26] M. a. Ruderman and C. Kittel. 'Indirect exchange coupling of nuclear magnetic moments by conduction electrons'. *Phys. Rev.*, **96**, 1; pp. 99–102 (1954).

[27] T. Kasuya. 'A theory of metallic ferro-and antiferromagnetism on Zener's model'. *Prog. Theor. Phys.*, **16**, 1; pp. 45–57 (1956).

[28] K. Yoshida. 'Magnetic Properties of Cu-Mn Alloys'. *Phys. Rev.*, **106**; pp. 893–898 (1957).

[29] J. Friedel. 'The distribution of electrons round impurities in monovalent metals'. *Philos. Mag. Ser. 7*, **43**, 337; pp. 153–189 (1952).

[30] H. A. Kramers. 'The interaction between the magnetogenic atoms in a paramagnetic crystal'. *PHYSICA*, **1**; pp. 182–192 (1934).

[31] C. Zener. 'Interaction between the d-shells in the transition metals. III. Calculation of the Weiss factors in Fe, Co, and Ni'. *Phys. Rev.*, **83**, 2; pp. 299–301 (1951).

[32] I. Dzyaloshinsky. 'A thermodynamic theory of weak ferromagnetism of antiferromagnetics'. *J. Phys. Chem. Solids*, **4**, 4; pp. 241–255 (1958).

[33] T. Moriya. 'Anisotropic Superexchange Interaction and Weak Ferromagnetism'. *Phys. Rev.*, **120**, 1; p. 91 (1960).

[34] M. Altarelli. 'Resonant X-ray Scattering : A Theoretical Introduction'. **242**; pp. 201–242 (2006).

[35] V. B. Berestetskii, E. M. Lifshitz, and L. P. Pitaevskii. *Quantum Electrodynamics, Landau and Lifshitz Course of Theoretical Physics. Vol 4.*, (Pergamin Press1982), 2 edition. ISBN 0-08-026504-9.

[36] A. Akhiezer and V. B. Bereststskii. *Quantum Electrodynamics, Monographs and Texts in Physics and Astronomy, Vol. 11*, (Interscience Publishers (a division of Wiley and sons)1965), 1 edition.

[37] I. A. Zaliznyak and S.-h. Lee. *Modern Techniques for Characterizing Magnetic Materials.* 1, (Springer US2005). ISBN 978-0-387-23395-6.

[38] 'http://www.isis.stfc.ac.uk/about/how-isis-works—in-depth4371.html'.

[39] 'http://www.isis.stfc.ac.uk/about/how-isis-works6313.html'.

[40] T. E. Mason, D. Abernathy, *et al.* 'The Spallation Neutron Source in Oak Ridge: A powerful tool for materials research'. *Phys. B Condens. Matter*, **385386**; pp. 955–960 (2006). Proceedings of the Eighth International Conference on Neutron Scattering.

[41] J. K. Cockcroft and S. Jacques. 'http://pd.chem.ucl.ac.uk/pdnn/inst3/pulsed.htm'.

[42] H. Kamitsubo. 'SPring-8 Program'. *J. Synchrotron Radiat.*, **5**; pp. 162–167 (1998).

[43] T. A. W. Beale, T. P. A. Hase, *et al.* 'RASOR: An advanced instrument for soft x-ray reflectivity and diffraction'. *Rev. Sci. Instrum.*, **81**, 7; p. 073904 (2010), arXiv:/1006.4258.

[44] 'Rasor Shematic'. http://www.diamond.ac.uk/Beamlines/Surfaces-and-Interfaces/I10/rasor.html Accessed: March 2017.

[45] S. S. Dhesi, S. A. Cavill, *et al.* 'The Nanoscience Beamline (I06) at Diamond Light Source'. *AIP Conf. Proc.*, **1234**, 1 (2010).

[46] L. C. Chapon, P. Manuel, *et al.* 'Wish: The New Powder and Single Crystal Magnetic Diffractometer on the Second Target Station'. *Neutron News*, **22**, 2; pp. 22–25 (2011).

[47] N. Greenfield. 'Using circular dichroism spectra to estimate protein secondary structure'. *Nat Protoc.*, **1**, 6; pp. 2876–2890 (2007).

[48] S. Georgakopoulou, R. Van Grondelle, and G. Van Der Zwan. 'Explaining the visible and near-infrared circular dichroism spectra of light-harvesting 1 complexes from purple bacteria: A modeling study'. *J. Phys. Chem. B*, **110**, 7; pp. 3344–3353 (2006).

[49] S. Collins and A. Bombardi. *Magnetism and Synchrotron Radiation*, (Springer Berlin Heidelberg2010). ISBN 978-3-642-04498-4.

[50] B. T. Thole, P. Carra P, F. Sette F., and G. der Laan. 'X-Ray Circular-Dichroism as a Probe of Orbital Magnetization'. *Phys. Rev. Lett.*, **68**, 12; pp. 1943–1946 (1992).

[51] P. Carra, B. T. Thole, M. Altarelli, and X. Wang. 'X-ray circular dichroism and local magnetic fields'. *Phys. Rev. Lett.*, **70**, 5; pp. 694–697 (1993).

[52] G. van der Laan. *Hitchhiker's Guide to Multiplet Calculations*, pp. 143–199, (Springer Berlin Heidelberg, Berlin, Heidelberg2006). ISBN 978-3-540-33242-8.

[53] J. Rodríguez-Carvajal. 'Recent advances in magnetic structure determination by neutron powder diffraction'. *Phys. B Condens. Matter*, **192**, 1; pp. 55–69 (1993).

[54] C. Detlefs, M. Sanchez del Rio, and C. Mazzoli. 'X-ray polarization: General formalism and polarization analysis'. *Eur. Phys. J. Spec. Top.*, **208**, 1; pp. 359–371 (2012), arXiv:/1106.4446.

[55] J. P. Hill and D. F. McMorrow. 'X-ray resonant exchange scattering: polarization dependence and correlation functions'. *Acta Crystallogr. Sect. A*, **52**; pp. 236–244 (1996).

[56] C. Mazzoli, S. B. Wilkins, *et al.* 'Disentangling multipole resonances through a full x-ray polarization analysis'. *Phys. Rev. B*, **76**; p. 195118 (2007).

[57] R. D. Johnson, S. R. Bland, *et al.* 'Determination of magnetic order of the rare-earth ions in multiferroic TbMn$_2$O$_5$'. *Phys. Rev. B*, **78**; p. 104407 (2008).

[58] V. Scagnoli, C. Mazzoli, *et al.* 'Linear polarization scans for resonant X-ray diffraction with a double-phase-plate configuration'. *J. Synchrotron Radiat.*, **16**; pp. 778–787 (2009).

[59] V. Scagnoli, C. Mazzoli, *et al.* 'Experimental evidence of anapolar moments in the antiferromagnetic insulating phase of V_2O_3 obtained from x-ray resonant Bragg diffraction'. *Phys. Rev. B*, **81**; p. 085107 (2010).

[60] D. K. Shukla, S. Francoual, *et al.* 'Ho and Fe magnetic ordering in multiferroic $HoFe_3$ (BO_3)$_4$'. *Phys. Rev. B*, **86**; p. 224421 (2012).

[61] S. Sulyanov, P. Dorovatovskii, and H. Boysen. 'A simple approach to determine the polarization coefficient at synchrotron radiation stations'. *J. Appl. Crystallogr.*, **47**, 4; pp. 1449–1451 (2014).

[62] A. M. Strydom. 'Thermal and electronic transport in $CeRu_2Al_{10}$: Evidence for a metal-insulator transition'. *Phys. B*, **404**, 19; pp. 2981–2984 (2009).

[63] T. Nishioka, Y. Kawamura, *et al.* 'Novel Phase Transition and the Pressure Effect in $YbFe_2Al_{10}$-type CeT_2Al_{10}(T = Fe, Ru, Os)'. *J. Phys. Soc. Japan*, **78**, 12; p. 123705 (2009).

[64] Y. Muro, J. Kajino, *et al.* 'Structural modification and metamagnetic anomaly in the ordered state of $CeOs_2Al_{10}$'. *Phys. Rev. B*, **81**; p. 214401 (2010).

[65] T. Takesaka, K. Oe, *et al.* 'Semiconducting behavior in $CeFe_2Al_{10}$ and $CeRu_2Al_{10}$ single crystals'. *J. Phys. Conf. Ser.*, **200**; p. 012201 (2010).

[66] K. Yutani, Y. Muro, *et al.* 'Crystal-field effect on anisotropic magnetic properties of CeT_2Al_{10} (T = Ru and Os)'. *J. Phys. Conf. Ser.*, **10**; pp. 9–12 (2012).

[67] D. T. Adroja, A. D. Hillier, *et al.* 'Long-range ordering of reduced magnetic moments in the spin-gap compound $CeOs_2Al_{10}$ as seen via muon spin relaxation and neutron scattering'. *Phys. Rev. B*, **82**; p. 104405 (2010), arXiv:/1008.3461.

[68] H. Kato, R. Kobayashi, *et al.* 'Magnetic Structure Determination of CeT_2Al_{10} (T=Ru and Os): Single Crystal Neutron Diffraction Studies'. *J. Phys. Soc. Japan*, **80**; pp. 073701–1–4 (2011).

[69] D. D. Khalyavin, A. D. Hillier, *et al.* 'Long-range magnetic order in $CeRu_2Al_{10}$ studied via muon spin relaxation and neutron diffraction'. *Phys. Rev. B*, **82**; p. 100405(R) (2010), `arXiv:/1006.1618`.

[70] R. Kobayashi, Y. Ogane, *et al.* 'Change in unusual magnetic properties by Rh substitution in $CeRu_2Al_{10}$'. *J. Phys. Soc. Japan*, **82**, 9; p. 093702 (2013).

[71] A. Kondo, K. Kindo, *et al.* 'Marked change in the ground state of $CeRu_2Al_{10}$ induced by small amount of Rh substitution'. *J. Phys. Soc. Japan*, **82**, 5; p. 054709 (2013).

[72] H. Guo, H. Tanida, *et al.* 'Magnetic instability induced by Rh doping in the Kondo semiconductor $CeRu_2Al_{10}$'. *Phys. Rev. B*, **88**; p. 115206 (2013).

[73] A. Bhattacharyya, D. D. Khalyavin, *et al.* 'Anomalous change of the magnetic moment direction by hole doping in $CeRu_2Al_{10}$'. *Phys. Rev. B*, **90**; p. 174412 (2014).

[74] D. T. Adroja, A. D. Hillier, *et al.* 'Contrasting effect of La substitution on the magnetic moment direction in the Kondo semiconductors CeT_2Al_{10} (T=Ru,Os)'. *Phys. Rev. B*, **92**; p. 094425 (2015).

[75] K. Hayashi, Y. Muro, *et al.* 'Effect of Si Substitution on the Antiferromagnetic Ordering in the Kondo Semiconductor $CeRu_2Al_{10}$'. *J. Phys. Soc. Japan*, **85**; p. 034714 (2016).

[76] D. D. Khalyavin, D. T. Adroja, *et al.* 'Change of magnetic ground state by light electron doping in $CeOs_2Al_{10}$'. *Phys. Rev. B*, **88**; p. 060403 (2013).

[77] D. D. Khalyavin, D. T. Adroja, *et al.* 'Magnetic ordering with reduced cerium moments in hole-doped $CeOs_2Al_{10}$'. *Phys. Rev. B*, **89**; p. 064422 (2014).

[78] A. Bhattacharyya, D. T. Adroja, *et al.* 'Contrasting carrier doping effects in the Kondo insulator $CeOs_2Al_{10}$: The influential role of c-f hybridisation on spin-gap formation'. *Phys. Rev. B*, **90**; p. 174422 (2014).

[79] F. Steglich, J. Aarts, C. D. Bredl, W. Lieke, D. Meschede, W. Franz and H. Schäfer. 'Superconductivity in the Presence of Strong Pauli Paramagnetism: CeCu$_2$Si$_2$'. *Phys. Rev. Lett.*, **437**, 25; pp. 1892–1896 (1979).

[80] K. Andres, J. Graebner, and H. Ott. '4f-Virtual-Bound-State Formation in CeAl$_3$ at Low Temperatures'. *Phys. Rev. Lett.*, **35**, 26; pp. 1779–1782 (1975).

[81] J. Kondo. 'Resistance Minimum in Dilute Magnetic Alloys'. *Prog. Theor. Phys.*, **32**, 1; pp. 37–49 (1964).

[82] S. Doniach. 'The Kondo lattice and weak antiferromagnetism'. *Phys. B+C*, **91**; pp. 231–234 (1977).

[83] A. Kumar, P. Ahluwalia, S. Kumar, and K. Sharma. 'Competition between Kondo effect and RKKY interactions in heavy-fermion systems: Specific heat'. *Phys. Rev. B*, **56**, 6; pp. 3145–3148 (1997).

[84] B. Coqblin, J. R. Iglesias, *et al.* 'Doniach diagram for ordered, disordered and underscreened Kondo lattices'. *J. Magn. Magn. Mater.*, **320**; pp. 1989–1994 (2008), arXiv:/0708.3807.

[85] J. Iglesias, C. Lacroix, and B. Coqblin. 'Revisited Doniach diagram: Influence of short-range antiferromagnetic correlations in the Kondo lattice'. *Phys. Rev. B*, **56**, 18; pp. 11820–11826 (1997).

[86] B. Coqblin, M. A. Gusmão, *et al.* 'Competition between magnetic order and Kondo effect in cerium compounds'. *J. Magn. Magn. Mater.*, **22**; pp. 115–117 (2001).

[87] P. De Gennes, P. Pincus, R. Velasco, and F. Brochard. 'Remarks on polyelectrolyte conformation'. *J. Phys. Fr.*, **37**, 12; pp. 1461–1473 (1976).

[88] Y. Muro, K. Motoya, Y. Saiga, and T. Takabatake. 'Formation of a hybridization gap in a cage-like compound CeFe$_2$Al$_{10}$'. *J. Phys. Soc. Japan*, **78**, 8; pp. 9–11 (2009).

[89] J. Freudenberger, G. Fuchs, *et al.* 'Breakdown of de Gennes scaling in Ho$_x$Lu$_{1-x}$Ni$_2$B$_2$C'. *J. Magn. Magn. Mater.*, **187**, 3; pp. 309–317 (1998).

[90] A. Yatskar, N. Budraa, *et al.* 'Heavy-electron behavior in single-crystal YbNi$_2$B$_2$C'. *Phys. Rev. B*, **54**, 6; pp. R3772–R3775 (1996).

[91] Y. Muro, J. Kajino, T. Onimaru, and T. Takabatake. 'Magnetic and Transport Properties of ROs$_2$Al$_{10}$ (R=Pr, Nd, Sm, and Gd)'. *J. Phys. Soc. Japan*, **80** (2011).

[92] G. Morrison, N. Haldoaarachchige, D. P. Young, and J. Y. Chan. 'Magnetic and transport properties of single crystal LnRu$_2$Al$_{10}$ (Ln = Pr, Gd, Yb).' *J. Phys. Condens. Matter*, **24**, 35; p. 356002 (2012).

[93] M. Sera, H. Nohara, *et al.* 'Unusual temperature-dependent exchange interaction in GdFe$_2$Al$_{10}$ in comparison with GdRu$_2$Al$_{10}$'. *Phys. Rev. B*, **88**; p. 100404 (2013).

[94] T. Ishiga, T. Wakita, *et al.* 'Electronic Structures of CeM$_2$Al$_{10}$ (M = Fe, Ru, and Os) Studied by Soft X-ray Resonant and High-Resolution Photoemission Spectroscopies'. *J. Phys. Soc. Japan*, **094717**; pp. 1–17 (2014), arXiv:/1407.6781.

[95] F. Strigari, T. Willers, *et al.* 'Crystal-field ground state of the orthorhombic Kondo insulator CeRu$_2$Al$_{10}$'. *Phys. Rev. B*, **86**; p. 081105(R) (2012), arXiv:/1208.2842v1.

[96] F. Strigari, T. Willers, *et al.* 'Crystal field ground state of the orthorhombic Kondo semiconductors CeOs$_2$Al$_{10}$ and CeFe$_2$Al$_{10}$'. *Phys. Rev. B*, **87**; p. 125119 (2013).

[97] S.-i. Kimura, T. Iizuka, *et al.* 'Optical study of charge instability in CeRu$_2$Al$_{10}$ in comparison with CeOs$_2$Al$_{10}$ and CeFe$_2$Al$_{10}$'. *Phys. Rev. B*, **84**; p. 165125 (2011).

[98] V. E. Dmitrienko. 'Anisotropy of Xray susceptibility and Bragg reflections in cubic crystals'. *Acta Crystallogr. Sect. A*, **40**, 2; pp. 89–95 (1984).

[99] M. Matsumura, Y. Kawamura, *et al.* 'Novel Phase Transition in CeRu$_2$Al$_{10}$ Probed by ^{27}Al-NQR/NMR -No Evidence of Magnetic Ordering-'. *J. Phys. Soc. Japan*, **78**, 12; p. 123713 (2009).

[100] Y. Joly, S. P. Collins, *et al.* 'Birefringence and polarization rotation in resonant x-ray diffraction'. *Phys. Rev. B*, **86**; p. 220101(R) (2012).

[101] C. T. Chantler. 'Detailed Tabulation of Atomic Form Factors, Photoelectric Absorption and Scattering Cross Section, and Mass Attenuation Coefficients in the Vicinity of Absorption Edges in the Soft X-Ray (Z=30-36, Z=60-89, E=0.1 keV-10 keV), Addressing Convergence Issues'. *J. Phys. Chem. Ref. Data*, **29**, 4; p. 597 (2000).

[102] J. Korger, T. Kolb, *et al.* 'The polarization properties of a tilted polarizer'. *Opt. Express*, **21**, 22; pp. 27032–27042 (2013), `arXiv:/1303.6974`.

[103] W. O'Brien and B. Tonner. 'Orbital and spin sum rules in x-ray magnetic circular dichroism'. *Phys. Rev. B*, **50**, 17; p. 12672 (1994).

[104] B. J. Campbell, H. T. Stokes, D. E. Tanner, and D. M. Hatch. 'ISODIS-PLACE: a web-based tool for exploring structural distortions'. *J. Appl. Crystallogr.*, **39**, 4; pp. 607–614 (2006).

[105] D. John O. 'Use of Symmetry in the Determination of Magnetic Structures'. **130**, 4; p. 1337 (1963).

[106] L. M. Sandratskii. 'Relation between spin and orbital magnetism in excited states of ferromagnetic materials'. *J. Phys. Condens. Matter*, **26**, 42; p. 426001 (2014).

[107] Q. Zhang, W. Tian, *et al.* 'Magnetic structures and interplay between rare-earth Ce and Fe magnetism in single-crystal CeFeAsO'. *Phys. Rev. B*, **88**; p. 174517 (2013).

[108] J. Hubbell and S. Seltzer. 'Tables of X-Ray Mass Attenuation Coefficients and Mass Energy-Absorption Coefficients (version 1.4)'. Available online at `nist.gov/pml/x-ray-mass-attenuation-coefficients`, accessed: May 2017.

[109] T. Frawley, R. Schoonmaker, *et al.* 'Elucidation of the helical spin structure of FeAs'. *Phys. Rev. B*, **95**; p. 064424 (2017).

[110] M. C. Langner, S. Roy, *et al.* 'Coupled Skyrmion Sublattices in Cu_2OSeO_3'. *Phys. Rev. Lett.*, **112**; p. 167202 (2014).

[111] J.-W. G. Bos, C. V. Colin, and T. T. M. Palstra. 'Magnetoelectric coupling in the cubic ferrimagnet Cu_2OSeO_3'. *Phys. Rev. B*, **78**; p. 094416 (2008).

[112] S. Seki, X. Z. Yu, S. Ishiwata, and Y. Tokura. 'Observation of Skyrmions in a Multiferroic Material'. *Science*, **336**, April; pp. 198–201 (2012).

[113] T. Skyrme. 'A Unified Field Theory of Mesons and Baryons'. *Nucl. Phys.*, **31**; p. 556 (1962).

[114] D. C. Wright and N. D. Mermin. 'Crystalline liquids: the blue phases'. *Rev. Mod. Phys.*, **61**, 2; pp. 385–432 (1989).

[115] A. Bogdanov and D. Yablonskii. 'Thermodynamically stable "vortices" in magnetically ordered crystals. The mixed state of magnets'. *Zh. Eksp. Teor. Fiz*, **95**, 1; p. 178 (1989).

[116] U. K. Rößler, A. N. Bogdanov, and C. Pfleiderer. 'Spontaneous skyrmion ground states in magnetic metals'. *Nature*, **442**, 7104; pp. 797–801 (2006).

[117] S. Mühlbauer, B. Binz, *et al.* 'Skyrmion Lattice in a Chiral Magnet'. *Science*, **323**, September; pp. 915–920 (2009).

[118] H. R. Karp. 'Magnetic Bubbles - a Technology in Making'. *Electronics*, **42**, 18; p. 83 (1969).

[119] A. H. Bobeck. 'Second Look at Magnetic Bubbles'. *IEEE Trans. Magn.*, **6**, 3; p. 445 (1970).

[120] A. H. Bobeck and H. E. D. Scovil. 'Magnetic Bubbles'. *Sci. Am.*, **224**, 6; p. 78 (1971).

[121] M. Hayashi, L. Thomas, *et al.* 'Current-Controlled Magnetic Domain-Wall Nanowire Shift Register'. *Science*, **320**, 5873; pp. 209–211 (2008).

[122] N. Nagaosa and Y. Tokura. 'Topological properties and dynamics of magnetic skyrmions.' *Nat. Nanotechnol.*, **8**, 12; pp. 899–911 (2013).

[123] F. Jonietz, S. Mulbauer, *et al.* 'Spin Transfer Torques in MnSi'. *Science*, **330**, September; pp. 1648–1652 (2011).

[124] X. Yu, M. Mostovoy, *et al.* 'Magnetic stripes and skyrmions with helicity reversals'. *Proc. Natl. Acad. Sci.*, **109**, 23; pp. 8856–8860 (2012).

[125] A. Rosch. 'Extra twist in magnetic bubbles.' *Proc. Natl. Acad. Sci.*, **109**, 23; p. 8793 (2012), `arXiv:/1204.4678v1`.

[126] A. Bogdanov and A. Hubert. 'Thermodynamically stable magnetic vortex states in magnetic crystals'. *J. Magn. Magn. Mater.*, **138**, 3; pp. 255–269 (1994).

[127] I. Kézsmárki, S. Bordács, *et al.* 'Néel-type skyrmion lattice with confined orientation in the polar magnetic semiconductor GaV$_4$S$_8$'. *Nat. Mater.*, **14**, September; p. 1116 (2015).

[128] X. Z. Yu, Y. Onose, *et al.* 'Real-space observation of a two-dimensional skyrmion crystal'. *Nature*, **465**, 7300; pp. 901–904 (2010).

[129] X. Z. Yu, N. Kanazawa, *et al.* 'Near room-temperature formation of a skyrmion crystal in thin-films of the helimagnet FeGe'. *Nat. Mater.*, **10**, February; p. 106 (2011).

[130] X. Z. Yu, N. Kanazawa, *et al.* 'Skyrmion flow near room temperature in an ultralow current density'. *Nat. Commun.*, **3**; p. 988 (2012).

[131] L. Kong and J. Zang. 'Dynamics of an insulating skyrmion under a temperature gradient'. *Phys. Rev. Lett.*, **111**; p. 067203 (2013), `arXiv:/1308.2343v1`.

[132] N. Romming, C. Hanneken, *et al.* 'Writing and deleting single magnetic skyrmions.' *Science*, **341**, 6146; pp. 636–9 (2013), `arXiv:/1504.0157`.

[133] T. Okubo, S. Chung, and H. Kawamura. 'Multiple-q states and the Skyrmion lattice of the triangular-lattice Heisenberg antiferromagnet under magnetic fields'. *Phys. Rev. Lett.*, **108**; p. 017206 (2012), `arXiv:/1109.6161`.

[134] S. Heinze, K. von Bergmann, *et al.* 'Spontaneous atomic-scale magnetic skyrmion lattice in two dimensions'. *Nat. Phys.*, **7**, 9; pp. 713–718 (2011).

[135] M. Amara, P. Morin, and F. Bourdarot. 'Experimental study of the magnetic phase diagrams of NdZn'. *J. Phys. Condens. Matter*, **9**; pp. 157–170 (1995).

[136] E. M. Forgan, E. P. Gibbons, K. A. McEwen, and D. Fort. 'Observation of a Quadruple-q Magnetic Structure in Neodymium'. *Phys. Rev. Lett.*, **62**, 4; pp. 470–473 (1989).

[137] J. Kouvel and J. Kasper. 'Long-range antiferromagnetism in disordered FeNiMn alloys'. *J. Phys. Chem. Solids*, **24**, 4; pp. 529–563 (1963).

[138] M. J. Longfield, J. A. Paixão, N. Bernhoeft, and G. H. Lander. 'Resonant x-ray scattering from multi-k magnetic structures'. *Phys. Rev. B*, **66**; p. 054417 (2002).

[139] P. G. Meunier and M. Bertaud. 'Constates cristallogrphiques de $CuSe_2O_5$, $CuSeO_3$, et Cu_2SeO_4'. *Crystallogr. Reports*, **9**, 4; pp. 364–366 (1976).

[140] K. Kohn. 'A New Ferrimagnet Cu_2SeO_4'. *J. Phys. Soc. Japan*, **42**, 6; p. 2065 (1977).

[141] T. Adams, A. Chacon, *et al.* 'Long-wavelength helimagnetic order and skyrmion lattice phase in Cu_2OSeO_3'. *Phys. Rev. Lett.*, **108**; p. 237204 (2012), `arXiv:/1204.3597`.

[142] V. P. Gnezdilov, K. V. Lamonova, *et al.* 'Magnetoelectricity in the ferrimagnetic Cu_2OSeO_3: symmetry analysis and Raman scattering study'. *Low Temp. Phys.*, **36**, 6; p. 550 (2010).

[143] M. Belesi, I. Rousochatzakis, *et al.* 'Magnetoelectric effects in single crystals of the cubic ferrimagnetic helimagnet Cu_2OSeO_3'. *Phys. Rev. B*, **85**; p. 224413 (2012), `arXiv:/1204.3783v1`.

[144] E. Ruff, P. Lunkenheimer, *et al.* 'Magnetoelectric effects in the skyrmion host material Cu_2OSeO_3'. *Sci. Rep.*, **5**; p. 15025 (2015), `arXiv:/1504.03918`.

[145] M. Binnewies, R. Glaum, M. Schmidt, and P. Schmidt. 'Chemical Vapor Transport Reactions - A Historical Review'. *Z. Anorg. Allg. Chem.*, , 1953; pp. 219–229 (2013).

[146] M. Belesi, I. Rousochatzakis, *et al.* 'Ferrimagnetism of the magnetoelectric compound Cu_2OSeO_3 probed by ^{77}Se NMR'. *Phys. Rev. B*, **82**; p. 094422 (2010), `arXiv:/1008.2010`.

[147] G. A. Bain and J. F. Berry. 'Diamagnetic Corrections and Pascal ' s Constants'. *J. Chem. Educ.*, **85**, 4; pp. 532–536 (2008).

[148] D. H. Templeton, L. K. Templeton, J. C. Phillips, and K. O. Hodgson. 'anomalous scattering of x-rays by cesium and cobalt measured with synchrotron radiation'. *Acta Crystallogr. Sect. A*, **36**, 3; pp. 436–442 (1980).

[149] L. K. Templeton, D. H. Templeton, and R. P. Phizackerley. 'L_3-Edge anomalous scattering by gadolinium and samarium measured at high-resolution with synchrotron raditaion'. *Acta Crystallogr. Sect. A*, **38**, JAN; pp. 74–78 (1982).

[150] V. E. Dmitrienko. 'Forbidden reflections due to anisotropic Xray susceptibility of crystals'. *Acta Crystallogr. Sect. A*, **39**, 1; pp. 29–35 (1983).

[151] N. W. Price, R. D. Johnson, *et al.* 'Coherent Magnetoelastic Domains in Multiferroic $BiFeO_3$ Films'. *Phys. Rev. B*, **117**; p. 177601 (2016).

[152] S. L. Zhang, A. Bauer, *et al.* 'Resonant elastic x-ray scattering from the skyrmion lattice in Cu_2OSeO_3'. *Phys. Rev. B*, **93**; p. 214420 (2016).

[153] J. H. Yang, Z. L. Li, *et al.* 'Strong Dzyaloshinskii-Moriya interaction and origin of ferroelectricity in Cu_2OSeO_3'. *Phys. Rev. Lett.*, **109**; p. 107203 (2012).

[154] P. Bak and M. H. Jensen. 'Theory of helical magnetic structures and phase transitions in MnSi and FeGe'. *J. Phys. C Solid State Phys.*, **13**, 31; pp. L881–L885 (2000).

[155] O. Nakanishi, A. Yanase, A. Hasegawa, and M. Kataoka. 'The origin of the helical spin density wave in MnSi'. *Solid State Commun.*, **35**, 12; pp. 995–998 (1980).

[156] N. Romming, A. Kubetzka, *et al.* 'Field-dependent size and shape of single magnetic Skyrmions'. *Phys. Rev. Lett.*, **114**; p. 177203 (2015), `arXiv:/1504.0157`.

[157] S. D. Matteo, Y. Joly, *et al.* 'Local Chiral-Symmetry Breaking in Globally Centrosymmetric Crystals'. *Phys. Rev. Lett.*, **91**, December; p. 257402 (2003).

[158] S. Agrestini, L. C. Chapon, *et al.* 'Nature of the Magnetic Order in $Ca_3Co_2O_6$'. *Phys. Rev. Lett*, **101**; p. 097207 (2008).

[159] V. Hardy, M. R. Lees, *et al.* 'Temperature and time dependence of the field-driven magnetization steps in $Ca_3Co_2O_6$ single crystals'. *Phys. Rev.*, **70**; p. 064424 (2004).

[160] T. Frawley. *Magnetism in Iron Based Compounds.* Ph.D. thesis, Durham University (2015).

[161] S. L. Zhang, G. V. D. Laan, and T. Hesjedal. 'topological winding number of skyrmions'. *Nat. Commun.*, **8**; p. 14619 (2017).

[162] A. M. Mulders, S. M. Lawrence, *et al.* 'Circularly polarized soft x-ray diffraction study of helical magnetism in hexaferrite'. *Phys. Rev. B*, **81**; p. 092405 (2010).

[163] A. K. Nayak, V. Kumar, *et al.* 'Magnetic antiskyrmions above room temperature in tetragonal Heusler materials'. *Nature*, **advance online publication** (2017).

[164] C. N. R. Rao Solid. 'Transition metal oxides1'. *Annu. Rev. Phys. Chern.*, **40**, 40; pp. 291–326 (1989).

[165] J.-p. Renard and A.-M. Haghiri-Gosnet. 'CMR manganites : physics , thin films and devices'. *J. Phys. D. Appl. Phys.*, **36**; p. R127 (2003).

[166] T. Kimura, T. Goto, *et al.* 'Magnetic control of ferroelectric polarization'. *Nature*, **426**, 6962; pp. 55–58 (2003). 10.1038/nature02018.

[167] T. Yamanaka, N. Hirai, and Y. Komatsu. 'Structure change of $Ca_{1-x}Sr_xTiO_3$ perovskite with composition and pressure'. *Am. Mineral.*, **87**, 1997; pp. 1183–1189 (2002).

[168] W. A. Harrison. *Electronic Structure and the Properties of Solids: The Physics of the Chemical Bond,* (Dover Publications1989). ISBN 978-0486660219.

[169] Y. Kumar, R. J. Choudhary, *et al.* 'Strain dependent stabilization of metallic paramagnetic state in epitaxial $NdNiO_3$ thin films'. *Appl. Phys. Lett.*, **101**, 13; p. 132101 (2012).

[170] J. H. Haeni, P. Irvin, *et al.* 'Room-temperature ferroelectricity in strained $SrTiO_3$.' *Nature*, **430**, August; pp. 758–761 (2004).

[171] A. M. Glazer. 'Simple ways of determining perovskite structures'. *Acta Crystallogr. Sect. A*, **31**, 6; pp. 756–762 (1975).

[172] K. Momma and F. Izumi. 'VESTA 3 for three-dimensional visualization of crystal, volumetric and morphology data'. *J. Appl. Crystallogr.*, **44**, 6; pp. 1272–1276 (2011).

[173] J. L. Garcia-Munoz, M. A. G. Aranda, J. A. Alonso, and M. J. Martinez-Lope. 'Structure and charge order in the antiferromagnetic band-insulating phase of $NdNiO_3$'. *Phys. Rev. B*, **79**; p. 134432 (2009).

[174] N. Nakagawa, H. Y. Hwang, and D. A. Muller. 'Why some interfaces cannot be sharp'. *Nat. Mater.*, **5**, 3; pp. 204–209 (2006).

[175] E. Benckiser, M. W. Haverkort, *et al.* 'Orbital reflectometry of oxide heterostructures'. *Nat. Mater.*, **10**, 3; pp. 189–193 (2011).

[176] H. Yamada, M. Kawasaki, *et al.* '$LaMnO_3$/$SrMnO_3$ interfaces with coupled charge-spin-orbital modulation'. *Appl. Phys. Lett.*, **89**, 5; p. 052506 (2006).

[177] S. Kobayashi, Y. Tokuda, *et al.* 'Quantitative analyses of oxidation states for cubic $SrMnO_3$ and orthorhombic $SrMnO_{2.5}$ with electron energy loss spectroscopy'. *J. Appl. Phys.*, **108**; pp. 2–5 (2010).

[178] C. Ritter, M. Ibarra, *et al.* 'Influence of oxygen content on the structural, magnetotransport, and magnetic properties of $LaMnO_{3+\delta}$'. *Phys. Rev. B*, **56**, 14; pp. 8902–8911 (1997).

[179] G. Banach and W. M. Temmerman. 'Half-Metallicity of LSMO'. *archive* (2003), `arXiv:/cond-mat/0308272`.

[180] G. Banach, R. Tyer, and W. M. Temmerman. 'Study of half-metallicity in LSMO'. *J. Magn. Magn. Mater.*, **272-276**; pp. 1963–1964 (2004).

[181] T. Takeda and S. Ohara. 'Magnetic Structure of the Cubic Perovskite Type SrMnO$_3$'. *JPSJ*, **37**; p. 275 (1974).

[182] R.-N. Song, M.-H. Hu, X.-R. Chen, and J.-D. Guo. 'Epitaxial growth and thermostability of cubic and hexagonal SrMnO$_3$ films on SrTiO$_3$(111)'. *Front. Phys.*, **10**, 3; pp. 321–326 (2015).

[183] X. Zhai, L. Cheng, *et al.* 'Correlating interfacial octahedral rotations with magnetism in (LaMnO$_{3+\delta}$)$_N$/(SrTiO$_3$)$_N$ superlattices.' *Nat. Commun.*, **5**; p. 4283 (2014).

[184] T. T. Fister, H. Zhou, *et al.* 'Octahedral rotations in strained LaAlO$_3$/SrTiO$_3$ (001) heterostructures'. *APL Mater.*, **2**, 2; pp. 0–9 (2014).

[185] J. He, A. Borisevich, *et al.* 'Control of octahedral tilts and magnetic properties of perovskite oxide heterostructures by substrate symmetry'. *Phys. Rev. Lett.*, **105**; p. 227203 (2010).

[186] H.-J. Liu, J.-C. Lin, *et al.* 'A Metal-Insulator Transition of the Buried MnO$_2$ Monolayer in Complex Oxide Heterostructure'. *Adv. Mater.*, **28**; pp. 9142–9151 (2016).

[187] B. C. Huang, Y. P. Chiu, *et al.* 'Mapping band alignment across complex oxide heterointerfaces'. *Phys. Rev. Lett.*, **109**; p. 246807 (2012).

[188] T. Niemöller, M. von Zimmermann, *et al.* 'The charge ordered phase in La$_{1-x}$Sr$_x$MnO$_3$ studied by means of high energy X-ray diffraction'. *Eur. Phys. J. B*, **8**, 1; pp. 5–8 (1999).

[189] R. Perez-Casero, J. Perrière, *et al.* 'Thin films of oxygen-deficient perovskite phases by pulsed-laser ablation of strontium titanate'. *Phys. Rev. B*, **75**; p. 165317 (2007).

[190] M. L. Scullin, J. Ravichandran, *et al.* 'Pulsed laser deposition-induced reduction of SrTiO$_3$ crystals'. *Acta Mater.*, **58**, 2; pp. 457–463 (2010).

[191] A. Ohtomo and H. Y. Hwang. 'A high-mobility electron gas at the LaAlO$_3$/SrTiO$_3$ heterointerface.' *Nature*, **427**, 6973; pp. 423–426 (2004).

[192] P. R. Willmott, S. A. Pauli, *et al.* 'Structural basis for the conducting interface between LaAlO$_3$ and SrTiO$_3$'. *Phys. Rev. Lett.*, **99**; p. 155502 (2007).

[193] a. H. De Vries, L. Hozoi, and R. Broer. 'Origin of the chemical shift in x-ray absorption near-edge spectroscopy at the Mn K-edge in manganese oxide compounds'. *Int. J. Quantum Chem.*, **91**, 1; pp. 57–61 (2002).

[194] T. Hishida, K. Ohbayashi, and T. Saitoh. 'Hidden relationship between the electrical conductivity and the Mn $2p$ core-level photoemission spectra in La$_{1-x}$Sr$_x$MnO$_3$'. *J. Appl. Phys.*, **113**, 4; pp. 1–7 (2013), `arXiv:/1301.2128v1`.

[195] H. Tan, J. Verbeeck, A. Abakumov, and G. V. Tendeloo. 'Oxidation state and chemical shift investigation in transition metal oxides by EELS'. *Ultramicroscopy*, **116**; pp. 24–33 (2012).

[196] S. Matzen, J. B. Moussy, *et al.* 'Epitaxial growth and ferrimagnetic behavior of MnFe$_2$O$_4$(111) ultrathin layers for room-temperature spin filtering'. *Phys. Rev. B - Condens. Matter Mater. Phys.*, **83**, 18; pp. 1–10 (2011).

[197] C. Piamonteze, P. Miedema, and F. M. F. De Groot. 'Accuracy of the spin sum rule in XMCD for the transition-metal L edges from manganese to copper'. *Phys. Rev. B - Condens. Matter Mater. Phys.*, **80**, 18; pp. 1–12 (2009).

[198] V. Blanco-Gutiérrez, E. Climent-Pascual, R. Sáez-Puche, and M. J. Torralvo-Fernández. 'Temperature dependence of superparamagnetism in CoFe$_2$O$_4$ nanoparticles and CoFe$_2$O$_4$/SiO$_2$ nanocomposites'. *Phys. Chem. Chem. Phys.*, pp. 9186–9193 (2016).

[199] B. Andrzejewski, W. Bednarski, *et al.* 'Magnetization Enhancement in Magnetite Nanoparticles capped with Alginic Acid'. pp. 1–9.

[200] M. Filippousi, M. Angelakeris, *et al.* 'Surfactant Effects on the Structural and Magnetic Properties of Iron Oxide Nanoparticles'. *Chem. Mater.*, **30**; pp. 16209–16217 (2014).

[201] M. Sneha, M. Sundaram, and N. M. Sundaram. 'Preparation and characterization of an iron oxide-hydroxyapatite nanocomposite for potential bone cancer therapy'. *Int. J. Nanomedicine*, **10**; pp. 99–106 (2015).

[202] H. M. Lu, W. T. Zheng, and Q. Jiang. 'Saturation magnetization of ferromagnetic and ferrimagnetic nanocrystals at room temperature'. *J. Phys. D. Appl. Phys.*, **40**, 2; pp. 320–325 (2007).

[203] S. Bedanta and W. Kleemann. 'Supermagnetism'. *J. Phys. D. Appl. Phys.*, **42**, 1; p. 13001 (2009).

[204] Y. Zhang, M. Liu, *et al.* 'Atomic layer deposition of superparamagnetic and ferrimagnetic magnetite thin films'. *J. Appl. Phys.*, **117**, 17 (2015).

[205] J. Balogh, I. Dezsi, *et al.* 'Magnetic properties of the Fe-MgO interface studied by Mossbauer spectroscopy'. *Phys. Rev. B*, **87**, 17 (2013).

[206] Y. Shiratsuchi, Y. Endo, and M. Yamamoto. 'Thickness dependence of magnetic state of Fe thin films grown on Al2O3(0001) substrates with an inclined angle'. *Sci. Technol. Adv. Mater.*, **5**, 1-2; pp. 73–78 (2004).

[207] D. Ravinder and P. Shalini. 'Investigation of superparamagnetism in Co-Zn ferrite thin films produced by pulsed-laser deposition'. *Appl. Phys. Lett.*, **82**, 26; pp. 4738–4739 (2003).

[208] V. Halpern. 'A Generalized Mechanism for Superexchange'. *Proc. R. Soc. Lond. A. Math. Phys. Sci.*, **291**, 1424; pp. 113–128 (1966).

[209] Q. A. Pankhurst, J. Connolly, S. K. Jones, and J. Dobson. 'Applications of magnetic nanoparticles in biomedicine'. *J. Phys. D. Appl. Phys.*, **36**, 13; p. R167 (2003).

[210] M. Misiorny, M. Hell, and M. R. Wegewijs. 'Spintronic magnetic anisotropy'. *Nat Phys*, **9**, 12; pp. 801–805 (2013).

[211] A. Caneschi, D. Gatteschi, and A. le Lirzin. 'Crystal structure and magnetic properties of a new ferrimagnetic chain containing manganese(II) and a

nitronyl-nitroxide radical. Magnetic ordering in Mn(hfac)2NITR compounds'. *J. Mater. Chem.*, **4**, 2; pp. 319–326 (1994).

[212] W. Hibbs, D. K. Rittenberg, *et al.* 'Solvent Dependence of the Structure and Magnetic Ordering of Ferrimagnetic Manganese (III) meso-Tetraphenylporphyrin Tetracyanoethenide, [MnTPP] +[TCNE]- x(solvent). Evidence for Orientationally Disordered [TCNE]-'. *Inorg. Chem.*, **40**, III; pp. 1915–1925 (2001).

[213] J. P. Chapman, J. P. Attfield, *et al.* 'A Ferrimagnetic Manganese Oxide with a Layered Perovskite Structure: YBaMn2O5'. *Angew. Chemie Int. Ed. English*, **35**, 21; pp. 2482–2484 (1996).

[214] K. Mandal, S. Mitra, and P. A. Kumar. 'Deviation from Bloch $T^{3/2}$ law in ferrite nanoparticles'. *Europhys. Lett.*, **75**, 4; pp. 618–623 (2006).

[215] B. Andrzejewski, W. Bednarski, *et al.* 'Magnetization enhancement in magnetite nanoparticles capped with alginic acid'. *Compos. Part B Eng.*, **64**; pp. 147–154 (2014).

[216] N. Fontaíña Troitiño, B. Rivas-Murias, B. Rodríguez-González, and V. Salgueiriño. 'Exchange Bias Effect in CoO@Fe3O4 CoreShell Octahedron-Shaped Nanoparticles'. *Chem. Mater.*, **26**, 19; pp. 5566–5575 (2014).